DISSERTATION

NAVIGATING THE THERMODYNAMIC LANDSCAPE IN SEARCH OF SYNTHETIC ROUTES TO TERNARY NITRIDES

Submitted by

Christopher Linfield Rom

Department of Chemistry

In partial fulfillment of the requirements

For the Degree of Doctor of Philosophy

Colorado State University

Fort Collins, Colorado

Fall 2022

Doctoral Committee:

Advisor: James R. Neilson
Co-Advisor: Amy L. Prieto

Justin Sambur
Grzegorz Szamel
Kristen Buchanan

ABSTRACT

NAVIGATING THE THERMODYNAMIC LANDSCAPE IN SEARCH OF SYNTHETIC ROUTES TO TERNARY NITRIDES

Ternary nitride materials—a class of ceramics composed of two different metals bound with anionic nitrogen (N^{3-}) as a solid—are underexplored because they are difficult to make. Nitrides rarely occur in nature, as the oxygen in the air (O_2) is more reactive towards metals than the nitrogen (N_2). Consequently, oxide minerals dominate the earth's crust while nitride minerals are extremely rare. Almost all ternary nitrides that have been discovered have synthesized, usually with rigorously air-free conditions. Despite much effort in the past century, the number of known ternary nitrides (approximately 450) pales in comparison to that of ternary oxides (over 4,000). Yet there are world-changing materials within this small number of compounds, like the (In,Ga)N alloys that underpin efficient blue light emitting diodes. Fortunately, recent computational work has predicted a number of theoretically stable ternary nitrides, providing targets for synthesis.

This dissertation focuses on the synthesis of new ternary nitrides. Guided by increasingly user-friendly computational tools, these chapters describe syntheses overcome the thermodynamic barriers that often inhibit the formation of new ternary nitrides. Along the way, several new materials are discovered and characterized for promising magnetic and semiconducting properties: $MnSnN_2$, $MgWN_2$ in two structure types, Mg_3WN_4, $MgZrN_2$, $CaZrN_2$, and $CaHfN_2$. These adventures in synthesis not only report new compounds, but also highlight promising strategies for future explorations of uncharted nitride phase space.

ACKNOWLEDGEMENTS

I gratefully acknowledge the various funding agencies that have supported this work. Initial progress in synthesizing nitrides was seeded by the Research Corporation for Science Advancement Scialog award 2018. Much of the bulk synthesis work conducted at CSU was supported by the National Science Foundation (NSF) Career award (DMR-1653863). My internship at the National Renewable Energy Laboratory was supported by the Office of Science Graduate Student Research (SCGSR) program funded by the Department of Energy (DOE). Additional funding support was provided by the NSF DMR-2210780 and the DOE Early Career Award "Kinetic Synthesis of Metastable Nitrides". This work utilized the RMACC Summit supercomputer, which is supported by the National Science Foundation (awards ACI-1532235 and ACI-1532236), the University of Colorado Boulder and Colorado State University. The RMACC Summit supercomputer is a joint effort of the University of Colorado Boulder and Colorado State University. Research here used beamlines 11-BM and 17-BM-B at Advanced Photon Source at Argonne National Laboratory and beamline 1-5 at the Stanford Synchrotron Radiation Lightsource. Use of the Advanced Photon Source at Argonne National Laboratory was supported by the U. S. Department of Energy, Office of Science, Office of Basic Energy Sciences, under Contract No. DE-AC02-06CH11357. Use of the Stanford Synchrotron Radiation Lightsource, SLAC National Accelerator Laboratory, is supported by the U.S. Department of Energy, Office of Science, Office of Basic Energy Sciences under Contract No. DE-AC02-76SF00515.

My family made this scientific journey possible. First, thanks to my grandparents (Ace, Grams, Granddad, and Grandmom) for living frugally and saving up to fund education for their children and grandchildren. Thanks in particular to Grandmom, who taught me the basics of algebra when I was five years old. Turns out, that's a pretty useful skill. Thanks also to my Granddad for teaching me the 5P's: prior planning prevents poor performance. And thanks to Ace, for his wisdom on presenting my science before an audience: stand up

to be seen, speak loud to be heard, and sit down to be appreciated. Next, thanks to all my aunts, uncles, and cousins who have endured my attempts to explain my research. Your curiosity and kindness helped me learn to speak about my science and kept me enthusiastic about my research. Perhaps more importantly, your gentle ribbing keeps me humble. Thanks in particular to my Aunt Gretchen. Your monthly letters never failed to bring me joy. Last but not least, thanks to all my parents. Dad and Ayse, Mom and Steve, I am so grateful for your love and support.

My friends made this scientific journey fun. Thanks to Jordan Ricker for the (mostly) weekly phonecalls from across the world. Thanks to Alex Koegel and Amanda Kale for helping me learn to dance salsa (growth mindset!). Thanks to Sam Miller for reminding me to appreciate the little things. Thanks to Evan Senie for being the best roommate I ever could have wished for. Thanks to Christy Cashen and Lacey Beck for helping me learn the basics of rock climbing. Thanks to Charlie and Amber Quann for helping me establish a social circle outside of the lab. Thanks to Bob and Bev Bacon for being my Fort Collins grandparents. Thanks to Foothills Unitarian Universalist Church for providing me a spiritually nourishing community. Thanks to the Geller Center Food for Thought group for being a community space full of kind and thoughtful people, especially John Forrest, Sean Simpson, and Christina Geldert, who reminded me that I am a human *being*, not a human *doing*. Thanks to my friends from earlier in my education, who have cheered me on from afar: Emmy, Manny, Owen, Katie, Preston, Patrick, and so many more. Thanks to all of my running buddies for helping me stay healthy in body, mind, and soul, especially Ryan Clarke, CeAnn Udovich, Jacob VanderRoest, Gavin McEwen, Steven Johnson, Ashley Brasovan, and Zoë Rom. I am so grateful for the miles and conversations we have shared.

My mentors helped me find my way through this scientific journey. Thanks of course to my primary co-advisors, Amy Prieto and James Neilson. I could not have asked for more supportive supervisors, and I am so grateful for the way you have generously shared your insights, enthusiasm, creativity, and wisdom with me. I am also immensely grateful for

your patience through my occasional stumbles on this adventure in science. Thanks also to my committee (Justin Sambur, Grzegorz Szamel, and Kristen Buchanan) for your support, patience, advice, and encouragement. Thanks to those who mentored me at NREL: Sage Bauers, Rebecca Smaha, Andriy Zakutayev, Yeyoung Ha, and Annie Greenaway. The American people are incredibly fortunate to have you working on their behalf towards the goal of a renewable energy future. And thanks to my mentors from my time as an undergraduate: Augusta Hofstead-Duffy, Yuye Tong, Nicole Vanagas, and Karah Knope. Your inspiration and encouragement helped launch me on this adventure.

My peers and colleagues helped me through the highs and lows on each day of this scientific journey. I am so grateful for all my colleagues over the years in the Neilson Lab, Prieto Lab, and NREL Materials Discovery team. In particular, thanks to mentorship from Eve Mozur, Paul Todd, Max Schulze, Rebecca Miller, Dan Agos, Jen Lee, Leslie Kraynak, Jeff Ma, Jacob Boissiere, and Jewels Fallon. Learning from y'all has been a privilege and an honor. Special thanks to Allison Wustrow for being my exceptionally patient lab buddy (and overall friend) through so many pandemic lab shifts. Thanks to Cal Knebel for being a talented, curious, and enthusiastic undergraduate. Thanks also to colleagues at other institutions, who remind me that I am part of a big community. Thanks especially to Matt McDermott, Rachel Woods-Robinson, Chris Bartel, Nicholas Singstock, Aaron Holder, Akira Miura, Shannon Rogers and Safia Jilani. Many thanks to the scientists working at the various beamlines that supported this work, either in their official role or just as a helpful and talented fellow user: Andrey Yakovenko, Wenqian Xu, Nicholas Strange, and Nathan Johnson. Teamwork makes the dream work.

Special thanks to my partner Maureen Walsh. Your love and support carried me through the completion of this dissertation. I am so excited for our future ahead.

Finally, thanks to my brother, Kitt. The photo of you sitting in a crew shell on the water, flashing a smile and a thumbs up, has encouraged me daily. Thank you.

DEDICATION

I would like to dedicate this dissertation to my mom; the first scientist I ever met and the one who continues to inspire me most.

TABLE OF CONTENTS

LIST OF TABLES

LIST OF FIGURES

Chapter 1

Introduction

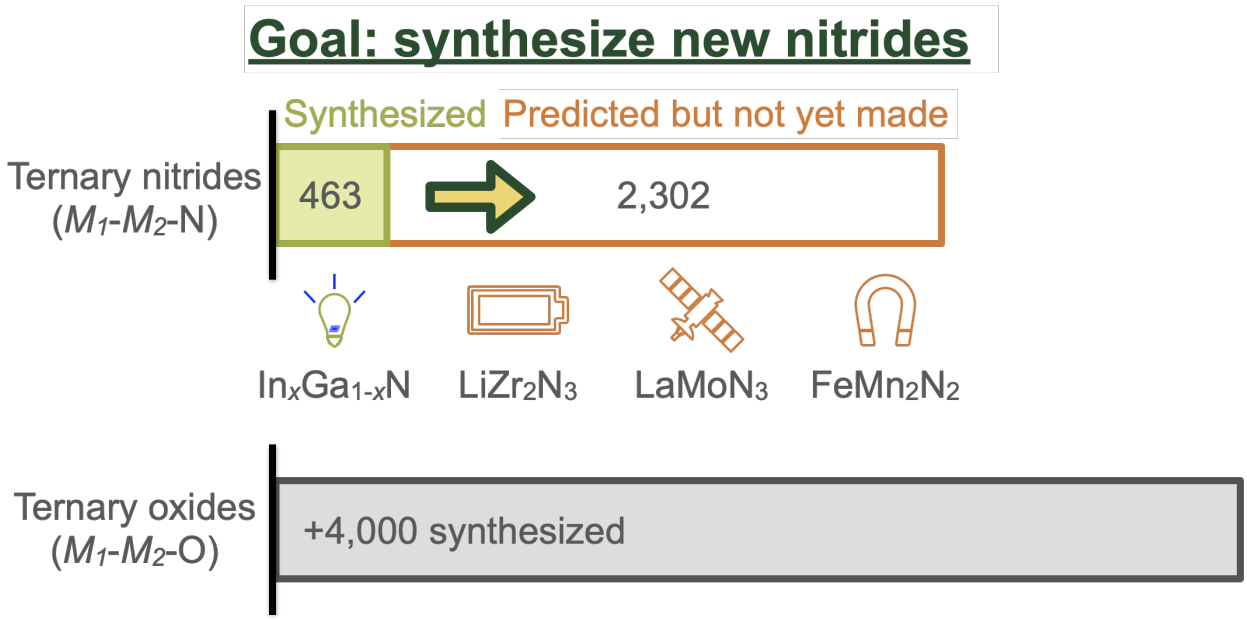

Figure 1.1: The main goal of my doctoral work has been to discover ways to synthesize new ternary nitrides, which have an order of magnitude fewer unique structures reported in the ICSD than ternary oxides. Structure counts from Greenaway, et al. (nitrides)[1] and Sun, et al. (oxides).[2]

Ternary nitrides—solid inorganic materials composed of two different metals bound with nitrogen anions (N^{3-})—are a promising area for materials discovery. Relatively few are known compared to more easily-synthesized materials like oxides. The number of known ternary nitrides in the Inorganic Crystal Structure Database in 2021 was 463, while over unique 4000 ternary oxide structures have been reported. Yet within this limited number of nitrides, there are world-changing materials. For example, $In_xGa_{1-x}N$ alloys are the key component of light emitting diodes (LEDs), a technology so important to modern life that the pioneers of the material earned the Nobel prize in 2014.[3]

Fortunately, computational studies have predicted a large number of new ternary nitrides worth targetting (Figure 1.1).[2,4–7] Most prominently, Sun, et al., mapped out a mas-

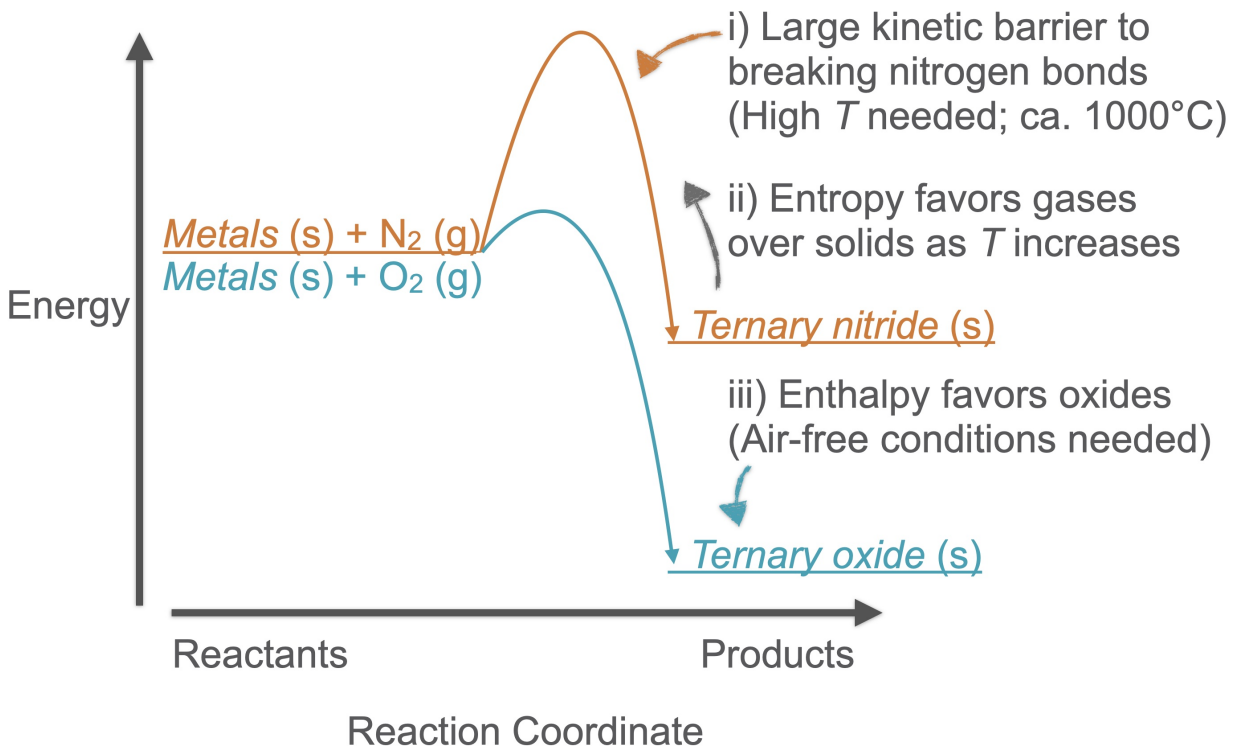

Figure 1.2: Three main challenges confront those seeking to synthesize nitrides: i) kinetic barriers like dissociating the strong triple-bond of molecular N_2, ii) increasing the synthesis temperature increases the entropic favorability of gases over solids, and iii) enthalpy favors oxides over nitrides, so rigorously air-free conditions are needed.

sive composition space 50×50 A-B-N composition space, predicting 244 new stable nitrides.[2] This long list of predicted phases holds are compounds which may help unlock better batteries (e.g., $LiZr_2N_3$), telecommunications (e.g., $LaMoN_3$), and magnets (e.g., $FeMn_2N_2$). However, technologies cannot be built upon materials that don't exist yet. The challenge of my doctoral work has been the synthesis of predicted ternary nitrides.

Solid state chemists like myself must confront three significant hurdles towards the goal of synthesizing new nitrides: i) kinetic barriers, ii) entropic challenges, and iii) enthalpic competition (Figure 1.2). The simplest kinetic barrier is the dissociation of elemental N_2 (941 kJ/mol dissociation energy). However, M-N bonds within solids are often strong too. These strong bonds can render metastable compounds synthetically accessible,[8] but can also inhibit synthesis by creating high energy barriers for rearranging the bonds within

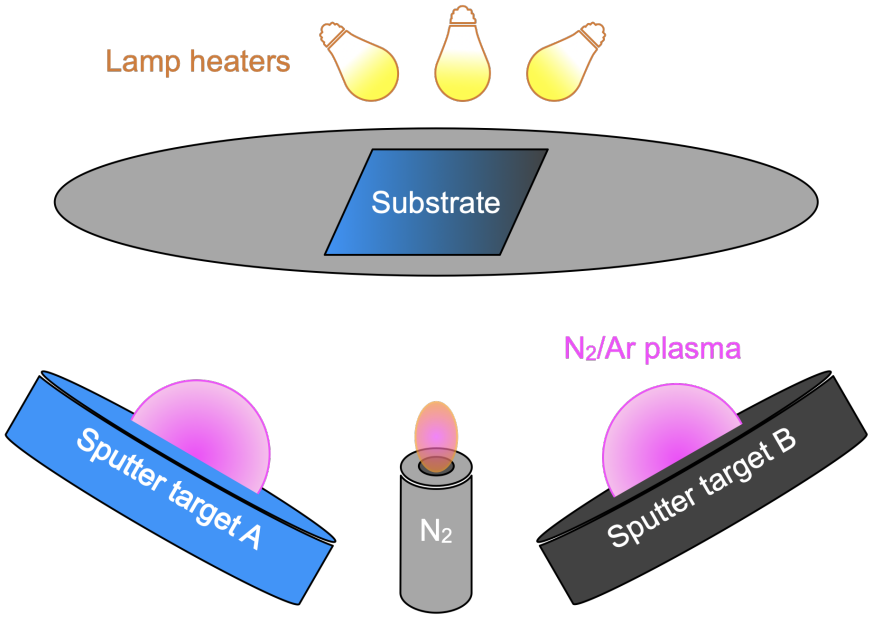

Figure 1.3: Diagram of a combinatorial sputtering experimental setup for synthesizing nitride thin films. Two sputter cathodes are positioned facing a stationary substrate. With the plasma on, they eject plumes of atoms towards the substrate. Based on this geometry, a compositional gradient is generated across the substrate (e.g. A-rich near cathode A, B-rich near cathode B). A gas mixture of Ar and N_2 can be used to make nitrides, with the option to increase the chemical potential (i.e., reactivity) of nitrogen using an N_2 cracker (bottom center). The substrate can be heated up to a maximum of 700 °C to 1000 °C (depending on the system) to change the structure of the deposited films.

binary precursors en route to ternary products. High temperatures are often needed to overcome these kinetic barriers, but there is a tradeoff. Increasing synthesis temperature also increases the entropic favorability ($T\Delta S$) of N_2 (g) formation, which can destabilize ternary nitrides relative to N_2 and/or binary nitrides. As for enthalpy, the simplest challenge is air-sensitivity. Oxides are more thermodynamically stable than nitrides (e.g., ΔH_f° = -0.90 eV/atom for Mg_3N_2, while ΔH_f° = -3.05 eV/atom for MgO).[9] Consequently, oxygen preferentially reacts with metals (or nitrides) to make oxides unless air-free techniques are used. In facing these challenges, I have helped synthesize six new ternary nitrides: $MnSnN_2$, $MgWN_2$ (in two-polymorphs), Mg_3WN_4, $MgZrN_2$, $CaZrN_2$, and $CaHfN_2$. As this dissertation largely focuses on synthesis challenges, the next few paragraphs focus on introducing the synthetic techniques used.

Combinatorial sputtering of nitride thin films has been the most promising strategy for materials discovery in recent years. Since 2018 (when Sun, et al., first posted their map on arXiv),[10] combinatorial sputtering has been used to discover numerous new ternary nitrides, including $MgTiN_2$, $MgZrN_2$, Mg_2NbN_3, $MgSnN_2$, Mg_2SbN_3, $MgHfN_2$, $ZnTiN_2$, Zn_2VN_3, Zn_2NbN_3, Zn_3MoN_4, Zn_2SbN_3, Zn_3WN_4, $LaWN_3$, $CeMoN_3$, and $CeWN_3$.[2,11–20] The technique is particularly powerful in its ability to increase the chemical potential of nitrogen (i.e., to "activate" nitrogen for reactivity) via the plasma used for sputtering.[21,22] This activated nitrogen allows combinatorial sputtering to synthesize metastable, nitrogen-rich phases.[23] Chapter 2 and Chapter 3 involve materials made by combinatorial sputtering, the experimental setup for which is diagrammed in Figure 1.3.

In contrast to combinatorial sputtering (which allows high-throughput synthesis of thin films), bulk synthesis methods produces free-standing powders. These powders allow detailed structural studies unhindered by a substrate and are important for many applications (e.g., abrasives).[24] Traditional ceramic syntheses are conducted by grinding together the desired elements (or binaries), and then heating the mixture of powders at elevated temperature in a controlled gas environment (Figure 1.4a). Using tube furnaces with flowing N_2, chemists have effectively excluded and/or removed oxygen to synthesize numerous compounds, as has been extensively reviewed.[1,25–30] Using ammonia (NH_3) instead of N_2 can raise the effective chemical potential (i.e., reactivity) of the nitrogen species and allow the use of oxide precursors (via $MO_x + 3x/2NH_3 \longrightarrow MN_{3x/2} + xH_2O$) in addition to metals or binary nitrides.[31–35] However, ammonia decomposes at elevated temperatures ($2\,NH_3 \longrightarrow N_2 + 3H_2$), leading to more reducing conditions than flowing nitrogen alone. Reactions can also be conducted in sealed ampules (made of glass, quartz, or various metals, Figure 1.4b) with the nitrogen already contained in the solid reactants or generated *in situ* by the decomposition of NaN_3 (which has the added benefit of assisting the crystallization of nitrides via a sodium flux).[36] Special apparatus built to contain high pressure ammonia can also be used to synthesize new nitrides in bulk.[37,38] While these methods pro-

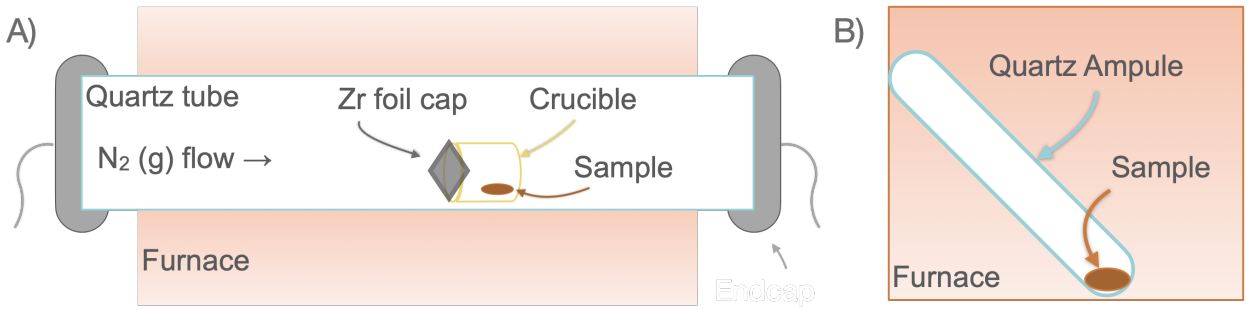

Figure 1.4: Diagrams of two furnace options for synthesizing nitrides. In A) a solid sample reacts by heating in a tube furnace under flowing N2 (g) at 1 atm pressure. Endcaps prevent air from seeping in. The sample is contained in a cylindrical crucible, turned sideways with the open end facing upstream. A Zr foil cap can be placed in front of the crucible opening to getter oxygen from the flowing gas and to inhibit evaporative loss from the sample. Custom endcaps with quick-disconnects allow for transfer of the process tube between a glovebox and the furnace without air exposure. In B), a sample is sealed in a quartz ampule under vacuum. Typically, ampules are sealed with a pressure < 15 mTorr, although it is possible to backfill the ampule with approximately 1/3 atm of pressure. Alternatively, gas can be generated *in situ*, either intentionally or unintentionally (CAUTION: pressurized tubes may explode, posing serious safety hazard). To induce reactivity, the ampule is heated in a box furnace.

vide advantages in terms of crystallinity, the simplicity of the traditional ceramic approach remains an effective way to make powder samples, as demonstrated by the Palacin group in their syntheses of $MgMoN_2$, $MgTa_2N_4$, and $CaTaN_2$.[39,40] Using the traditional ceramic approach, we synthesized $MgWN_2$ described in Chapter 3.

However, the kinetic and thermodynamic challenges described previously mean that ceramic methods may fail to make a predicted phase, and so we need to find alternative strategies to navigate the thermodynamic landscape towards new ternary nitrides. As the Neilson group has expertise in studying metathesis reactions,[41–46] most of my PhD work focused on using this route to target the predicted materials of interest: $MgSnN_2$, $MgZrN_2$, and $CaZrN_2$. We almost always conducted these reactions in sealed ampules (Figure 1.4b), as the halide reactants are volatile and need to be contained near the nitride source. I was never able to successfully synthesize $MgSnN_2$, but others were successful using high pressure[47] and combinatorial sputtering[13] techniques. These techniques boost the chemical potential of nitrogen,[1] stabilizing the phase which becomes thermodynamically unstable at ambient pressure by approximately 500 K (relative to $Mg_3N_2 + 3\,Sn + 2\,N_2$, Figure 6.3).

However, metathesis reactions did yield $MgZrN_2$ and $CaZrN_2$, which I describe in Chapter 4 and Chapter 5. Notably, the metathesis strategy we employ is conducted in evacuated ampules (or occasionally near ambient pressure), in stark contrast to the high-pressure (ca. 5 GPa) metathesis reactions that other groups have successfully employed to make $MgSnN_2$ and $CaSnN_2$.[47,48]

Overall, this dissertation focuses on how we can synthesize new ternary nitrides, with an eye towards how materials chemists can use thermodynamic calculations to better plan their syntheses. The four body chapters describe the synthesis of five new ternary nitrides: $MnSnN_2$, $MgWN_2$ & Mg_3WN_4, $MgZrN_2$, and $CaZrN_2$. In sum, these chapters show how I (with help from several teams of wonderful colleagues) have advanced the field by not only discovering new materials, but also by identifying generalizable strategies to make yet more ternary nitrides in the future.

Chapter 2 highlights an example of how combinatorial sputtering can target metastable ternary nitrides as thin films to find new magnetic materials. We describe the synthesis of $MnSnN_2$, a new ternary nitride with a wurtzite-like structure type and cation-disorder across a large compositional range ($20\% \leq Mn/(Mn+Sn) \leq 60\%$). The material exhibits semiconducting properties with an optical absorption onset of 1.0 eV. Magnetic susceptibility measurements reveal a low temperature magnetic transition ($T^* \approx$10 K) indicative of antiferromagnetic correlations. This low temperature magnetic behavior contrasts starkly with the literature on similar phases—$MnSiN_2$ and $MnGeN_2$—that were synthesized in bulk and which exhibit magnetic transitions above room temperature (490 K and 448 K, respectively).

Chapter 3 reports the discovery of several new phases in the previously empty Mg-W-N phase space by using a combination of thin film and bulk methods. Combinatorial sputtering reveals cation disordered phases: a rocksalt structure $MgWN_2$ and a h-BN structure for Mg_3WN_4. In contrast, bulk syntheses using a traditional ceramic approach yielded $MgWN_2$

in an ordered structure we call "rocksaline", with rocksalt-like layers of octahedral Mg and nickeline-like layers of trigonal-prismatic W.

Chapter 4 describes the bulk synthesis of $MgZrN_2$ and solid solutions of $Mg_xZr_{2-x}N_2$ ($0 \leq x \leq 1$). Prior to our report, this semiconducting material had only been synthesized as a thin film.[11,49] We show how traditional bulk methods fail to synthesize the material, but how instead a two-step metathesis reaction could crystallize the phase. Thermodynamic calculations help us rationalize this two-step process.

Chapter 5 extends this bulk metathesis work to the discovery of new semiconductors, $CaZrN_2$ and $CaHfN_2$. The synthesis differs in surprising ways from that of $MgZrN_2$, which we explore using *in situ* synchrotron X-ray diffraction. Again, we compare the synthesis procedure with thermodynamic calculations to rationalize the observed pathway and provide generalizable knowledge to improve future syntheses.

Chapter 6 summarizes the synthetic advancements made through our studies in the context of an improving set of computational and theoretical tools. In particular, I highlight how computed phase diagrams and reaction network analysis reveal promising synthetic strategies. As a test case, I predict a strategy for the bulk synthesis of $LaWN_3$ at ambient pressure. This new ternary nitride has a perovskite structure useful for optoelectronic applications, but has only recently been synthesized as thin films via sputtering[19] reported in 2021 and via a high-pressure metathesis reaction in Fall of 2022.[50]

Lastly, science does not happen in a vacuum, but rather in community. Chapter 7 focuses on how one aspect of the scientific community—academic seminar Q&A sessions—perpetuate gender inequity. My quantitative observations of question-asking behavior add to the growing body of literature showing that women are underrepresented in seminar Q&A sessions. This chapter highlights the urgent need to re-examine academic traditions to create more inclusive scientific communities.

Chapter 2

Combinatorial synthesis of cation-disordered manganese tin nitride $MnSnN_2$ thin films with magnetic and semiconducting properties*

Overview

Magnetic semiconductors may soon improve the energy efficiency of computers, but materials exhibiting these dual properties remain underexplored. Here, we report the computational prediction and realization of a new magnetic and semiconducting material, $MnSnN_2$, via combinatorial sputtering of thin films. Grazing incidence wide angle

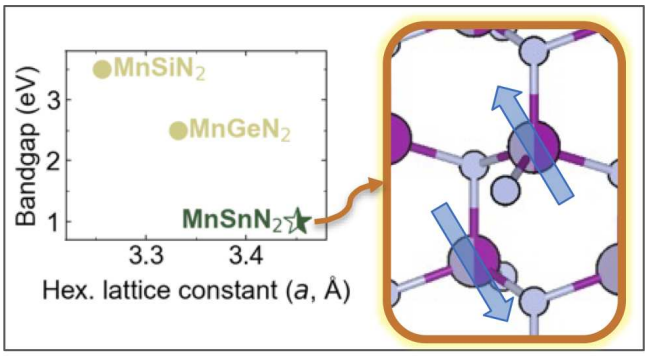

Figure 2.1: Overview of findings: newly synthesized $MnSnN_2$ is a semiconductor with an optical bandgap near 1 eV and antiferromagnetic correlations at low temperature (<10 K).

* Substantial portions of this chapter has been reproduced with permission from C.L. Rom, R.W. Smaha, C.L. Melamed, R.R. Schnepf, K. N. Heinselman, S. Lany, L.T. Schelhas, S.R. Bauers, A.L. Greenaway, J.R. Neilson, S. Bauers, J.S. Andrew, A.C. Tamboli, Combinatorial synthesis of manganese tin nitride $MnSnN_2$ thin films with magnetic and semiconducting properties, 2022, arXiv:2206.03594. J.S.A. and A.C.T. conceptualized the project. J.S.A. and C.L.R. conducted depositions, XRF, and XRD measurements. C.L.R. and R.W.S conducted magnetism and electronic conductivity measurements. R.R.S. and C.L.M. conducted ellipsometry measurements. L.T.S. and C.L.R. conducted synchrotron GIWAXS measurements. K.N.H. conducted RBS analysis. J.S.M. conducted microscopy. S.J.L. conducted XAS measurements. S.L. conducted DFT calculations. C.L.M. and A.L.G. aided in synthesis and maintenance of the deposition chamber. C.L.R. wrote the majority of the manuscript with guidance from S.R.B., J.R.N., A.C.T., and J.S.A., with contributions from all other authors.

X-ray scattering and laboratory X-ray diffraction studies show a wide composition tolerance for this wurtzite-like $MnSnN_2$, ranging from $20\% <$ Mn/(Mn+Sn) $< 65\%$ with cation disorder across this composition space. Magnetic susceptibility measurements reveal a low-temperature transition ($T^* \approx 10$ K) for $MnSnN_2$ and strong antiferromagnetic correlations, although the ordering below this transition may be complex. This finding contrasts with bulk $MnSiN_2$ and $MnGeN_2$, which exhibited antiferromagnetic ordering above 400 K in previous studies. Spectroscopic ellipsometry identifies an optical absorption onset of 1 eV for the experimentally-synthesized phase exhibiting cation disorder, consistent with the computationally-predicted 1.2 eV bandgap for the cation-ordered structure. Electronic conductivity measurements confirm the semiconducting nature of this new phase by showing increasing conductivity with increasing temperature. This work adds to the set of known semiconductors that are paramagnetic at room temperature and will help guide future work targeted at controlling the structure and properties of semiconducting materials that exhibit magnetic behavior.

2.1 Introduction

Ternary nitrides are an emerging class of semiconducting materials.[1] In particular, II-IV-N_2 compounds offer a highly tunable platform that are structurally compatible with well-developed III-N technologies (e.g., GaN).[51,52] In the past few years, many new compounds were discovered in this phase space as thin films (e.g., $MgTiN_2$, $ZnMoN_2$, $ZnZrN_2$),[2,18,53] bulk solids (e.g., $CaSnN_2$, $CaTiN_2$),[48,54] or both (e.g., $MgSnN_2$, $MgZrN_2$).[11,13,47,55] These particular compounds—with Mg^{2+}, Ca^{2+}, and Zn^{2+} as the divalent cation—have been investigated for their semiconducting properties. However, using transition metals with unpaired electrons—like Mn^{2+}—in semiconductors may add magnetic properties useful for applications in spintronic devices,[56,57] so exploratory syntheses of Mn-containing nitrides may discover technologically relevant materials.

II-IV-N_2 semiconductors with Mn^{2+} offer an underexplored platform for magnetic semiconductors. Bulk methods have been used to synthesize $MnSiN_2$ and $MnGeN_2$, and these phases are known to be antiferromagnetic (AFM) semiconductors with Néel temperatures of $T_N = 490$ K and 448 K, respectively.[58,59] These materials take on a wurtzite-derived structure, with cations and anions in tetrahedral coordination environments. They are structurally analogous to GaN, suggesting the possibility of AFM spintronic integration into III-N based device stacks. In this vein, Liu, et al. reported epitaxial growth of $MnGeN_2$ films by molecular-beam epitaxy and identified magnetic properties that varied with composition and substrate.[60] However, much remains to be learned about the fundamental chemistry and physics of these materials.

We note that the tin-containing analogue, $MnSnN_2$, has not yet been reported. Thus, the discovery of $MnSnN_2$ presents an opportunity to deepen our understanding of ternary II-IV-N_2 nitrides in general as well as the physics underlying this $MnMN_2$ (M = Si, Ge, Sn) wurtzite family in particular. With the powerful tool of combinatorial sputtering, we can answer questions like: How much off-stoichiometry can $MnSnN_2$ accommodate? How does the cation ratio affect the unit cell? How does composition affect magnetism? To begin answering these questions, we report on our prediction, synthesis, and characterization of thin films of $MnSnN_2$, a new paramagnetic semiconductor.

2.2 Methods

2.2.1 Computational methods

First-principles density functional theory (DFT) calculations were performed using the Vienna Ab initio Simulation Package (VASP).[61,62] Electronic structure and band gap calculations were performed using the GW approximation[63] as described previously.[64] Calculations were spin polarized to account for the expected magnetic moment of Mn. Computational results and details are available in the NREL Materials Database with ID 287033 (GW) and 287034 (DFT, https://materials.nrel.gov/).

2.2.2 Synthesis

The Mn-Sn-N phase space was explored using combinatorial radiofrequency (RF) co-sputtering methods. Libraries were deposited using an AJA International ATC 2200-V sputtering chamber. The chamber base pressure was between 2 and 5×10^{-8} Torr prior to depositions. During depositions, the pressure was maintained at 12 ± 1 mTorr with 15 sccm N_2 and 5 sccm Ar. The N_2 was activated by passing the gas through an electron-cyclotron resonance plasma source set at 150 W.

To create compositional gradients within each 2" x 2" sample library, metals were co-sputtered from 3" diameter Mn and Sn targets aimed towards the substrate (Kurt J. Lesker; 99.95% and 99.998%, respectively). The substrate was held stationary during deposition, and the relative position of the sputtering targets (180 ° relative to one another in the plane of the substrate) resulted in 1-dimensional gradients in composition across the substrate. Prior to each deposition, the targets were presputtered for 30 min with the shutters closed. Subsequently, the shutters were opened and deposition was conducted for 120 min. The sample platens were heated with lamp heaters during the depositions, with substrate temperature denoted here as T_{dep}. This temperature was calibrated without sputtering, and therefore provides a lower bound for the sample temperature, as the impact of sputtered elements raises the substrate temperature. Depositions were conducted between $T_{\text{dep}} = 25$ °C nominally (ambient conditions) and 275 °C. Cation composition was tuned by varying magnetron power, with Mn held at 108 W and Sn at either 36 W or 48 W. Most substrates were *p*-type Si wafers with native surface oxide, although select samples were grown on Eagle Corning XG glass (EXG, optically transparent and electronically insulating) and *p*-type Si with 100 nm of thermal oxide (electronically insulating) for certain property measurements as denoted in the text.

2.2.3 Characterization

Each 2" $\times$ 2" sample library was mapped as a 4×11 grid following the standard combinatorial mapping workflow at the National Renewable Energy Laboratory (NREL).[65] Experimental data used by this study have been analyzed using the COMBIgor software package[65] and are publicly available in the high-throughput experimental materials database at https://htem.nrel.gov.[66]

High-throughput X-ray diffraction (XRD) mapping was conducted using a Bruker D8 Discover (Cu Kα radiation) equipped with an area detector. High resolution synchrotron grazing incidence wide angle X-ray scattering (GIWAXS) measurements were conducted on select samples at beamline 11-3 of the Stanford Synchrotron Radiation Lightsource, SLAC National Accelerator Laboratory with $\lambda = 0.9744$ Å, a 3° incident angle, and spot size of 50 microns vertical $\times$ 150 microns horizontal. GIWAXS images were integrated with GSAS-II.[67] LeBail refinements were used to extract lattice parameters for $MnSnN_2$ in the $P6_3mc$ space group, performed with TOPAS Academic v6.[68] Peak broadening was modeled via the Thompson-Cox-Hastings pseudo-Voigt "TCHZ" peak type as implemented in TOPAS. Reference patterns were generated using VESTA for visual comparisons.[69] As the $MnSnN_2$ phase has not been previously reported, we modeled the structure as follows: starting from the wurtzite AlN structure,[70] we replaced Al^{3+} with a 1:1 mixture of Mn^{2+} and Sn^{4+} and shifted the unit cell parameters to match the LeBail refinement for the near-stoichiometric $MnSnN_2$ pattern (51% Mn/(Mn+Sn)). Those refined cell parameters are $a = 3.441$ Å and $c = 5.562$ Å (Table A.3).

Compositional analysis was performed with X-ray fluorescence (XRF) and Rutherford Back-Scattering (RBS) methods. Metal ratios were mapped using a Fischer XDV-SDD XRF with a Rh source and a 3 mm diameter spot size. The measurements were performed at ambient pressure with an exposure time of 60 s for each measurement. Nitrogen and oxygen ratios for select samples were quantified with RBS. RBS was run in a 168° backscattering configuration using a model 3S-MR10 RBS system from National Electrostatics Cor-

poration with a 2 MeV He^+ beam energy. Samples were measured for a total integrated charge of 160 uC. RBS spectra were modeled with the RUMP software package.[71] Agreement on metal ratios between XRF and RBS are shown in Figure A.9. A representative RBS spectrum and fit are shown in Figure A.10.

Film thicknesses were measured using a Dektak profilometer and were approximately 200 to 300 nm following 2 h growth times. Cross-sectional scanning electron microscopy (SEM) was conducted for select samples on a Hitachi S-4800 SEM operating at 3 keV accelerating voltage and 8 mm working distance to corroborate film thickness measurements and identify film morphology.

Room temperature conductivity was measured using a custom built collinear four-point probe instrument by sweeping current between the outer two pins while measuring voltage between the inner pins (1 mm between each pin). Conventional geometric corrections were applied to convert the measured resistance into sheet resistance and then conductivity.[72] Error bars are propagated from sheet resistance error (from I-V curve fits) and an estimated 5% relative error in profilometry thickness measurements.

Temperature-dependent electrical conductivity was measured using a Lake Shore Cryotronics Model 8425. A 5 mm $\times$ 5 mm square was scribed out of a library deposited on EXG at approximately 200 °C. Although the deposition temperature on EXG was not calibrated, XRD patterns appeared similar to those deposited on at a calibrated $T_{\text{dep}} = 225$ °C on silicon (i.e., XRD showed only $MnSnN_2$ with no signs of Sn or Mn_3N_2 decomposition products). Indium contacts were pressed into the square near the corners of the film, and temperature-dependent sheet resistance was measured from 104 K to 298 K. Conductivity was calculated using the profilometry-measured thickness of 260 nm.

Spectroscopic ellipsometry was performed on a single row of a select sample library (11 points per row) using a J.A. Woollam Co. M-2000 variable angle ellipsometer. CompleteEASE software (version 6.56) was used to do the modeling. The data were modeled by

fitting the imaginary part of the dielectric function with a combination of one Tauc-Lorentz, one Gaussian, and one Drude oscillator.

DC magnetic susceptibility was measured in a Quantum Design Magnetic Properties Measurement System (MPMS3) via vibrating sample magnetometry. The films were measured from 2 K to 300 K under applied fields from -7 to +7 T, with the applied field parallel to the plane of the film. The measured samples were 5 mm $\times$ 5 mm squares from a sample library deposited at $T_{\text{dep}} = 225$ °C on a substrate of 100 nm of SiO_2 on pSi(100). Each square was characterized by XRF and synchrotron GIWAXS to ensure magnetic properties were accurately correlated with composition and structure. To isolate the signal of the films, a bare substrate (100 nm of SiO_2 on pSi(100)) was also measured and subtracted (Figure A.14). Additional analysis details are in the Supplementary Information.

2.3 Results and Discussion

2.3.1 Computational findings

To investigate the stability of a possible $MnSnN_2$ phase, we performed density functional theory (DFT) calculations. We hypothesized that this phase would form in the wurtzite-derived structure and therefore constructed a cation-ordered $MnSnN_2$ structure in the orthorhombic space group $Pna2_1$. DFT calculations suggest that this cation-ordered orthorhombic $MnSnN_2$ is slightly metastable (+0.038 eV/atom above the hull, Figure 2.2A). Therefore, a traditional bulk synthetic approach of reacting Mn and Sn under 1 atm of N_2 would likely fail. However, sputtering in an activated nitrogen atmosphere (i.e., a N_2 plasma) stabilizes metastable phases (e.g., Cu_3N and Sn_3N_4) by increasing the chemical potential of nitrogen up to +1 eV/atom.[21,22] Figure 2.2A shows that while $MnSnN_2$ is metastable with respect to Sn+N_2 and Mn_3N_2, the phase is stable with respect to Sn_3N_4 and Mn_3N_2. Therefore, the nitrogen plasma environment that rendered Sn_3N_4 synthetically accessible should also stabilize $MnSnN_2$.

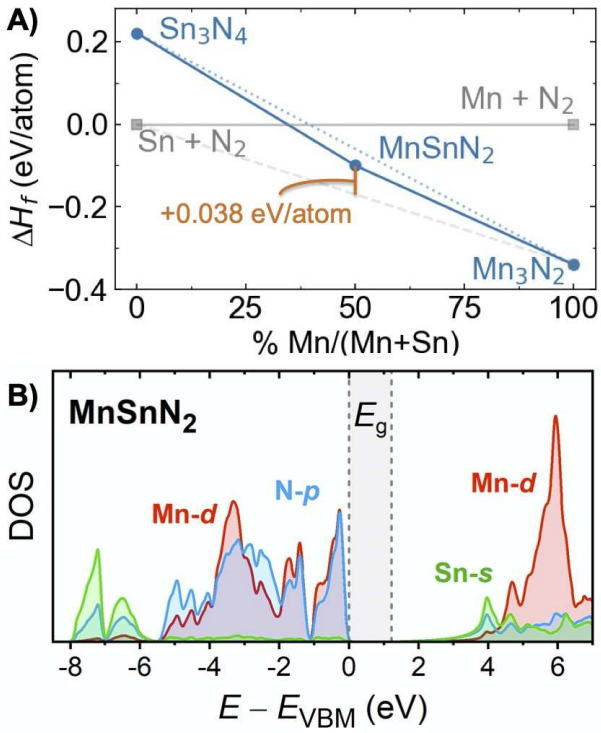

Figure 2.2: A) A psuedobinary phase diagram of the space from Sn_3N_4 to Mn_3N_2 at $T = 0$ K. The solid blue trace shows the hull under activated nitrogen conditions ($\mu_N = +1$ eV/atom), as occurs in plasma synthesis.[21,73] Cation-ordered $MnSnN_2$ is more stable than a linear combination of these two binary nitrides. B) Total density of states calculated for cation-ordered $MnSnN_2$ in the $Pna2_1$ space group. The calculated band gap (E_g) is 1.22 eV, shown in grey. N-p and Mn-d states comprise the valence band, while the conduction band consists of Sn-s and N-p states.

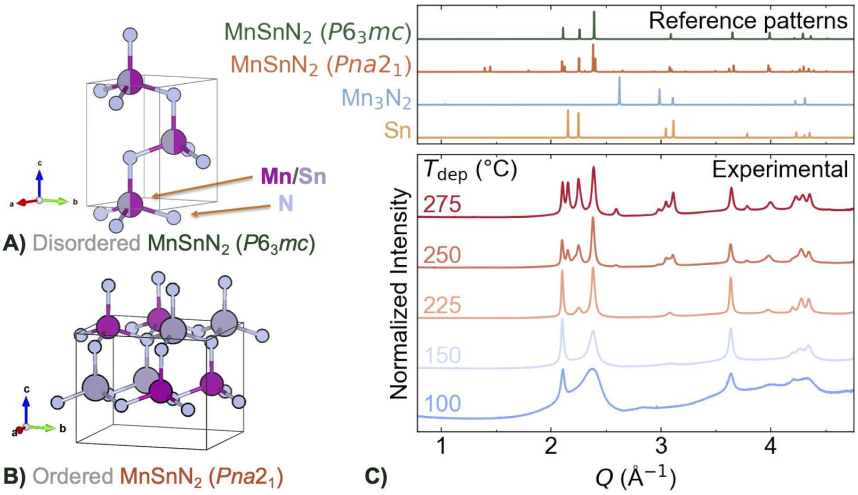

Figure 2.3: A) The unit cell of $MnSnN_2$ in the experimentally observed cation-disordered hexagonal structure ($P6_3mc$), and the B) computationally predicted ordered orthorhombic structure ($Pna2_1$). C) Synchrotron GIWAXS data of samples with Mn/(Mn+Sn) = 50% deposited at various temperatures (T_{dep}) are shown in the bottom box, with reference patterns shown in the top box. The optimal deposition temperature for single phase crystalline $MnSnN_2$ ($P6_3mc$) is $T_{\text{dep}} = 225$ °C. The ordered $MnSnN_2$ ($Pna2_1$) phase is not observed.

Our calculations also suggest that $MnSnN_2$ should exhibit semiconducting properties and antiferromagnetic behavior. The calculated bandgap is 1.22 eV (Figure 2.2B), with a density of states (DOS) effective hole mass of $m_h^* = 5.9m_0$. The band effective mass is $m_e^* = 0.22m_0$. The low electron mass is remarkable for a transition metal compound (Mott insulator), but not uncommon for Mn^{2+}.[74,75] The local magnetic moment is calculated as $\mu_{\text{eff}} = 4.3\ \mu_{\text{B}}$ per Mn. This μ_{eff} is less than the spin-only value expected for high-spin Mn^{2+} ($S = \frac{5}{2}$; $\mu_{\text{eff}} = 5.9\ \mu_{\text{B}}$), indicating that some spin density resides on the nitride. The four Mn atoms per cell exhibit antiferromagnetic order in the ground state, resulting in a net moment of 0 μ_{B} per cell.

2.3.2 Synthesis and structure of $MnSnN_2$ thin films

Stability and cation disorder

We synthesized $MnSnN_2$ films using combinatorial co-sputtering and assessed the crystallinity using X-ray diffraction techniques (synchrotron GIWAXS and laboratory XRD). Synchrotron GIWAXS of stoichiometric films shows that $MnSnN_2$ crystallizes in a phase-

pure cation-disordered wurtzite structure at $T_{\mathrm{dep}} = 225$ °C (Figure 2.3A,C). The absence of supercell reflections (peaks near $Q = 1.5$ Å^{-1}) of the $Pna2_1$ space group indicate that long-range ordering of cations in $MnSnN_2$ does not occur in these samples (Figure 2.3B,C). Above $T_{\mathrm{dep}} = 225$ °C, Sn and Mn_3N_2 are also observed in the diffraction patterns, while below 225 °C, the material is poorly crystalline. These trends are true across the compositional gradient (Figure A.5). This relatively low decomposition temperature ($T_{\mathrm{dep}} \approx 250$ °C) suggests that $MnSnN_2$ is less stable than related ternary nitrides like $MgSnN_2$ (stable up to 500 °C in the same deposition chamber)[13] and $ZnSnN_2$ (stable up to 340 °C).[76] Annealing experiments under flowing N_2 suggest that, once deposited, $MnSnN_2$ films are stable up to $T_{\mathrm{anneal}} = 300$ °C, but decomposition is still observed by $T_{\mathrm{anneal}} = 400$ °C (Figure A.7).

We conducted these annealing experiments in an attempt to induce cation ordering,[77] but saw no evidence of cation order below the decomposition temperature of $T_{\mathrm{anneal}} = 400$ °C (Figure A.7). By the methods applied here, long-range cation ordering of $MnSnN_2$ appears inaccessible. In contrast, the bulk synthesis methods employed for $MnSiN_2$ and $MnGeN_2$ yielded cation-ordered phases (space group $Pna2_1$).[58,59] The prior report on thin films of $MnGeN_2$ did not assess cation ordering via diffraction, although the authors suggested that Ge-antisite defects contributed to the observed net magnetic moment.[60]

The lack of long-range cation ordering exhibited by $MnSnN_2$ is common in sputtered films. $MgSnN_2$ and $ZnSnN_2$ thin films are both cation disordered,[13,76] and $ZnGeN_2$ forms as a cation-disordered thin film but crystallizes in the ordered $Pna2_1$ structure when synthesized by bulk ammonolysis.[34,78] The high effective temperature of the sputtering synthesis technique, along with the entropic benefit of disorder, can stabilize a disordered structure by approximately 0.1 eV/atom relative to the DFT-predicted ordered structures.[53] II-Sn-N_2 phases in particular have a tendency for disorder because Sn^{4+} is closer in ionic radius (0.55 Å) to the divalent cations—Mn^{2+} (0.66 Å), Mg (0.57 Å), and Zn (0.60 Å)—than the other main group elements—Ge^{4+} (0.39 Å) and Si^{4+} (0.26 Å).[13,79,80] This size similarity

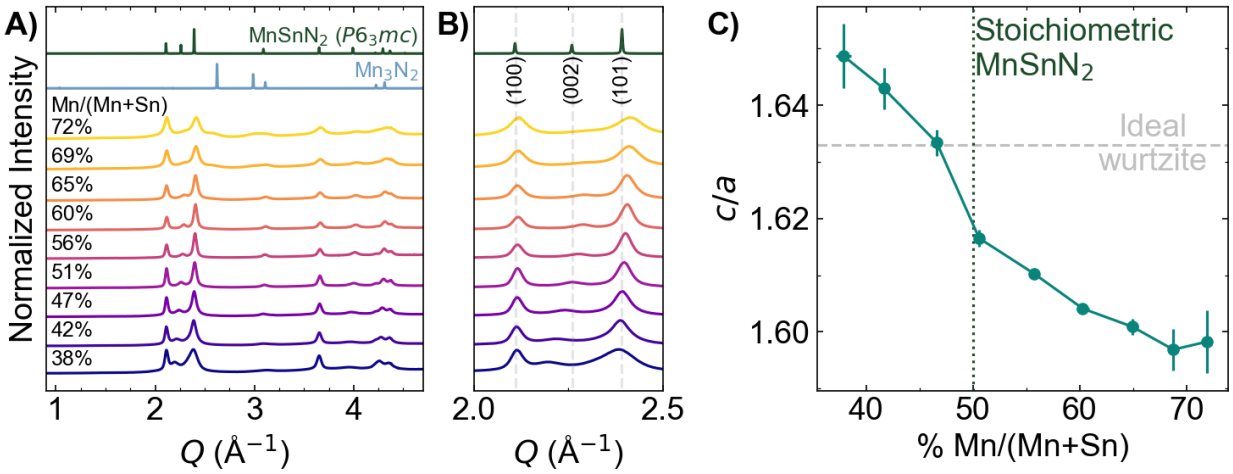

Figure 2.4: A) Synchrotron GIWAXS data of select samples from a combinatorial library row deposited at $T_{\text{dep}} = 225$ °C shows that reflections can be indexed to the $P6_3mc$ space group, indicative of a cation-disordered wurtzite structure. B) Magnified Q range of the diffraction patterns, showing the shift in the (002) reflection with changing Mn/(Mn+Sn). C) The *c* axis contracts relative to the *a* axis with increasing Mn content, which causes the c/a ratio to decrease. The vertical dotted line indicates the composition of stoichiometric $MnSnN_2$ and the horizontal dashed line indicates the ideal *c/a* ratio of the wurtzite structure ($\sqrt{8}/3$). Fits to the data are shown in Figure A.3.

leads to cation disorder even in bulk $MgSnN_2$.[47] While short-range ordering is possible even with the absence of a supercell reflection and may impact properties,[35,77,81] such analysis is beyond the scope of this study.

Compositional and structural trends

Despite this low thermal stability, the wurtzite structure of $MnSnN_2$ accommodates a wide range of cation off-stoichiometry ($18\% <$ Mn/(Mn+Sn) $< 65\%$) when deposited at the optimal temperature of $T_{\text{dep}} = 225$ °C. Within the composition range of Mn/(Mn+Sn) = 38% to 65%, all reflections in the GIWAXS patterns can be indexed to $P6_3mc$ symmetry (Figure 2.4). In laboratory XRD, we observe $MnSnN_2$ down to Mn/(Mn+Sn) = 18% (the Mn-poor limit of the library, Figure A.8). However, this may not be the true lower compositional limit of this phase. In contrast, we have determined that the upper limit of Mn content in $MnSnN_2$ by diffraction is Mn/(Mn+Sn) $\approx 65\%$. At high Mn content ($> 65\%$), the lattice parameters of $MnSnN_2$ plateau and the uncertainty in the refinement grows (Figures 2.4C and A.4). Broad peaks that index to Mn_3N_2 also appear, indicative of a

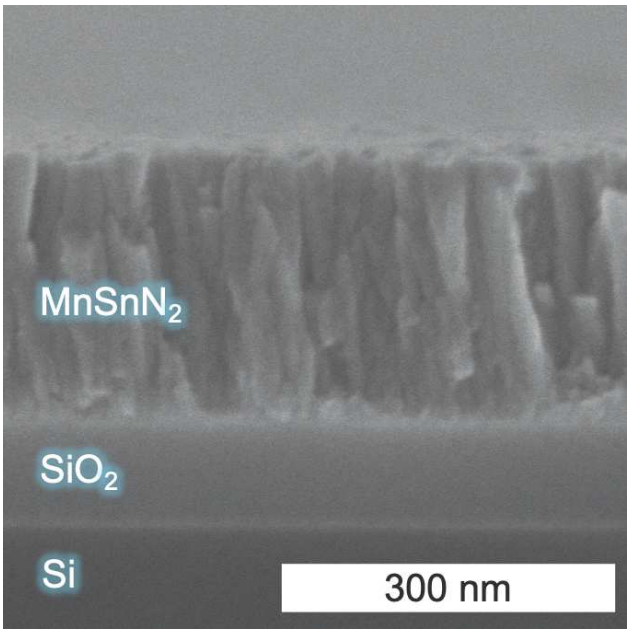

Figure 2.5: Cross-sectional SEM micrograph showing columnar grains typical of sputtered films. This representative image shows a 50% Mn/(Mn+Sn) film deposited on a silicon substrate with 100 nm of SiO_2. The scale bar is 300 nm.

two-phase region. The only other known Mn-Sn-N ternary compound is the antiperovskite Mn_3SnN (Mn/(Mn+Sn) = 75%),[82,83] which is more Mn-rich than our depositions and does not appear in our diffraction patterns.

This wide range of off-stoichiometry can make naming ternary nitrides difficult, as noted by Woods-Robinson, et al.[53] A precise formula would be $Mn_xSn_{1-x}N_{1-y}O_y$, where x is the cation fraction of Mn/(Mn+Sn) and y is the amount of oxygen substitution for nitrogen (estimated to be $y \approx 0.2$ by RBS, Figure A.9B). The oxygen likely originates from oxide contamination of the Mn sputter target, and either charge balances with Mn^{2+} via $(MnSnN_2)_{1-x}(MnO)_x$ or with Mn^{3+} via $Mn_{1+x}Sn_{1-x}N_{2-x}O_x$. For simplicity, we use "$MnSnN_2$" to refer to the cation-disordered wurtzite-like phase across the whole composition range and specify a cation fraction as a percentage of Mn/(Mn+Sn) where relevant (i.e., stoichiometric $MnSnN_2$ has Mn/(Mn+Sn) = 50%).

The *c/a* ratio of $MnSnN_2$ varies with composition, but deviates only slightly from the ideal wurtzite value of 1.633 (Figure 2.4C). For stoichiometric $MnSnN_2$, $c/a = 5.562$ Å /

3.441 Å $= 1.616$, which—although smaller than the ideal wurtzite—is larger than $MgSnN_2$ (1.598).[13] The change in *c/a* is driven primarily by a change in the *c* lattice parameter while the *a* lattice parameter remains largely unchanged (Figure A.4A), suggesting that the tetrahedra may be distorting along the *c* axis. That shift may be caused by metal vacancies, a change in electron count of the metals, oxygen incorporation (observed by RBS, Figure A.9B), or some combination thereof as the system shifts to maintain charge neutrality across this compositional range. However, since atomic positions cannot be resolved from the synchrotron GIWAXS data sets, we cannot more precisely identify the cause of this distortion.

To probe the microstructure of the film, we turn to electron microscopy and diffraction analysis. SEM shows columnar grain morphology that is typical for sputtered films (Figure 2.5). Diffraction images display some signs of texturing (Figure A.2). The (002) reflection appears towards the edges of the integration window, suggesting the {002} planes are oriented normal to the plane of the substrate. In contrast, the (100) reflection appears strongly in the center axis of the frame, 90 ° relative to the (002) reflection, and diminishes in intensity towards the edge of the integration window, suggesting preferential growth along the [100] direction (Figure 2.4B). This finding stands in contrast to typical wurtzite films, which tend to grow with (002) preferential orientation.[76,84]

2.3.3 Optoelectronic properties

Room temperature conductivity measurements show that the $MnSnN_2$ films exhibit conductivity on the order of 20 S/cm (Figure 2.6A). Conductivity decreases slightly as Mn content increases from 38% to 60% Mn/(Mn+Sn) but then increases as a metallic secondary phase (Mn_3N_2) grows in. This increase in conductivity for Mn/(Mn+Sn) $\geq 60\%$ suggests that the true single-phase region may have a lower Mn limit (≈60% maximum) than detected by GIWAXS (≈65% maximum). For the Mn/(Mn+Sn) $< 60\%$ region, conductivity is likely tuned by carrier concentration. Prior work on $ZnSnN_2$ demonstrated

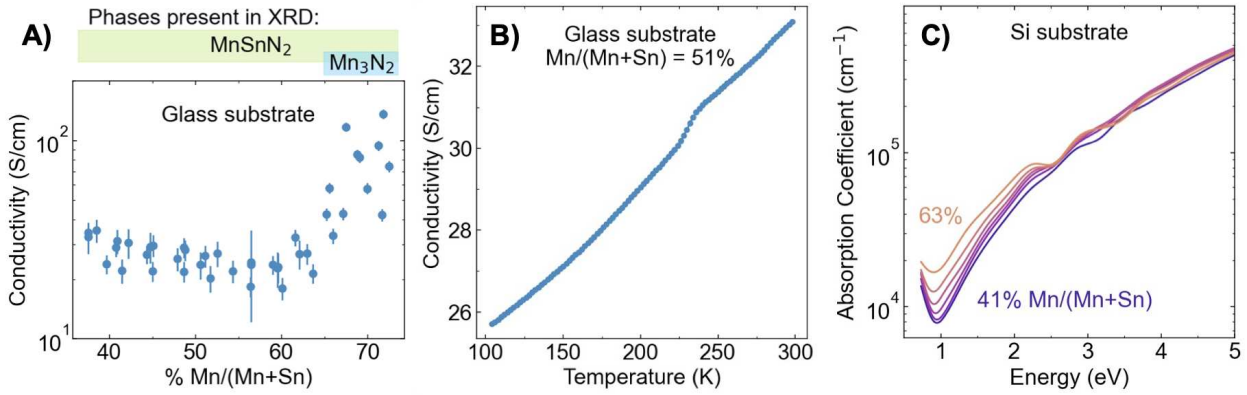

Figure 2.6: A) Room temperature conductivity measurements performed in a collinear four-point probe configuration show that conductivity initially decreases slightly with increasing Mn content, then increases rapidly above 60% Mn/(Mn+Sn). B) Conductivity increases as a function of temperature, confirming the semiconducting nature of $MnSnN_2$ films. The anomaly in slope near 250 K is an instrumental artifact. C) Optical ellipsometry measurements indicate a gradual absorption onset, with minima in the absorption coefficients near 1 eV.

that a similar trend (decreasing conductivity with increasing Zn) was correlated with a decrease in carrier concentration (while mobility was unaffected).[76] In both cases ($MnSnN_2$ and $ZnSnN_2$), the conductivity reaches a minimum in the Sn-poor region (i.e., Zn or Mn ≈60%), as the excess Zn or Mn compensate for oxygen substitution on nitrogen sites. At Mn/(Mn+Sn) = 60%, the charge-balanced chemical formula is $Mn_{0.6}Sn_{0.4}N_{0.8}O_{0.2}$ (assuming Mn^{2+} and Sn^{4+}), consistent with the oxygen content identified by RBS (Figure A.9B).

Temperature-dependent conductivity measurements show that conductivity increases with increasing temperature, consistent with semiconducting behavior for $MnSnN_2$ (Figure 2.6B). This trend suggests that mobile carriers are thermally activated (i.e., a bandgap is present in the material). However, the conductivity is only weakly dependent on temperature, with the conductivity at 298 K only 30% greater than the conductivity at 104 K. These measurements were performed in Van der Pauw geometry on films grown on insulating EXG glass, so contact resistance and substrate conductivity do not contribute to the conductivity reported here.

Ellipsometry measurements and modeling show that $MnSnN_2$ has a gradual absorption onset near 1 eV (Figure 2.6C). Overall, the absorptivity increases slightly with increasing

Mn content, although the absorption onset stays relatively constant. This absorption onset may be attributable to a bandgap, as the bandgap for this material is expected to be lower than the experimentally reported bandgaps in cation-ordered $MnSiN_2$ (3.5 eV) and $MnGeN_2$ (2.5 eV).[38] The DFT-calculated bandgap for cation-ordered $MnSnN_2$ is 1.22 eV (Figure 2.2B), and the cation-disorder of the material synthesized here tends to lower the bandgap relative to cation-ordered analogues.[77] However, Mn^{2+} *d-d* transitions are also known to occur in this energy region,[58] and unfortunately, this technique cannot distinguish between single-ion electronic transitions and bandgap excitations. We also attempted UV-vis measurements of films deposited on transparent substrates to verify the optical absorption onset, but the onset was below the 1.2 eV limit of the instrument (Figure A.12). Regardless, the optoelectronic behavior of this new compound present opportunities for further study.

2.3.4 Magnetic properties

Given the presence of tetrahedrally-coordinated Mn^{2+} cations in $MnSnN_2$ (expected: $S = \frac{5}{2}$ and μ_{eff} =5.9 μ_{B}), as well as the possible presence of Mn^{3+} (expected: $S = 2$ and μ_{eff} =4.9 μ_{B}) in Mn-rich compositions, DC magnetic susceptibility was employed to investigate the magnetic response of several thin films with a range of compositions from 42% $\leq$ Mn/(Mn+Sn) $\leq$ 56%. We cannot independently measure the film mass, so susceptibility (χ) was calculated from the raw moment data using the calculated mass for each sample (Tables A.2 and A.3). Uncertainty in film thickness, composition, and porosity may introduce substantial error in the calculated mass of the films, and by extension, the absolute value of χ. In addition, each measured sample contains a compositional gradient of approximately 4% Mn/(Mn+Sn). Despite these caveats, errors from sample to sample are likely systematic, allowing us to identify trends in magnetism related to composition. Additional details and discussion are in the Supplementary Information (Section 4).

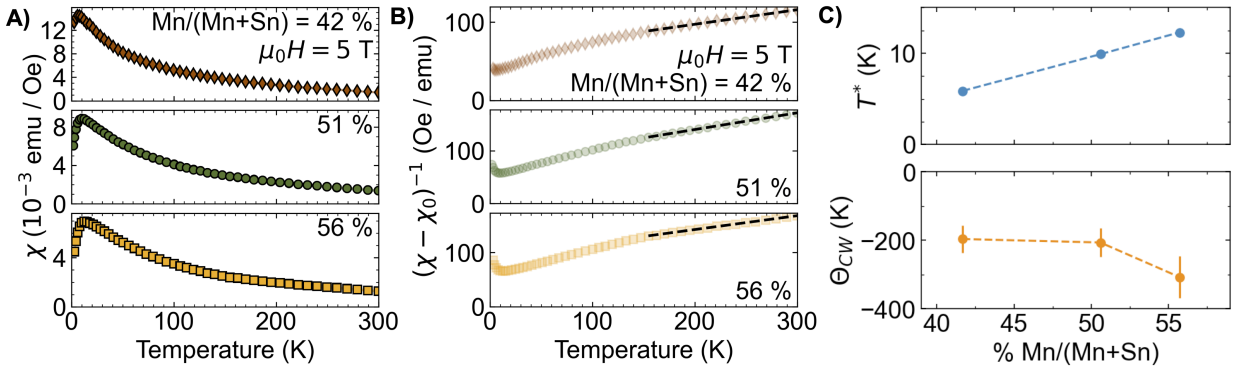

Figure 2.7: A) Zero-field-cooled (ZFC) DC magnetic susceptibility (χ) as a function of temperature measured in an applied field of $\mu_0 H = 5$ T, show a peak in χ at $T^* \approx 10$ K across a range of Mn contents. B) Inverse susceptibility $(\chi - \chi_0)^{-1}$) plotted as a function of temperature with a diamagnetic correction on the order of $\chi_0 = -3 \times 10^{-3}$ emu Oe^{-1} (Table A.4). The dashed traces show the Curie-Weiss fits from 150 K to 300 K. C) Extracted transition temperatures (T^*, top) and Weiss temperatures (Θ_{CW}, bottom) as a function of Mn content. We estimate an error bar of 20 % on each Θ_{CW} value.

Thin film $MnSnN_2$ exhibits a low temperature magnetic transition suggestive of antiferromagnetic (AFM) correlations. As shown in Figure 2.7A, zero-field-cooled (ZFC) temperature-dependent susceptibility measurements performed at high applied field exhibit cusps near 10 K, indicating a magnetic transition. This cusp is consistent with either AFM ordering or a spin-glass transition, but as we cannot precisely determine which, we designate it T^* (as opposed to T_N to T_c). The T^*, extracted as the temperature where χ reaches a maximum, increases slightly with increasing Mn content, from $T^* \approx 6$ K at 42% Mn to $T^* \approx 12$ K at 56% Mn (Figure 2.7C). Prior work on rocksalt $Mn_xMg_{1-x}S$,[85] and zinc-blende $Mn_xHg_{1-x}Te$[86] solid solutions similarly found increasing transition temperatures with increasing Mn content. This transition occurs at much lower temperatures than magnetic transitions of Mn-containing phases that might be impurities—Mn_4N has $T_N = 745$ K,[87] Mn_3N_2 has $T_N = 920$ K,[88] Mn_6N_5 has $T_N = 655$ K,[88] and MnO has $T_N = 118$ K[89]—therefore, we attribute this observed magnetic behavior to $MnSnN_2$.

Curie-Weiss fits in the paramagnetic region 150–300 K show large, negative Weiss temperatures (Θ_{CW}, Figure 2.7B), consistent with overall AFM correlations. However, the uncertainties in background subtraction and in the calculation of χ inhibit meaningful

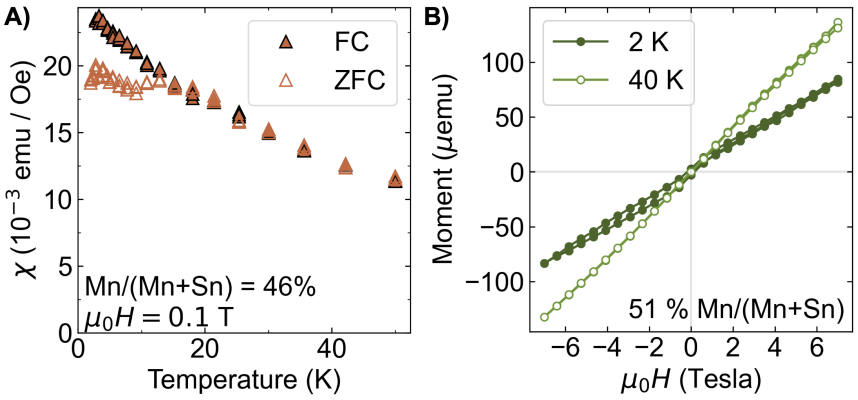

Figure 2.8: A) ZFC and field-cooled (FC) DC magnetic susceptibility measurements at lower applied field of $\mu_0 H = 0.1$ T show bifurcation below the transition temperature. B) Background-subtracted isothermal magnetization measurements of near-stoichiometric $MnSnN_2$ at $T = 2$ K (solid circles) and $T = 40$ K (open circles).

extraction of Curie constants and effective moments from these fits (see Supplementary Information Section 4). While the extracted Θ_{CW} values vary depending on the temperature region used in the fits (see Supplementary Information Section 4), the values are always negative.

Field-dependent measurements also indicate AFM correlations in $MnSnN_2$ thin films. Temperature-dependent susceptibility measurements in lower applied field ($\mu_0 H = 0.1$ T; Figure 2.7C) show clear bifurcation in ZFC and field-cooled (FC) susceptibility below the transition temperature, which is consistent with either long-range AFM order or a spin-glass ground state. The magnetic moment measured as a function of applied field at $T = 2$ K (below the transition at $T^* \approx 10$ K) is also consistent with AFM correlations, shown for Mn/(Mn+Sn) = 51% in Figure 2.8B and for the remaining samples in Figure A.16. In the $T = 2$ K data of all samples measured, there is small but observable hysteresis with a minute net moment at zero field, which may be attributable to a trace ferromagnetic impurity. The deposition chamber, which is largely made of steel components, may be the source of such an impurity, although the samples measured were not in direct contact with these components. However, similar net magnetic moments were observed in thin films of $MnGeN_2$ and were attributed to cation site disorder.[60] Above T^*, (e.g., at $T = 40$ K),

the linear behavior is consistent with paramagnetism. The traces do not plateau at high fields, indicating that the magnetic moment is not saturated at $\mu_0 H = \pm 7$ T. To probe the possibility of spin glass behavior, we performed AC susceptibility measurements, but the signal was below the instrumental sensitivity limit.

Overall, the susceptibility measurements and Curie-Weiss fit results point to clear, strong AFM correlations in $MnSnN_2$ with a transition near $T^* \approx 10$ K. This transition shifts slightly as a function of Mn/(Mn+Sn). We are unable to determine whether the ground state below this transition temperature is long-range AFM order or spin glass.[90] If the ground state is an ordered AFM, it would likely be complex, especially given the cation disorder and compositional gradients in these samples. The small net moment observed at $T < T^*$ may imply the presence of spin canting, Dzyaloshinsky-Moriya interactions, uncompensated residual spins, or impurities, as mentioned above, and the ZFC-FC splitting suggests a relaxation process. However, the Mn content in these samples (41–56%) is well above the percolation threshold (20% for this hexagonal close packed metal sublattice),[91] so the AFM correlations likely extend throughout the crystalline domains.

The low-temperature magnetic transition ($T^* \approx 10$ K) of the cation-disordered $MnSnN_2$ thin films examined here contrasts starkly with the high-temperature AFM ordering of cation-ordered $MnGeN_2$ ($T_N = 448$ K) and $MnSiN_2$ ($T_N = 490$ K) synthesized as bulk single crystals.[58,59] To explain these differences, we posit that cation ordering is an important factor in determining the energy scale of magnetic order in this family of wurtzite ternary nitrides. That influence may be exerted via magnetic frustration, if the ground state is AFM order: the tetrahedrally-based lattice of Mn^{2+}, together with the large ratio of the Weiss temperatures ($\Theta_{CW} \approx -200$ K) and the low transition temperatures ($T^* \approx 10$ K) of these films, suggest the presence of a high degree of magnetic frustration.[90,92] This is not unexpected, as triangular-based lattices are one of the most common hosts of geometric frustration, and frustration also often arises from cation disorder.[93,94] In addition, frustration was observed even in the cation-ordered $MnSiN_2$.[58] Should bulk powders or

single crystals of $MnSnN_2$ be synthesized—perhaps by the high pressure metathesis routes to $ZnSnN_2$, $MgSnN_2$, and $CaSnN_2$ used by Kawamura, et al.[47,48,95]—comparing their magnetic properties and defect chemistry with the thin film behavior observed here would be illuminating.

2.4 Conclusions

We have synthesized thin films of a new ternary nitride material, $MnSnN_2$, using combinatorial co-sputtering. The material crystallizes in a cation-disordered wurtzite-like structure common for II-IV-N_2 semiconductors with lattice parameters $a = 3.441$ Å and $c = 5.562$ Å for the stoichiometric material. $MnSnN_2$ exhibits semiconducting properties, including a bandgap near 1 eV—the lowest bandgap yet observed in the Mn*M*N_2 wurtzite family.[38] We observe a magnetic transition in cation-disordered $MnSnN_2$ at low temperature (T^* ≈10 K) consistent with AFM correlations, which contrasts dramatically with the high AFM ordering temperatures of cation-ordered $MnGeN_2$ and $MnSiN_2$ ($T_N = 448$ K and 490 K, respectively).[58,59] These discoveries suggest that future work could use composition and cation disorder in the Mn-M-N_2 (M = Si, Ge, Sn) system to tune both semiconducting and magnetic properties.

Chapter 3

Bulk and film synthesis of three new ternary Mg-W-N materials*

Overview

The Mg-W-N ternary phase space is a promising area of exploration for new functional materials. Recent computational work predicts Mg_3WN_4 may form as a cation-ordered wurtzite-like material with a 5 eV bandgap. However, our combinatorial co-sputtering syntheses revealed cation disordered phases in the rocksalt and hexagonal boron-nitride structure types. Bulk methods yielded a cation ordered polymorph of $MgWN_2$ in the rocksaline structure, with alternating layers of rocksalt-like [MgN_6] octahedra and nickeline-like [WN_6] trigonal prisms. We also show that rapid thermal annealing can convert disordered rocksalt films to ordered rocksaline structures, but only near the $MgWN_2$ stoichiometry. Electronic measurements show that Mg_3WN_4 is a semiconductor. These findings highlight how rapid thermal annealing can convert cation-disordered films into the thermodynamically more favorable ordered structures, adding a new strategy for the rapid exploration of thermodynamic stability in uncharted phase spaces.

3.1 Introduction

High-throughput computational techniques have led to the prediction of many new ternary nitrides,[2] and combinatorial co-sputtering has proven to be a powerful tool for

* Substantial portions of this chapter has been reproduced with permission from C.L. Rom, R.W. Smaha, C.A. Knebel, K. N. Heinselman, S.R. Bauers, J.R. Neilson, A. Zakutayev, *Prepared Manuscript*. 2022 C.L.R., J.R.N., and A.Z. conceptualized the project. R.S. conducted GIWAXS measurements. C.A.K. conducted bulk syntheses and analysis. K.H. conducted RBS measurements. C.L.R. and A.Z. conducted thin film co-sputtering experiments. A.Z. and C.L.R. conducted annealing experiments and electronic property measurements. C.L.R. wrote the manuscript with guidance from J.R.N., S.R.B., and A.Z., with feedback from all other authors.

experimentally realizing these predicted materials.[1,52] However, the materials produced as thin films by combinatorial co-sputtering often crystallize in cation-disordered structures, whereas the computationally predicted phases are cation-ordered. This discrepancy can sometimes be beneficial, such as when cation-disorder lowers the bandgap into the visible range.[14] In other cases, cation disorder negatively impacts optoelectronic properties by localizing charge carriers,[96] or producing phases with totally different structures (and properties) than the intended (ordered) structure.[53] Recent work has shown that combinatorial co-sputtering tends to produce structures that tolerate cation disorder (e.g. rocksalt phases),[53] but how to control this cation disorder is still an open question. Annealing conditions are known to affect the degree of cation (dis)order,[34,97] but that control is often material-specific and difficult to explore in a high-throughput manner.[77] Therefore, gaining control of cation (dis)order in ternary nitrides remains a pressing challenge for the field to fully realize the tunable properties of this promising class of materials.

In this report, we describe the discovery of several new Mg-W-N compounds in this previously-unexplored ternary phase space, and demonstrate how post-deposition annealing of thin films can rapidly explore cation ordering effects on structure. Figure 3.1 summarizes the prediced and synthesized structures explored in this study. Cation-ordered wurtzite-like Mg_3WN_4 was initially targeted for its high predicted bandgap (5 eV),[1] but this structure has evaded synthesis. However, thin film combinatorial co-sputtering methods yielded cation-disordered rocksalt (RS, $Fm\bar{3}m$ spacegroup) and hexagonal boron-nitride-derived structures (h-BN, $P6_3/mmc$ spacegroup). In contrast, bulk ceramic methods yielded $MgWN_2$ in a $P6_3/mmc$ spacegroup, which thermodynamic calculations confirm is the ground state in the Mg-W-N system. Rapid thermal annealing of combinatorial films converted the disordered rocksalt structure to the ordered structure, but only in a narrow composition window near the $MgWN_2$ stoichiometry. These findings show how rapid thermal annealing of disordered films can build upon existing combinatorial co-sputtering techniques to rapidly assess the synthesizability of a predicted cation ordered phase.

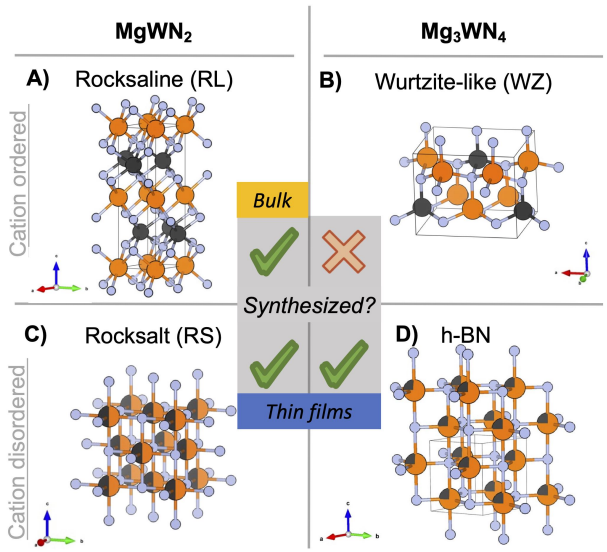

Figure 3.1: Predicted and synthesized compounds in the Mg-W-N phase space. Cation ordered phases in A) a rocksaline (RL) polymorph of $MgWN_2$ with layers of Mg^{2+} in an octahedral site and W^{4+} in a trigonal prismatic site ($P6_3/mmc$ spacegroup), and B) the initially-predicted most-stable polymorph of Mg_3WN_4, exhibiting a wurtzite-like structure (WZ) with tetrahedrally coordinated cations($Pmn2_1$ spacegroup). Disordered polymorphs exhibit C) a rocksalt (RS) structure of $MgWN_2$ with cations in an octahedral site ($Fm\bar{3}m$ spacegroup), and D) a hexagonal boron nitride (h-BN) structure near the composition of Mg_3WN_4 with cations in a trigonal bipyramidal site ($P6_3/mmc$ spacegroup). The WZ structure was not observed in either an ordered or disordered configuration, but the other phases were synthesized by thin film combinatorial co-sputtering (RS and h-BN) or by bulk synthesis (RL). The RL phase was also accessed by briefly annealing thin films.

3.2 Methods

3.2.1 Computational methods

Formation energies were calculated using density functional theory (DFT) using the corrected generalized gradient approximate (GGA+U) implemented in the Vienna Ab initio Structural Package (VASP). These calculated values were sourced from the Materials Project (v2021.11.10).[9,98] Calculations for additional structures that were not already in the Materials Project database were conducted using Atomate (v1.0.3)[99] and Fireworks (v2.0.2)[100] to execute the structure optimization workflow with compatibility with Materials Project entries. Pymatgen (v2022.4.19) was used to construct the ternary phase diagram shown in Figure 3.2.[101]

3.2.2 Thin film synthesis and annealing experiments

Combinatorial co-sputtering of Mg-W-N film libraries were conducted in two custom vacuum chambers, both with base pressures of $< 10^{-7}$ Torr. Mg and W targets (2 inch diameter) were angled towards a stationary substrate and sputtered using radiofrequency (RF) excited plasma of the Ar/N_2 gas mixture in the chamber. Sputter powers ranged from 30 W to 90 W for each target, to shift the Mg/(Mg+W) ratio across the whole composition window. Gases were introduced at 50 sccm Ar and 50 sccm N_2, with a 10 Torr process pressure maintained via a gate valve. The N plasma intensity was enhanced by RF plasma source at 350 W. Most samples were deposited on (001)-oriented Si substrates. Select samples were deposited on insulating substrates (e.g., 100 nm SiO_2 on Si or 100 nm Si_3N_4 on Si) for electronic property measurements, as indicated in the text. A diagram for this system is shown in Figure 3.3A.

Select samples were subject to rapid thermal annealing (RTA) in flowing N_2 atmosphere at ambient pressure. Heating profiles started with 3 min at 100 °C to drive off water, followed by a +100 °C/min ramp to a T_{anneal} set-point in the 600-1200 °C range for a 3

min dwell. Samples were cooled by turning off the heating source. A diagram for this experimental setup is shown in Figure 3.4A.

Combinatorial libraries were measured using the standard 4×11 grid employed at NREL, with data analysis conducted using the COMBIgor software package.[65] Each library was mapped with XRD using a Bruker D8 Discover with Cu Kα radiation and an area detector. Select samples were measured by high-resolution synchrotron grazing incidence wide angle X-ray scattering (GIWAXS) at the Stanford Synchrotron Radiation Lightsource (SSRL) at a wavelength of 0.9744 Å, a 3° incident angle, and spot size of 50 microns vertical × 150 microns horizontal. GIWAXS images were integrated with GSAS-II.[67] LeBail refinements were used to extract lattice parameters from GIWAXS patterns and were performed with TOPAS Academic v6.[68] Peak broadening was modeled via the Thompson-Cox-Hastings pseudo-Voigt "TCHZ" peak type as implemented in TOPAS. Reference patterns were generated using VESTA for visual comparisons.[69]

Compositional analysis was performed with X-ray fluorescence (XRF) and Rutherford Back-Scattering (RBS) methods. Metal ratios were mapped using a Bruker M4 Tornado XRF with a Rh source operating at 50 kV and 200 μA. The spot size was 25 μm in diameter. The measurements were performed under vacuum (<20 mbar) with an exposure time of 200 s for each measurement. Nitrogen and oxygen ratios for select samples were quantified with RBS. RBS was run in a 168° backscattering configuration using a model 3S-MR10 RBS system from National Electrostatics Corporation with a 2 MeV He^+ beam energy. Samples were measured for a total integrated charge of 160 uC. RBS spectra were modeled with the RUMP software package.[71]

Room temperature conductivity was measured using a custom built collinear four-point probe instrument by sweeping current between the outer two pins while measuring voltage between the inner pins (1 mm between each pin). Conventional geometric corrections were applied to convert the measured resistance into sheet resistance and then conduc-

tivity.[72] The measured films were deposited on insulating substrates (either 100 nm thick SiO_2 on Si or 100 nm thick Si_3N_4 on Si) to avoid contribution from the substrates.

Temperature-dependent electrical resistivity was measured using a Lake Shore Cryotronics Model 8425. A 5 mm $\times$ 5 mm squares were scribed out of libraries deposited on insulating substrates. For compositions near $MgWN_2$, indium contacts were pressed into the film near the corners of the squares. Indium contacts were non-ohmic on Mg_3WN_4 films, so Ti/Au contacts were deposited by evaporation. Temperature-dependent sheet resistance was measured from 104 K to 298 K, with resistivity calculated from XRF-measured film thickness.

3.2.3 Bulk synthesis

As reagents are air sensitive, solid-state precursors were prepared and stored in an argon filled glovebox ($O_2 < 0.1$ ppm, $H_2O < 0.5$ ppm). Powders of Mg_3N_2 (Alfa Aesar, > 99.6%, 325 mesh) and W (Sigma-Aldrich, 99%, 42 μm) were used as received. Bulk reactions were prepared by grinding together the reagent powders with an agate mortar and pestle, pelletizing the mixture by cold-pressing in a 0.25 in die at 300 MPa (approximately 100–200 mg per pellet), loading the pellet into an alumina crucible held horizontally in an alumina boat, and loading the boat into a mullite or quartz process tube. A Zr foil cap was fit into the mouth of the alumina crucible to decrease Mg_3N_2 loss by volatization and to sacrificially react with any trace O_2. The process tube was sealed with custom endcaps, removed from the glovebox, and attached to a purified N_2 (g) line (ca. 20 mL/min flow rate). A diagram for this system is shown in Figure 3.5A. Reactions were conducted by heating the sample in a tube furnace and dwelling for approximately 5–20 h at various temperatures up to 1100 °C. Samples were recovered into the Ar glovebox, ground again in with a mortar and pestle, and prepared for PXRD. This procedure was adapted from the strategy used by Verrelli, et al. to synthesize $MgMoN_2$.[39]

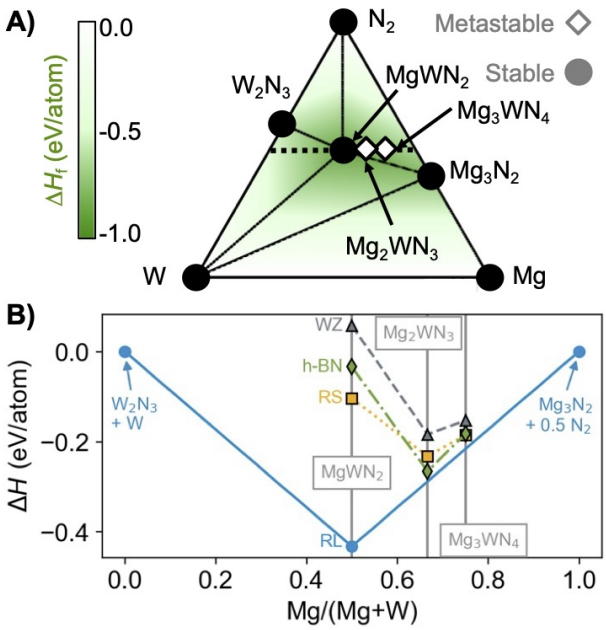

Figure 3.2: A) Calculated ternary phase diagram for the Mg-W-N system. B) Pseudobinary hull diagram calculated with a 1:1 M:N ratio (corresponding to the black dotted trace from A). The vertical axis shows the relative formation energy (ΔH) at $T = 0$ K compared to the most stable point in the binary hulls at this cation:anion ratio ($W_2N_3 + W$ and $Mg_3N_2 + \frac{1}{2}N_2$). The RL $MgWN_2$ structure defines the deepest point on the hull. The calculated, ordered polymorphs for $MgWN_2$, Mg_2WN_3, and Mg_3WN_4 in the WZ, h-BN, and RS-like structure types are metastable to varying degrees. Several highly metastable ternary phases in the NRELmatDB and Materials Project databases are omitted for clarity.

PXRD measurements were performed using a Bruker DaVinci diffractometer with CuKα X-ray radiation. All samples were prepared for PXRD from within the glovebox by placing powder on off-axis cut silicon single crystal wafers to reduce the background, and then covered with polyimide tape to slow exposure to the atmosphere. However, the product $MgWN_2$ proved to be air stable, so the PXRD shown in Figure 3.5 was collected without the tape so as to minimize the large scattering background. A structural model was created by substituting W for Mo in the previously reported $MgMoN_2$ structure[39] and refining the model using TOPAS v6. Structural visualizations were performed with VESTA.[69]

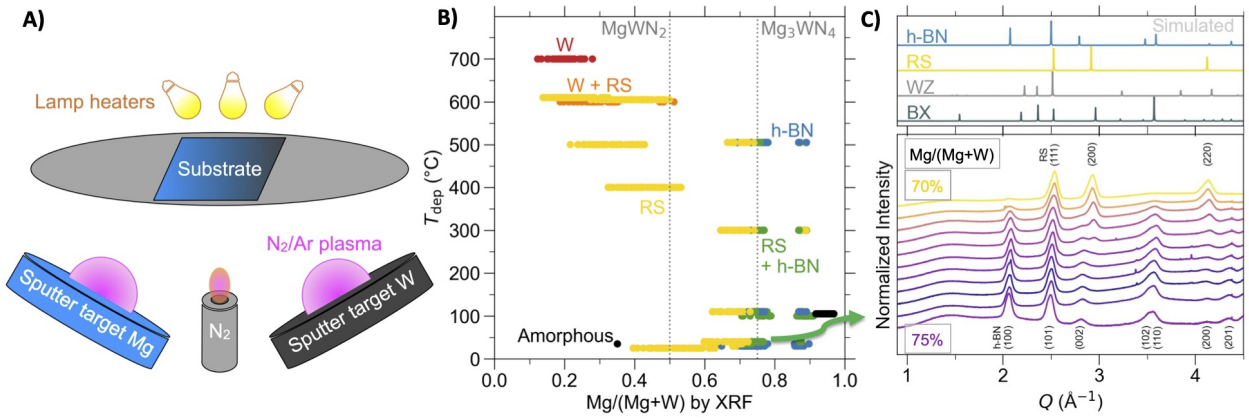

Figure 3.3: A) Diagram of the experimental setup for combinatorial co-sputtering. B) Depositions conducted at various temperatures (T_{dep}) produced RS and h-BN structures of Mg-W-N phases with $T_{\text{dep}} \leq 600$ °C, with higher temperatures leaving W as the only structure detected by XRD. RS (yellow markers) accommodates a wide range of compositions ($0.1 <$Mg/(Mg+W)< 0.9). Near Mg/(Mg+W) = 0.75, the h-BN phase appears in some cases, often coexisting with the RS structure. C) GIWAXS patterns from a library deposited at ambient conditions, showing the transition between the RS and h-BN structures. The wurtzite (WZ) and anti-bixbyite (BX, Mg_3N_2) structures are not observed.

3.3 Results and Discussion

3.3.1 Thermodynamic analysis

Calculated formation energies relative to the binaries show that RL $MgWN_2$ is the only thermodynamically stable ternary in the Mg-W-N system, according to DFT calculations of the cation-ordered structures (Figure 3.2). The cation-ordered WZ, h-BN, and RS-like polymorphs in the $MgWN_2$, Mg_2WN_3, and Mg_3WN_4 compositions are all metastable to varying degrees. A h-BN structure ($C2/c$ spacegroup) is closest to the hull for the Mg_2WN_3 composition (+0.031 eV/atom metastable), and a RS structure ($I4/mmm$ spacegroup) is closest to the hull for the Mg_3WN_4 composition. The WZ-like phase of Mg_3WN_4 that initially sparked our interest in this space is higher in energy than the h-BN and RS polymorphs. However, these calculated structures are all ordered, whereas combinatorial co-sputtering often yields cation disordered nitrides.[1,53]

3.3.2 Synthesis of Mg-W-N thin films by combinatorial co-sputtering

Combinatorial co-sputtering from Mg and W targets in a N_2/Ar environment resulted in cation-disordered phases with either the RS or the h-BN structure, as determined by XRD (Figure 3.3). The RS structure shows the greatest degree of stability, crystallizing across a wide range of temperatures compositions ($0.1 < x < 0.9$ for $Mg_xW_{1-x}N$) and temperatures (up to 600 °C). At elevated temperatures (ca. 700 °C), Mg appears to volatilize, leaving behind metallic W. At metal ratios near $x = 0.75$ (Mg_3WN_4), a h-BN structure is observed by XRD in some libraries (Figure 3.3C). However, some Mg-rich points still show the RS structure. Other Mg-rich points did not exhibit any crystalline phases and are marked as amorphous in Figure 3.3B.

The coexistence of h-BN and RS polymorphs near the Mg_3WN_4 stoichiometry suggests the phases may be energetically similar for this Mg/(Mg+W) ratio. Indeed, they are structurally related, the h-BN structure being an intermediate in a displacive transformation between the RS and WZ structures.[102] This h-BN structure appears to be uncommon among ternary nitrides. The only prior report we can identify in literature is that of $ZnZrN_2$.[53] However, the five-fold coordination environment of the h-BN is analogous to the transition state experienced by WZ-type ferroelectric materials (e.g. AlScN) as they undergo switching).[103] As another example of a simlar motif, $Mg_3Al_3N_5$ has an Al^{3+} ion split across two face-sharing tetrahedral sites,[104] which is structurally similar to the WZ to h-BN to WZ displacement of ferrolectrics. Lastly, a prior study predicted the ground state for Mg_2NbN_3 and Mg_2TaN_3 to be this h-BN structure type,[52] although sputtering experiments subsequently showed that Mg_2NbN_3 crystallizes as a cation-disordered rocksalt.[11,105] The infrequent occurrence of this polymorph suggests decreased stability relative to other high-symmetry phases like the RS polymorph, a hypothesis supported by our rapid thermal annealing experiments (Figure B.1).

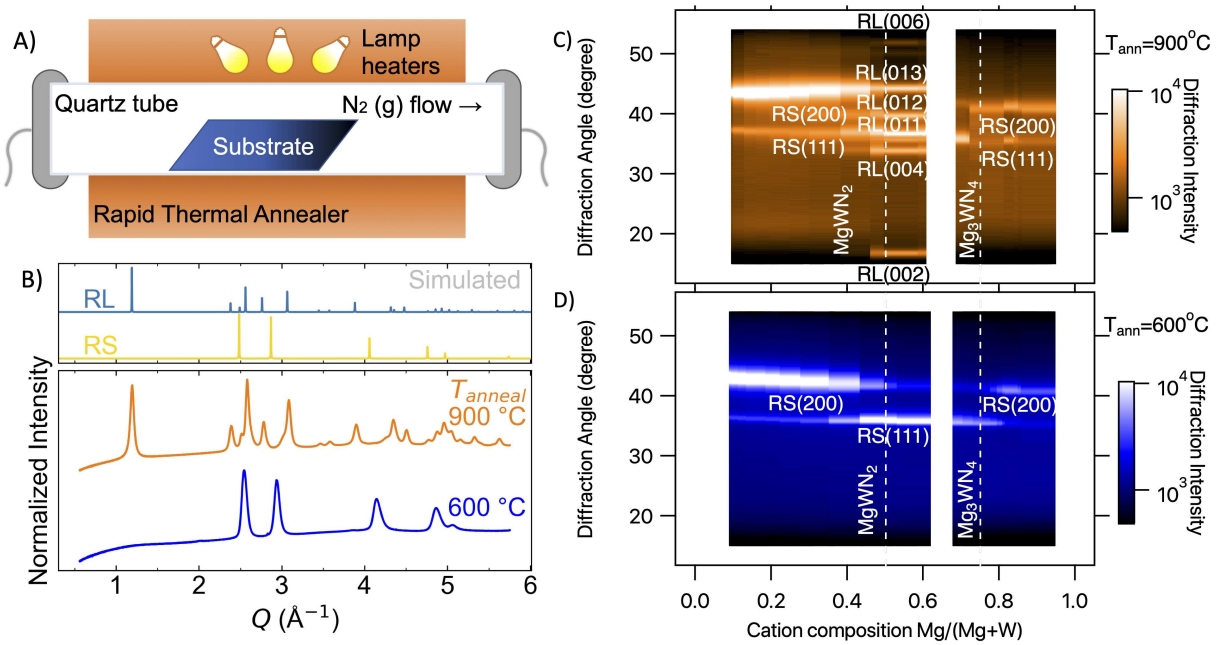

Figure 3.4: A) Diagram of experimental setup used for rapid thermal annealing of combinatorial thin film libraries. B) Synchrotron GIWAXS patterns show that a film (initially deposited in the RS structure with stoichiometry near $MgWN_2$) annealed at 600 °C for 3 min retains the RS structure, but annealing at 900 °C for 3 min induced cation ordering, as indicated by the formation of the RL structure. C, D) Diffraction heatmaps as a function of Mg/(Mg+W) show that libraries annealed at 600 °C exhibit the RS structure across the whole composition range, while libraries annealed at 900 °C exhibit the RL structure between $0.42 \leq$Mg/(Mg+W)≤ 0.62, with the RS structure persisting in Mg-rich and Mg-poor regions (relative to $MgWN_2$).

3.3.3 Rapid thermal annealing of combinatorial libraries

Rapid thermal annealing experiments of combinatorial film libraries show that annealing can induce cation ordering near the $MgWN_2$ stoichiometry (Figure 3.4). The portion of the library near the stoichiometric $MgWN_2$ composition retained the RS structure up to T_{anneal} = 600 °C, but a clear structure transition to the RL polymorph occurred by T_{anneal} = 900 °C (Figure 3.4b). However, this transformation only occurs in a narrow composition window near Mg/(Mg+W) = 0.5 (i.e., $MgWN_2$, Figure 3.4C). For Mg-poor compositions with Mg/(Mg+W)< 0.42 and Mg-rich compositions with Mg/(Mg+W)> 0.62, the RS structure persisted at T_{anneal} = 900 °C. This shows that the ordered RL structure has a narrow compositional tolerance, while the RS structure can accommodate a large degree of off-stoichiometry. These results, along with the thermodynamic calculations (Figure 3.2) suggest that the RL phase is the thermodynamic ground state, a fact further supported by bulk syntheses.

3.3.4 Bulk synthesis of cation ordered $MgWN_2$

Bulk syntheses yielded $MgWN_2$ in the cation-ordered RL structure (Figure 3.5). The RL $MgWN_2$ phase formed from a reaction between $2Mg_3N_2 + 3W$ powders heated at 1080 °C for 10 h. Syntheses conducted at lower temperatures did not yield reaction, suggesting a significant kinetic barrier to reactivity between the Mg_3N_2 and W. Refining the degree of site inversion (x) for $(Mg_{1-x}W_x)(W_{1-x}Mg_x)N_2$ leads to x = 0.11, suggesting some degree of cation disorder. For comparison, x = 0.5 would indicate full cation disorder, and x = 0 would indicate a fully ordered phase. However, site occupancy is modeled by fitting relative peak intensities, and peak intensities also vary with preferred orientation, thermal parameters, and corrections for absorption or surface roughness.[106] These data may not be of sufficient quality to reliably refine site occupancy when convoluted with all these variables. Cation ordering is most clearly visible in the supercell reflection (002) at $2\theta = 17°$ (Figure B.3), and the strong supercell reflection in Figure 3.5B suggests a substantial

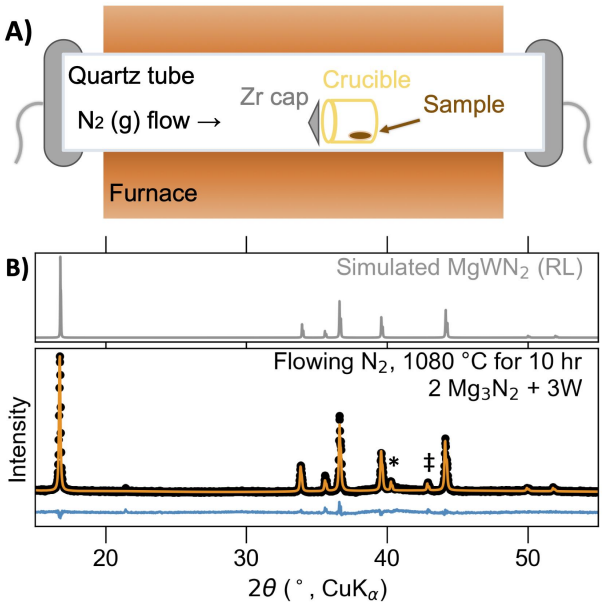

Figure 3.5: A) Diagram of the experimental setup used for the bulk synthesis of $MgWN_2$. B) Rietveld refinement (orange trace) of a PXRD pattern (black dots) of $MgWN_2$ produced by heating $2Mg_3N_2 + 3W$ (100% excess Mg_3N_2) under flowing N_2 for 10 h at 1080 °C. The difference trace is shown in blue. The simulated pattern of RL $MgWN_2$ is shown for reference in the box above. Trace W (*) and MgO (‡) impurity phases are present in the pattern. The excess Mg_3N_2 volatilized away from the pelletized sample and does not appear in the PXRD pattern.

degree of cation ordering. The isostructural $MgMoN_2$ synthesized by the same method was modeled to be fully-ordered by combined synchrotron XRD and neutron diffraction.[39] High-resolution synchrotron measurements could improve the reliability of the refinement, particularly as these W-containing samples are highly absorbing.

The formation of RL $MgWN_2$ by high-temperature ceramic synthesis verifies that the RL polymorph defines the thermodynamic ground state. The excess Mg_3N_2 used in bulk syntheses did not lead to any signs of a more Mg-rich phase (i.e., Mg_2WN_3 or Mg_3WN_4), so we hypothesize any ordered configurations of those materials (e.g., $Pmn2_1$ WZ) may be destabilized at the elevated temperatures required for ceramic synthesis. However, these findings show that the RTA treatment of combinatorial thin films is a powerful tool for exploring the thermodynamic stability of new materials. We expect this RTA method to unlock more tunable properties for nitride materials in the future.

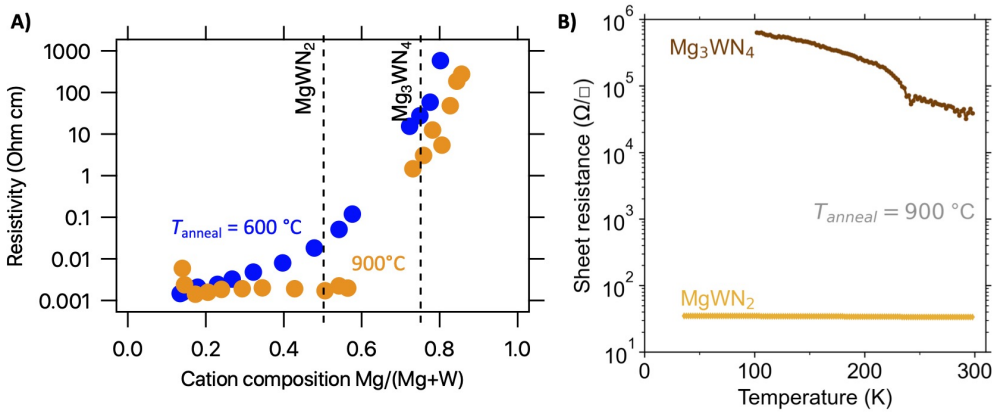

Figure 3.6: A) Resistivity as a function of Mg/(Mg+W) shows increasing resistivity with increasing Mg content. B) Resistivity as function of temperature show constant resistivity for RL $MgWN_2$ suggestive of metallic behavior. Resistivity decreases with increasing temperature for RS Mg_3WN_4, indicating thermally activated hopping consistent with semiconducting behavior.

3.3.5 Electronic properties

Measurements of electronic properties on thin film samples show metallic behavior for $MgWN_2$ in both the RS and RL polymorphs, and semiconducting behavior for RS Mg_3WN_4 (Figure 3.6). Resistivity increases as a function of Mg-content, with Mg-poor samples exhibiting resistivity $< 1\Omega$cm and Mg-rich samples exhibiting resistivity $> 1\Omega$cm (Figure 3.6A). Annealing at 900 °C decreases resistivity slightly across the whole composition range (compared to samples annealed at 600 °C), consistent with decreased grain-boundary resistance. Temperature-dependent resistivity measurements on annealed samples ($T_{anneal} = 900$ °C, Figure 3.6B) show constant resistivity for RL $MgWN_2$, consistent with metallic-like charge transport. In contrast, the resistivity of Mg_3WN_4 decreases with increasing temperature, as expected for a semiconductor. Additional measurements are underway to explore the effect of annealing on optical, electronic, and magnetic behavior.

The metallic nature of $MgWN_2$ and semiconducting nature of Mg_3WN_4 is consistent with their expected d-electron count and with prior reports in similar systems. $MgWN_2$ has tungsten in a 4+ oxidation state, with a $5d^2$ valence electron configuration contributing mobile charge carriers. In contrast, Mg_3WN_4 has tungsten in the 6+ oxidation state, which has a $5d^0$ electron configuration at the valence level and no mobile charges at the valence

band (aside from those introduced by unintentional doping). Similar trends in conductivity were observed in the Zn-Mo-N system, where films of a wurtzite structure spanned metallic $ZnMoN_2$ to insulating Zn_3MoN_4.[18]

3.4 Conclusions

We synthesized three new polymorphs of magnesium tungsten nitrides in a previously empty ternary phase space. Combinatorial co-sputtering yielded cation-disordered rocksalt structures across a wide composition range including $MgWN_2$, while samples near the Mg_3WN_4 stoichiometry crystallized in either a cation-disordered rocksalt or a cation-disordered hexagonal boron nitride structure. Rapid thermal annealing of these combinatorial libraries show that rocksalt $MgWN_2$ converts to a cation-ordered rocksaline structure at T_{anneal} = 900 °C, but only in a narrow compositional window. This cation ordered $MgWN_2$ phase also appeared in bulk ceramic syntheses, indicating that annealing of thin film libraries can potentially access the thermodynamic ground state of ternary nitrides. Resistivity measurements show that $MgWN_2$ is metallic and Mg_3WN_4 is a semiconductor. In sum, these findings expand the toolkit through which combinatorial co-sputtering experiments can explore the thermodynamic landscape in search of new nitride compounds.

Chapter 4

Bulk synthesis, structure, and electronic properties of magnesium zirconium nitride solid solutions*

Overview

Ternary nitride phase space holds great potential for new functional materials, as suggested by computational predictions of yet-to-be discovered stable phases. Here, we report a metathesis route to bulk powders of $MgZrN_2$ and the solid solutions $Mg_xZr_{2-x}N_2$ ($0 < x < 1$). These ternary phases only result when lower temperature reactions are used, in contrast to previous work using the similar Mg-based metathesis reactions that resulted in the formation of exclusively ZrN. Thermochemical calculations illustrate why lower-temperature metathesis reactions yield the incorporation of Mg, while higher temperature and ceramic reactions yield exclusively ZrN. Experimental *in situ* X-ray diffraction of metathesis reactions during heating reveals two stages in the reaction pathway: initial consumption of the precursors to make an amorphous product ($T_{rxn} > 350$ °C) followed by crystallization at higher temperatures ($T_{rxn} > 500$ °C). Changing the ratio of the metathesis precursors (Mg_2NCl and $ZrCl_4$) controllably varies the composition of $Mg_xZr_{2-x}N_2$, which crystallizes as a cation-disordered rock salt, as evidenced by high-resolution synchrotron X-ray diffraction, electron microscopy, and bulk compositional analysis. Variation in composition leads to a gradual metal-to-insulator transition with increasing *x*, similar

* Reprinted with permission from C.L. Rom, M.J. Fallon, A. Wustrow, A.L. Prieto, J.R. Neilson, Bulk Synthesis, Structure, and Electronic Properties of Magnesium Zirconium Nitride Solid Solutions, *Chem. Mater*. 2021. 33 (13), 5345-5354. Copyright 2021, American Chemical Society. C.L.R. and J.R.N. conceptualized the project. M.J.F. and A.W. assisted with *in situ* X-ray diffraction experiments and analysis. C.L.R. performed the experiments and wrote the manuscript with guidance of A.L.P. and J.R.N.

to other reports of analogous thin film specimens produced by combinatorial sputtering. Meanwhile, the optical behavior of these powders suggests nanoscale compositional inhomogeneity, as signatures of ZrN-like absorption are detectable even in Mg-rich samples. This metathesis approach appears to be generalizable to the synthesis of bulk ternary nitride materials.

4.1 Introduction

Nitride-based ceramics, with anionic nitrogen coordinating metals or metaloids, are an important but under-explored class of functional materials. Many binary early transition metal nitrides are mechanically hard metals that superconduct at cryogenic temperatures (e.g., ZrN, TiN).[107] Improved processing of GaN resulted in the widespread use of that binary nitride in inorganic light emitting diodes, as well as a Nobel prize.[3] In general, incorporating a third element to form ternary nitrides adds the possibility of tuning their functional properties.[1,51] For example, the solid solution $In_xGa_{1-x}N$ has a tunable band gap ranging from 3.4 eV to 1.1 eV with x.[108] Ternaries can also crystallize in distinct structures and properties relative to their binaries, as highlighted by the semiconducting perovskite $LaWN_3$ compared to metallic rock salts LaN and WN.[19] In addition to functional optoelectronic materials, ternary nitrides are also of interest as catalysts,[109,110] magnets,[111] and battery materials.[39,40] While technologically useful, relatively few ternary nitrides are known.[1] For comparison, the phase space of ternary oxide-based compounds spans >4,000 unique crystal structures, whereas only approximately 400 ternary nitride crystal structures have been reported.[2] This dearth of known nitrides calls for improved synthetic methods to access this family of materials.

Computational mapping of the ternary nitride phase spaces has accelerated the synthesis of new materials. Data-mining-based structure prediction and density functional theory (DFT) calculations predicted 244 new thermodynamically stable ternaries, which is more than double the 213 known at the time.[2] Subsequently, some of these

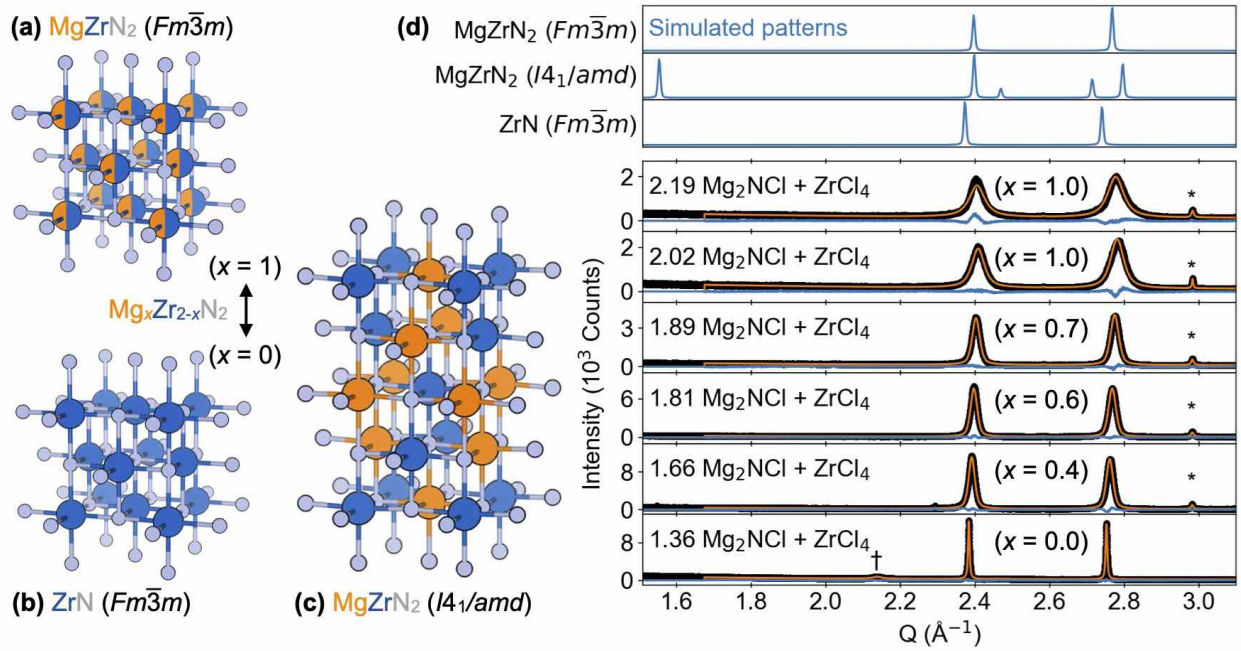

Figure 4.1: (a) The cation-disordered $MgZrN_2$ observed in this study adopts a cubic rock salt structure. This material and its solid solutions $Mg_xZr_{2-x}N_2$ ($0 < x < 1$) are isostructural with (b) binary ZrN, in contrast to (c) the predicted tetragonal cation-ordered structure of $MgZrN_2$. (d) Simulated SPXRD patterns are shown in blue traces (top). SPXRD data from 11-BM-B ($\lambda \approx 0.4579$ Å) of the washed reaction products from $n$$Mg_2NCl + ZrCl_4$ heated to a 800 °C set point under vacuum in sealed ampules for 12 h show that increasing Mg_2NCl relative to $ZrCl_4$ leads to a smaller unit cell for the rock salt structure, broader peaks, and increasing x. No additional reflections that would be consistent with an ordered $I4_1/amd$ $MgZrN_2$ phase are observed. Trace MgO (*) and $Zr_4N_2O_5$ (†) are present in some of the samples. Data (black dots), calculated patterns from Rietveld analysis (orange trace), and difference curves (blue trace) are shown. The vertical axis is a linear scale. Full patterns are shown in Figure C.4.

new ternary phases have been synthesized via combinatorial sputtering in a nitrogen-based plasma (e.g., $LaWN_3$, Mg_3SbN, Mg_2SbN_3),[12,19] high-pressure ceramic synthesis (e.g., $(Si_{1-x}Ti_x)_3N_4$),[112] high-pressure metathesis (e.g., $MgSnN_2$),[47] or self-combustion metathesis (e.g., $M_xMo_{1-x}N_{0.5}$ where M = Mn, Fe, Co).[113] Sputtering methods have also been used to synthesize a set of ternary nitrides crystallizing with disordered rock salt structures (e.g., $MgTiN_2$, $MgZrN_2$, $MgHfN_2$, and Mg_2NbN_3).[11] Circling back, these experimental synthesis results have revealed the importance of cation site disorder, which better informs predictive models.[53]

Of these new nitrides, $MgZrN_2$ has garnered particular interest due to the metal-to-insulator transition and compatibility of this rock salt structure with common electronic substrates like Si and MgO. As a thin film produced by sputtering, $MgZrN_2$ crystallizes with a disordered rock salt structure, isostructural with the binary superconductor ZrN (Figure 4.1a and b).[11,49,114,115] In such studies, combinatorial sputtering was used to survey a broad range of stoichiometries around the targeted line compound $MgZrN_2$, with x in $Mg_xZr_{2-x}N_2$ between 0.5 and 1.6. The behavior transitions from metallic (10^3 S/cm at $x < 1.0$) to semiconducting (10^{-3} S/cm at $x \geq 1.0$) as Mg^{2+} replaces formally charged Zr^{3+}, which is oxidized to Zr^{4+}. An absorption onset of 2.2 eV appears with $x \approx 1$ and shifts to 1.8 eV by $x \approx 1.6$. There, they show that oxide incorporation charge balances the phase, resulting in $Mg_xZr_{2-x}N_{4-2x}O_{2x-2}$ for $1 < x < 2$.[49] In addition to Mg-content, the degree of cation order is also expected to influence semiconducting properties,[51,77] but cation ordering has not yet been observed. Bulk samples with additional synthetic degrees of freedom are needed to further investigate these materials.

Here, we describe the synthesis of bulk $Mg_xZr_{2-x}N_2$ powders ($0 < x < 1$) via metathesis (i.e., double-displacement) reactions between $ZrCl_4$ and Mg_2NCl or Mg_3N_2. *In situ* powder X-ray diffraction (PXRD) measurements along the reaction pathway identify reactivity differences between these two Mg-based precursors. Thermochemical calculations rationalize why the metathesis route produces $Mg_xZr_{2-x}N_2$, yet traditional ceramic reactions

yield only ZrN. Solid solution behavior in a disordered rock salt crystal structure is observed by high-resolution synchrotron powder X-ray diffraction (SPXRD); no evidence for cation ordering is observed. The ratio of Mg to Zr in the reaction products were studied by Rietveld analysis of synchrotron X-ray diffraction data, energy dispersive X-ray spectroscopy (EDS), and inductively coupled plasma atomic emission spectroscopy (ICP-AES). Electronic measurements show metallic behavior in Mg-poor phases and semiconducting behavior in near-stoichiometric $MgZrN_2$ phases ($x \approx 1$ in $Mg_xZr_{2-x}N_2$). Optical measurements suggest the presence of small ZrN domains within Mg-rich $Mg_xZr_{2-x}N_2$. This metathesis synthesis yields a ternary nitride where traditional ceramic techniques fail, offering a route to other predicted (but not yet synthesized) ternary nitrides.

4.2 Methods

4.2.1 Synthesis

Caution: Solid-state metathesis reactions can be highly exothermic and can yield gaseous byproducts (e.g., N_2). These properties pose explosion and fire hazards, particularly when sealing reagents in closed containers and when scaling up reactions. Keep nitride precursors away from flammable materials and under inert conditions to avoid fires. Calculate the expected pressure in a closed system prior to heating to ensure the pressure does not exceed safe limits. Exercise caution when cleaning nitride-contaminated materials once removed from the glovebox.

All precursors were prepared and stored in an argon filled glovebox ($O_2 < 0.1$ ppm, $H_2O < 0.5$ ppm, unless explicitly mentioned). Mg_2NCl was synthesized as previously reported with Mg_3N_2 (Alfa Aesar, 99% purity) and $MgCl_2$ (Sigma Aldrich, 98% purity).[116] Stoichiometric amounts of Mg_3N_2 (≈3 g) and $MgCl_2$ (≈3 g) were combined in an agate mortar and pestle and ground into a homogeneous tan powder. The powder was then cold pressed (P ≈ 80 MPa) into a dense pellet (diameter = 0.5 in) and placed in a quartz ampule (14 mm inner diameter, 16 mm outer diameter). This ampule was then brought out of the

glovebox and quickly sealed under vacuum ($\leq$20 mTorr, as determined by a Pirani gauge) using an oxygen/methane torch. The sealed ampule ($\approx$15 cm^3 internal volume) was then heated at 10 °C/min in a muffle furnace to a set point of 550 °C. The reaction was held at temperature for 5 days, and then allowed to cool to room temperature before opening the ampule in the glovebox. $ZrCl_4$ (Acros, 98%) was purified by heating approximately 4 g in a sealed quartz ampule ($\approx$30 cm long) in a 3-zone horizontal tube furnace to transport $ZrCl_4$ from the hot zone (400 °C set point) to the colder zone (300 °C set point), leaving behind less volatile, oxide-based impurities (e.g., ZrO_2).

Throughout this manuscript, reaction temperatures are described as either set point temperatures or as the recorded temperature during *in situ* experiments. Temperatures experienced by the sample may be as much as 40 °C lower than the specified furnace set point due to thermal gradients within furnaces. Furnace temperatures were ramped at a nominal rate of 10 °C/min and cooled by turning off power to the heating elements, unless otherwise specified. *In situ* reaction temperatures have been calibrated against reference samples by monitoring the thermal expansion via X-ray diffraction and are accurate within ± 10 °C.

Syntheses of $Mg_xZr_{2-x}N_2$ powders were conducted by grinding $ZrCl_4$ (ca. 200 mg–500 mg) with either Mg_2NCl (ca. 200 mg–500 mg) or Mg_3N_2 (ca. 100 mg–300 mg) in various ratios. The ratio between magnesium and zirconium precursors is represented by the molar coefficient n (i.e., $n Mg_2NCl + ZrCl_4$ indicates a mol ratio of $ZrCl_4$:Mg_2NCl :: 1:n). The mixtures were loaded into quartz ampules (either as 0.25 in diameter pellets cold pressed at 300 MPa or loose powders, ca. 300 mg–1000 mg), sealed under vacuum ($\leq$20 mTorr, approximately 10 cm^3 internal volume), and heated in muffle or tube furnaces. Reactivity was induced by heating samples at a 500 °C set point in a box furnace for 12 hours, followed by annealing at a 800 °C set point for 12 hours to crystallize the $Mg_xZr_{2-x}N_2$ material. To remove byproduct $MgCl_2$ from the target compound, samples were washed with anhydrous methanol (dried over molecular sieves for at least five days)[117] in a N_2 glove-

box. The products are moisture sensitive (Figure C.3), so all steps of the process were conducted under inert conditions unless otherwise specified.

Control reactions followed traditional ceramic synthetic methods, exemplified by the synthesis of $MgMoN_2$.[39] Mg_3N_2 (ca. 400 mg) and 3/2 molar equivalents of Zr powder (ca. 500 mg) were ground together (i.e., excess Mg_3N_2), pelletized (ca. 300 mg pellets), placed in an alumina crucible with a Zr foil cap (to reduce Mg_3N_2 loss by evaporation and to react with adventitious oxygen) and heated in a tube furnace under flowing purified N_2. The N_2 gas was purified by flowing through a Supelco high capacity gas purifier (Model # 29542-U) prior to flowing into a quartz reaction tube fitted with custom endcaps that permit disconnection from the gas line without air exposure. Samples were recovered directly into an Ar glovebox at room temperature for further analysis.

4.2.2 X-ray diffraction experiments

The products of all reactions were characterized by powder X-ray diffraction (PXRD) and analyzed by the Rietveld method. PXRD measurements were performed using a Bruker DaVinci diffractometer with CuKα X-ray radiation. All samples were prepared for PXRD from within the glovebox by placing powder on off-axis cut silicon single crystal wafers to reduce the background, and then covered with polyimide tape to slow exposure to the atmosphere.

Select samples were sent to Argonne National Laboratory for synchrotron powder X-ray diffraction data (SPXRD). Washed samples were flame sealed under vacuum in quartz capillaries (0.5 mm inner diameter, 0.6 mm outer diameter) under Ar (g). SPXRD measurements were collected on the high-resolution diffractometer at beamline 11-BM-B with a wavelength of either 0.457879 Å or 0.457900 Å.[118] SPXRD patterns are shown in Q-space to account for this small difference in wavelength ($Q = 4\pi \sin(\theta)/\lambda$).

In situ PXRD measurements at elevated temperatures were made on capillary-held samples in a Panalytical Empyrean diffractometer in Debye-Scherrer geometry using a well

insulated Anton Parr HTK1200N high temperature sample environment. AgKα X-ray radiation and focusing X-ray optics were used, and data sets were collected from 2θ scans of the GaliPIX 2D detector. Capillaries of the reagents were heated at a rate of 10 °C/min between scans and held isothermally for 7 minutes during collection of each diffraction pattern. A temperature correction was applied to the measurements via a calibration curve determined from the temperature dependence of MgO and Al_2O_3 lattice parameters measured under the same heating conditions.

4.2.3 X-ray diffraction analysis

Quantitative phase analysis of the PXRD, SPXRD, and *in situ* PXRD data and structural refinement of previously-reported crystal structures (e.g., lattice parameters, cation occupancies) were performed using the Rietveld method as implemented in TOPAS v6 (Bruker AXS). To determine lattice parameters, Si powder was added to aliquots of the reaction products, gently homogenized in an agate mortar, and used as an internal standard in the PXRD experiments. The Si powder was sourced from a single crystal wafer, pulverized in a glovebox to minimize the presence of surface oxide.

To compare the relative amounts of phases in the *in situ* PXRD data sets, a weighted scale factor (Q_p) was calculated such that $Q_p = S_p \times V_p \times M_p$. S_p is the scale factor calculated from Rietveld for phase p, V_p is the volume of the unit cell for phase p, and M_p is the atomic mass of the unit cell for phase p. These experiments did not include a Si internal standard. Amorphous, liquid, and gaseous phases are not detected by this method.

For Rietveld analysis of the rock salt phase, cubic ($Fm\bar{3}m$) ZrN was used as a starting model, with both Mg^{2+} and Zr^{4+} occupying the cation site. Cation occupancy (*x*) was constrained to equal anion occupancy (i.e., Mg + Zr = N). The anion site was fixed at fully occupancy. The atomic displacement parameters were refined isotropically. Lattice parameter, crystallite size (Lorentzian) and microstrain (Gaussian) were also refined. The

background was fit independently for each pattern with a six-term polynomial. An impurity phase of MgO or $Zr_4N_2O_5$ was fit to each pattern if observed, although only the unit cell and crystallite size parameters were refined. To better estimate error in metal occupancy, sequential refinements were carried out by fixing the Mg occupancy parameter between $x = 0.0$ to $x = 2.0$ in increments of 0.1, and refining all other parameters as described above. Mg occupancy uncertainties were estimated from a 1% increase in the refinement Goodness of Fit parameter relative to the best fit. Total μR for samples range from 1.5 ($MgZrN_2$) to 3.0 (ZrN), assuming a 0.5 packing fraction, which suggests that absorption corrections should be applied. However, control refinements accounting for absorption using the calculated, nominal absorption do not lead to meaningful changes in the refined occupancies or their calculated uncertainty.

4.2.4 Additional Characterization

Scanning electron microscopy (SEM) measurements were made using a JEOL JSM-6500F instrument. Energy dispersive X-ray spectroscopy (EDS) measurements were made with the attached Oxford 80 X-MAX silicon drift detector and analyzed using AZtec software (Oxford Instruments). Samples for SEM-EDS analysis were pelletized in an Ar glovebox, adhered to SEM stubs with double-sided carbon tape, and quickly transferred from the glovebox to the instrument (< 5 min air exposure). SEM imaging and mapping was conducted at 15 kV. A 5 kV accelerating voltage was used for quantitative EDS measurements. Averages of the elemental composition were calculated from point-defined EDS measurements made at six different locations on each pellet.

Inductively coupled plasma atomic absorption spectroscopy (ICP-AES) analysis of the metal compositional ratios were conducted by Huffman Hazen Laboratories (Golden, CO) following digestion of the samples using nitric, perchloric and hydrofluoric acids. The error in the Mg results are ± 0.1 % w/w and the error in the Zr results are ± 0.5 % w/w.

Resistivity measurements were conducted on pelletized samples enclosed in Swagelok® cells with PTFE bodies and PTFE compression fittings around the stainless steel current collectors (0.25 inch diameter, 0.317 cm^2 surface area). Samples were prepared in an Ar (g) glovebox but were removed from the box for measurement after being sealed within the measurement cells. A cold-pressed pellet (P ≈ 300 MPa) with mass of approximately 0.1 g was loaded into each cell. Sample thicknesses were calculated from the difference in length between empty and loaded cells as measured by calipers (± 0.01 mm). The cells were removed from the glovebox and connected to a Gamry Reference 3000 potentiostat. Electrochemical Impedance Spectroscopy (EIS) measurements were conducted at room temperature (24 °C) by applying a 50 mV excitation voltage relative to open circuit potential across a frequency range from 3×10^5 Hz to 3×10^{-1} Hz. The samples all exhibited electronically conductive behavior (Figure C.20), and resistance (R) was taken as the low frequency limit of the impedance magnitude (e.g., Z at 300 mHz). Resistance of the contacts (0.05 Ω) was determined by measuring blank cells (stainless steel electrodes in direct contact with one another) and subtracted out to determine sample resistance (R_s). Sample conductivity (σ) was calculated from $\sigma = (t)/(R_s A)$ where t is pellet thickness and A is cross-sectional area (0.317 cm^2). Pellets were recovered post-measurement and analyzed by PXRD to confirm that no chemical changes occurred.

Optical spectroscopy measurements were made with an Ocean Optics tungsten-halogen light source (HL-2000-FHSA) and an Ocean Insight Flame Spectrometer with an integrating sphere. A fiber optic cable was used to illuminate the flat base of a borosilicate glass vial covered by loose powder of the sample. A photograph of this setup is shown in Figure C.18. A vial with $BaSO_4$ was used as a white reflectance standard. Samples were prepared by homogeneously mixing a small portion of sample into $BaSO_4$ using an agate mortar and pestle in an argon glovebox (≈ 7 wt% sample in $BaSO_4$). Mixtures were then loaded into vials (containing an inert Ar atmosphere in the headspace) and were sealed with electrical tape before removing the vials from the glovebox for measurement. The Kubelka-Munk

transform was calculated via $k/s = ((1-R)^2)/(2R)$ where k is the absorption coefficient, s is the scattering coefficient, and R is the diffuse reflectance.

4.2.5 Thermodynamic calculations

Thermochemical equilibrium calculations were made using a method described by Bartel, et al.[119] Briefly, the Gibbs free energy of formation as a function of temperature, $\Delta G_f(T)$, is calculated from the sum of density functional theory formation energy ΔH_f, tabulated elemental chemical potentials $G_i(T)$, and a machine-learning calculated correction factor $G^\delta(T)$ that largely corrects for vibrational entropy. The tabulated elemental chemical potentials are referenced to the FactSage database.[120] These calculations source crystal structures, unit cell volumes, and DFT-computed ΔH_f from the Materials Project[9] or our prior work in the case of Mg_2NCl.[44] The calculations are implemented using open source code.[119] From the estimated Gibbs free energies of each phase, reaction energies are calculated by summing formation energies multiplied by molar coefficients ($\Delta G_{rxn} = \Sigma n \Delta G_f$). Calculated ($T$ = 0 K) ternary isopleths of the quaternary phase diagram are shown in Figure C.14. Relevant phase formation energies are tabulated in Table C.1. Temperature-dependent reaction energies are plotted in Figure C.15.

4.3 Results and Discussion

4.3.1 Synthesis pathways to $Mg_xZr_{2-x}N_2$

Bulk $Mg_xZr_{2-x}N_2$ powders are synthesized via metathesis reactions between $ZrCl_4$ and Mg_3N_2 or Mg_2NCl. The ideal stoichiometric reactions to produce $MgZrN_2$ from these precursors are:

$$\mathrm{Mg_3N_2} + \mathrm{ZrCl_4} \longrightarrow \mathrm{MgZrN_2} + 2\,\mathrm{MgCl_2}\ (\Delta G_{rxn}(1100\text{ K}) = \text{-0.378 eV/atom}), \quad (4.1)$$

$$2\,\mathrm{Mg_2NCl} + \mathrm{ZrCl_4} \longrightarrow \mathrm{MgZrN_2} + 3\,\mathrm{MgCl_2}\ (\Delta G_{rxn}(1100\text{ K}) = \text{-0.324 eV/atom}). \quad (4.2)$$

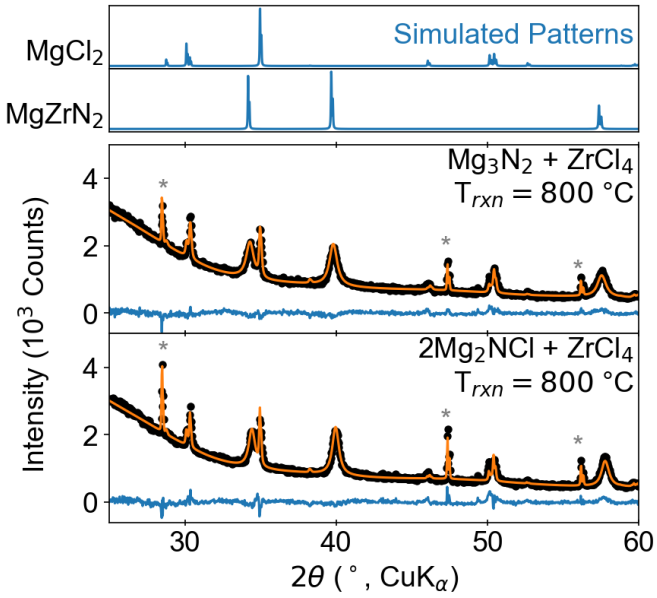

Figure 4.2: PXRD patterns of reaction products from syntheses targeting $MgZrN_2$ via Equations 4.1 and 4.2 show complete reactivity after annealing at a 800 °C set point for 12 h. Data (black dots), calculated patterns from Rietveld analysis (orange trace), and difference curves (blue trace) are shown. Silicon powder (denoted by the grey *) was mixed into the sample post-reaction to serve as an internal standard against which the lattice parameters were refined. Simulated patterns of the products, $MgCl_2$ and cation disordered rock salt $MgZrN_2$, are shown for reference (top boxes).

Upon completion of the reaction, $MgCl_2$ is washed away with dry methanol in an argon glovebox, leaving one crystalline phase remaining as shown by SPXRD (Figures 4.1, C.4). All of the reflections of this phase are indexed to a $Fm\bar{3}m$ phase of a disordered rock salt structure type (Figures 4.1, 4.2, C.4). Diffraction peaks indicative of the cation ordered $I4_1/amd$ $MgZrN_2$ phase are not observed. Thin film work in the Mg-Zr-N phase space similarly finds no evidence for cation-ordered $MgZrN_2$, only the disordered rock salt $Mg_xZr_{2-x}N_2$.[11,49,114,115] This finding is consistent with recent exploration of the Zn-Zr-N phase space with combinatorial sputtering, which found that the disordered rock salt structure was entropically stabilized compared to the cation ordered structure.[53] While both the Mg_3N_2 and Mg_2NCl precursors react with $ZrCl_4$ to form the cation disordered rock salt $MgZrN_2$, the reactivities of these precursors differ.

In situ PXRD data show subtle differences between the two different Mg-containing precursors (Figure 4.3). Most prominently, the Mg_2NCl reaction yields $MgCl_2$ at a lower

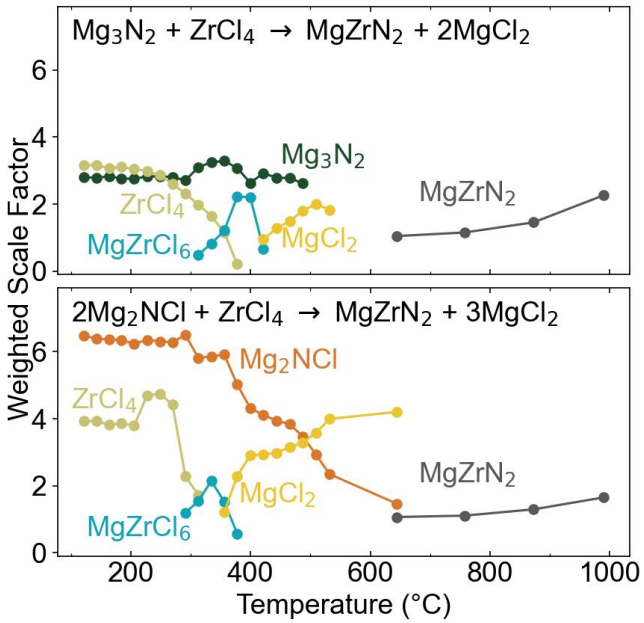

Figure 4.3: Weighted scale factor of each phase from Rietveld refinements of *in situ* PXRD data as a function of temperature. This quantitative phase analysis reveals that Mg_2NCl reacts more readily than Mg_3N_2. In both reactions, $MgZrCl_6$ forms near 300 °C, indicating reactivity of the Mg-based reactant. However, the reaction of $2\,Mg_2NCl + ZrCl_4$ (bottom plot) yields $MgCl_2$ by 350 °C. In contrast, $Mg_3N_2 + ZrCl_4$ (top plot) does not yield $MgCl_2$ until $T_{rxn} = 420$ °C. Therefore, Mg_2NCl is more reactive at lower temperatures than Mg_3N_2. Capillaries of the reagents were heated at a rate of 10 °C/min between scans and held isothermally for 7 minutes during collection of each diffraction pattern. Measurements were carried out inside a high temperature stage of a laboratory diffractometer with a Ag Kα source and focusing optics. Selected PXRD patterns are shown in Figure C.8.

temperature (350 °C) than Mg_3N_2 (420 °C). While both reactions produce $MgZrCl_6$ near 300 °C, indicating some degree of reactivity, when using Mg_2NCl, the intermediate $MgZrCl_6$ fully reacts below 400 °C, while $MgZrCl_6$ persists until 420 °C in the Mg_3N_2 reaction. In both cases, the rock salt product, $MgZrN_2$, does not crystallize until heated above 600 °C. The $ZrCl_4$ phase fraction decrease is also attributed to volatization in addition to reactivity. The differences revealed by *in situ* PXRD are corroborated by *ex situ* PXRD from longer timepoint experiments.

Ex situ PXRD data show that reactions with Mg_2NCl proceed to completion within 12 h of heating at a 500 °C set point, while those beginning with Mg_3N_2 are still incomplete under identical conditions (Figure C.7). This difference is not attributable to the increased reactivity of smaller particles, as the Mg_2NCl precursor used is composed of larger particle sizes than the Mg_3N_2 precursor (Figure C.2). This finding is consistent with our prior study using metathesis to synthesize Mn_3N_2, where we identify Mg_2NCl as a more kinetically competent precursor relative to Mg_3N_2 (i.e., Mg_2NCl reacts quickly and specifically).[44] Therefore, we used Mg_2NCl for most of our synthetic work reported here. This kinetic competence allows the metathesis routes to be selective[43] by accessing the $Mg_xZr_{2-x}N_2$ phase, while traditional "ceramic" reactions yield only ZrN.

Previous metathesis reactions targeting ZrN using Mg_3N_2 overlooked the possibility of ternary formation. For example, reactions between Mg_3N_2 and ZrO_2 at 1000 °C produced ZrN nanoparticles (along with MgO and N_2 byproducts).[121] Additionally, that procedure involved washing with water, removing any of the $MgZrN_2$ that may have formed (which we have found to be moisture sensitive, Figure C.3). Reactions between Mg_3N_2 and various transition metal chlorides yielded binary nitrides and subnitrides (e.g., TiN, HfN, VN, V_2N, TaN, Ta_2N, CrN, Cr_2N) and reduced metals (e.g., Mo, W).[122,123] These metathesis reactions therefore missed ternary phases that have subsequently been synthesized by other methods (e.g., $MgTiN_2$, $MgMoN_2$, $MgTa_2N_3$, and $Mg_2Ta_2N_4$).[11,39,40] The results reported

here emphasize that careful control of the reaction conditions is needed to yield ternary phases.

Control reactions following a ceramic route fail to yield the ternary $MgZrN_2$ target (Figure 4.4). The ceramic reaction should nominally proceed via:

$$Mg_3N_2 + 3Zr + 2N_2 \longrightarrow 3\,MgZrN_2 \qquad (\Delta G_{rxn}(1100\text{ K}) = \text{-0.829 eV/atom}), \qquad (4.3)$$

by analogy to the synthesis of $MgMoN_2$.[39] Analysis of diffraction data show that, rather than yielding the ternary, the product rock salt phase was ZrN with negligible Mg incorporation ($x \leq 0.05$ for $Mg_xZr_{2-x}N_2$ after 100 h of heating at 800 °C, Figure C.10). Therefore, the first reaction step is likely $2\,Zr + N_2 \longrightarrow 2\,ZrN$ (ΔG_{rxn}(1100 K) = -1.363 eV/atom), followed by negligibly slow incorporation of Mg. Although thermodynamics predict both ceramic and metathesis routes should yield $MgZrN_2$, differing intermediates suggest that kinetics allow metathesis reactions succeed where the ceramic route fails.

4.3.2 Thermodynamic and kinetic rationale for metathesis

Although $MgZrN_2$ is thermodynamically stable at the synthesis temperature, this phase is impractically slow to form via the ceramic route. Gibbs free energy calculations show that at the synthesis temperature (≈ 1000 °C), ZrN formation provides the most exergonic reaction per atom (Figure 4.5). Experimentally, the first phase to form in the ceramic synthesis is ZrN (Figure 4.4; $2\,Zr + N_2 \longrightarrow 2\,ZrN$; ΔG_{rxn}(1300 K) = -1.271 eV/atom), consistent with literature showing that ceramic syntheses proceed through sequential pairwise reactions and that the most exothermic reaction tends to occur first.[124,125] Although the subsequent reaction to yield $MgZrN_2$ is still exergonic ($Mg_3N_2 + 3\,ZrN + 0.5N_2 \longrightarrow 3\,MgZrN_2$; ΔG_{rxn}(1300 K) = -0.142 eV/atom), we observe the process to be negligibly slow. ZrN is a refractory ceramic, often used as a diffusion barrier in microelectronics to inhibit atom migration.[126] Consequently, the interdiffusion of Mg into the ZrN lattice is not observed. Figure 4.5 also shows the differing thermodynamic landscapes for a successful

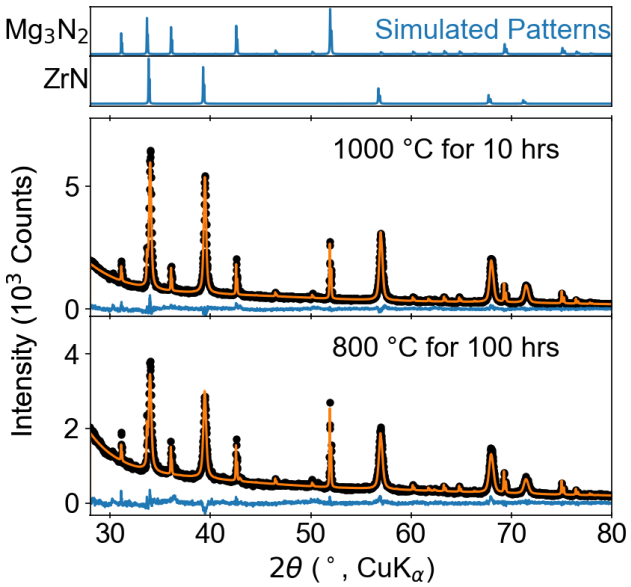

Figure 4.4: PXRD patterns of control reactions showing that traditional bulk syntheses fail to produce $Mg_xZr_{2-x}N_2$. Mg_3N_2 and 3 equivalents of Zr powder were ground together, pelletized, placed in an alumina crucible with a Zr foil cap (to reduce Mg_3N_2 loss by evaporation and to remove adventitious oxygen) and heated in a tube furnace under flowing, purified, N_2. Diffraction patterns from the recovered samples show ZrN and unreacted Mg_3N_2. Rietveld analysis of the rock salt phase indicates negligible incorporation of Mg (i.e., $x \leq 0.05$ for $Mg_xZr_{2-x}N_2$; Figure C.10).

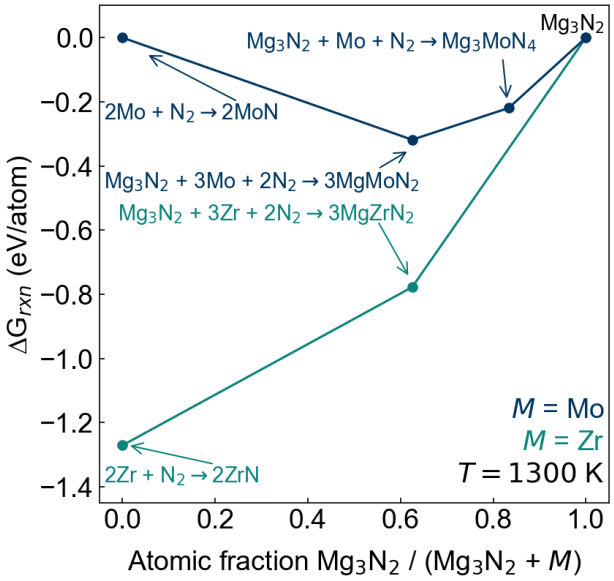

Figure 4.5: Gibbs free energy calculations show that $MgZrN_2$ is on the thermodynamic convex hull when Mg_3N_2 and Zr are combined with an open nitrogen atmosphere ($p = 1$ atm) at 1300 K (1023 °C). However, ZrN formation is much more energetically favorable than $MgZrN_2$ formation on a per-atom basis. Experimental results show ZrN forms first, and subsequent interdiffusion to form $MgZrN_2$ is negligibly slow (Figure 4.4). In contrast, $MgMoN_2$ can successfully be synthesized via the ceramic route[39] because formation of the binary (MoN) is less exergonic than formation of the ternary. ΔG_{rxn}(1300 K) calculations used ΔG_{f}(1300 K) values determined via the method described by Bartel, et al.[119]

ceramic synthesis, $MgMoN_2$, which Verrelli, et al. made via $Mg_3N_2 + 3\,Mo + 2\,N_2 \longrightarrow 3\,MgMoN_2$.[39] In the Mg-Mo-N system, binary formation (MoN) is less exergonic than ternary formation ($MgMoN_2$), and therefore $MgMoN_2$ synthesis is not inhibited by a refractory intermediate. Circumventing the formation of a refractory binary is key to ternary formation.

While the metathesis reaction is less exothermic than the ceramic route, this route successfully synthesizes $MgZrN_2$ by largely bypassing ZrN formation. This finding is analogous to recent work targeting the ternary sulfide, $MgCr_2S_4$.[127] Examining reaction enthalpies show that three stoichiometric reactions are thermodynamically competitive in a narrow composition space:

$$\mathrm{Mg_2NCl} + \mathrm{ZrCl_4} \longrightarrow \mathrm{ZrNCl} + 2\,\mathrm{MgCl_2}\ (\Delta G_{rxn}(1100\text{ K}) = \text{-0.340 eV/atom}), \tag{4.4}$$

$$\frac{4}{3}\mathrm{Mg_2NCl} + \mathrm{ZrCl_4} \longrightarrow \mathrm{ZrN} + \frac{1}{6}\mathrm{N_2} + \frac{8}{3}\mathrm{MgCl_2}\ (\Delta G_{rxn}(1100\text{ K}) = \text{-0.337 eV/atom}), \tag{4.5}$$

$$2\,\mathrm{Mg_2NCl} + \mathrm{ZrCl_4} \longrightarrow \mathrm{MgZrN_2} + 3\,\mathrm{MgCl_2}\ (\Delta G_{rxn}(1100\text{ K}) = \text{-0.324 eV/atom}). \tag{4.6}$$

Our *in situ* PXRD data show that $MgCl_2$ begins forming by 350 °C when Mg_2NCl is used as a precursor and 420 °C when Mg_3N_2 is used (Figure 4.3). However, we are not able to detect other crystalline products at low reaction temperatures (350–500 °C), so we cannot distinguish which of these reactions (Equations 4.4, 4.5, or 4.6) is occurring by diffraction alone.

We hypothesize that both Equations 4.4 and 4.6 occur to some degree at low temperatures (≈ 350 °C to 500 °C) to yield intermediate nitride species undetected by XRD. ZrNCl formation is supported by the presence of yellow-green coatings that form on the side of the ampules near 500 °C. Although these deposits are too scant for PXRD char-

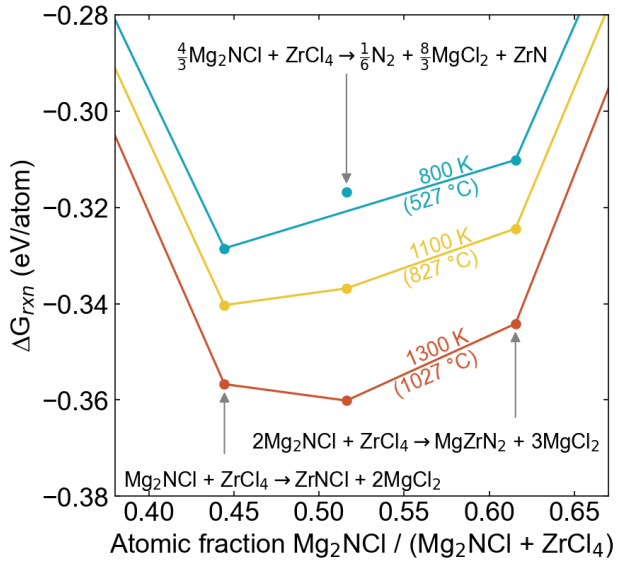

Figure 4.6: Gibbs free energy calculations show that $MgZrN_2$ is on the thermodynamic hull of the Mg_2NCl—$ZrCl_4$ phase space, along with ZrNCl, at each temperature calculated. At high temperatures ($\geq$ 1100 K), ZrN production also becomes favorable. $\Delta G_{\text{rxn}}(T)$ calculations used $\Delta G_{\text{f}}(T)$ values determined via the method described by Bartel, et al.[119] At low temperatures (e.g., 527 °C), the reaction producing ZrN (with N_2 gas loss) is not thermodynamically favored relative to the other two reactions. The full compositional range of the convex hull is shown in Figure C.16.

acterization, ZrNCl is known to be pale yellow-green in color and is susceptible to vapor transport.[128,129] The entropically-favored release of N_2(g) in Equation 4.5 makes ZrN formation increasingly favorable at high temperatures (Figure 4.6). The relative stability of ZrN at $T = 1100$ K could yield the irreversible formation of ZrN and N_2 as the composition various during the course of the reaction (Figure C.17). Therefore low temperature reactivity (≈ 500 °C) is critical for the preferential formation of $MgZrN_2$.

At elevated temperatures (≈ 800 °C), Gibbs free energy calculations show that $MgZrN_2$, ZrN, and ZrNCl are stable metathesis products in the Mg-Zr-N-Cl phase space, depending on the composition. $MgZrN_2 + 3\,MgCl_2$ is the most thermodynamically stable product combination given reactants $2\,Mg_2NCl + ZrCl_4$ (Equation 4.6, Figure 4.6). At $ZrCl_4$:Mg_2NCl :: 1:n ratios near $n = 1.33$, $ZrN + \frac{1}{6}N_2 + \frac{8}{3}MgCl_2$ is thermodynamically competitive (Equation 4.5), followed by $ZrNCl + 2MgCl_2$ near $n = 1.0$ (Equation 4.4). We have experimentally observed crystalline ZrNCl formation at $n = 1.16$ ($T_{rxn} = 950$ °C, Figure C.5). While

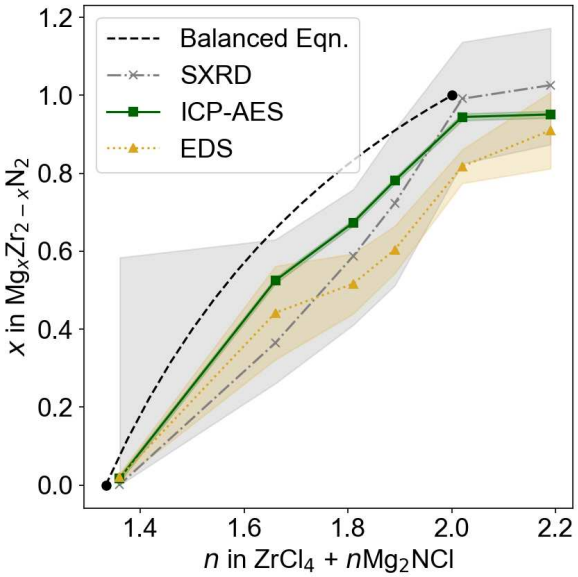

Figure 4.7: SPXRD, EDS, and ICP-AES show similar trends in cation composition in the metathesis product as a function of precursor ratios. As Mg_2NCl increases relative to $ZrCl_4$, Mg-content in $Mg_xZr_{2-x}N_2$ increases systematically. However, the amount of Mg into the rock salt structure is less than predicted by the balanced equation ($x = (6n-8)/(3n-2)$ for $4/3 \leq n \leq 2$, black dashed trace, Equation 4.7). Shaded regions show uncertainty, as defined by a 1% increase in the goodness of fit parameter (SPXRD), or one standard deviation about the mean from replicate measurements (ICP-AES, EDS). Sources of uncertainty are discussed in the text.

these calculations consider line compounds (e.g., $MgZrN_2$) rather than non-stoichiometric compounds like $Mg_xZr_{2-x}N_2$, the fact that both ZrN and $MgZrN_2$ are thermodynamically stable and structurally similar supports the mixing of those two phases at the atomic level (i.e., as a solid solution), as biphasic mixtures, or somewhere in between.

4.3.3 Solid solution behavior of $Mg_xZr_{2-x}N_2$

$Mg_xZr_{2-x}N_2$ exhibits solid solution behavior in the rock salt structure. SPXRD data shown in Figure 4.1 were analyzed with the Rietveld method to show that Mg content in the rock salt increases as the amount of Mg_2NCl increases relative to $ZrCl_4$ in the precursor mix (Figure 4.7). This trend is also correlated with a shift in diffraction peaks to higher angles with increasing Mg content (Figure 4.1d). This lattice shift tracks with Vegard's law (Figure 4.9a). The lack of additional diffraction peaks, the shift in lattice parameter, and

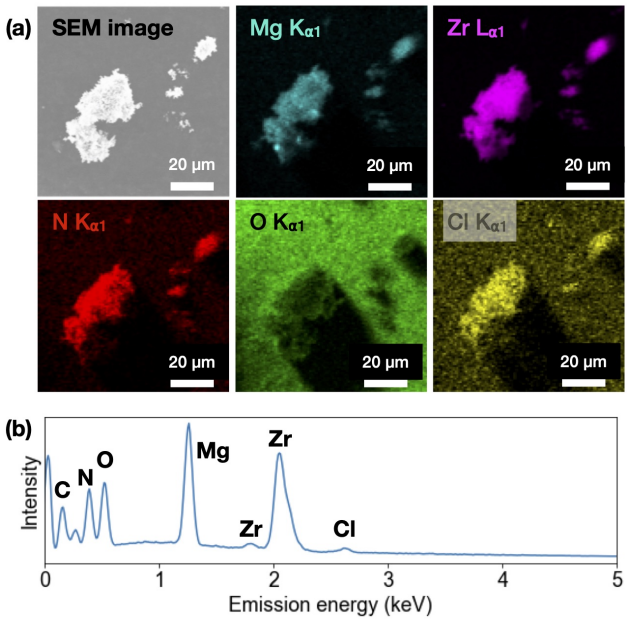

Figure 4.8: (a) A representative SEM-derived EDS map of a powdered $n = 2.02$ sample shows that Mg, Zr, and N are colocalized in the same particles. Oxygen is also present both in the particles and on the carbon tape. Mapping suggests chlorine persists in the sample, but (b) a representative EDS spectrum from a pelletized sample ($n = 2.02$) shows only a weak signal from this element, likely due to residual $MgCl_2$. Carbon and oxygen signals may be from adventitious carbon or from the carbon tape used to mount the pellet. Relative atomic fractions are shown in Figure C.13.

the variable Mg/Zr site occupancy is consistent with solid solution behavior, $Mg_xZr_{2-x}N_2$. However, Rietveld analysis alone exhibited a high degree of uncertainty, so complementary methods were used to confirm the elemental composition of the material. Uncertainty in the Rietveld analysis (shown by the grey shading in Figure 4.7) stems from the fact that the Goodness of Fit (χ^2) is relatively insensitive to x (Figure C.9). EDS and ICP-AES measurements corroborate the trend in the SPXRD data.

Equation 4.7 relates the stoichiometry of the precursors to the expected solid solution behavior of $Mg_xZr_{2-x}N_2$. Due to the N_2-based redox, the overall balanced reaction is shown by Equation 4.7 and visualized in Figure C.11. We use n to describe the ratio of precursors ($ZrCl_4$:Mg_2NCl :: 1:n). That ratio relates to magnesium content of the rock salt product (x in $Mg_x\,Zr_{2-x}\,N_2$) by $n = (8-2x)/(6-3x)$, which shows how magnesium content

in the rock salt is controlled by the precursor ratio:

$$\frac{8-2x}{6-3x}\mathrm{Mg_2NCl} + \mathrm{ZrCl_4} \longrightarrow \frac{1}{2-x}\mathrm{Mg}_x\,\mathrm{Zr}_{2-x}\,\mathrm{N_2} + \frac{1-x}{6-3x}\mathrm{N_2} + \frac{16-7x}{6-3x}\mathrm{MgCl_2} \tag{4.7}$$

This equation is valid for $\frac{4}{3} \leq n \leq 2$, which allows for $0 \leq x \leq 1$. Plotting this equation along with experimental measurements of x as a function of n (black dashed trace, Figure 4.7) shows that reactions systematically yield Mg-deficient $\mathrm{Mg}_x\mathrm{Zr}_{2-x}\mathrm{N_2}$ compared to the expected Mg content. A deficiency in Mg is consistent with the hypothesis that the $\mathrm{Mg}_x\mathrm{Zr}_{2-x}\mathrm{N_2}$ is an inhomogeneous mixture of Mg-rich domains with ZrN-like domains, which is discussed below in light of the optical properties. In our reactions, we observe brown deposits on the side of the quartz ampules for $T_{rxn} \approx 800$ °C, consistent with loss of Mg from the reaction.

Diffraction peak broadness can also be explained by nanoscale inhomogeneity within $\mathrm{Mg}_x\mathrm{Zr}_{2-x}\mathrm{N_2}$. When the precursor mixture is near $\frac{4}{3}\mathrm{Mg_2NCl} + \mathrm{ZrCl_4}$ in composition, sharp rock salt peaks are observed (Figure 4.1d), consistent with large crystallites of pure ZrN forming via Equation 4.5. However, with a higher $\mathrm{Mg_2NCl}$ concentration, peak broadness increases, which we model as decreasing crystallite size and increasing strain (Figure 4.9b, c). This peak broadness was modeled as double-Voigt functions for size and strain, after convolving with instrument broadening.[132] This strain may arise at interfaces between ZrN-like domains ($a \approx 4.58$ Å) and $\mathrm{MgZrN_2}$-like domains ($a \approx 4.54$ Å). Strain (e) between two such structures is on the same order of magnitude as the strain modeled here ($e = (4.58 - 4.54)/(4.54) = 0.9\%$; Figure 4.9c). This microstrain analysis is consistent with both Equations 4.5 and 4.6 proceeding with precursor ratios of $2\,\mathrm{Mg_2NCl} + \mathrm{ZrCl_4}$.

4.3.4 Optoelectronic properties of $\mathrm{Mg}_x\mathrm{Zr}_{2-x}\mathrm{N_2}$

EIS measurements show a conducting to semiconducting transition with increasing x in $\mathrm{Mg}_x\mathrm{Zr}_{2-x}\mathrm{N_2}$ (Figure 4.10). Although the magnitude of conductivity differs from the thin films deposited by Kim, et al., the correlation between magnesium content and electronic

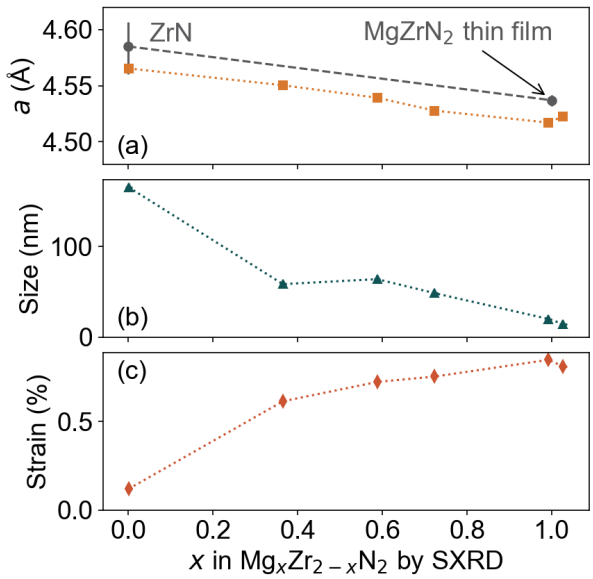

Figure 4.9: (a) Rietveld analysis of PXRD data (referenced to a silicon internal standard) shows that the lattice parameter (a) decreases with increasing Mg content in the rock salt $Mg_xZr_{2-x}N_2$. For reference, Vegard's law between single crystal ZrN ($a = 4.585$ Å)[130] and thin film $MgZrN_2$ ($a = 4.537$ Å)[49] is shown by the grey dashed line. The error bar around ZrN approximates the lattice parameter variation with nitrogen off-stoichiometry and oxygen incorporation.[131] Increasing Mg content is correlated with broader PXRD peaks, which are best modeled by (b) decreasing crystallite size and (c) increasing strain. Crystallite size refers to the average diameter of ordered domains.[132] The dotted lines connect the dots through the reaction precursor ratios of $n Mg_2NCl + ZrCl_4$, with $n = 1.36$ on the left going to $n = 2.19$ on the right.

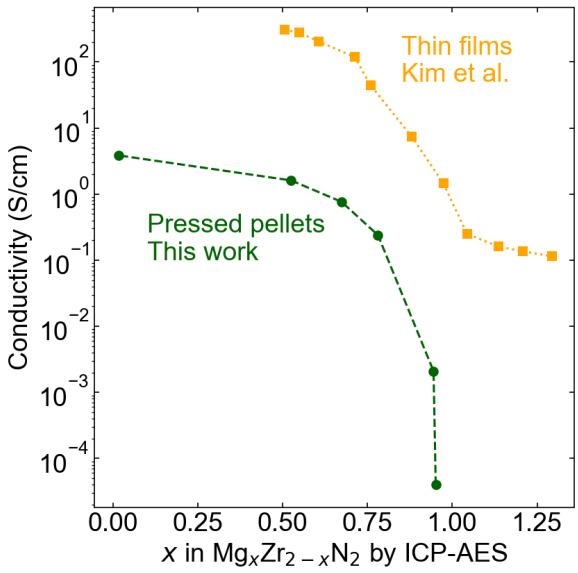

Figure 4.10: Conductivity values as a function of Mg-content (x, as quantified by ICP-AES) in pressed pellets of $Mg_xZr_{2-x}N_2$, compared to thin films synthesized and measured by Kim, et al.[115] The conductivity decreases as Mg content (x) increases. The bulk samples in this work are approximately two orders of magnitude less conductive than the films.

properties is consistent.[115] The lower conductivity of the measurements here is attributable to grain- and particle-boundary resistance, porosity, or oxide incorporation.

Diffuse reflectance optical spectroscopy data do not show evidence of a semiconducting optical absorption onset, but they are instead consistent with the hypothesis that ZrN domains are present in otherwise Mg-rich $Mg_xZr_{2-x}N_2$ (Figure 4.11). These bulk samples appear black or black with a hint of dark blue, and are absorbing across the visible spectrum at all values of x. Similarly, the absorption profile previously reported for thin films of $Mg_xZr_{2-x}N_2$ show high absorption coefficients for metallic compositions (i.e., $x < 0.8$).[49,115] In contrast, Mg-rich thin films, with $Mg_xZr_{2-x}N_2$ having $x > 0.8$, show an absorption onset of 1.8-2.2 eV, with high absorption coefficients ($\approx 10^5$ cm^{-1}) above the bandgap and low absorption coefficients below the bandgap ($\approx 10^4$ cm^{-1}). The bulk powders here show peaks in the optical spectra (as opposed to plateaus). Nanoparticles of ZrN are known to exhibit plasmon resonances, with absorption peaks in the range of 1.9 eV to 2.1 eV (653 nm to 585 nm).[121,133,134] These absorption peaks vary in energy with particle

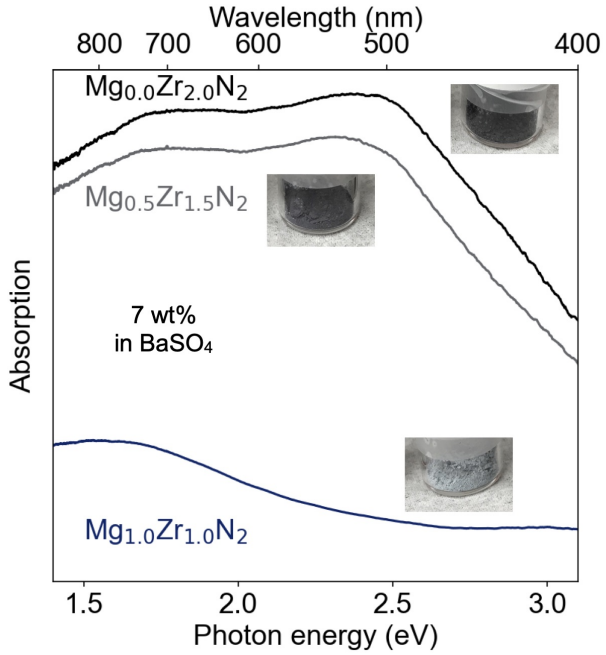

Figure 4.11: Kubelka-Munk transformations of diffuse reflectance optical spectroscopy data show that the $Mg_xZr_{2-x}N_2$ do not match the expected absorption profile for a pure semiconductor. Rather, absorption maxima suggest the presence of plasmonic ZrN nanoparticles and oxygen-substituted ZrN, as discussed in the text. All samples appear mostly black, although the Mg-rich phase ($n = 2.0$; $Mg_{1.0}Zr_{1.0}N_2$) has a slightly blue tint. Inset images show the measured samples. These samples were annealed at a 800 °C set point for 12 h, washed with methanol, and diluted to 7 wt% in $BaSO_4$. Reflectance spectra are shown in Figure C.19.

size, shape, and surrounding dielectric media.[135] Small degrees of Mg incorporation may further change the absorption energy in ways that go beyond the scope of this study.[136] Small ZrN nanoparticles included within $Mg_xZr_{2-x}N_2$ may explain the absorption peak observed for ($Mg_{1.0}Zr_{1.0}N_2$). While bulk ZrN typically appears golden in color (due to surface plasmon resonance), oxide incorporation turns the material black.[137] Therefore, it is possible that our Mg-poor samples (e.g. $x \leq 0.5$) contain some amount of oxygen, likely from the commercially sourced Mg_3N_2 used to make Mg_2NCl. Furthermore, the low conductivity of Mg-rich samples suggests that any ZrN-domains that formed are electrically isolated, and therefore are a minor phase.

4.4 Conclusions

Metathesis reactions, between $nMg_2NCl + ZrCl_4$, yield bulk powders of the ternary rock salt $Mg_xZr_{2-x}N_2$ ($0 < x < 1$), where the resulting composition (x) depends on the input composition (n). The reaction proceeds first to a poorly-crystalline product at low temperatures (350 °C–500 °C), and annealing above 600 °C increases the crystallinity of the ternary. Together, SPXRD, EDS, and ICP-AES show that a solid solution forms between ZrN and $MgZrN_2$. *In situ* PXRD shows how Mg_2NCl is a more kinetically competent precursor than Mg_3N_2. However, thermodynamic calculations and microstructure analysis suggest inhomogeneity in the product phase, even with a more kinetically competent precursor. Gibbs free energy calculations suggest both ZrN and $MgZrN_2$ are likely to form via metathesis. Therefore, ZrN domains are likely mixed in with $Mg_xZr_{2-x}N_2$. Optical absorption measurements support this hypothesis, with absorption features likely due to ZrN nanoparticle plasmon resonance. Measurements of bulk electronic properties show a transition from metallic to semiconducting behavior with increasing Mg-content, consistent with thin-film literature on $Mg_xZr_{2-x}N_2$.[11,49,114,115]

Low-temperature metathesis may provide a generalizable approach for targeting additional ternary nitrides. Analogous nitride halide precursors (e.g., Ca_2NCl, Zn_2NCl)[138,139]

could be paired with the appropriate transition metal chloride to target a variety of ternary transition metal nitrides. While prior work using Mg_3N_2 and Ca_3N_2 as metathesis precursors often yielded binary transition metal nitrides, subnitrides, or reduced metals,[121,122] we suspect that more kinetically competent nitride halide precursors may permit even lower temperature routes to new phases. This work therefore illustrates a promising strategy for future success in synthesizing ternary nitrides.

Chapter 5

Mechanistically-guided materials chemistry: synthesis of new ternary nitrides $CaZrN_2$ and $CaHfN_2$*

Overview

Recent computational studies have predicted many new ternary nitrides, revealing synthetic opportunities in this underexplored phase space. However, synthesizing new ternary nitrides is difficult, in part because intermediate and product phases often have high cohesive energy that inhibits diffusion and/or low thermodynamic stability against decomposition at elevated temperatures. Here, we report the synthesis of two new phases, calcium zirconium nitride ($CaZrN_2$) and calcium hafnium nitride ($CaHfN_2$), by solid state metathesis reactions between Ca_3N_2 and MCl_4 (M = Zr, Hf). Although the reaction nominally proceeds to the target phases in a 1:1 ratio of the precursors via $Ca_3N_2 + MCl_4 \longrightarrow CaMN_2 + 2CaCl_2$, reactions prepared this way result in Ca-poor materials ($Ca_xM_{2-x}N_2$, $x < 1$). A small excess of Ca_3N_2 (ca. 20 mol%) is needed to yield stoichiometric $CaMN_2$, as confirmed by powder X-ray diffraction, energy-dispersive X-ray spectroscopy, and X-ray photoelectron spectroscopy. *In situ* synchrotron X-ray diffraction studies reveal that stoichiometric reactions produce Zr(III) intermediates early on in the reaction pathway, showing that the excess Ca_3N_2 is necessary to yield a product with Zr(IV).

* Substantial portions of this chapter has been reproduced with permission from C.L. Rom, J.R. Gallawa, D.C. Asebiah, E.N. Storck, B.C. McBride, R.C. Miller, A.L. Prieto, and A. Zakutayev, and J.R. Neilson, Mechanistically-guided materials chemistry: synthesis of new ternary nitrides, $CaZrN_2$ and $CaHfN_2$. *Prepared Manuscript*. 2022. C.L.R. and J.R.N. conceptualized the project. J.R.G. conducted X-ray photoelectron spectroscopy measurements. D.C.A. conducted optical property measurements. C.L.R., E.N.S., and B.C.M. conducted syntheses. C.L.R. conducted the synchrotron diffraction experiments (remotely, with on-site support from Andrey Yakovenko) analyzed the data. R.C.M. and C.L.R. conducted electron microscopy and energy dispersive X-ray spectroscopy measurements. A.L.P., A.Z., and J.R.N. supervised the project.

This synthesis pathway contrasts with that of another recently discovered phase, $MgZrN_2$, in which the reaction proceeds through a ZrNCl intermediate, which retains the Zr(IV) oxidation state. Applying the hypothesis that the reaction interface locally follows equilibrium, we show that computed predominance diagrams predict those equilibrium intermediates and rationalize the reaction pathway. Lastly, diffuse reflectance UV-Vis measurements shows that $CaZrN_2$ has a bandgap near 2.0 eV, making it a promising material for optoelectronic applications. In addition to the discovery of a new material, these findings highlight the power of *in situ* diffraction studies and computed predominance diagrams, with implications for designing reaction pathways that will enable the discovery of more predicted materials.

5.1 Introduction

Nitrides are an emerging class of semiconducting materials, as many have bandgaps in the range of visible light and are structurally with other electronic materials.[1,51,140] In particular, ternary nitrides build on the success of binary III-N materials (e.g., GaN) by replacing the III cation into equal parts II and IV cations, resulting in II-IV-N_2 phases with greater structural diversity and tunability than their binary counterparts.[51] The II cation is often Zn^{2+} or an alkali earth (Mg^{2+}, Ca^{2+}, Sr^{2+}, Ba^{2+}), whereas the IV cation can be a main-group element (Si^{4+}, Ge^{4+}, Sn^{4+}) or a transition metal (Ti^{4+}, Zr^{4+}, Hf^{4+}). Recent computational studies have predicted stable phases in some of these previously uncharted spaces,[2] accelerating the discovery of new phases like $MgSnN_2$,[13] $CaSnN_2$,[48] and $MgZrN_2$.[11]

All of the AMN_2 phases (A = Mg, Ca, Sr, Ba; M = Ti, Zr, Hf) have been synthesized previously,[11,54,141–143] with the exception of $CaZrN_2$ and $CaHfN_2$.[52] As summarized in Figure 5.1, these phases crystallize with several structure types: rocksalt ($Fm\bar{3}m$), $KCoO_2$-type ($P4/nmm$), and $\alpha-NaFeO_2$ ($R\bar{3}m$). Given the intermediate size of Ca^{2+} (radius = 1.0 Å) relative to Zr^{4+} (0.72 Å) and Hf^{4+} (0.71 Å),[144] $CaZrN_2$ and $CaHfN_2$ were predicted to crys-

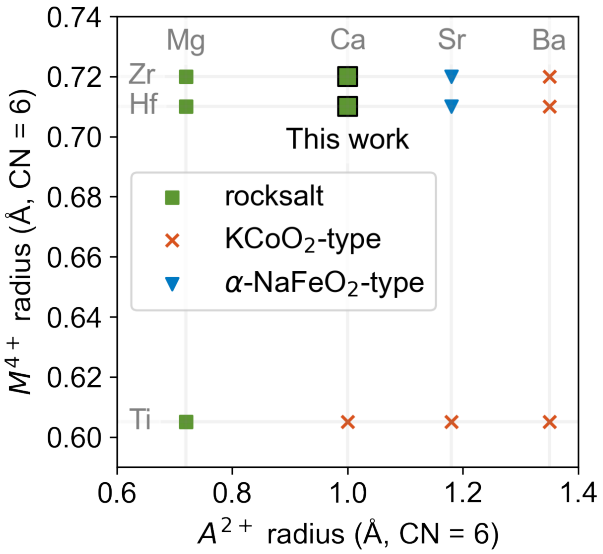

Figure 5.1: The AMN_2 ternaries with larger alkali earth cations (Sr and Ba) crystallize in cation-ordered phases of the $KCoO_2$-type and $\alpha-NaFeO_2$-type structures,[142,143,147] while $MgMN_2$ phases take the disordered rocksalt structure.[11] Although $CaTiN_2$ forms a cation-ordered $KCoO_2$-type phase,[54] this work shows that $CaZrN_2$ and $CaHfN_2$ crystallize in the cation-disordered rocksalt structure.

tallize in the $\alpha-NaFeO_2$ structure type.[145] However, syntheses of $CaZrN_2$ and $CaHfN_2$ have not been previously reported, although one group reported some synthetic attempts that yielded only ZrN and HfN.[146]

Here we report the discovery of $CaZrN_2$ and $CaHfN_2$ in the rocksalt structure synthesized by a mechanistism-guided metathesis reaction. Heating Ca_3N_2 and $ZrCl_4$ or $HfCl_4$ up to a high temperature dwell (ca. 1000 °C) for a brief period of time (10 min) yields $CaZrN_2$ and $CaHfN_2$ as fine powders (along with a byproduct $CaCl_2$). Importantly, a slight excess of Ca_3N_2 is needed, a fact we rationalize based on our *in situ* synchrotron X-ray diffraction studies of the reaction pathway that show reduced Zr(III) intermediates and from computational analysis of the high-dimensional thermodynamic phase diagram. This metathesis approach succeeds where other strategies failed, including a flux-assisted ceramic approach[146] and a two-step metathesis approach we previously reported for $MgZrN_2$, Mg_2NbN_3, and $MgMoN_2$.[55,105] Computed predominance diagrams rationalize the thermodynamics behind the observed reactions, accurately predicting differences in the reaction

pathway between the Ca_3N_2-based and Mg_2NCl-based metathesis reactions. In sum, these findings provide guidance for future syntheses of other elusive ternary nitrides.

5.2 Methods

5.2.1 Synthesis

All reagents are moisture-sensitive, and were therefore handled in an argon-filled glovebox unless otherwise noted ($O_2 < 0.1$ ppm, $H_2O < 0.5$ ppm). Ca_3N_2 (Chem Cruz or Alfa Aesar, >98 % metals basis), Mg_3N_2 (Alfa Aesar, >98% metals basis), and $MgCl_2$ (Sigma Aldrich, anhydrous, >98% metals basis) were used as received. $ZrCl_4$ (Acros, 98%) and $HfCl_4$ (Sigma Aldrich, 99% metals basis, except for Zr, with $< 2.7\%$) were purified by heating approximately 4 g in a sealed quartz ampule (10 mm inner diameter, 12 mm outer diameter, ca. 30 cm long) in a 3-zone horizontal tube furnace to transport $ZrCl_4$ from the hot zone (400 °C) to the colder zone (300 °C), leaving behind less volatile, oxide-based impurities (e.g., ZrO_2). $CaCl_2$ (anhydrous, Alfa Aesar, 98%) was dried under flowing Ar for 24 h at 300 °C.

Ca_2NCl was synthesized following a method adapted from literature.[148] Stoichiometric amounts of Ca_3N_2 and $CaCl_2$ were combined in an agate mortar and pestle and ground into a homogeneous pink powder (ca. 2 g). The powder was then cold pressed ($P \approx 300$ MPa) into a dense pellet (diameter = 0.25 in) and placed in a niobium tube (10 cm long, 0.375 inch outer diameter, 0.015 inch wall thickness). Prior to use, the surface oxide of the niobium was removed by scrubbing with an abrasive scour pad in the glovebox. The ends of the tube were crimped down using the arbor press. This ampule was then brought out of the glovebox and quickly sealed under an argon atmosphere via arc-melting of the crimped ends of the niobium. The sealed metal ampule was then sealed in a quartz ampule under vacuum and heated at 5 °C/min in a muffle furnace to a set point of 740 °C. The reaction was held at temperature for 50 h, and then allowed to cool to room temperature before opening the ampule in the glovebox.

M_2NCl was synthesized following a method adapted from literature,[116] as we described previously.[55] Stoichiometric amounts of Mg_3N_2 (ca. 3 g) and $MgCl_2$ (ca. 3 g) were combined in an agate mortar and pestle and ground into a homogeneous tan powder. The powder was then cold pressed ($P \approx 80$ MPa) into a dense pellet (diameter = 0.5 in) and placed in a quartz ampule (14 mm i.d., 16 mm o.d.). This ampule was then brought out of the glovebox and quickly sealed under vacuum (≤ 20 mTorr, as determined by a Pirani gauge) by using an oxygen/methane torch. The sealed ampule (ca. 15 cm^3 internal volume) was then heated at 10 °C/min in a muffle furnace to a set point of 550 °C. The reaction was held at temperature for 5 days and then allowed to cool to room temperature before opening the ampule in the glovebox.

Reaction mixtures targeting $CaZrN_2$ and $CaHfN_2$ were prepared by combining the desired reagents in specific mole ratios (e.g., $1.17Ca_3N_2 + ZrCl_4$, as specified in the text) and homogenizing with an agate mortar and pestle. Reaction scales ranged from ca. 50 mg to ca. 500 mg total charge of reactants. Reaction mixtures were loaded into crucibles as loose powders or as 0.25 inch diameter pellets (cold pressed at 300 MPa) and sealed under vacuum in quartz ampules (< 30 mTorr). Many syntheses were conducted using alumina crucibles, but optimized syntheses used welded stainless steel tubes to minimize oxygen contamination (3/8 in outer diameter, 0.020 in wall thickness, TP-304L). The optimized synthesis involved pelletized reaction mixtures (ca. 500 mg) held in the steel tubes, open on one end and welded closed on the other, which were loaded into quartz ampules along with a 1 g graphite rod as an oxygen getter, physically separated from the pellet. These ampules were transferred from the glovebox to a vacuum manifold using a custom air-free transfer valve, and sealed flame-sealed under vacuum (< 30 mTorr) using an oxygen/methane torch. Optimized reactions were heated in a muffle furnace at $+5$ °C/min to the specified dwell temperature, allowed to thermally equilibrate for 10 min, and then air-quenched by removing the ampule from the furnace and placing it in an insulating brick holder on the benchtop. Other heating profiles are specified in the text where relevant.

Samples were prepared for *in situ* synchrotron PXRD by loading powders into extruded quartz capillaries (0.9 mm inner diameter, 1.1 mm outer diameter) and flame-sealing under vacuum.

Control experiments were also conducted for comparison with the above metathesis approach. A ceramic approach was attempted following the method described by Verrelli, et al.[39] Ca_3N_2 (100.6 mg) and 3/2 mol equiv of Zr powder (87.0 mg) were ground together (i.e., excess Ca_3N_2), pelletized (150 mg), placed in a steel crucible with a Zr foil cap (to reduce Ca_3N_2 loss by evaporation and to react with adventitious oxygen) and heated in a tube furnace under flowing ultra-high purity N_2. Custom self-sealing end-caps were used, permitting transfer of the enclosed process tube between the glovebox and the furnace without air exposure. Samples were recovered directly into an Ar glovebox at room temperature for further analysis.

Alternative metathesis reactions were also attempted by using ZrNCl as a zirconium source, targeting $Ca_2NCl + ZrNCl \longrightarrow CaZrN_2 + CaCl_2$. ZrNCl was synthesized via stoichiometric mixtures of $Mg_2NCl + ZrCl_4$ to yield $ZrNCl + 2MgCl_2$. As ZrNCl is known to undergo chemical vapor transport when trace water is present,[129] ZrNCl was synthesized and purified simultaneously by conducting the reaction in an evacuated quartz ampule (30 cm long) placed in a three-zone furnace with the pellet located in a 800 °C zone and the purified ZrNCl collected from the 900 °C zone after cooling. Reactions targeting $Ca_2NCl+ZrNCl \longrightarrow CaZrN_2+CaCl_2$ were conducted by heating sealed ampules containing pelletized reaction mixtures in a muffle furnace as specified in the text.

5.2.2 X-ray diffraction experiments

The products of all reactions were characterized by powder X-ray diffraction (PXRD) and analyzed by the Rietveld method. PXRD measurements were performed by using a Bruker DaVinci diffractometer with Cu Kα X-ray radiation. Prior to collecting PXRD, silicon powder was ground in with the reaction mixtures as an internal standard for lattice

parameters. All samples were prepared for PXRD from within the glovebox by placing powder on off-axis cut silicon single crystal wafers to reduce the background and then covered with polyimide tape to slow exposure to the atmosphere.

In situ synchrotron powder X-ray diffraction (SPXRD) were conducted at the 17-BM-B end station of the Advanced Photon Source at Argonne National lab. For SPXRD experiments ($\lambda = 0.24101$ Å), the PerkinElmer plate detector was positioned 700 mm away from the sample. Homogenized precursors were packed into quartz capillaries in an Ar glovebox and flame-sealed under vacuum (< 30 mTorr). Capillaries were loaded into a flow-cell apparatus[149] and heated at 5 °C/min to the specified temperature. *Caution: N_2 gas formation within the capillary can cause it to break at high temperatures.* Diffraction pattern images were collected every 30 s by summing 20 exposures of 0.5 s each, followed by 20 s of deadtime. Images collected from the plate detector were radially integrated using GSAS-II and calibrated using a silicon standard.

5.2.3 X-ray diffraction analysis

Quantitative phase analysis of PXRD and *in situ* SPXRD data was conducted using the Rietveld method as implemented in TOPAS v6. For laboratory-diffraction PXRD experiments (Bruker system, Cu Kα radiation), the sample displacement was first refined against the silicon standard. The sample displacement was then fixed, and the relevant phases were added to the fit. For each phase, lattice parameters, size broadening, and atomic thermal parameters were refined.

Due to the number and positional overlap of intermediates during the sequential refinements, thermal displacement parameters were fixed at 5 Å^2 for each phase to better account for changes in peak intensity during the reaction. Crystalline size domain was fixed at 200 nm (as modeled using a Lorentzian broadening term) for most phases, except $CaZrN_2$ and ZrNCl, which exhibited noticeable peak broadening. For ZrNCl and $CaZrN_2$, peak widths were manually refined using the scan with the highest intensity of the pri-

mary reflection. Atoms were fixed at full occupancy for each site, unless otherwise specified (i.e., attempts to refine $Ca_xM_{2-x}N_2$). In order to compare the relative fractions of phases determined from Rietveld calculations, a weighted scale factor (WSF) is defined as $Q_p = S_p \times V_p \times M_p$ where Q_p = weighted scale factor of phase p, S_p = Scale factor calculated from Rietveld, V_p is the volume of the unit cell, and M_p is the atomic mass of the unit cell. It should be noted that we omit the Brindley coefficient for microabsorption correction in our calculation of weighted scale factor due to the unreliable refinement of particle sizes for individual phases. Amorphous material and product lost as vapor are not accounted for in the sequential refinement, hence we use the WSF instead of relative wt % or mol %. We reference all phases by their nominal stoichiometric formula; however, the actual chemical formula may be distinct from the written formula as XRD data alone cannot typically resolve nonstoichiometric compounds.

5.2.4 Imaging and compositional analysis

Scanning electron microscopy (SEM) measurements were made by using a JEOL JSM-6500F instrument. Energy dispersive X-ray spectroscopy (EDS) measurements were made with the attached Oxford 80 X-MAX silicon drift detector and analyzed by using AZtec software (Oxford Instruments). Samples for SEM-EDS analysis were prepared by using an agate pestle to smoothly press powders into double-sided carbon tape that was adhered to aluminum SEM stubs. The SEM sample-holder was quickly transferred from the glovebox to the instrument (< 5 min air exposure). SEM imaging and EDS mapping were conducted at 10 kV accelerating voltage. Semi-quantitative elemental analysis was conducted using the spectra generated from EDS mapping. Relative Ca, Zr, and Cl atomic % were calculated from the map spectra of three separate areas per sample (sum of these three elements = 100 %) using the AZtec software. These values were then averaged to identify the Ca/Zr ratios of the samples, as further detailed in the Supplemental.

5.2.5 Optical characterization

Diffuse reflectance optical spectroscopy measurements were made by using an Ocean Optics tungsten-halogen light source (HL-2000-FHSA) and an Ocean Insight flame spectrometer with an integrating sphere. A fiber-optic cable was used to illuminate the flat base of a borosilicate glass vial covered by loose powder of the sample. A vial with $BaSO_4$ was used as a white reflectance standard. Vials containing washed reaction products were sealed with electrical tape (keeping an inert Ar atmosphere in the headspace) and briefly (< 30 min) removed the glovebox for measurement. The Kubelka–Munk transform was calculated via $k/s = ((1-R)^2)/(2R)$, where k is the absorption coefficient, s is the scattering coefficient, and R is the diffuse reflectance.

5.2.6 Thermochemical analysis

Thermodynamic calculations were performed using DFT-computed values and tools from the Materials Project (v2021.11.10) and pymatgen (v2022.7.19).[9,101] Reaction energies were calculated from the Gibbs formation energies as a function of temperature, using the method of Bartel, et al.[119] Predominance diagrams were generated in the method of Yokokawa[150] as detailed by Todd et al.[151] and implemented in pymatgen.

5.3 Results and Discussion

5.3.1 Structural and compositional analysis

PXRD shows that $CaZrN_2$ and $CaHfN_2$ crystallize in the rocksalt structure ($Fm\bar{3}m$) with disordered cations when reacting Ca_3N_2 and MCl_4 (M = Zr, Hf, Figure 5.2). Rietveld analysis of washed samples of $CaZrN_2$ reveal a lattice parameter near $a = 4.75$ Å, which varies slightly with the precursor ratio and heating conditions (Figure 5.3C). Although the binary ZrN also crystallizes in the rock salt structure, the lattice parameter of ZrN (a =4.58 Å)[152] is substantially smaller than that of $CaZrN_2$. $CaHfN_2$ exhibits a unit cell of $a = 4.725$ Å, slightly smaller than $CaZrN_2$ but still larger than HfN ($a = 4.52$ Å).[153] These

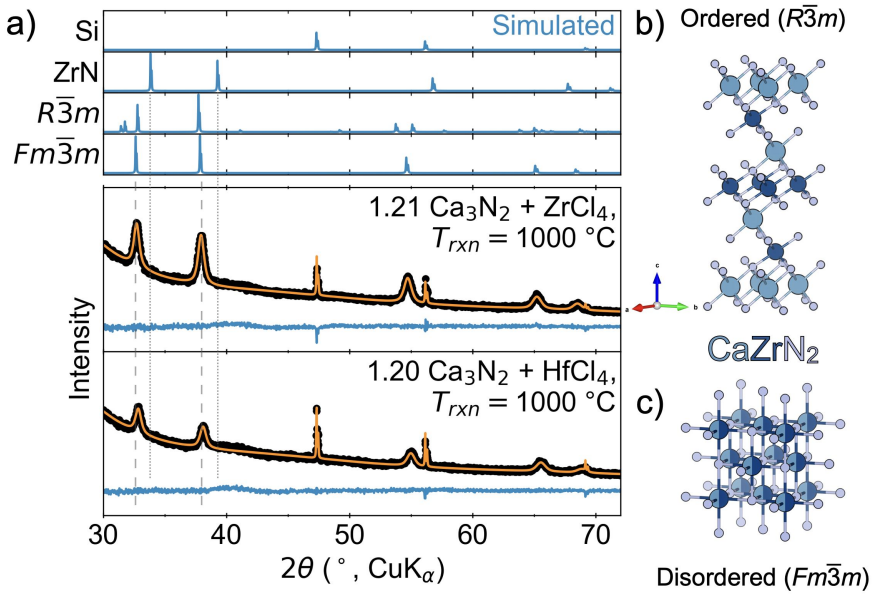

Figure 5.2: a) PXRD show that $CaZrN_2$ and $CaHfN_2$ crystallize in a $Fm\bar{3}m$ spacegroup, indicating a cation-disordered rocksalt structure. Insets specify synthesis conditions, and samples were washed and mixed with Si prior to measuring PXRD. The elevated background at lower angles comes from the kapton tape used to protect the samples from moisture. Simulated patterns are shown for reference (top) for $CaZrN_2$ in the predicted, ordered structure ($R\bar{3}m$) and the observed cation-disordered rocksalt structure. Vertical dashed lines guide the eye to the shift in peaks between the ZrN and $CaZrN_2$ $Fm\bar{3}m$ structures. Structures of b) the cation ordered $R\bar{3}m$ structure and c) the cation disordered $Fm\bar{3}m$ structure are visualized with VESTA.[69] Full diffraction patterns are shown in the appendix (Figure D.2, $2\theta = 20°$ to 100 °).

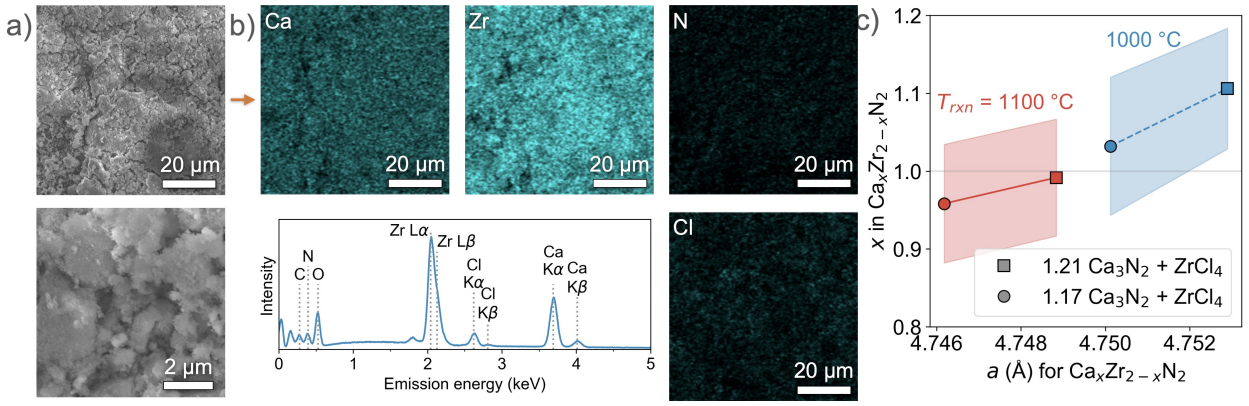

Figure 5.3: a) SEM images at in wide-field (top) and close magnification (bottom) show the powders are composed of tiny (< 1 μm), homogeneous grains. b) EDS mapping of the wide-field image shows that Ca, Zr, N, and Cl are evenly dispersed and colocalized. Color intensity is normalized to the spectrum intensity (also shown). c) Ca content in the rocksalt phase (x in $Ca_xZr_{2-x}N_2$) as calculated from EDS measurements correlates well with the lattice parameter, a, as measured by PXRD. Colors indicate the reaction temperature used, and shapes indicate the precursor ratios used. The top of the shaded region indicates the value for x assuming all Cl is bound to $CaCl_2$, and the bottom of the shaded region assumes all Cl is bound to Ca_2NCl. The solid points marking the average of those two values (See Supplemental for further details).

phases were predicted to crystallize in the cation-ordered $\alpha-NaFeO_2$ structure type,[145] but the formation of the cation-disordered rocksalt is not unprecedented. Several similar Ca-M-N ternary nitrides have been reported in the cation-disordered rock salt structure: $La_{1-x}Ca_xN_{1-x/3}$,[154] Ca_3UN_4,[155] and $CaCeN_2$.[156] However, Rietveld refinement of the metal site occupancy for our $Ca_xZr_{2-x}N_2$ and $Ca_xHf_{2-x}N_2$ phases likely overestimate Ca content using this laboratory PXRD data (refining to approximately $x = 1.6$ and $x = 1.1$, respectively), so occupancy was fixed to $x = 1$ for the refinements shown and for all subsequent analysis. We focused most of our work on the Zr analog, since Zr and Hf typically exhibit analogous chemistry. To confirm metal ratios, we conducted complementary methods of elemental analysis.

SEM/EDS verifies that Ca and Zr are homogeneously dispersed in the powder, with the metal ratio Ca/(Ca+Zr) near the value expected for $CaZrN_2$ (Figure 5.3a,b). However, EDS spectra indicate a small amount of Cl persisting despite four sequential washes with dry methanol (Figure 5.3b), even though PXRD shows only phase pure $CaZrN_2$ (Figure

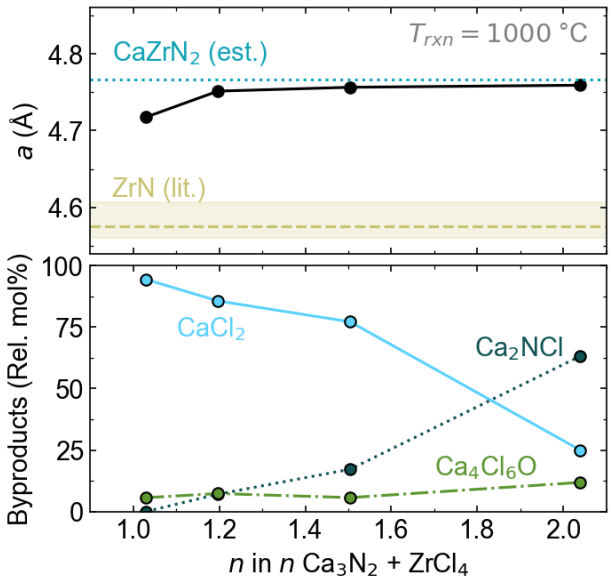

Figure 5.4: The precursor ratio (expressed as n in $nCa_3N_2 + ZrCl_4$) impacts the lattice parameter of the rocksalt phase (top) and the distribution of byproduct phases (bottom), as determined by Rietveld analysis. Approximately 20% mole excess ($n = 1.2$) Ca_3N_2 is necessary to yield stoichiometric $CaZrN_2$, as indicated by the expected value of $a = 4.767$ Å (dotted line, estimate of $CaZrN_2$ lattice parameter from the Ca-N-Zr distance in the predicted $R\bar{3}m$ structure, Figure D.1). However, some of that excess Ca_3N_2 also yields a Ca_2NCl byproduct by reacting with $CaCl_2$ (bottom). The byproduct relative mol % of $CaCl_2$, Ca_2NCl, and Ca_4Cl_6O sum to 100 % (i.e., $Ca_xZr_{2-x}N_2$ is not included owing to uncertainty in x). These data were from samples held in alumina crucibles sealed in ampules under vacuum and heated at 5 °C/min to 1000 °C, dwelled for 10 min, then quenched by removing the ampule from the furnace and placing on the benchtop.

5.2). The atomic ratios for Ca:Zr:Cl were approximately 5:4:1 by EDS (Figure D.10). As that chloride indicates the presence of either $CaCl_2$ or Ca_2NCl, we estimated Ca content attributable to $Ca_xZr_{2-x}N_2$ by subtracting the Ca estimated to be in these impurity phases (Figure D.10). Figure 5.3c shows that the lattice parameter a of the rocksalt is correlated with Ca content, as expected for a solid solution $Ca_xZr_{2-x}N_2$. Therefore, we can use the lattice parameter as a proxy for metal content, as also demonstrated for $Mg_xZr_{2-x}N_2$.[55] This proxy allows us to distinguish stoichiometric $CaZrN_2$ from Ca-poor phases with diffraction data alone.

A slight excess of Ca_3N_2 (ca. 20 mol%) is required to yield stoichiometric $CaZrN_2$ (Figure 5.4), as measured by the lattice parameter. Although the nominal balanced equation for the reaction is $Ca_3N_2 + ZrCl_4 \longrightarrow CaZrN_2 + 2CaCl_2$, a 1:1 precursor ratio yields a

lattice parameter of 4.72 Å, suggesting a Ca-poor phase. The lattice parameter approaches 4.76 Å with addition of more and more excess Ca_3N_2. The Ca-N-Zr distance in the computationally predicted $CaZrN_2$ structure is 4.767 Å, which serves as an estimate for the theoretical rocksalt lattice parameter (Figure D.1). Some of the excess Ca_3N_2 reacts with the $CaCl_2$ byproduct to make Ca_2NCl, which is observed in an increasing mol% with increasing Ca_3N_2 content above $n = 1.17$. This requirement of excess Ca_3N_2 is not attributable to the oxide impurity in the Ca_3N_2 precursor, which is estimated at < 5 wt% of our precursor by quantitative Rietveld analysis. We also note that increasing dwell time from 10 min to 4 h did not substantially change the rock salt lattice parameter, size, or strain for Ca-rich reactions ($2.0Ca_3N_2 + ZrCl_4$, $T_{\mathrm{rxn}} = 1000$ °C, Figure D.4). However, increasing dwell times for Ca-poor reactions decreased the rocksalt lattice parameter (Figure D.5). Increasing temperature also decreases the lattice parameter but increases the crystallite size ($1.2Ca_3N_2 + ZrCl_4$, dwell time = 10 min, Figure D.3). Additional synthetic details are discussed in the Supplemental Information. The key observation is that excess Ca_3N_2 is necessary. This result is explained by observations from our *in situ* SPXRD measurements, as will be discussed in the next section.

Using ion exhange (metathesis) reactions is also a key synthetic choice for the synthesis of $CaZrN_2$, as this process circumvents the solid-state diffusion challenges common to traditional ceramic syntheses.[157,158] A control reaction between Ca_3N_2 and Zr under flowing N_2 at 1000 °C for 10 h produced only ZrN alongside unreacted Ca_3N_2, indicating that Ca diffusion into the ZrN is slow (Figure D.7). Literature also shows difficulty of making $CaZrN_2$ and $CaHfN_2$. In their report on the synthesis of Ca_4TiN_4 and Ca_5NbN_5 with the assistance of a Li_3N flux, Hunting, et al., noted that similar reactions between Ca_3N_2 and Zr or Hf powders in Li_3N flux only yielded the ZrN and HfN.[146] And although many closely related compounds have been synthesized by ceramic techniques (i.e., $CaTiN_2$, $SrZrN_2$, $BaZrN_2$),[54,142,147] the absence of $CaZrN_2$ and $CaHfN_2$ from the literature implies that a synthetic strategy had previously been elusive.

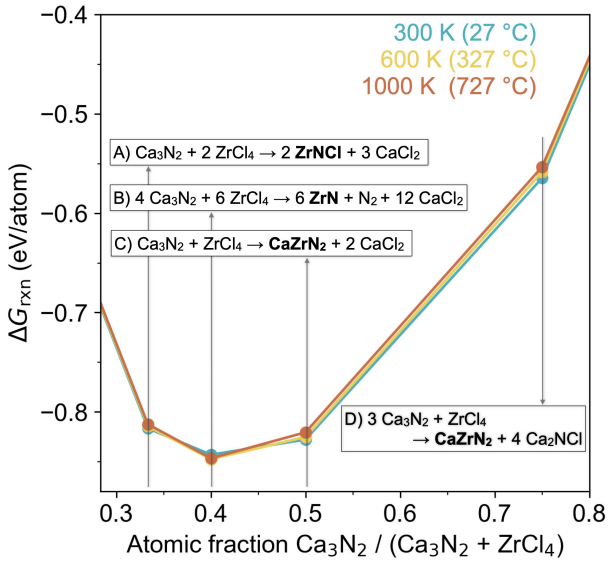

Figure 5.5: Gibbs free energy calculations at various temperatures show that the convex hull as a function of $Ca_3N_2/(Ca_3N_2 + ZrCl_4)$ ratio is defined by the formation of ZrNCl (Reaction A), ZrN (Reaction B), and $CaZrN_2$ (Reactions C and D). Reaction energies were calculated using the method of Bartel, et al.[119] The full convex hull is shown in Figure D.12.

5.3.2 Thermochemical calculations

The calculated convex hull shows that ZrN formation on the hull across the range of synthetically relevant temperatures (Figure 5.5). Therefore, the reduction of Zr(IV) to Zr(III) is always thermodynamically competitive with the desired reaction ($CaZrN_2$ formation). This finding contrasts with the Mg-Zr-N-Cl system, in which we observed that at $T < 800$ K, ZrN formation was not on the hull.[55] Consequently, a low-temperature two-step process is unlikely to avoid Zr(IV) to Zr(III) reduction.

The computed predominance diagrams shown in Figure 5.6 describe the chemical potential surfaces through which these metathesis reactions proceed. These models are computed using calculated phase energies from the Materials Project database,[9] and are constructed in the generalized style described by Yokokawa.[150] Each visible facet is a stable phase in the A-Zr-Cl system, with larger facets indicating phases with a deeper stability on the convex hull of a compositional phase diagram. The colored polytopes projected into these three dimensional A-Zr-Cl spaces show N-containing phases. Intersection points,

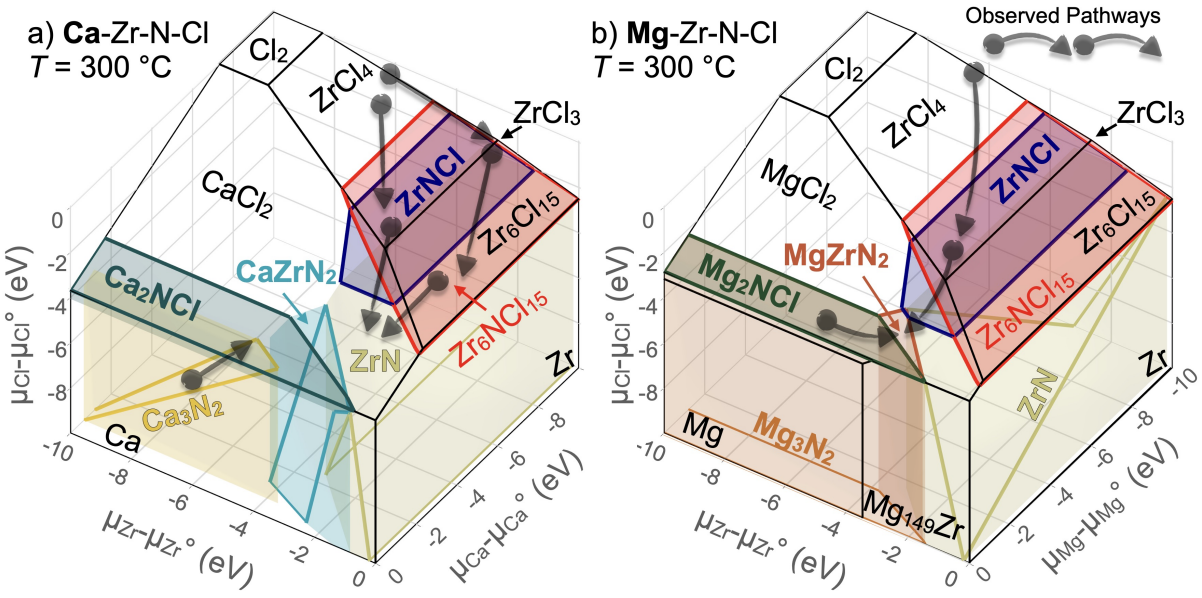

Figure 5.6: Predominance diagrams for a) the Ca-Zr-N-Cl chemical system and b) the Mg-Zr-N-Cl chemical system calculated at 300 °C. Select nitrogen-containing phases are shown as colored volumes projected into the (Ca or Mg)-Zr-Cl 3-dimensional space. For the Ca-Zr-N-Cl system, the $CaZrN_2$ target is connected in chemical potential space to Ca_3N_2, Ca_2NCl, and ZrN, but not to ZrNCl, indicating that there is not a Zr^{4+} intermediate capable of linking the $ZrCl_4$ precursor to the targeted product. Therefore, this diagram predicts that reduced Zr^{3+} species must form along the reaction pathway, and must then be re-oxidized back to Zr^{4+} to make $CaZrN_2$. In contrast, the Mg-Zr-N-Cl system shows connectivity in chemical potential space between ZrNCl and the $MgZrN_2$ target. This border in chemical potential space allows Zr^{4+} ions to transfer from the $ZrCl_4$ precursor to the $MgZrN_2$ product via the ZrNCl intermediate, allowing the reaction to proceed stoichiometrically. The black curved arrows show the pathways identified by our *in situ* SPXRD measurements, which show the reduction of Zr^{4+} to Zr^{3+} in the Ca-Zr-N-Cl system, but the preservation of the tetravalent oxidation state in the Mg-Zr-N-Cl system when Mg_2NCl is used as the precursor.

edges, or faces between these regions of chemical potential space indicate where stable interfaces can form between phases. It has previously been observed that a chemical reaction proceeding under local equilibrium conditions will follow a pathway between adjacent phases.[151]

Figure 5.6a shows that no Zr(IV) species in the Ca-Zr-N-Cl phase space shares a stable interface with the $CaZrN_2$ product, indicating that equilibrium necessitates passing through Zr(III) intermediates. Specifically, the ZrN chemical potential space connects both the Zr_6NCl_{15} and ZrNCl spaces to the $CaZrN_2$ space, indicating that ZrN should form along the pathway. However, the true border between the ZrN and $CaZrN_2$ spaces is fuzzy, as the Materials Project database used to create these diagrams holds only stoichiometric, ordered phases. In reality, the disordered and non-stoichiometric $Ca_xZr_{2-x}N_2$ likely spans both the phase spaces depicted here as ZrN and $CaZrN_2$.

In contrast, Figure 5.6b shows that ZrNCl shares a stable interface with both the precursor $ZrCl_4$ and the product $MgZrN_2$. This suggests that ZrNCl can be a key intermediate that forms at the interface between $ZrCl_4$ and Mg_2NCl, allowing Zr(IV) ions to diffuse from the reactants to the product without undergoing reduction. This calculation is also consistent with our *in situ* SPXRD studies, described herein.

5.3.3 *In situ* synchrotron X-ray diffraction

Quantitative phase analysis of *in situ* SPXRD data (17-BM) from a reaction between $Ca_3N_2 + ZrCl_4$ show reduced Zr(III) species forming at the low reaction temperatures (Figure 5.7). $ZrCl_3$ is the first intermediate to form, appearing by 200 °C. This reduction of Zr(IV) to Zr(III) indicates the loss of nitrogen from the system, following Reactions 5.1 and 5.2,

$$6ZrCl_4 + 6e^- \longrightarrow 6ZrCl_3, \tag{5.1}$$

$$2N^{3-} \longrightarrow N_2 + 6e^-. \tag{5.2}$$

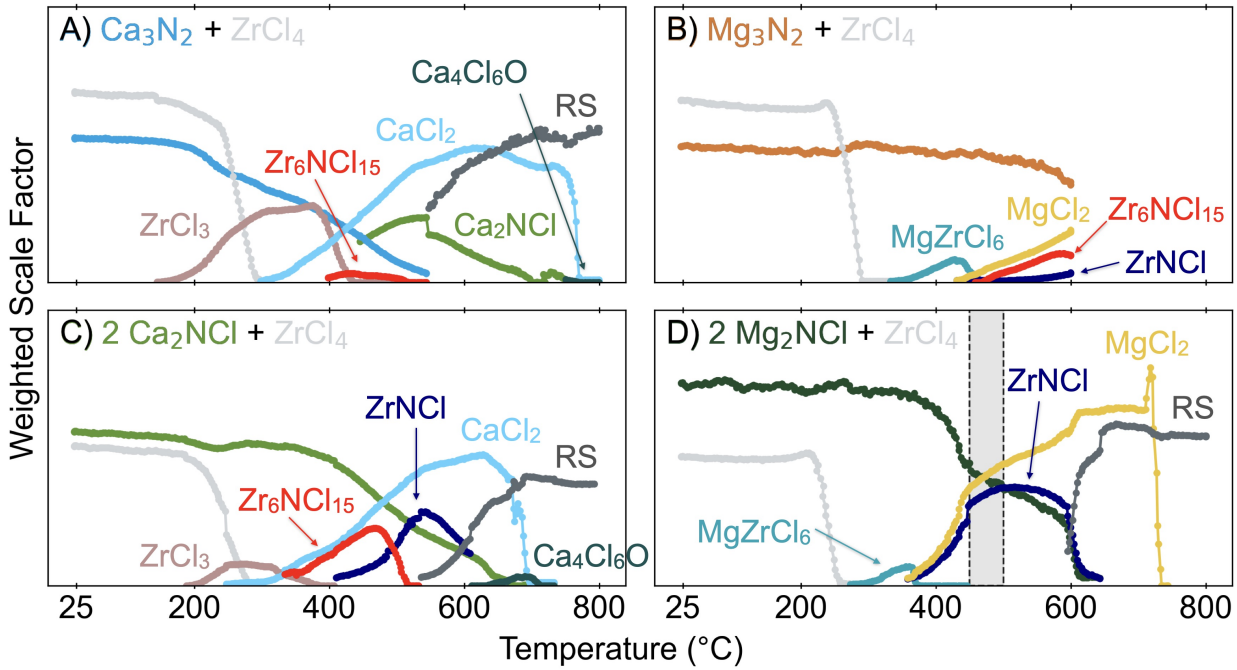

Figure 5.7: Rietveld analysis of *in situ* SXRD data show weighted scale factors for reactants, intermediates, and products as a function of temperature upon heating precursor mixtures of A) $Ca_3N_2 + ZrCl_4$, B) $Mg_3N_2 + ZrCl_4$, C) $2Ca_2NCl + ZrCl_4$, and D) $2Mg_2NCl + ZrCl_4$. Each reaction was balanced to target $AZrN_2$ + 2 (or 3) ACl_2 stoichiometrically. In reactions with Mg_3N_2, Ca_3N_2, and Ca_2NCl, trivalent Zr species are observed ($ZrCl_3$ and Zr_6NCl_{15}), indicating reduction of Zr(IV) to Zr(III) and loss of N_2. Only the reaction using Mg_2NCl maintains the tetravalent oxidation state of Zr. The rocksalt structures of $Ca_xZr_{2-x}N_2$ and $Mg_xZr_{2-x}N_2$ are denoted as "RS". The grey highlighted region of (D) shows the temperature range used for step 1 of the two-step synthesis of $MgZrN_2$ detailed in prior reports.[55,105]

Subsequently, $ZrCl_4$ disappears as it sublimes (T_{sub} = 331 °C), at which point $CaCl_2$ begins to grow in. Near 400 °C, the $ZrCl_3$ converts to a nitride chloride, Zr_6NCl_{15}. Throughout this process, the Ca_3N_2 precursor steadily declines. Ca_3N_2 is fully consumed by 600 °C, with some of it reacting with the $CaCl_2$ byproduct to make Ca_2NCl. That Ca_2NCl phase persists up to 700 °C. Above 600 °C, the rocksalt (RS) phase $Ca_xZr_{2-x}N_2$ begins to grow in, along with a minor phase of Ca_4Cl_6O indicating a small degree of oxygen impurity. The reaction of $2Ca_2NCl + ZrCl_4$ proceeds in a similar fashion as $Ca_3N_2 + ZrCl_4$. However, using Ca_2NCl as a precursor seems to retain a portion of the Zr(IV), as evident by the presence of a ZrNCl-like phase. Both reactions yield rocksalt phases with $a \approx 4.60$ Å at 800 °C, consistent with ZrN. These pathways contrast with the Mg-Zr-N-Cl system.

In situ SPXRD in the analogous Mg system show reactivity differences between Mg_3N_2 and Mg_2NCl, with Mg_2NCl conserving the tetravalent state of Zr^{4+} throughout the reaction pathway. Both the reaction of $Mg_3N_2 + ZrCl_4$ and the reaction of $2Mg_2NCl + ZrCl_4$ first start with $ZrCl_4$ subliming, followed by the formation of a small amount of $MgZrCl_6$ as the reaction temperature increases during the experiment. However, the reaction with Mg_3N_2 goes on to produce Zr_6NCl_{15} indicating the reduction of Zr(IV) to Zr(III). Furthermore, the amount of Mg_3N_2 has only decreased slightly by the point at which we stopped the measurement at 600 °C. On the other hand, the Mg_2NCl reaction does not produce any distinct Zr(III) species (i.e., $ZrCl_3$ and Zr_6NCl_{15} do not form). Instead, the Mg_2NCl decreases in a stepwise fashion near 440 °C coincident with the formation of ZrNCl and the rapid increase of $MgCl_2$. A second stepwise decrease in Mg_2NCl occurs near 600 °C, coincident with the consumption of the ZrNCl and the formation of the rocksalt ($Mg_xZr_{2-x}N_2$).

These data highlight differing reaction pathways towards two similar products, rocksalt $CaZrN_2$ via a pathway with changing Zr oxidation states and rocksalt $MgZrN_2$ via a pathway with Zr exclusively in the tetravalent state, as predicted by our predominance diagrams (Figure 5.6). Using Mg_2NCl as a precursor maintains Zr(IV) in the tetravalent

state, proceeding through two reaction steps illustrated by Reactions 5.3 and 5.4.

$$\mathrm{Mg_2NCl} + \mathrm{ZrCl_4} \longrightarrow \mathrm{ZrNCl} + 2\mathrm{MgCl_2}, \tag{5.3}$$

$$\mathrm{Mg_2NCl} + \mathrm{ZrNCl} \longrightarrow \mathrm{MgZrN_2} + \mathrm{MgCl_2}, \tag{5.4}$$

As noted in prior reports, heating directly to a high temperature (ca. 800 °C) results in an Mg-poor rocksalt, but a two-step process yields stoichiometric $MgZrN_2$.[55,105] The first step of that two-step process (T_{react}) is a 12 to 24 h dwell at 450–500 °C (the highlighted grey temperature region in Figure 5.7). These *in situ* results suggest that dwelling for ≥ 12 h at 450–500 °C results in Reaction 5.3 followed by Reaction 5.4 producing the amorphous material we observed (presumably $MgZrN_2$).[55] The second reaction step then crystallizes $MgZrN_2$ ($T_{cryst} = 800$ °C). In contrast, two-step reactions provide no advantage for towards $CaZrN_2$, as reduced Zr(III) intermediates are the first to form along the pathway.

Following the chemical potential hypothesis illustrated by the predominance diagram (Figure 5.6a), the synthesis of $CaZrN_2$ must proceed through Zr(III) intermediates, requiring oxidation back to Zr(IV) somewhere along the reaction pathway. As deduced from the *in situ* SPXRD data, the initial reaction sequence proceeds through Reactions 5.5 and 5.6:

$$\mathrm{Ca_3N_2} + 6\mathrm{ZrCl_4} \longrightarrow 6\mathrm{ZrCl_3} + \mathrm{N_2} + 3\mathrm{CaCl_2}, \tag{5.5}$$

$$\mathrm{Ca_3N_2} + 12\mathrm{ZrCl_3} \longrightarrow 2\mathrm{Zr_6NCl_{15}} + 3\mathrm{CaCl_2}. \tag{5.6}$$

Subsequently, *in situ* XRD shows that the rocksalt phase appears as Zr_6NCl_{15} disappears, suggesting that the trivalent Zr_6NCl_{15} species is consumed to make $Ca_xZr_{2-x}N_2$. In this particular *in situ* experiment, the rocksalt lattice parameter refines to $a = 4.61$ Å, suggesting a Ca-poor phase and a substantial fraction of the Zr remains in the trivalent state. However, we suspect that reactions with excess Ca_3N_2 go through the same sequence of intermediates, as reactions typically proceed through pairwise interactions.[125] Therefore

the formation of stoichiometric $CaZrN_2$ involves the oxidation of Zr(III) in Zr_6NCl_{15} back up to Zr(IV) in $CaZrN_2$.

We hypothesize that the "excess" Ca_3N_2 required for $CaZrN_2$ synthesis provides the necessary oxidant, either directly through a solid-solid reaction or by producing a N_2 partial pressure within the evacuated ampule. In the latter case, N_2 released previously in the process (Reaction 5.5) could subsequently react with the solid,

$$9\mathrm{Ca_3N_2} + 2\mathrm{Zr_6NCl_{15}} + 2\mathrm{N_2} \longrightarrow 12\mathrm{CaZrN_2} + 15\mathrm{CaCl_2}. \tag{5.7}$$

If Reaction 5.7 is the final step, then the net reaction (combining Reactions 5.5, 5.6, and 5.7) still simplifies to,

$$\mathrm{Ca_3N_2} + \mathrm{ZrCl_4} \longrightarrow \mathrm{CaZrN_2} + 2\mathrm{CaCl_2}, \tag{5.8}$$

implying a precursor ratio of $n = 1$. The pressure generated within the reaction vessel by our scaled up reactions (using ca. 0.2 g $ZrCl_4$) only generate on the order of pN_2 = 0.001 atm at 1100 °C. Control experiments with ampules backfilled with room-temperature N_2 at 0.0002 atm and 0.002 atm show a lattice parameter approximately 4.66 Å and 4.61 Å, respectively (Figure D.8), smaller than the 4.72 Å produced without backfilling. This finding likely stems from oxygen contamination in the nitrogen, despite our best efforts at purging the vacuum manifold with ultrahigh purity N_2 prior to use. Oxygen incorporation is expected to decrease the lattice parameter of the rocksalt (Figure D.9). Future experiments to test this hypothesis could use NaN_3 to generate controllable amounts of N_2 while minimizing the chance of oxygen exposure.

Alternatively, the direct solid-solid reaction could occur between the two solids without the need for the incorporation of N_2:

$$11\mathrm{Ca_3N_2} + 2\mathrm{Zr_6NCl_{15}} \longrightarrow 12\mathrm{CaZrN_2} + 15\mathrm{CaCl_2} + 6\mathrm{Ca}. \tag{5.9}$$

The net reaction then simplifies to,

$$7\mathrm{Ca_3N_2} + 6\mathrm{ZrCl_4} \longrightarrow 6\mathrm{CaZrN_2} + 12\mathrm{CaCl_2} + \mathrm{N_2} + 3\mathrm{Ca}, \tag{5.10}$$

where $n = \frac{7}{6} = 1.167$. This precursor ratio closely matches the ratio we observe as experimentally necessary for $CaZrN_2$, $n \approx 1.2$. If Reaction 5.9 proceeds, then the Ca should be observable. However, the fraction of Ca should be small; only 5.0 weight percent (wt%) relative to 39.7 wt% for $CaZrN_2$ and 55.3 wt% for $CaCl_2$. Ca melts at 842 °C and has a vapor pressure of 13 Torr at 1000 °C,[159] so it may volatilize away from the pellet. We have not observed Ca in our diffraction patterns. However, we note a small mass loss from each reaction (ca. 1 to 10 wt%) and a darkening of alumina crucibles used in our syntheses. The darkening may indicate the reduction of Al^{3+} by Ca, as Ca is more oxophilic than Al:

$$3\mathrm{Ca} + \mathrm{Al_2O_3} \longrightarrow 2\mathrm{Al} + 3\mathrm{CaO}\ (\Delta H_{rxn} = \text{-}0.340\ \text{eV/atom}). \tag{5.11}$$

Residual oxygen in the sealed ampules, despite the carbon getters, could also react with a Ca byproduct, leading to a slightly larger weight fraction of Ca_4Cl_6O than would be expected from the impurity in the starting materials alone. Lastly, any Ca present in the reaction mixture could potentially react with the methanol used for washing to form calcium methoxide.[160] Such a byproduct would be difficult to detect by PXRD, but could be revealed by IR spectroscopy.

The suggestion that a highly electropositive element like Ca could be produced by such a reaction is bold, but this hypothesis has basis in prior literature. Gregory, et al., also saw byproduct Sr metal (and SrO), as expected for their sealed-tube synthesis $Sr_2N + ZrN \longrightarrow SrZrN_2 + Sr$.[142] This example provides direct evidence that the formation of $AZrN_2$ phases may be sufficiently thermodynamically favorable that Zr(III) to Zr(IV) oxidation can be paired with A(II) to A(0) reduction. Similarly, Barker, et al., synthesized single crystals of Sr_3CrN_3 and Ba_3CrN_3 in stainless steel tubes from Cr combined with Sr_2N

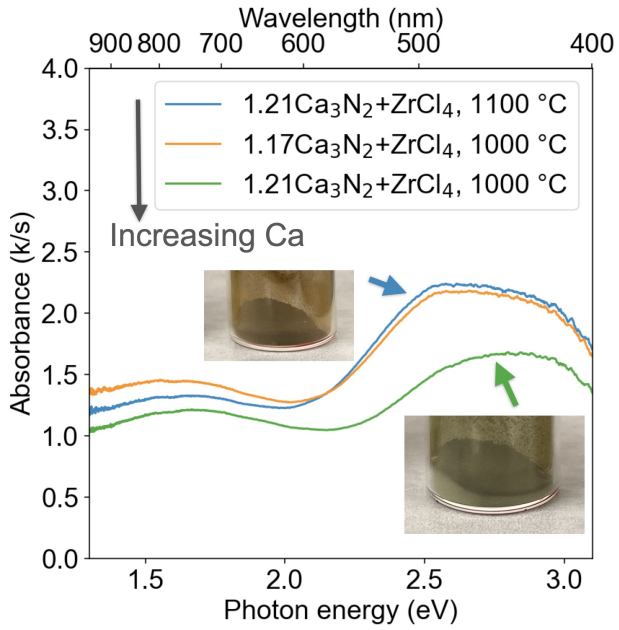

Figure 5.8: Kubelka-Munk transformations of diffuse reflectance UV-Vis spectroscopy shows a bandgap near 2.0 eV. Powders appear black, reddish or greenish depending on processing conditions (see inset). The appearance of decreasing absorptivity above 3.0 eV is an artifact of decreasing intensity from the light source.

or Ba_3N_2, implying the reactions $3Sr_2N + Cr \longrightarrow Sr_3CrN_3 + 3Sr$ and $Ba_3N_2 + 2Cr \longrightarrow Ba_3CrN_3 + 3Ba$.[161] However, they saw only unreacted Cr, SrO, and BaO byproducts by PXRD. In contrast, Hunting, et al., saw clear evidence of Li metal product when Li_3N flux served as the oxidant for the synthesis of Ca_4TiN_4 and Ca_5NbN_5.[146] In sealed tubes under Ar, the following reactions oxidized the transition metal by reducing the lithium: $\frac{4}{3}Ca_3N_2 + TiN + \frac{1}{3}Li_3N \longrightarrow Ca_4TiN_4 + Li$ and $\frac{5}{3}Ca_3N_2 + NbN + \frac{2}{3}Li_3N \longrightarrow Ca_5NbN_5 + 2Li$. In these cases, Li metal was observed surrounding the crystals of the ternary nitride product. While these examples support the hypothesis that Reaction 5.9 could be the final reaction step, future *in situ* SPXRD experiments would need to be conducted to observe the rocksalt lattice under different precursor ratios. For now, we shift to studying the properties of the newly synthesized phases.

5.4 Optoelectronic properties

Kubelka-munk transformations of diffuse reflectance spectra show an optical absorption onset near 2.2 eV for $CaZrN_2$ (Figure 5.8). This feature leads to a 2.0 eV bandgap by Tauc analysis. This value is substantially greater than the DFT-computed bandgap for the $R\bar{3}m$ structure of 0.45 eV,[145] but only slightly larger than the 1.5 eV bandgap predicted by calculations on the disordered rocksalt structure.[11] The $MgZrN_2$ phase exhibits a 1.8 eV bandgap in thin film form,[49] but powder measurements of the material made by metathesis did not exhibit an optical absorption onset.[55] Assuming the valence band is composed of N-p states and the conduction band is metal d or s states, the change from Mg to Ca would be expected to raise the conduction band and expand the bandgap, as Ca is less electronegative than Mg. In contrast, $SrZrN_2$ in the ordered $R\bar{3}m$ structure has a lower calculated bandgap of 1.4 eV and is of interest for thermoelectric applications.[162]

Resistivity measurements on pressed pellets (not sintered) were attempted, but resistance was higher than the sensitivity of the multimeter (> 20 MΩ). This finding may stem from the low packing density of the unsintered pellets (ca. 25 %) and from grain boundary resistance of the small particles (See Figure 5.3). Future work could attempt to measure resistivity on sintered pellets, but sintering is likely a non-trivial challenge as high temperatures are often needed (e.g., 1200 °C for $CaTiN_2$),[54] at which point Ca-loss by volatility may become problematic.[163] However, as these findings suggest that $CaZrN_2$ a new semiconductor with is a 2.0 eV bandgap, future efforts to optimize this material may prove fruitful.

5.5 Conclusion

We report the discovery of two new ternary nitrides, $CaZrN_2$ and $CaHfN_2$, via metathesis synthesis of bulk powders. These phases crystallize in the cation-disordered rocksalt structure ($Fm\bar{3}m$), as opposed to the computationally predicted $\alpha-NaFeO_2$ structure type. *In situ* synchrotron powder X-ray diffraction analysis shows how Zr(III) intermediates form

early on in the reaction process, which rationalizes why excess of the Ca_3N_2 reagent is synthetically necessary. These findings stand in contrast to our prior synthesis of $MgZrN_2$, which proceeds stoichiometrically from $2Mg_2NCl + ZrCl_4$ to $MgZrN_2 + 2MgCl_2$ via a ZrNCl intermediate. These observed synthetic pathways match well with the predictions generated by computed predominance diagrams. Preliminary property measurements show $CaZrN_2$ and $CaHfN_2$ are semiconductors with bandgaps near 2 eV. In sum, these findings demonstrate a generalizable strategy for predicting and conducting metathesis reactions with the goal of synthesizing new ternary nitrides.

Chapter 6

Outlook and Future Directions

My graduate research began with a list of predicted compounds and the challenge to go make them. To a naive and over-confident first-year graduate student, this task seemed straightforward. Yet, success was not simple. In the subsequent 5 years, my colleagues and I successfully synthesized six new compounds in the phase spaces we targeted (Figure 6.1), but only by overcoming unforeseen challenges. Fortunately, the alignment of theory with experiment has improved dramatically in the past few years. This final chapter aims to summarize the three main advances in using computational guidance to synthesize new nitrides (Figure 6.2), and provide an outlook for future developments in the field.

The initial list of ternary nitrides to synthesize came from a large computational study that used a data-mined structure predictor and density functional theory (DFT) calculations to map out huge swaths of unexplored phase space.[2] This landmark computational effort by Sun, et al., initially posted on arXiv in 2018,[10] used 340 known structures within a 50×50 set of ternary spaces ($M1$-$M2$-N) to generate 6000 candidate structures. DFT was then used to calculate the formation energy of these structures, which could be compared to the known binaries and ternaries (Figure 6.2A). These comparisons resulted in the prediction of 244 new stable structures, suggesting plausible synthetic targets in 93 previously-empty ternary spaces.

While this study helped unleash a wave of newly synthesized nitrides,[52] there were shortcomings. First, as the data-mined structure predictor relied on ionic-substitutions starting with known nitrides in their dataset, the predicted compounds were limited to known structure types (i.e., interpolation) rather than the wholesale generation of novel materials (extrapolation). This approach appears to have missed certain structures. For example, the computational study predicted Mg_3WN_4 in a $P31c$ spacegroup (Materials Project id: mp-1030015) to be the most stable ternary in the Mg-W-N system, but our

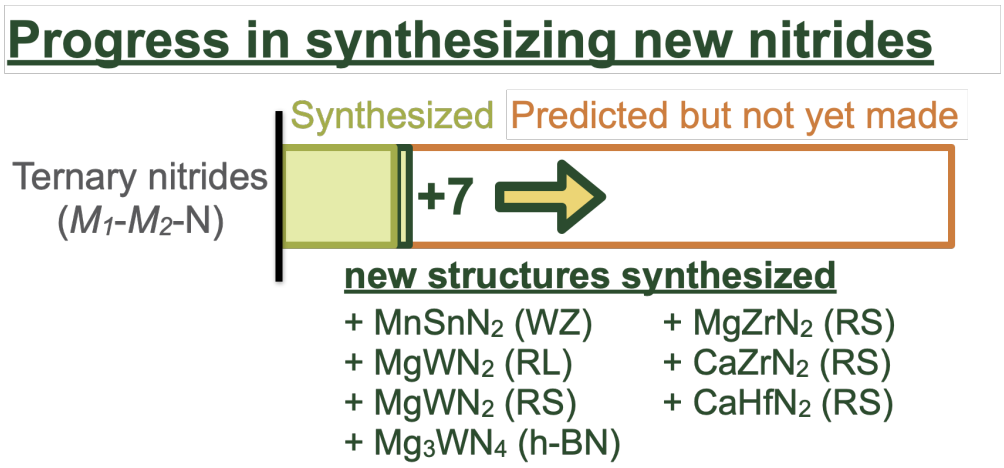

Figure 6.1: This dissertation reports the synthesis of six nitride structures: the discovery of $MnSnN_2$ in the wurtzite (WZ) structure using thin film syntheses in Chapter 2, discovery of three Mg-W-N structures using thin film and bulk syntheses in Chapter 3, the first bulk synthesis of rocksalt (RS) $MgZrN_2$ in Chapter 4, and the discovery of RS $CaZrN_2$ and $CaHfN_2$ using bulk methods in Chapter 5.

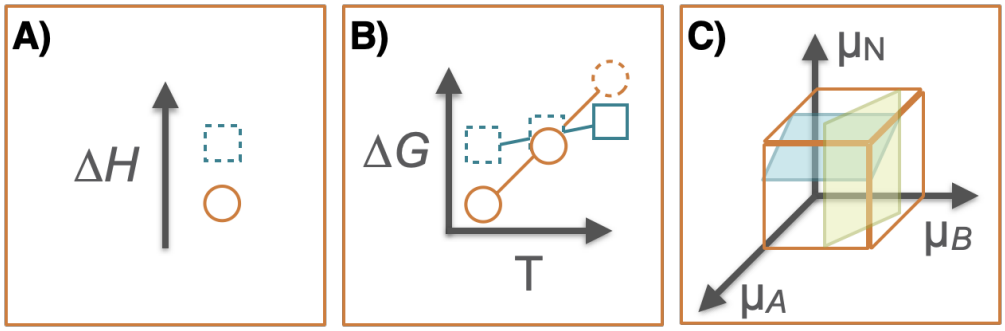

Figure 6.2: Schematic representation of the recent advances in computational guidance for synthetic efforts. A) DFT studies predict the relative formation enthalpies (ΔH) of hypothetical compounds, suggesting which ternary targets may be more stable than binaries or elements.[2] B) A machine-learning model estimates formation energies (ΔG) as a function of temperature,,[119] allowing the comparison of phase stability at synthetically relevant temperatures. C) Computed predominance diagrams emerge as a way to visualize reaction network analysis in hyperdimensional phase spaces.[164] These computed predominance diagrams and reaction network analysis provide theoretical guidance on reaction pathways.

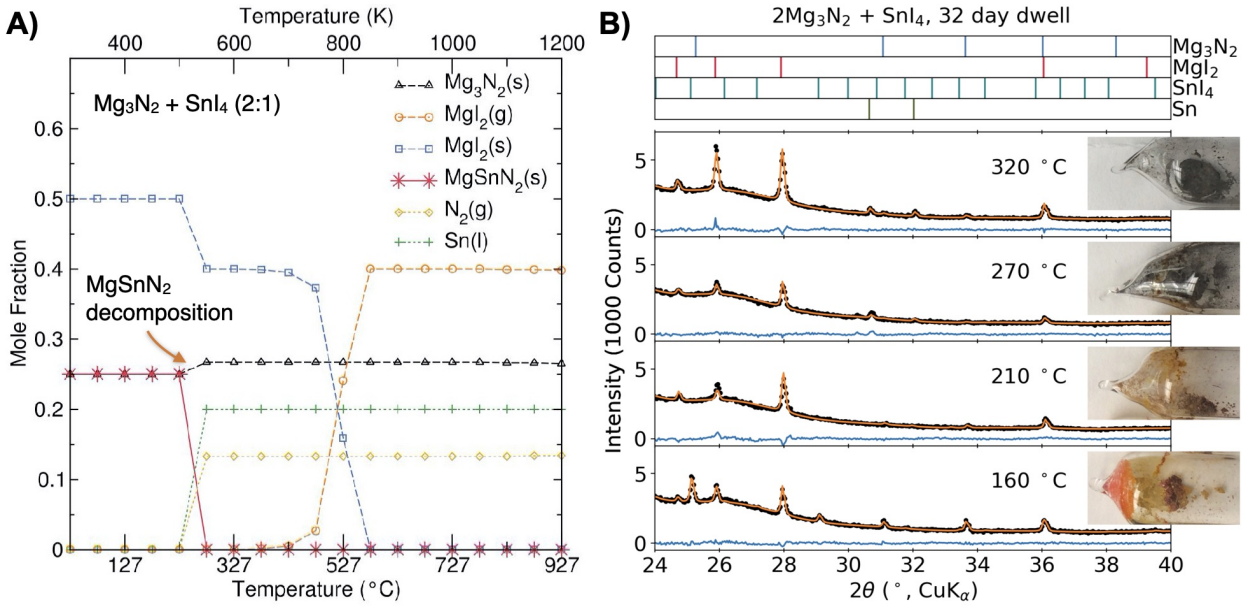

Figure 6.3: A) $\Delta G(T)$ and equilibrium calculations using the method described by Bartel, et al.[119] show that $MgSnN_2$ is a thermodynamically stable product when Mg_3N_2 and SnI_4 (2:1 mole ratio) are used as starting materials, provided the temperature is kept < 227 °C. At temperatures > 227 °C, tin(IV) reduction and N_2(g) evolution become thermodynamically preferred. B) PXRD data of metathesis reactions of $2Mg_3N_2 + SnI_4$ in sealed ampules placed in a tube furnace at various temperatures for 32 days. Temperatures were measured by placing the tip of thermocouple next to the pellet. At temperatures ≥ 270 °C, Sn reduction is observed, as noted by the two peaks near $2\theta = 32°$ and the black color of the pellet (photos on right). At 210 °C, the metathesis product, MgI_2, appears to be the only crystalline phase, indicating some degree of reactivity but no crystallization of $MgSnN_2$. At 160 °C residual starting materials are detected, in addition to MgI_2, indicating very slow reactivity. Tick marks in the top box indicate peak positions for the relevant phases.

experiments and targeted DFT calculations ultimately showed that $MgWN_2$ in the rock-saline structure ($P6_3/mmc$) defines the deepest point in the thermodynamic hull (Chapter 3). Second, these DFT predictions only calculated the enthalphy of formation (ΔH_f) at $T = 0$ K. As real syntheses must occur at finite temperatures, this shortcoming proved problematic at times.

Fortunately, the second main advance in computationally-guided syntheses came when Bartel, et al., reported a method for rapidly calculating formation energies as a function of temperature.[119] In that work, Bartel, et al., trained a machine learning model to predict the temperature-dependence of the Gibbs formation energy, given only a calculated structure (Figure 6.2B). The model was built upon datasets of temperature-dependent thermody-

namic quantities from both experiment and high-accuracy computations, and ultimately produced a root-mean-square error of ± 50 meV in the predicted Gibbs free energy values. This tool for calculating $\Delta G(T)$ can even be used to predict the equilibrium distribution of products given initial elemental conditions (i.e., reactants) and is now incorporated into pymatgen.[101] Importantly, the computational tool factored in the elemental reference energies as a function of temperature. Including this elemental reference is essential when targeting nitrides, as the absolute Gibbs free energy of N_2 (at 1 atm pressure) decreases from -0.3 eV/atom at 300 K to -1.7 eV/atom at 1800 K.[119] This substantial change in chemical potential can destabilize nitrides that were predicted stable by 0 K DFT, as was the case for $MgSnN_2$ (Figure 6.3). This advancement in computational guidance helped explain why our efforts targeting $MgSnN_2$ yielded Sn instead, and helped us successfully identify a synthetic strategy for $MgZrN_2$ (Chapter 4). While this Gibbs-predictor is a powerful tool for determining equilibrium conditions under real synthesis conditions, the pathway towards that equilibrium point is also an important factor determining the synthesizability of a material.

Here, a recently published tool by McDermott, et al., provides computational guidance on reaction pathways.[164] Bulk solid-state syntheses require physically mixing reactants and inducing diffusion to drive chemical mixing of the atoms towards the desired products. That process of chemical mixing leads atoms down chemical potential gradients, with intermediates in the reaction determined by the chemical potential windows that different phases can tolerate.[165] With the Reaction Network analysis codebase built by McDermott and colleagues, users can query the Materials Project database for structures in a given phase space (e.g., Mg-Zr-N-Cl) and identify all possible links between the phases. This linked network, combined with ΔG_{rxn} calculations building on the work of Bartel, et al.,[119] can generate a ranked list of reactions. Reactions can also be ranked by chemical potential distance—a geometric quantity calculated from the distance between two multidimensional polytopes—representing the chemical stability of compounds relative to

one another. Compounds with a chemical potential distance of 0 allow for the continuous diffusion of atoms across an interface between the two, enabling reaction selectivity as demonstrated in the Y-Mn-O system.[151] In Chapter 5, we demonstrated how these calculations can describe reaction pathways for nitride systems as well. Computed predominance diagrams help visualize these relationships, as phases with a chemical potential distance of 0 eV boarder one another in these multidimensional maps (Figure 6.2C). Together, Reaction Network analysis and computed predominance diagrams provide a roadmap to help synthetic chemists find promising routes from known reactants to the soon-to-be-discovered products.

While the advances of Sun, Bartel, McDermott, and their teams have improved the computational guidance available to experimentalists, the tools they developed still have some limitations. First, they rely on computational databases that are large but incomplete. The Reaction Network analysis cannot predict a pathway through an unidentified intermediate. This shortcoming bolsters the case for rapid feedback between experimentalists and computationalists, as each newly discovered phase expands the capacity of the Reaction Network to predict routes to other phases. The second main shortcoming is that these thermodynamic tools rely on computed energies for ordered structures. While the ordered phases are a useful approximation, real nitrides are often highly disordered.

Looking forwards, computational-guidance for materials synthesis can further be improved by accounting for disorder. In this vein, Woods-Robinson, et al., developed a method to account for this disorder when considering the relative stability of different polymorphs of a new ternary nitride – $ZnZrN_2$.[53] Using the DFT-calculated energies for special quasirandom structures (SQS),[166] Woods-Robinson, et al., compared the relative stability and disorder tolerance of several $ZnZrN_2$ polymorphs. The thermodynamic ground state was the "wurtz-salt" structure (WS, with alternating layers of wurtzite-like Zn tetrahedra and rocksalt-like Zr octahedra) among the ordered structures. However, the SQS analysis showed that hexagonal boron nitride (h-BN) and rocksalt (RS) polymorphs paid less of

an energetic penalty in disordered configurations, as these structures only have a single cation site (trigonal bipyramidal and octahedral, respectively). Combinatorial sputtering experimentally confirmed the synthesizability of these h-BN and RS polymorphs, and did not observe the WS polymorph, highlighting the importance of considering disorder when targeting compounds for synthesis. Unfortunately, this approach is computationally expensive at the moment, and so impractical for incorporation with high-throughput tools like Reaction Network analysis. Future work to increase the accessibility of this approach should be applauded by the synthetic community.

While there is still room for improved computational guidance for solid state synthesis, the tools already available offer powerful ways to accelerate discovery. The remainder of this chapter will focus on applying those tools to generate hypotheses towards the synthesis of yet-to-be-discovered ternary nitrides. In particular, the Reaction Network tool developed by McDermott, et al., provides the most powerful guidance for synthetic chemists working with solid-state reactions.

Reaction network analysis highlights a strategy for synthesizing $LaWN_3$ in bulk, a perovskite phase that has only recently been discovered by thin film combinatorial sputtering.[19] As the perovskite structure can have subtle distortions in symmetry that can dramatically impact properties (e.g., ferroelectricity useful for telecommunications technology), bulk synthesis of this phase would be a worthwhile effort, as bulk powders can be characterized by X-ray and neutron scattering techniques with greater fidelity than thin films. Reaction network analysis was conducted in the Li-La-W-N-Cl phase space (Table 6.1). Sorting the reactions by distance in chemical potential space can identify those that are most likely to proceed directly to the product (without the formation of intermediates).

This analysis identifies the following solid state reaction as a promising method for producing $LaWN_3$ in bulk,

$$\mathrm{Li_6WN_4 + 2La_2NCl_3 \longrightarrow 2LaN + 4LiCl + LaWN_3}. \tag{6.1}$$

Table 6.1: Reaction network analysis of the Li-La-W-N-Cl chemical system using the method described by McDermott, et al., (code available on github: https://github.com/GENESIS-EFRC/reaction-network).[164] The quintary phase space includes 88 entries in the Materials Project, of which 17 are stable at 400 °C. Reaction network analysis calculated 2276 possible reactions between these stable phases that yield $LaWN_3$. These reactions were ranked in order of increasing chemical potential distance (only the top ten are shown here). The first eight reactions listed are unlikely to be viable, as they involve refractory precursors (e.g., W, W_2N_3). However, reaction 9 involves two precursors that are likely to be kinetically competent (Li_6WN_4 and La_2NCl_3) owing to the Li and Cl ions that can facilitate diffusion. I hypothesize that these two reagents may be a viable way to synthesize $LaWN_3$ in bulk for the first time.

#	Reaction	ΔG(400 °C) (eV/atom)	dist. (eV)
1	$LaN + W + N_2 \rightarrow$ LaWN3	-0.45	0.00
2	$LaN + 0.5W_2N_3 + 0.25N_2 \rightarrow$ LaWN3	-0.30	0.00
3	$3LaN + 2W_2N_3 \rightarrow$ W + 3 LaWN3	-0.23	0.00
4	$2W_2N_3 + 3Li_6WN_4 + 6LaCl_3 \rightarrow$ W + 6 LaWN3 + 18 LiCl	-0.16	0.00
5	$W + N_2 + La_2NCl_3 \rightarrow$ LaWN3 + LaCl3	-0.14	0.00
6	$2W_2N_3 + Li_6WN_4 + 2La_2NCl_3 \rightarrow$ W + 4 LaWN3 + 6 LiCl	-0.13	0.00
7	$2W_2N_3 + 4La_2NCl_3 + N_2 \rightarrow$ 4 LaWN3 + 4 LaCl3	-0.06	0.00
8	$2W_2N_3 + 3La_2NCl_3 \rightarrow$ W + 3 LaWN3 + 3 LaCl3	-0.03	0.00
9	$Li_6WN_4 + 2La_2NCl_3 \rightarrow$ 2 LaN + 4 LiCl + LaWN3	-0.02	0.00
10	$5LaN + Li_6WN_4 + 8LaCl_3 \rightarrow$ 6 LiCl + 6 La2NCl3 + LaWN3	-0.15	0.10
...	...	...	...

The computed predominance diagram for this process is shown in Figure 6.4, visualizing the connection in chemical potential space between the reactants of Equation 6.1 and the products. Both Li_6WN_4 and La_2NCl_3 are known phases with simple preparations,[167,168] an important note given that this Reaction Network analysis includes phases that exist in the Materials Project database but may not yet have known syntheses. Li_6WN_4 can be made via a reaction of Li_3N and W under flowing N_2,[167] a procedure which I have successfully replicated. In addition to the reported synthesis of $Li_3N + 2LaCl_3 \longrightarrow La_2NCl_3 + 3LiCl$,[168] we have also made La_2NCl_3 via $Mg_2NCl + 2\,LaCl_3 \longrightarrow La_2NCl_3 + 2\,MgCl_2$ (unpublished results). One problem with this synthesis is that the byproduct LaN produced by Reaction 6.1 might be difficult to remove. If $LaWN_3$ proves to be more air- or water-stable than LaN, washing with dilute acid may be a viable purification strategy, as 3.5 M HNO_3 (aq) was used for removing trace Mo following the bulk ceramic synthesis of $MgMoN_2$.[39]

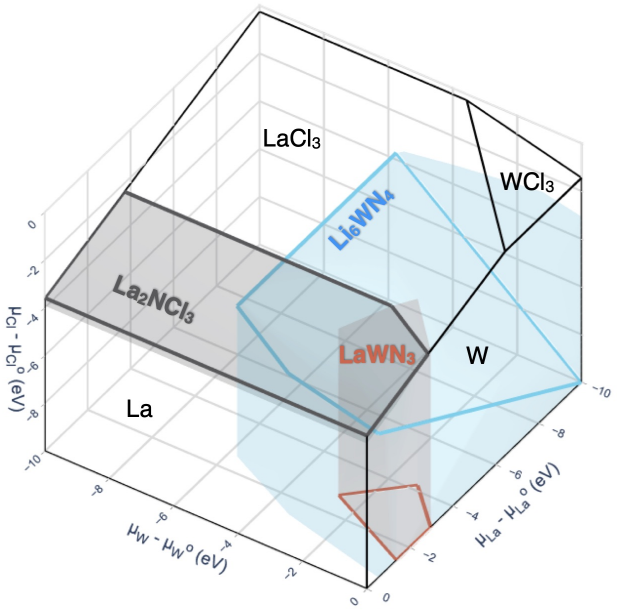

Figure 6.4: Computed predominance diagram of the Li-La-W-N-Cl phase space shown along the La-W-Cl axes, with select Li and N containing phases are projected into this space in the colored volumes. This diagram visualizes the connectivity between La_2NCl, Li_6WN_4, and $LaWN_3$. This connectivity indicates that ions could diffuse between these phases, enabling the controlled synthesis of $LaWN_3$ as described in Equation 6.1.

A bulk high-pressure metathesis route to $LaWN_3$ was reported in November 2022, near-coincidental with the submission of this dissertation.[50] The approach used BN crucibles in a belt-type high pressure apparatus to provide a high-pressure environment for the reaction $LaCl_3 + WCl_6 + 3Li_3N \longrightarrow LaWN_3 + 9LiCl$. The authors noted that ambient pressure reactions between these precursors yielded only LiCl and W, indicating that the high-pressure was necessary to keep nitrogen in the solid. However, the pathway of this reaction was not explored. Therefore, the proposed reaction of $Li_6WN_4 + La_2NCl_3$ may provide an ambient pressure route to this material.

We will see in the coming years if this prediction bears out or if unforeseen factors inhibit this synthetic approach. Regardless, the interplay of computational guidance with creative synthetic approaches will undoubtedly lead to the discovery of many more ternary nitrides in the years to come. It has been an honor to play a part in this process so far, and I look forward to the discoveries that await.

Chapter 7

Assessment of gender equity in academic seminar Q&A sessions*

Overview

Achieving gender equity in Science, Technology, Engineering, and Math (STEM) is necessary for a fair and just society. However, women are underrepresented in STEM fields, with the disparity increasing at each level of the career ladder. This disparity is not only unfair, it also inhibits the ability of our STEM communities to address the most urgent technical challenges of our day (e.g., climate change). The causes of this disparity are myriad. One aspect of this disparity is the decreased visibility of women in academic seminars, which are important opportunities for professional advancement. In particular, prior research has shown that women ask disproportionally fewer questions during the question and answer (Q&A) session that typically follows a seminar. This decreased visibility likely originates with the social environment around these Q&A sesssions, which can be tuned to some degree by the format of the session. Prior researchers in this area have hypothesized that a brief intra-audience discussion period prior to the open Q&A session could help bring about gender parity. This structure is analogous to the "think-pair-share" pedagogical technique that is well-established in K-12 and undergraduate education. In this chapter, I present my findings on the gender disparity during academic seminars I attended in both the traditional Q&A format and with the think-pair-share format. The gender disparity persists in both, suggesting future efforts at restructuring seminar Q&A sessions are needed.

---

* Chris Rom conceptualized the project, collected and analyzed the data, and wrote the manuscript. Nancy Levinger provided support through the IRB approval process.

7.1 Introduction

Gender-diverse teams produce more novel and impactful research,[169] so the persistent underrepresentation of women in STEM fields is not only unfair, it also hampers the ability of the scientific community to solve the big problems facing society. This underrepresentation originates with "the leaky pipeline problem", in which women disproportionately leave STEM fields at every point along a career progression.[170] Survey data shows that this disproportionate attrition is often driven by academic culture.[171] While there are many aspects of academic culture, one ubiquitous component is the academic seminar, where researchers publicly present their work and engage with the work of others.

A recent and growing body of literature documents how women are underrepresented in the Q&A sessions of seminars, negatively impacting their visibility in their academic communities. Researchers have found that women ask disproportionately fewer questions at seminars in a range of fields spanning astronomy,[172,173] conservation biology,[174] economics,[175] genetics,[176] molecular biology,[177] and psychology.[178] As question askers are highly visible in a community, this underrepresentation means women are less visible, which potentially hurts their career prospects and may contribute to the underrepresentation of women in STEM leadership. Fortunately, talking about this problem can help. Telis, et al. noted that "following wide public discussion of the relative under-participation of women, women choose to ask more questions. This response suggests that women see value in increased question asking at conferences."[176] However, the proportion of women asking questions was still smaller than the proportion of women in the audience. Therefore, there is a need to identify other strategies that can bring about gender parity.

Each of these reports has possible suggestions for improving gender equity during Q&A sessions, and our scientific communities should test these out and adopt the ones that work. In particular, I noted that Carter, et al. advised, "it could help both women and men to provide a small break between the talk and the question period, which would give people time to formulate a question and try it out on a colleague". This recommendation

is analogous to the "think-pair-share" format often used in K-12 and university classrooms to improve cognitive engagement.[179–182] By chance, I attended a conference in which the organizers implemented this "think-pair-share" approach to the seminar Q&A format, creating an opportunity to assess this recommendation.

This project shows that the Q&A inequity identified by prior researchers extrapolates to the chemistry community. Women were underrepresented in both traditional Q&A sessions and think-pair-share Q&A sessions, with the latter exhibiting greater disparity. These findings reinforce that we must make a more concerted effort to bring about gender equity in academic seminars and in academia more broadly.

7.2 Methods

Seminar participation was observed in departmental seminars at my home institution and in regional and national conferences, between 2018 and 2022. These seminars were observed opportunistically, representing a subsection of seminars skewed towards the author's interests in materials, ceramics, and inorganic chemistry. At each seminar, the number of men and women in the audience were tallied, as well as the number of questions asked by men and the number of questions asked by women. This tallying was done discretely. Virtual and hybrid talks were not included. Seminars with too large of an audience to reliably count while seated amongst the audience were not included either (maximum audience size = 58 people). These data are used to calculate two key numbers: i) the fraction of women in the audience and ii) the fraction of questions asked by women. By chance, one of these conferences implemented a "think-pair-share" approach to the seminar Q&A format, creating a natural experiment that serves as the basis for comparison.

I acknowledge that this study relies on the assumption of each audience member's gender identity, which is inherently flawed in several ways. First, as I only included audience members under the men/women binary, I over-simplify the gender spectrum and exclude non-binary individuals from this study. I acknowledge the dark irony of excluding people

in this attempt to move towards a more inclusive scientific community. Second, I may mis-gender people accidentally. To the best of my ability, I attempted to tally people in accordance with their expressed gender pronouns (i.e., she= woman, he = man, neither = not included in the tally), but this approach is limited to personal networking. In many cases, I had to rely on my assumptions based on how individuals look and sound.

The Colorado State University Institutional Review Board classified this project as "exempt" under 45CFR46.104(d)(2).

7.3 Results and Discussion

Figure 7.1 shows that both seminar Q&A types (traditional and think-pair-share) are skewed towards an over-representation of men and an underrepresentation of women. This finding confirms that past research in other disciplines extrapolates to chemistry subfields (materials, inorganic, ceramics). On average, 13.4 ± 3.3 % fewer questions came from women in traditional Q&A sessions than would be expected given their share of each audience (the negative imbalance in Figure 7.1c, n = 55), but the imbalance grew to 24.3 ± 9.7 % fewer questions in the think-pair-share sessions (Figure 7.1d, n = 8). Incidentally, one can also note that the audiences of these seminars were on average 31% women, highlighting the current degree of underrepresentation in these communities. Although the dataset is limited, these data indicate that the think-pair-share approach to seminar Q&A sessions led to a worse degree of underrepresentation for women (Figure 1b and 1d) compared to the traditional Q&A format (Figure 7.1a, c). This worse imbalance during think-pair-share Q&A sessions is likely related to the fact that such sessions were shorter than traditional sessions (averaging 5.5 and 5.9 questions per session, respectively). I evaluated the gender imbalance as a function of number of questions asked, and found no significant difference in the imbalance between traditional and think-pair-share sessions when controlling for the number of questions asked (Figure 7.2) All else equal, dedicating time for the think-pair part of the process involved reducing time for the public Q&A, and

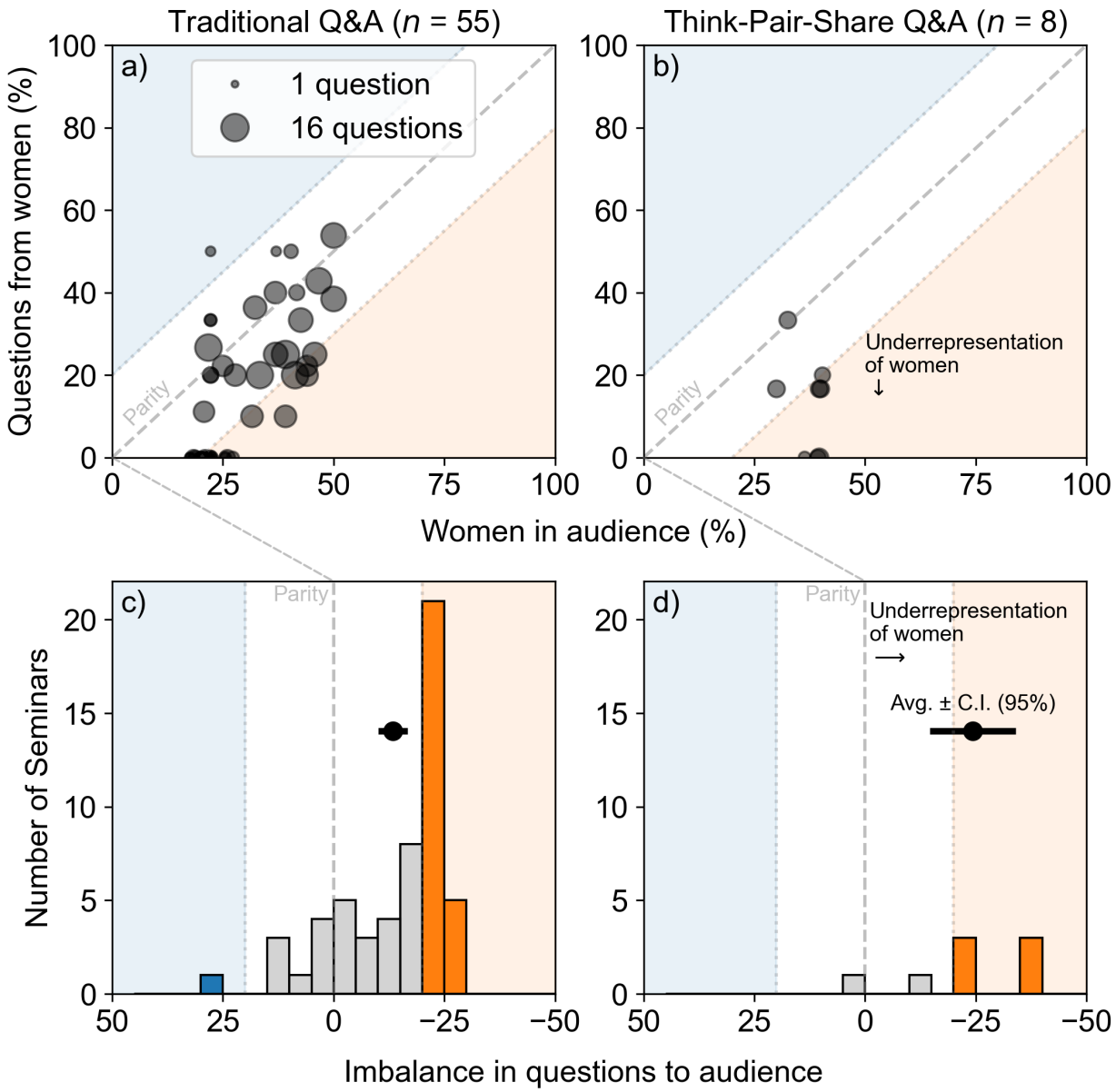

Figure 7.1: A comparison of the percentage of women in the audience (horizontal axis) to the percentage of questions publicly asked by women for a) seminars with traditional Q&A sessions compared to those with b) think-pair-share Q&A sessions. The diagonal dashed line shows where those two quantities would be equal (gender parity). The marker size corresponds to the number of questions asked in the session. The imbalance between the number of questions asked by women minus the number of women in the audience is shown in c) for traditional Q&As and in d) for think-pair-share Q&As. Negative imbalance values indicate women are underrepresented. The black marker shows the mean imbalance with error bars showing the confidence interval at the 95% level.

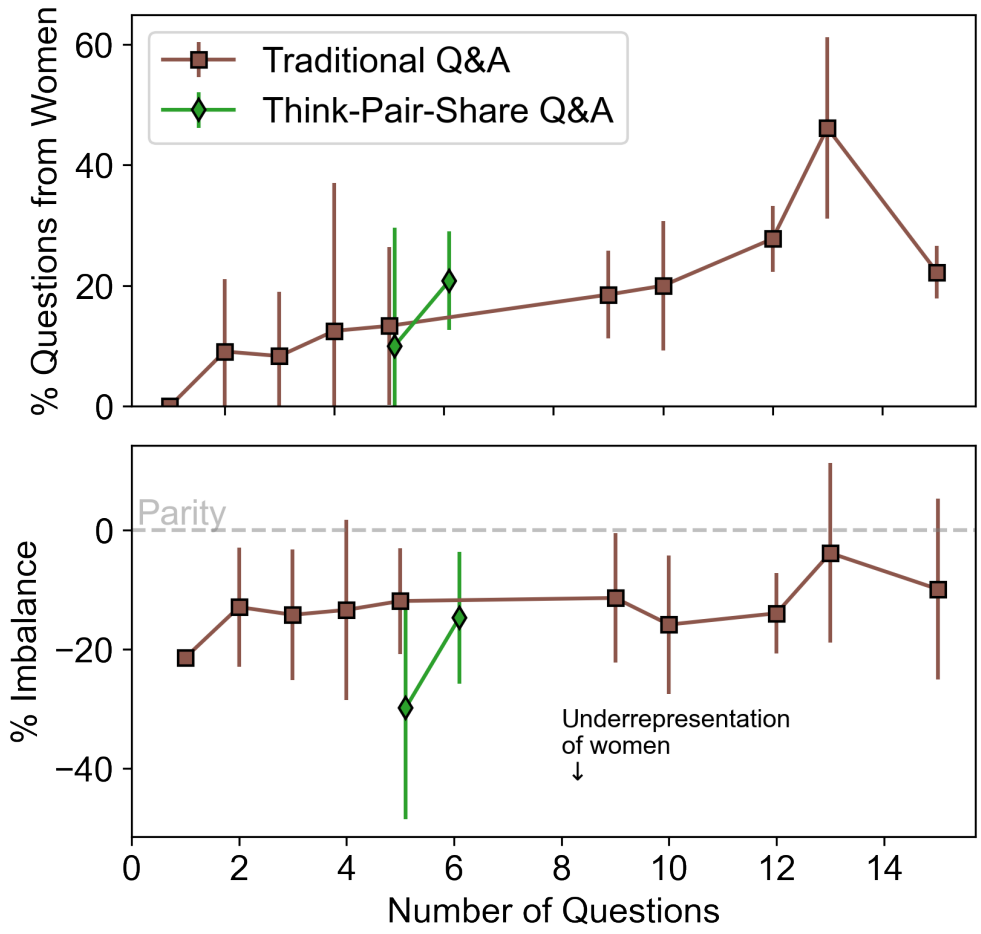

Figure 7.2: The proportion of questions from women increases with an increasing number of questions asked in a session (top), consistent with literature.[172] However, the gender imbalance of these Q&A sessions persists irrespective of the total number of questions asked (bottom). Points are only shown if more than one seminar elicited that number of questions. Error bars show a confidence interval calculated at the 95% level. Traces are offset slightly along the horizontal axis for clarity.

Schmidt, et al. noted that sessions with fewer questions tended to have less participation by women.[172] Additionally, a recent review of classroom interactions of the think-pair-share approach indicate that inequities persist there as well.[182] This does not mean that the think-pair-share sessions were necessarily without benefit, but they do not appear to accomplish the hypothesized goal of improving gender equity during these Q&As.

Where does this leave us in our mission to make academic seminars more equitable? As Telis, et al. noted, the simple act of recognizing and engaging with these data has

the potential to reduce inequity.[176] They collected data through a multi-day conference, presented their findings of inequity part-way through, and found that subsequent sessions had more equitable Q&A sessions. However, full equity was not achieved. Therefore, some argue that Q&A sessions should be scraped entirely. To quote, Cooper, et al., "While [Q&A] sessions may seem inextricably linked to the culture of science,... this aspect of the culture of science is deeply exclusionary, an impediment to diversifying science, and is likely undercutting our attempts to solve complex problems in the natural world."[182]

Networking and small group discussion may be a better use of time than public Q&A sessions. Mathematician Eugenia Cheng noted this Q&A inequity in her book "X+Y: a Mathematicians Manifesto for Rethinking Gender" and solved them by replacing her post-seminar Q&A sessions with small group discussions amongst the audience.[183] As audience members converse with one another, and she circulates through the room to hear what topics sparked interest or confusion. After a few minutes, she would return to the lectern and address those key points further. In addition to prioritizing questions that multiple people may have, the audience members get more time to engage with one another, increasing cognitive engagement with the content and strengthening networks between audience members. Those networks may have more positive impacts on people's careers than the visibility that comes from publicly asking a question in a traditional Q&A, as networking is particularly beneficial for the professional advancement of women.[184] As recent research has shown that gains in the representation of women among academic faculty are stalling,[185] we must consider bold choices to bring about a more equitable academic culture.

7.4 Conclusions and Outlook

The preliminary evidence presented here suggests that think-pair-share Q&A sessions are not effective at improving gender equity. Academics who aspire to foster more inclusive communities should therefore seek other strategies, which may include replacing the Q&A

session entirely with a more effective use of time. All deeply rooted academic traditions are worth re-examining in the quest to foster equitable and inclusive scientific communities.

Bibliography

[1] Greenaway, A. L.; Melamed, C. L.; Tellekamp, M. B.; Woods-Robinson, R.; Toberer, E. S.; Neilson, J. R.; Tamboli, A. C. *Annual Review of Materials Research* **2021**, *51*, 591–618.

[2] Sun, W.; Bartel, C. J.; Arca, E.; Bauers, S. R.; Matthews, B.; Orvañanos, B.; Chen, B.-R.; Toney, M. F.; Schelhas, L. T.; Tumas, W.; Tate, J.; Zakutayev, A.; Lany, S.; Holder, A. M.; Ceder, G. *Nature Materials* **2019**, *18*, 732–739.

[3] Amano, H. *Reviews of Modern Physics* **2015**, *87*, 1133–1138.

[4] Gharavi, M. A.; Armiento, R.; Alling, B.; Eklund, P. *Journal of materials science* **2018**, *53*, 4294–4305.

[5] Hinuma, Y.; Hatakeyama, T.; Kumagai, Y.; Burton, L. A.; Sato, H.; Muraba, Y.; Iimura, S.; Hiramatsu, H.; Tanaka, I.; Hosono, H., et al. *Nature communications* **2016**, *7*, 1–10.

[6] Sarmiento-Perez, R.; Cerqueira, T. F.; Körbel, S.; Botti, S.; Marques, M. A. *Chemistry of Materials* **2015**, *27*, 5957–5963.

[7] Ching, W.; Mo, S.-D.; Tanaka, I.; Yoshiya, M. *Physical Review B* **2001**, *63*, 064102.

[8] Sun, W.; Dacek, S. T.; Ong, S. P.; Hautier, G.; Jain, A.; Richards, W. D.; Gamst, A. C.; Persson, K. A.; Ceder, G. *Science advances* **2016**, *2*, e1600225.

[9] Jain, A.; Ong, S. P.; Hautier, G.; Chen, W.; Richards, W. D.; Dacek, S.; Cholia, S.; Gunter, D.; Skinner, D.; Ceder, G., et al. *APL materials* **2013**, *1*, 011002.

[10] Sun, W.; Bartel, C.; Arca, E.; Bauers, S.; Matthews, B.; Orvañanos, B.; Chen, B.-R.; Toney, M. F.; Schelhas, L. T.; Tumas, W., et al. *arXiv preprint arXiv:1809.09202* **2018**,

[11] Bauers, S. R.; Holder, A.; Sun, W.; Melamed, C. L.; Woods-Robinson, R.; Mangum, J.; Perkins, J.; Tumas, W.; Gorman, B.; Tamboli, A., et al. *Proceedings of the National Academy of Sciences* **2019**, *116*, 14829–14834.

[12] Heinselman, K. N.; Lany, S.; Perkins, J. D.; Talley, K. R.; Zakutayev, A. *Chemistry of Materials* **2019**, *31*, 8717–8724.

[13] Greenaway, A. L.; Loutris, A. L.; Heinselman, K. N.; Melamed, C. L.; Schnepf, R. R.; Tellekamp, M. B.; Woods-Robinson, R.; Sherbondy, R.; Bardgett, D.; Bauers, S., et al. *Journal of the American Chemical Society* **2020**, *142*, 8421–8430.

[14] Greenaway, A. L.; Ke, S.; Culman, T.; Talley, K. R.; Mangum, J. S.; Heinselman, K. N.; Kingsbury, R. S.; Smaha, R. W.; Gish, M. K.; Miller, E. M., et al. *Journal of the American Chemical Society* **2022**, *144*, 13673–13687.

[15] Zhuk, S.; Kistanov, A. A.; Boehme, S. C.; Ott, N.; La Mattina, F.; Stiefel, M.; Kovalenko, M. V.; Siol, S. *Chemistry of Materials* **2021**, *33*, 9306–9316.

[16] Arca, E.; Perkins, J. D.; Lany, S.; Mis, A.; Chen, B.-R.; Dippo, P.; Partridge, J. L.; Sun, W.; Holder, A.; Tamboli, A. C., et al. *Materials Horizons* **2019**, *6*, 1669–1674.

[17] Zakutayev, A. *Journal of Physics: Condensed Matter* **2021**, *33*, 354003.

[18] Arca, E.; Lany, S.; Perkins, J. D.; Bartel, C.; Mangum, J.; Sun, W.; Holder, A.; Ceder, G.; Gorman, B.; Teeter, G., et al. *Journal of the American Chemical Society* **2018**, *140*, 4293–4301.

[19] Talley, K. R.; Perkins, C. L.; Diercks, D. R.; Brennecka, G. L.; Zakutayev, A. *Science* **2021**, *374*, 1488–1491.

[20] Sherbondy, R.; Smaha, R. W.; Bartel, C. J.; Holtz, M. E.; Talley, K. R.; Levy-Wendt, B.; Perkins, C. L.; Eley, S.; Zakutayev, A.; Brennecka, G. L. *Chemistry of Materials* **2022**, *34*, 6883–6893.

[21] Caskey, C. M.; Richards, R. M.; Ginley, D. S.; Zakutayev, A. *Materials Horizons* **2014**, *1*, 424–430.

[22] Caskey, C. M.; Seabold, J. A.; Stevanović, V.; Ma, M.; Smith, W. A.; Ginley, D. S.; Neale, N. R.; Richards, R. M.; Lany, S.; Zakutayev, A. *Journal of Materials Chemistry C* **2015**, *3*, 1389–1396.

[23] Sun, W.; Holder, A.; Orvañanos, B.; Arca, E.; Zakutayev, A.; Lany, S.; Ceder, G. *Chemistry of Materials* **2017**, *29*, 6936–6946.

[24] Pierson, H. O. *Handbook of refractory carbides & nitrides: properties, characteristics, processing and applications*; William Andrew, 1996.

[25] Niewa, R.; Jacobs, H. *Chemical reviews* **1996**, *96*, 2053–2062.

[26] Niewa, R.; DiSalvo, F. *Chemistry of materials* **1998**, *10*, 2733–2752.

[27] DiSalvo, F. J.; Clarke, S. J. *Current Opinion in Solid State and Materials Science* **1996**, *1*, 241–249.

[28] Gregory, D. H. *Journal of the Chemical Society, Dalton Transactions* **1999**, 259–270.

[29] Tareen, A. K.; Priyanga, G. S.; Behara, S.; Thomas, T.; Yang, M. *Progress in Solid State Chemistry* **2019**, *53*, 1–26.

[30] Vennos, D. A. *An investigation of new nitrides: Synthesis, structure, and properties*; Cornell University, 1992.

[31] Elder, S.; DiSalvo, F.; Topor, L.; Navrotsky, A. *Chemistry of materials* **1993**, *5*, 1545–1553.

[32] Trócoli, R.; Frontera, C.; Oró-Solé, J.; Ritter, C.; Alemany, P.; Canadell, E.; Palacín, M. R.; Fontcuberta, J.; Fuertes, A. *Chemistry of Materials* **2022**, *34*, 6098–6107.

[33] Marchand, R.; Tessier, F.; DiSalvo, F. J. *Journal of Materials Chemistry* **1999**, *9*, 297–304.

[34] Blanton, E. W.; He, K.; Shan, J.; Kash, K. *Journal of Crystal Growth* **2017**, *461*, 38–45.

[35] Quayle, P. C.; Blanton, E. W.; Punya, A.; Junno, G. T.; He, K.; Han, L.; Zhao, H.; Shan, J.; Lambrecht, W. R.; Kash, K. *Physical Review B* **2015**, *91*, 205207.

[36] Yamane, H.; DiSalvo, F. J. *Progress in Solid State Chemistry* **2018**, *51*, 27–40.

[37] Richter, T. M.; Niewa, R. *Inorganics* **2014**, *2*, 29–78.

[38] Häusler, J.; Niklaus, R.; Minár, J.; Schnick, W. *Chemistry–A European Journal* **2018**, *24*, 1686–1693.

[39] Verrelli, R.; Arroyo-de Dompablo, M. E.; Tchitchekova, D.; Black, A.; Frontera, C.; Fuertes, A.; Palacin, M. R. *Physical Chemistry Chemical Physics* **2017**, *19*, 26435–26441.

[40] Verrelli, R.; Black, A. P.; Frontera, C.; Oró-Solé, J.; Arroyo-de Dompablo, M. E.; Fuertes, A.; Palacín, M. R. *ACS Omega* **2019**, *4*, 8943–8952.

[41] Martinolich, A. J.; Neilson, J. R. *Chemistry of Materials* **2017**, *29*, 479–489.

[42] Todd, P. K.; Smith, A. M. M.; Neilson, J. R. *Inorganic Chemistry* **2019**, *58*, 15166–15174.

[43] Todd, P. K.; Neilson, J. R. *Journal of the American Chemical Society* **2019**, *141*, 1191–1195.

[44] Rognerud, E. G.; Rom, C. L.; Todd, P. K.; Singstock, N. R.; Bartel, C. J.; Holder, A. M.; Neilson, J. R. *Chemistry of Materials* **2019**, *31*, 7248–7254.

[45] Wustrow, A.; Huang, G.; McDermott, M. J.; O'Nolan, D.; Liu, C.-H.; Tran, G. T.; McBride, B. C.; Dwaraknath, S. S.; Chapman, K. W.; Billinge, S. J., et al. *Chemistry of Materials* **2021**, *33*, 3692–3701.

[46] Wustrow, A.; McDermott, M. J.; O'Nolan, D.; Liu, C.-H.; Tran, G. T.; McBride, B. C.; Vornholt, S. M.; Feng, C.; Dwaraknath, S. S.; Chapman, K. W., et al. *Chemistry of Materials* **2022**,

[47] Kawamura, F.; Imura, M.; Murata, H.; Yamada, N.; Taniguchi, T. *European Journal of Inorganic Chemistry* **2020**, *2020*, 446–451.

[48] Kawamura, F.; Murata, H.; Imura, M.; Yamada, N.; Taniguchi, T. *Inorganic Chemistry* **2021**, *60*, 1773–1779.

[49] Bauers, S. R.; Hamann, D. M.; Patterson, A.; Perkins, J. D.; Talley, K. R.; Zakutayev, A. *Japanese Journal of Applied Physics* **2019**, *58*, SC1015.

[50] Matsuishi, S.; Iwasaki, D.; Hosono, H. *Journal of Solid State Chemistry* **2022**, *315*, 123508.

[51] Martinez, A. D.; Fioretti, A. N.; Toberer, E. S.; Tamboli, A. C. *Journal of Materials Chemistry A* **2017**, *5*, 11418–11435.

[52] Zakutayev, A.; Bauers, S. R.; Lany, S. *Chemistry of Materials* **2022**, *34*, 1418–1438.

[53] Woods-Robinson, R.; Stevanović, V.; Lany, S.; Heinselman, K. N.; Horton, M. K.; Persson, K. A.; Zakutayev, A. *Physical Review Materials* **2022**, *6*, 043804.

[54] Li, X.; Wang, X.; Han, Y.; Jing, X.; Huang, Q.; Kuang, X.; Gao, Q.; Chen, J.; Xing, X. *Chemistry of Materials* **2017**, *29*, 1989–1993.

[55] Rom, C. L.; Fallon, M. J.; Wustrow, A.; Prieto, A. L.; Neilson, J. R. *Chemistry of Materials* **2021**, *33*, 5345–5354.

[56] Wolf, S.; Awschalom, D.; Buhrman, R.; Daughton, J.; von Molnár, v. S.; Roukes, M.; Chtchelkanova, A. Y.; Treger, D. *Science* **2001**, *294*, 1488–1495.

[57] Baltz, V.; Manchon, A.; Tsoi, M.; Moriyama, T.; Ono, T.; Tserkovnyak, Y. *Reviews of Modern Physics* **2018**, *90*, 015005.

[58] Esmaeilzadeh, S.; Hålenius, U.; Valldor, M. *Chemistry of Materials* **2006**, *18*, 2713–2718.

[59] Wintenberger, M.; Guyader, J.; Maunaye, M. *Solid State Communications* **1972**, *11*, 1485–1488.

[60] Liu, Y.; Lazarov, V.; Cheung, S.; Keavney, D.; Gai, Z.; Gajdardziska-Josifovska, M.; Weinert, M.; Li, L. *Physical Review B* **2012**, *85*, 144113.

[61] Kresse, G.; Joubert, D. *Physical Review B* **1999**, *59*, 1758.

[62] Shishkin, M.; Kresse, G. *Physical Review B* **2006**, *74*, 035101.

[63] Hedin, L. *Physical Review* **1965**, *139*, A796.

[64] Lany, S. *Physical Review B* **2013**, *87*, 085112.

[65] Talley, K. R.; Bauers, S. R.; Melamed, C. L.; Papac, M. C.; Heinselman, K. N.; Khan, I.; Roberts, D. M.; Jacobson, V.; Mis, A.; Brennecka, G. L., et al. *ACS combinatorial science* **2019**, *21*, 537–547.

[66] Zakutayev, A.; Wunder, N.; Schwarting, M.; Perkins, J. D.; White, R.; Munch, K.; Tumas, W.; Phillips, C. *Scientific data* **2018**, *5*, 1–12.

[67] Toby, B. H.; Von Dreele, R. B. *Journal of Applied Crystallography* **2013**, *46*, 544–549.

[68] Coelho, A. A. *Journal of Applied Crystallography* **2018**, *51*, 210–218.

[69] Momma, K.; Izumi, F. *Journal of applied crystallography* **2011**, *44*, 1272–1276.

[70] Schulz, H.; Thiemann, K. *Solid State Communications* **1977**, *23*, 815–819.

[71] Barradas, N.; Arstila, K.; Battistig, G.; Bianconi, M.; Dytlewski, N.; Jeynes, C.; Kótai, E.; Lulli, G.; Mayer, M.; Rauhala, E., et al. *Nuclear Instruments and Methods in Physics Research Section B: Beam Interactions with Materials and Atoms* **2008**, *266*, 1338–1342.

[72] Smits, F. *Bell System Technical Journal* **1958**, *37*, 711–718.

[73] Caskey, C. M.; Holder, A.; Shulda, S.; Christensen, S. T.; Diercks, D.; Schwartz, C. P.; Biagioni, D.; Nordlund, D.; Kukliansky, A.; Natan, A., et al. *The Journal of chemical physics* **2016**, *144*, 144201.

[74] Peng, H.; Ndione, P. F.; Ginley, D. S.; Zakutayev, A.; Lany, S. *Physical Review X* **2015**, *5*, 021016.

[75] Hautier, G.; Miglio, A.; Waroquiers, D.; Rignanese, G.-M.; Gonze, X. *Chemistry of Materials* **2014**, *26*, 5447–5458.

[76] Fioretti, A. N.; Zakutayev, A.; Moutinho, H.; Melamed, C.; Perkins, J. D.; Norman, A. G.; Al-Jassim, M.; Toberer, E. S.; Tamboli, A. C. *Journal of Materials Chemistry C* **2015**, *3*, 11017–11028.

[77] Schnepf, R. R.; Cordell, J. J.; Tellekamp, M. B.; Melamed, C. L.; Greenaway, A. L.; Mis, A.; Brennecka, G. L.; Christensen, S.; Tucker, G. J.; Toberer, E. S., et al. *ACS Energy Letters* **2020**, *5*, 2027–2041.

[78] Melamed, C. L.; Pan, J.; Mis, A.; Heinselman, K.; Schnepf, R. R.; Woods-Robinson, R.; Cordell, J. J.; Lany, S.; Toberer, E. S.; Tamboli, A. C. *Journal of Materials Chemistry C* **2020**, *8*, 8736–8746.

[79] Khan, I. S.; Heinselman, K. N.; Zakutayev, A. *Journal of Physics: Energy* **2020**, *2*, 032007.

[80] Shannon, R. T.; Prewitt, C. T. *Acta Crystallographica Section B: Structural Crystallography and Crystal Chemistry* **1969**, *25*, 925–946.

[81] Melamed, C. L.; Miller, M. K.; Cordell, J.; Pucurimay, L.; Livingood, A.; Schnepf, R. R.; Pan, J.; Heinselman, K. N.; Vila, F. D.; Mis, A., et al. *Chemistry of Materials* **2022**, *34*, 3910—3919.

[82] Nardin, M.; Lorthioir, G.; Barberon, M.; Madar, R.; Fruchart, E.; Fruchart, R. *Comptes Rendus Hebdomadaires des Seances des Sciences, Serie C, Sciences Chimiques* **1972**, *274*, 2168–2171.

[83] Mekata, M. *Journal of the Physical Society of Japan* **1962**, *17*, 796–803.

[84] Fay, S.; Kroll, U.; Bucher, C.; Vallat-Sauvain, E.; Shah, A. *Solar Energy Materials and Solar Cells* **2005**, *86*, 385–397.

[85] Heikens, H.; Kuindersma, R.; Van Bruggen, C.; Haas, C. *Journal of Magnetism and Magnetic Materials* **1978**, *8*, 130–141.

[86] Grochulski, T.; Leibler, K.; Sienkiewicz, A.; Gałazka, R. *physica status solidi (b)* **1979**, *91*, K73–K76.

[87] Takei, W.; Heikes, R.; Shirane, G. *Physical Review* **1962**, *125*, 1893.

[88] Tabuchi, M.; Takahashi, M.; Kanamaru, F. *Journal of alloys and compounds* **1994**, *210*, 143–148.

[89] Shull, C. G.; Strauser, W.; Wollan, E. *Physical Review* **1951**, *83*, 333.

[90] Mugiraneza, S.; Hallas, A. M. *Communications Physics* **2022**, *5*, 1–12.

[91] van der Marck, S. C. *Physical Review E* **1997**, *55*, 6593.

[92] Ramirez, A. P. *Annu. Rev. Mater. Sci.* **1994**, *24*, 453–480.

[93] Ney, V.; Henne, B.; Lumetzberger, J.; Wilhelm, F.; Ollefs, K.; Rogalev, A.; Kovacs, A.; Kieschnick, M.; Ney, A. *Phys. Rev. B* **2016**, *94*, 224405.

[94] Simonov, A.; Goodwin, A. *Nat. Rev. Chem.* **2020**, *4*, 657–673.

[95] Kawamura, F.; Yamada, N.; Imai, M.; Taniguchi, T. *Crystal Research and Technology* **2016**, *51*, 220–224.

[96] Lany, S.; Fioretti, A. N.; Zawadzki, P. P.; Schelhas, L. T.; Toberer, E. S.; Zakutayev, A.; Tamboli, A. C. *Physical Review Materials* **2017**, *1*, 035401.

[97] Fetzer, C.; Lee, R.; Stringfellow, G.; Liu, X.; Sasaki, A.; Ohno, N. *Journal of applied physics* **2002**, *91*, 199–203.

[98] Jain, A.; Hautier, G.; Ong, S. P.; Moore, C. J.; Fischer, C. C.; Persson, K. A.; Ceder, G. *Physical Review B* **2011**, *84*, 045115.

[99] Mathew, K.; Montoya, J. H.; Faghaninia, A.; Dwarakanath, S.; Aykol, M.; Tang, H.; Chu, I.-h.; Smidt, T.; Bocklund, B.; Horton, M., et al. *Computational Materials Science* **2017**, *139*, 140–152.

[100] Jain, A.; Ong, S. P.; Chen, W.; Medasani, B.; Qu, X.; Kocher, M.; Brafman, M.; Petretto, G.; Rignanese, G.-M.; Hautier, G., et al. *Concurrency and Computation: Practice and Experience* **2015**, *27*, 5037–5059.

[101] Ong, S. P.; Richards, W. D.; Jain, A.; Hautier, G.; Kocher, M.; Cholia, S.; Gunter, D.; Chevrier, V. L.; Persson, K. A.; Ceder, G. *Computational Materials Science* **2013**, *68*, 314–319.

[102] Limpijumnong, S.; Lambrecht, W. R. *Physical Review B* **2001**, *63*, 104103.

[103] Fichtner, S.; Wolff, N.; Lofink, F.; Kienle, L.; Wagner, B. *Journal of Applied Physics* **2019**, *125*, 114103.

[104] Schmidt, R.; Ströbele, M.; Eichele, K.; Meyer, H.-J. *European Journal of Inorganic Chemistry* **2017**, *2017*, 2727–2735.

[105] Todd, P. K.; Fallon, M. J.; Neilson, J. R.; Zakutayev, A. *ACS Materials Letters* **2021**, *3*, 1677–1683.

[106] Dinnebier, R. E.; Leineweber, A.; Evans, J. S. *Rietveld Refinement*; de Gruyter, 2018.

[107] Toth, L. E. *Transition Metal Carbides and Nitrides*; Refractory Materials; Academic Press: New York, 1971; Vol. 7.

[108] Kuykendall, T.; Ulrich, P.; Aloni, S.; Yang, P. *Nature Materials* **2007**, *6*, 951–956.

[109] Fu, G.; Cui, Z.; Chen, Y.; Xu, L.; Tang, Y.; Goodenough, J. B. *Nano Energy* **2017**, *39*, 77–85.

[110] Kreider, M. E.; Gallo, A.; Back, S.; Liu, Y.; Siahrostami, S.; Nordlund, D.; Sinclair, R.; Nørskov, J. K.; King, L. A.; Jaramillo, T. F. *ACS Applied Materials & Interfaces* **2019**, *11*, 26863–26871.

[111] Gregory, D. H.; Barker, M. G.; Edwards, P. P.; Slaski, M.; Siddons, D. J. *Journal of Solid State Chemistry* **1998**, *137*, 62–70.

[112] Bhat, S.; Lale, A.; Bernard, S.; Zhang, W.; Ishikawa, R.; Haseen, S.; Kroll, P.; Wiehl, L.; Farla, R.; Katsura, T.; Ikuhara, Y.; Riedel, R. *Scientific Reports* **2020**, *10*, 7372.

[113] Odahara, J.; Sun, W.; Miura, A.; Rosero-Navarro, N. C.; Nagao, M.; Tanaka, I.; Ceder, G.; Tadanaga, K. *ACS Materials Letters* **2019**, *1*, 64–70.

[114] Bauers, S. R.; Mangum, J.; Harvey, S. P.; Perkins, J. D.; Gorman, B.; Zakutayev, A. *Applied Physics Letters* **2020**, *116*, 102102.

[115] Kim, J.; R. Bauers, S.; S. Khan, I.; Perkins, J.; Park, B.-I.; R. Talley, K.; Kim, D.; Zakutayev, A.; Shin, B. *Journal of Materials Chemistry A* **2020**, *8*, 9364–9372.

[116] Li, Y.; George, J.; Liu, X.; Dronskowski, R. *Zeitschrift fur anorganische und allgemeine Chemie* **2015**, *641*, 266–269.

[117] Williams, D. B. G.; Lawton, M. *The Journal of organic chemistry* **2010**, *75*, 8351–8354.

[118] Wang, J.; Toby, B. H.; Lee, P. L.; Ribaud, L.; Antao, S. M.; Kurtz, C.; Ramanathan, M.; Von Dreele, R. B.; Beno, M. A. *Review of Scientific Instruments* **2008**, *79*, 085105.

[119] Bartel, C. J.; Millican, S. L.; Deml, A. M.; Rumptz, J. R.; Tumas, W.; Weimer, A. W.; Lany, S.; Stevanović, V.; Musgrave, C. B.; Holder, A. M. *Nature Communications* **2018**, *9*, 4168.

[120] Bale, C. W. et al. *Calphad* **2016**, *54*, 35–53.

[121] Karaballi, R. A.; Humagain, G.; Fleischman, B. R. A.; Dasog, M. *Angewandte Chemie International Edition* **2019**, *58*, 3147–3150.

[122] Hector, A. L.; Parkin, I. P. *Chemistry of Materials* **1995**, *7*, 1728–1733.

[123] Aguas, M. D.; Nartowski, A. M.; Parkin, I. P.; MacKenzie, M.; Craven, A. J. *Journal of Materials Chemistry* **1998**, *8*, 1875–1880.

[124] Miura, A.; Bartel, C. J.; Goto, Y.; Mizuguchi, Y.; Moriyoshi, C.; Kuroiwa, Y.; Wang, Y.; Yaguchi, T.; Shirai, M.; Nagao, M., et al. *Advanced Materials* **2021**, 2100312.

[125] Bianchini, M.; Wang, J.; Clément, R. J.; Ouyang, B.; Xiao, P.; Kitchaev, D.; Shi, T.; Zhang, Y.; Wang, Y.; Kim, H.; Zhang, M.; Bai, J.; Wang, F.; Sun, W.; Ceder, G. *Nature Materials* **2020**, *19*, 1088–1095.

[126] Takeyama, M. B.; Noya, A.; Sakanishi, K. *Journal of Vacuum Science & Technology B: Microelectronics and Nanometer Structures Processing, Measurement, and Phenomena* **2000**, *18*, 1333–1337.

[127] Miura, A.; Ito, H.; Bartel, C.; Sun, W.; Rosero-Navarro, N. C.; Tadanaga, K.; Nakata, H.; Maeda, K.; Ceder, G. **2019**, *7*, 1310–1316.

[128] Ohashi, M.; Yamanaka, S.; Sumihara, M.; Hattori, M. *Journal of Solid State Chemistry* **1988**, *75*, 99–104.

[129] Ohashi, M.; Yamanaka, S.; Hattori, M. *Journal of Solid State Chemistry* **1988**, *77*, 342–347.

[130] Christensen, A. *Acta Chemica Scandinavica* **1975**, *29a*, 563–564.

[131] Zhao, S.; Ma, J.; Xu, R.; Lin, X.; Cheng, X.; Hao, S.; Zhao, X.; Deng, C.; Liu, B. *Scientific Reports* **2019**, *9*, 19199.

[132] Balzar, D. *International union of crystallography monographs on crystallography* **1999**, *10*, 94–126.

[133] Exarhos, S.; Alvarez-Barragan, A.; Aytan, E.; Balandin, A. A.; Mangolini, L. *ACS Energy Letters* **2018**, *3*, 2349–2356.

[134] Reinholdt, A.; Detemple, R.; Stepanov, A.; Weirich, T.; Kreibig, U. *Applied Physics B: Lasers & Optics* **2003**, *77*, 681.

[135] Kelly, K. L.; Coronado, E.; Zhao, L. L.; Schatz, G. C. *The Journal of Physical Chemistry B* **2003**, *107*, 668–677.

[136] Metaxa, C.; Kassavetis, S.; Pierson, J.; Gall, D.; Patsalas, P. *ACS Applied Materials & Interfaces* **2017**, *9*, 10825–10834.

[137] Constant, K.; Kieffer, R.; Ettmayer, P. *Monatshefte für Chemie / Chemical Monthly* **1975**, *106*, 823–832.

[138] Bowman, A.; Smith, R. I.; Gregory, D. H. *Journal of Solid State Chemistry* **2005**, *178*, 1807–1817.

[139] Liu, X.; Wessel, C.; Pan, F.; Dronskowski, R. *Journal of Solid State Chemistry* **2013**, *203*, 31–36.

[140] Zakutayev, A. *Journal of Materials Chemistry A* **2016**, *4*, 6742–6754.

[141] Gregory, D.; Barker, M.; Edwards, P.; Siddons, D. *Inorganic chemistry* **1998**, *37*, 3775–3778.

[142] Gregory, D.; Barker, M.; Edwards, P.; Siddons, D. *Inorganic chemistry* **1996**, *35*, 7608–7613.

[143] Shiraishi, A.; Kimura, S.; He, X.; Watanabe, N.; Katase, T.; Ide, K.; Minohara, M.; Matsuzaki, K.; Hiramatsu, H.; Kumigashira, H., et al. *Inorganic chemistry* **2022**, *61*, 6650–6659.

[144] Shannon, R. D. *Acta crystallographica section A: crystal physics, diffraction, theoretical and general crystallography* **1976**, *32*, 751–767.

[145] Orisakwe, E.; Fontaine, B.; Gregory, D. H.; Gautier, R.; Halet, J.-F. *RSC advances* **2014**, *4*, 31981–31987.

[146] Hunting, J. L.; Szymanski, M. M.; Johnson, P. E.; Kellar, C. B.; DiSalvo, F. J. *Journal of Solid State Chemistry* **2007**, *180*, 31–40.

[147] Gregory, D. H.; Barker, M. G.; Siddons, D. J.; Edwards, P. P.; Slaski, M. *MRS Online Proceedings Library (OPL)* **1998**, *547*.

[148] Hadenfeldt, C.; Herdejürgen, H. *Zeitschrift für anorganische und allgemeine Chemie* **1987**, *545*, 177–183.

[149] Chupas, P. J.; Chapman, K. W.; Kurtz, C.; Hanson, J. C.; Lee, P. L.; Grey, C. P. *Journal of Applied Crystallography* **2008**, *41*, 822–824.

[150] Yokokawa, H. *Journal of phase equilibria* **1999**, *20*, 258–287.

[151] Todd, P. K.; McDermott, M. J.; Rom, C. L.; Corrao, A. A.; Denney, J. J.; Dwaraknath, S. S.; Khalifah, P. G.; Persson, K. A.; Neilson, J. R. *Journal of the American Chemical Society* **2021**, *143*, 15185–15194.

[152] Christensen, A. *Acta chemica scandinavica* **1990**, *44*, 851–852.

[153] Aigner, K.; Lengauer, W.; Rafaja, D.; Ettmayer, P. *Journal of alloys and compounds* **1994**, *215*, 121–126.

[154] Clarke, S.; DiSalvo, F. *Journal of Solid State Chemistry* **1997**, *129*, 144–146.

[155] Heckers, U.; Jacobs, H.; Kockelmann, W. *Zeitschrift fuer Anorganische und Allgemeine Chemie* **2003**, *629*, 2431–2432.

[156] Prots', Y.; Niewa, R.; Schnelle, W.; Kniep, R. *Zeitschrift für anorganische und allgemeine Chemie* **2002**, *628*, 1590–1596.

[157] Martinolich, A. J.; Kurzman, J. A.; Neilson, J. R. *Journal of the American Chemical Society* **2016**, *138*, 11031–11037.

[158] Gillan, E. G.; Kaner, R. B. *Chemistry of materials* **1996**, *8*, 333–343.

[159] De Maria, G.; Piacente, V. *The Journal of Chemical Thermodynamics* **1974**, *6*, 1–7.

[160] Liu, X.; Piao, X.; Wang, Y.; Zhu, S.; He, H. *Fuel* **2008**, *87*, 1076–1082.

[161] Barker, M. G.; Begley, M. J.; Edwards, P. P.; Gregory, D. H.; Smith, S. E. *Journal of the Chemical Society, Dalton Transactions* **1996**, 1–5.

[162] Ohkubo, I.; Mori, T. *Inorganic Chemistry* **2014**, *53*, 8979–8984.

[163] Chern, M. Y.; DiSalvo, F. J. *Journal of Solid State Chemistry* **1990**, *88*, 459–464.

[164] McDermott, M. J.; Dwaraknath, S. S.; Persson, K. A. *Nature communications* **2021**, *12*, 1–12.

[165] Schmalzried, H. *Chemical kinetics of solids*; John Wiley & Sons, 2008.

[166] Zunger, A.; Wei, S.-H.; Ferreira, L.; Bernard, J. E. *Physical review letters* **1990**, *65*, 353.

[167] Yuan, W.; Hu, J.; Song, Y.; Wang, W.; Xu, Y. *Powder diffraction* **2005**, *20*, 18–21.

[168] Gibson, K.; Ströbele, M.; Blaschkowski, B.; Glaser, J.; Weisser, M.; Srinivasan, R.; Kolb, H.-J.; Meyer, H.-J. *Zeitschrift für anorganische und allgemeine Chemie* **2003**, *629*, 1863–1870.

[169] Yang, Y.; Tian, T. Y.; Woodruff, T. K.; Jones, B. F.; Uzzi, B. *Proceedings of the National Academy of Sciences* **2022**, *119*, e2200841119.

[170] Nelson, D. J.; Rogers, D. C. *A national analysis of diversity in science and engineering faculties at research universities*; Citeseer, 2003.

[171] Callister, R. R. *The Journal of Technology Transfer* **2006**, *31*, 367–375.

[172] Schmidt, S. J.; Davenport, J. R. *Nature Astronomy* **2017**, *1*, 1–2.

[173] Pritchard, J.; Masters, K.; Allen, J.; Contenta, F.; Huckvale, L.; Wilkins, S.; Zocchi, A. *Astronomy & Geophysics* **2014**, *55*, 6–8.

[174] Hinsley, A.; Sutherland, W. J.; Johnston, A. *PloS one* **2017**, *12*, e0185534.

[175] Dupas, P.; Modestino, A. S.; Niederle, M.; Wolfers, J., et al. *Gender and the dynamics of economics seminars*; 2021.

[176] Telis, N.; Glassberg, E. C.; Pritchard, J. K.; Gunter, C. *The American Journal of Human Genetics* **2019**, *105*, 189–197.

[177] Käfer, J.; Betancourt, A.; Villain, A. S.; Fernandez, M.; Vignal, C.; Marais, G. A.; Tenaillon, M. I. *Genome biology and evolution* **2018**, *10*, 901–908.

[178] Carter, A. J.; Croft, A.; Lukas, D.; Sandstrom, G. M. *PloS one* **2018**, *13*, e0202743.

[179] Allen, D.; Tanner, K. *Cell Biology Education* **2002**, *1*, 3–5.

[180] Kaddoura, M. *Educational Research Quarterly* **2013**, *36*, 3–24.

[181] Tanner, K. D. *CBE—Life Sciences Education* **2013**, *12*, 322–331.

[182] Cooper, K. M.; Schinske, J. N.; Tanner, K. D. *CBE—Life Sciences Education* **2021**, *20*, fe1.

[183] Cheng, E. *X+Y: a mathematicitain's manifesto for rethinking gender.*; Basic Books: New York, 2020.

[184] Yang, Y.; Chawla, N. V.; Uzzi, B. *Proceedings of the National Academy of Sciences* **2019**, *116*, 2033–2038.

[185] Wapman, K. H.; Zhang, S.; Clauset, A.; Larremore, D. B. *Nature* **2022**, 1–8.

[186] Niewa, R.; Hu, Z.; Grazioli, C.; Rößler, U.; Golden, M.; Knupfer, M.; Fink, J.; Giefers, H.; Wortmann, G.; De Groot, F., et al. *Journal of alloys and compounds* **2002**, *346*, 129–133.

[187] Cramer, S.; DeGroot, F.; Ma, Y.; Chen, C.; Sette, F.; Kipke, C.; Eichhorn, D.; Chan, M.; Armstrong, W.; Libby, E., et al. *Journal of the American Chemical Society* **2002**, *113*, 7937–7940.

[188] Baker, T. *Acta Crystallographica* **1958**, *11*, 300–300.

[189] Lerch, M.; Lerch, J.; Hock, R.; Wrba, J. *Journal of Solid State Chemistry* **1997**, *128*, 282–288.

[190] Lerch, M.; Boysen, H.; Radaelli, P. *Journal of Physics and Chemistry of Solids* **1997**, *58*, 1557–1568.

Appendix A

Supporting Information for Chapter 2: Combinatorial synthesis of cation-disordered manganese tin nitride $MnSnN_2$ thin films with magnetic and semiconducting properties

A.1 Synthesis of $MnSnN_2$ by combinatorial sputtering

The experimental setup for the synthesis of $MnSnN_2$ films by combinatorial sputtering is shown in Figure A.1. The position of the targets relative to the stationary substrate leads to films that are Mn-rich closer to the Mn target and Sn-rich closer to the Sn target. Nitride anions incorporate throughout the film, with the chemical potential of N_2 being increased by the nitrogen cracker positioned directly beneath the substrate. This experimental setup results in nitrogen-rich films with 1-dimensional composition gradients in Mn/(Mn+Sn) ratio (Figure A.1B). For a select library, the back of the substrate was laser-scribed with 5 mm $\times$ 5 mm squares prior to deposition, such that individual samples could be easily broken out of the library for detailed electronic and magnetic measurements (Figure A.1C).

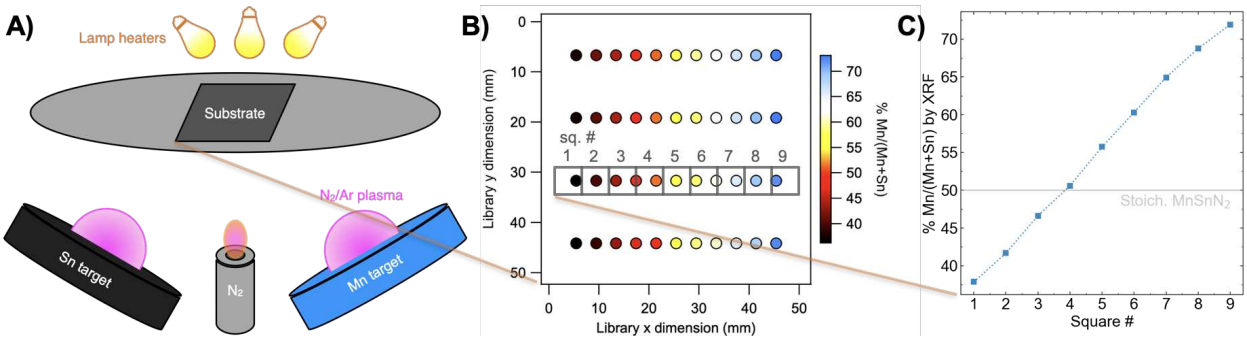

Figure A.1: A) Scheme showing the arrangement of the Mn and Sn sputtering targets positioned beneath and angled towards a substrate. B) This geometry produces a 1-dimensional compositional gradient across the substrate, which is characterized in the standard 4×11 grid used for high-throughput combinatorial experiments at NREL.[65] For more thorough electronic and magnetic characterizations, small 5 mm $\times$ 5 mm squares were broken out of a select library (grey squares). C) These were again characterized by XRF to identify the average composition of each square.

A.2 Structural characterization

Synchrotron grazing incidence wide angle X-ray scattering (GIWAXS) reveals the polycrystalline nature of the films deposited on silicon with a 100 nm surface layer of SiO_2 (Figure A.2). Hot pixels were manually masked when identified to avoid spurious peaks in the integrated patterns. Broad and weak reflection spots are visible and attributable to silicon, but these spots were not masked owing to significant overlap with the powder rings. These spots contribute to elevated background scattering in the integrated diffraction patterns. Full LeBail fits for the patterns shown in Figure 2.4 are shown in Figure A.3. Figure A.4A shows the extracted hexagonal lattice parameters and Figure A.4B show the fit residuals.

Fitting residuals were minimized for the patterns with slight excess Mn, with worsening fits in the Mn-poor and Mn-rich regions (Figure A.4B). Fit residuals also increase in the Mn-rich region, here owing to the growth of a secondary Mn_3N_2 phase that is visible as broad peaks but was not modeled. Some of this broadening may also be due to scattering from the silicon substrate, which may vary from sample to sample depending on the exact orientation of the substrate. Lastly, some degree of texturing is observed (Figure A.2), which affects the relative heights of integrated peaks.

A major finding in the thin film synthesis of $MgSnN_2$ by Greenaway, et al. was a wurtzite-to-rocksalt structural transition, and we find a small amount of evidence that a similar phenomenon occurs in the $MnSnN_2$ system (Figure A.6). In our studies of $MnSnN_2$, a single synchrotron GIWAXS pattern revealed a rocksalt type structure at Mn/(Mn+Sn) = 68%. The rocksalt appears under similar conditions needed for rocksalt $MgSnN_2$ (Sn poor, low T_{dep}). However, the refined lattice parameter for our $MnSnN_2$ rock salt ($a = 4.378$ Å) is very similar to the rocksalt lattice parameter for MnO ($a = 4.446$ Å); the ternary is 1.5% smaller than the binary. In contrast, rocksalt $MgSnN_2$ ($a = 4.483$ Å) is 6.3% larger than MgO ($a = 4.217$ Å). The presence of a rocksalt polymorph in the Mn-Sn-N system may merit further study.

Rapid thermal annealing experiments revealed that the $MnSnN_2$ phase is stable against decomposition up to at least $T_{\text{anneal}} = 300$ °C for 30 minutes (Figure A.7). At $T_{\text{anneal}} = 400$ °C, the ternary phase begins decomposing to Sn, Mn_4N, and N_2. This stability up to 300 °C suggests either i) that cation-disordered $MnSnN_2$ is more thermodynamically stable that predicted for the cation-ordered phase (+0.038 eV/atom above the hull) or ii) that decomposition up to 300 °C is kinetically slow.

To assess the limits of off stoichiometry in the hexagonal $MnSnN_2$ phase, one library was deposited with a lower power on the Mn target (54 W as opposed to the typical 108 W), leading to a Mn-poor film (Figure A.8). This Mn-poor film still exhibited wurtzite-like reflections down to approximately 18% Mn/(Mn+Sn), limited by the edge of the library rather than by a structural change. This composition nominally corresponds to $Mn_{0.36}Sn_{1.64}N_2$ (assuming a fixed anion content). For compositions with Mn/(Mn+Sn)$<$ 50%, charge balancing must occur through either Sn^{2+} substitution for Mn^{2+} or metal vacancies. Although we did not explore this Mn-poor region further, this finding suggests that Mn-poor $MnSnN_2$ could be of interest for dilute magnetic semiconductor studies.

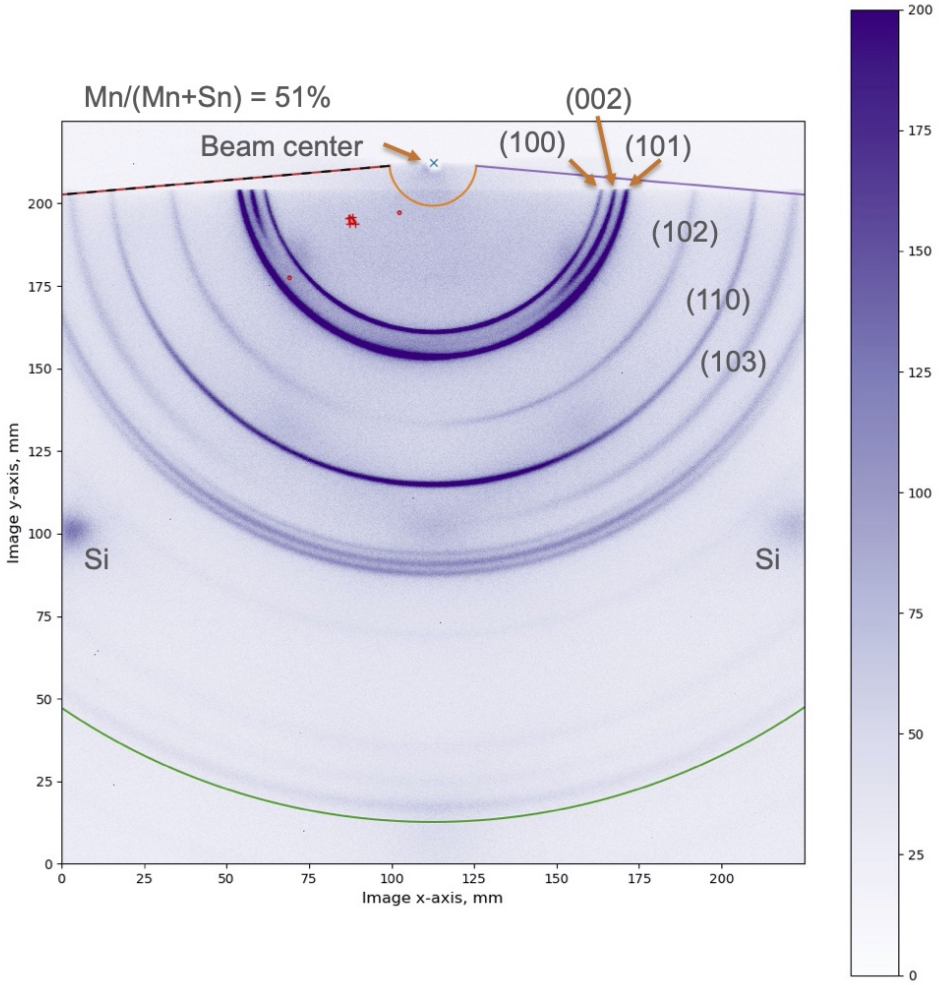

Figure A.2: A representative 2-D diffraction image from a GIWAXS measurement at SSRL beamline 11-3. Hot pixels are masked in red to avoid background contribution to the integrated diffraction pattern. The first six reflections of $MnSnN_2$ are also labeled. Strong spots from the Si substrate (331) planes are visible near the edge of the frame.

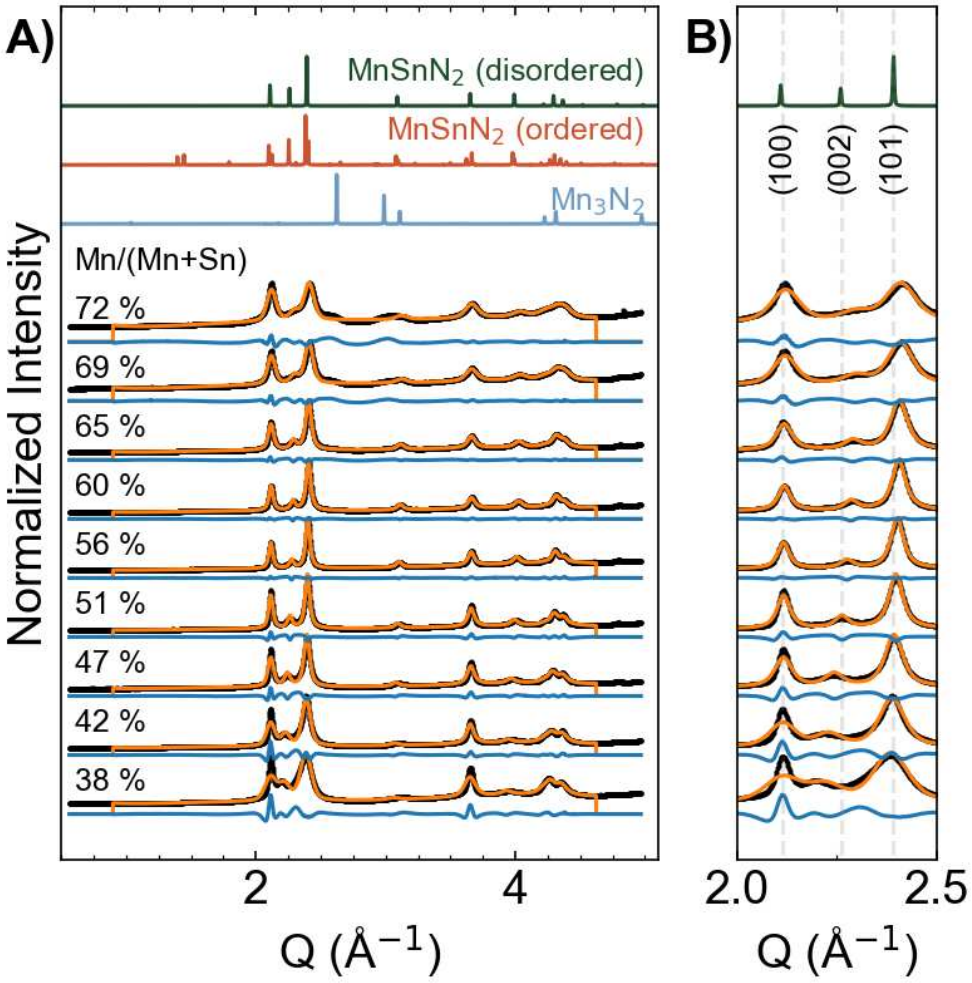

Figure A.3: A) Full patterns of the GIWAXS data presented in Figure 2.4 of the main text. VESTA-generated reference patterns are shown at the top. The main reflections match the $P6_3mc$ space group of the cation-disordered wurtzite structure type $MnSnN_2$. Evidence of cation ordering is not observed in diffraction. At Mn-rich compositions ($\geq$ 69 %), broad peaks corresponding to Mn_3N_2 appear. LeBail refinements were conducted on these patterns to extract lattice parameters of the wurtzite phase $MnSnN_2$. Black points are data, orange traces are fits, and blue traces are difference curves. B) Focused Q-range of fits to the first three wurtzite reflections, corresponding to Figure 2.4B of the main text. Although the peak broadness is poorly captured owing to anisotropic broadening, the peak positions are relatively well described by the fit.

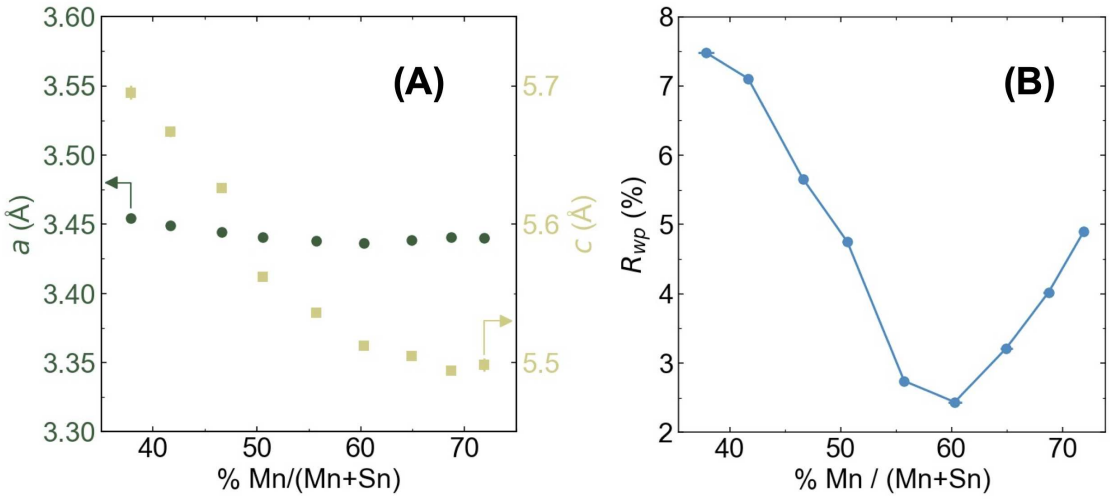

Figure A.4: A) Extracted lattice parameters a (green circles) and c (gold squares) from LeBail refinements used to calculate the c/a ratio in Figure 2.4C. Error bars are within the size of the markers. B) Residuals from the LeBail refinements presented in Figure A.3. The modeled $P6_3mc$ phase fits best with the slightly Mn-rich composition. Anisotropic peak broadening worsens the fit in the Mn-poor region. A poorly crystalline Mn_3N_2 secondary phase, which was not included in the model, worsens the fit in the Mn-rich region.

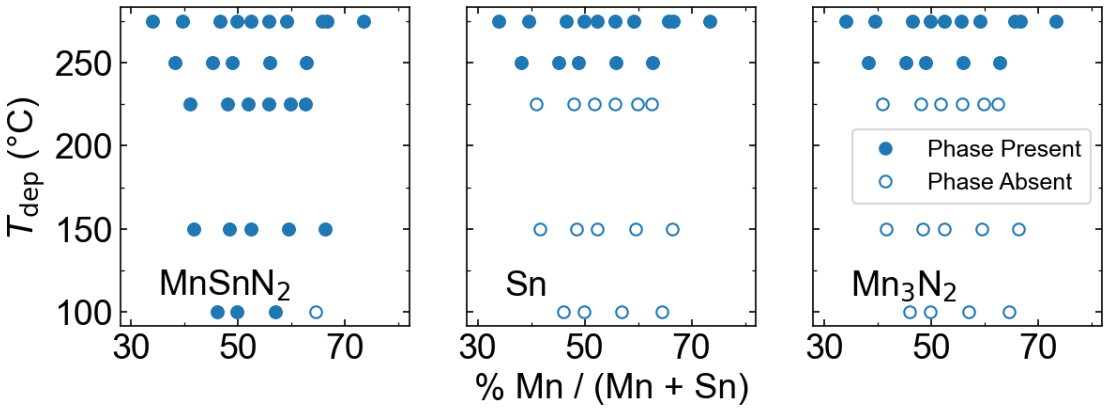

Figure A.5: GIWAXS patterns were collected on select points from a variety of libraries. Manual inspection revealed the predominance of a single phase, $MnSnN_2$ up to 225 °C. However, at higher temperatures, the $MnSnN_2$ phase begins decomposing into Mn_3N_2 and Sn. The coexistence of all three suggests non-equilibrium conditions.

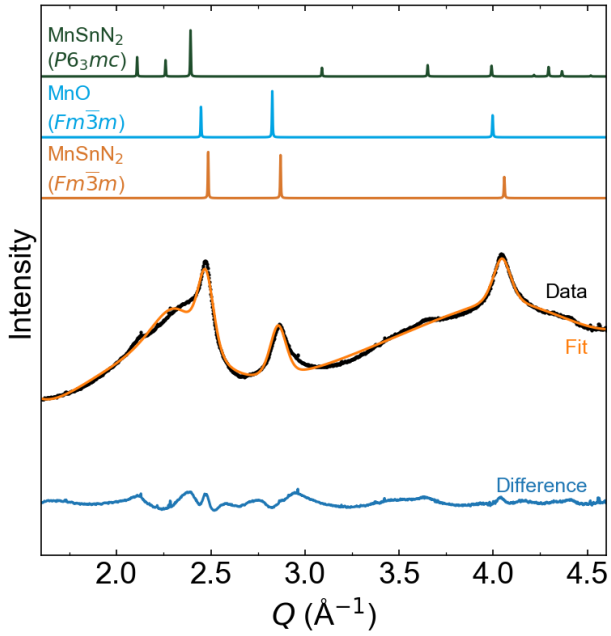

Figure A.6: GIWAXS pattern for a sample at 68% Mn/(Mn+Sn) and T_{dep} = 100 °C showing a rocksalt ($Fm\bar{3}m$) crystal structure ($a = 4.378$ Å).

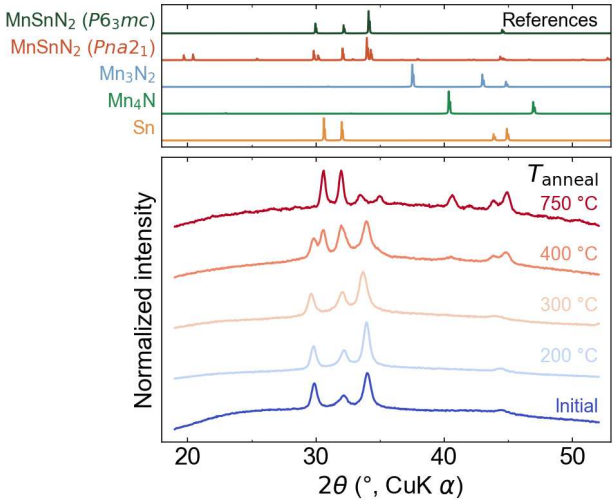

Figure A.7: Rapid thermal annealing experiments show that a library row synthesized at $T_{\text{dep}} = 225$ °C is stable up to an annealing temperature of 300 °C. Annealing experiments were conducted on individual rows from a library, first heated to 100 °C to drive off adsorbed water, then heated to the T_{anneal} temperature for a 30 min anneal. Heating ramps for each step were conducted in 1 minute, and cooling occurred by turning the power to the furnace off. The sample was enclosed in flowing N_2 for the duration of the experiment.

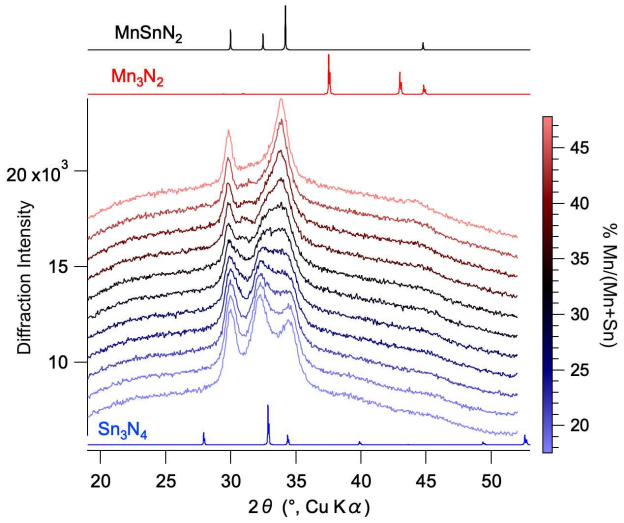

Figure A.8: A library deposited under Mn-poor conditions at $T_{\text{dep}} = 225$ °C show the continued presence of wurtzite peaks. A structural change to the spinel Sn_3N_4 is not observed, although prior sputtering syntheses of this binary phase revealed poor crystallinity of binary Sn-N nitrides.[73]

A.3 Compositional characterization

A.3.1 RBS

RBS measurements for select samples corroborate the high-throughput XRF measurements done for each combinatorial film (Figure A.9A). Furthermore, RBS measurements identify the presence of oxygen in the $MnSnN_2$ films (Figure A.9B). The convolution of the N and O signals in RBS with the signal from the substrate inhibit the quantitative relation of anion content (N+O) with cation content (Mn+Sn) (Figure A.10), but the qualitative comparison of the trends in O/(N+O) as a function of cation content are still valid. Oxygen content increases with increasing Mn content, consistent with the lower electronegativity of Mn (1.55 on the Pauling scale) compared to Sn (1.96). The width of the oxygen region of the RBS spectra is similar to the width of the other elemental regions, suggesting that oxygen is distributed throughout the film thickness rather than being isolated to the surface. Oxygen substitution might help charge balance excess Mn via $Mn_{1+y}Sn_{1-y}N_{2-y}O_y$, where y is both the number of oxides substituting for nitrides and the number of Mn^{3+} ions substituting for Sn^{4+}. Alternatively, oxygen substitution could occur with exclusively Mn^{2+}, following a formula of $(MnO)_x(MnSnN_2)_{(1-x)}$, similar to the oxygen balancing seen in $MgZrN_2$ thin films.[49]

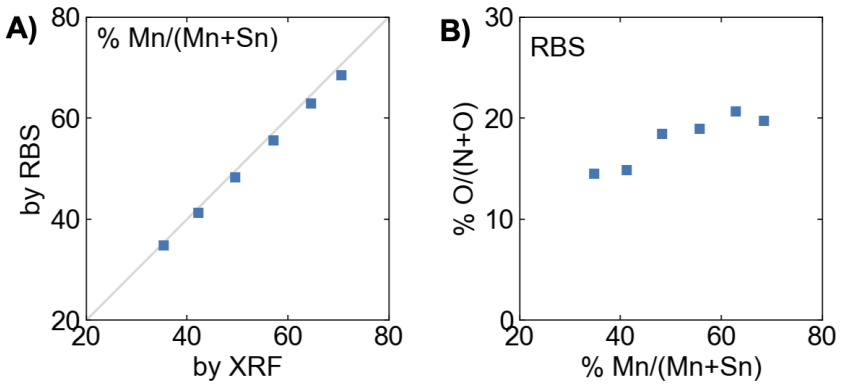

Figure A.9: A) XRF measurements of % Mn/(Mn+Sn) agree well with measurements by RBS. The grey trace represents perfect agreement between the techniques. Blue squares are the data. B) RBS measurements of % O/(N+O) show that the proportion of oxygen content increases slightly with increasing Mn content.

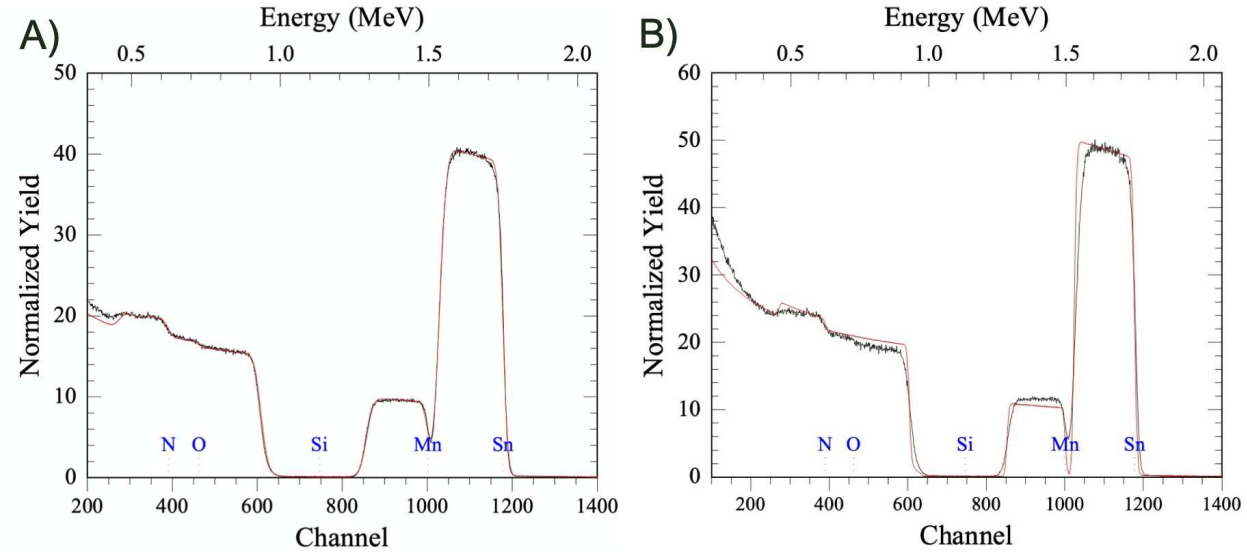

Figure A.10: Representative RBS data (black traces) of one sample and fits (red traces) following different fitting procedures. A) Fit by freely varying a fuzz parameter, film thickness, and relative amounts of Mn, N, O, normalized to Sn = 1. The minimization overfits the anion content, leading to an unreasonable ratio of (N+O)/(Mn+Sn) = 1.6 (expecting 1 for the wurtzite structure). B) Fitting the same data by refining thickness and Mn content and constraining N content to N = Mn+Sn (i.e., Sn = 1, Mn = 0.8, N = 1.8). While the lack of a fuzz parameter leads to poor fitting of curvature, the constrained anion content still produces a reasonable fit to the intensity in the 0.5 MeV region. Quantitative assessment of low-atomic number anion content is therefore tricky given the low signal and high background. However, these data show a non-zero oxygen content with a substantially larger proportion of nitrogen content.

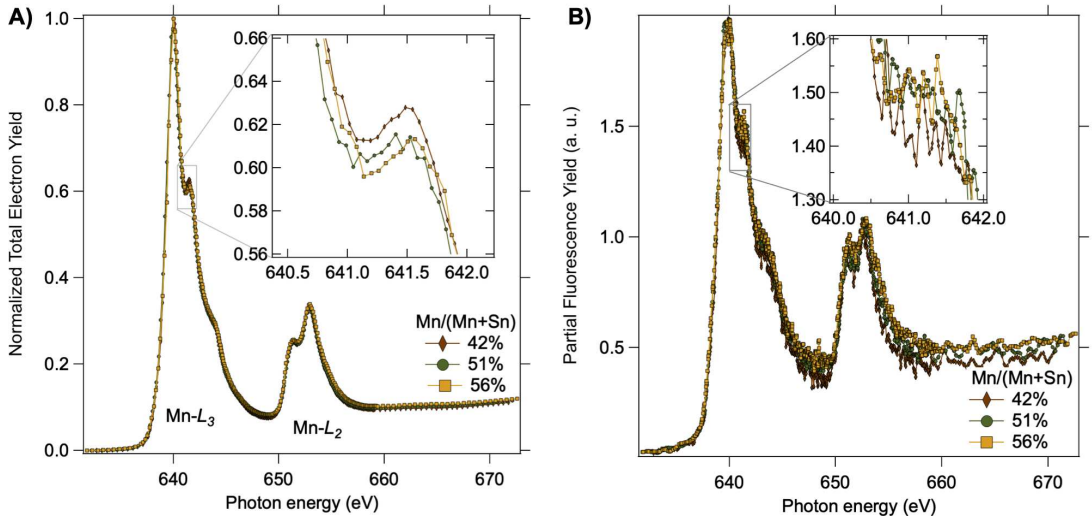

Figure A.11: The XANES total electron yield (A) and partial fluorescence yield (B) of the Mn-*L* edge shows that all three samples used for the magnetism measurements have similar spectral profiles. This profile matches Mn^{2+} compounds in literature.[186,187] Subtle differences can be seen on the peak shoulders of the L3 edge, but these shifts are near the noise level of the measurement.

A.3.2 XANES

In an attempt to identify the presence of Mn^{3+} and assess Mn^{2+}:Mn^{3+} ratios, high-resolution Mn L_3-edge X-ray absorption near-edge spectroscopy (XANES) measurements were conducted. Measurements were carried out on thin films at room temperature at the Stanford Synchrotron Radiation Lightsource (SSRL), SLAC National Accelerator Laboratory, beamline 10-1. Samples were measured under high vacuum conditions of $\sim 2.7 \times 10^{-6}$ Pa ($\sim 2 \times 10^{-8}$ Torr) with a ring current of 500 mA. The synchrotron radiation was monochromatized using the beamline's 600 line/mm monochromator with entrance and exit slits of 35 μm. A transition edge sensor (TES) spectrometer was used to collect resonant inelastic x-ray scattering (RIXS) planes with a resolution of 2 eV. The energy measured by the TES was calibrated by periodically measuring a reference sample of graphite, BN, Fe_2O_3, NiO, and CuO, which provide a stable set of emission lines. From the RIXS planes, we extracted the L_α and L_β lines, leading to partial fluorescence yield XAS.

XANES measurements (Figure A.11) show consistent spectra across the measured composition range, so we are not able to identify a change in oxidation state. There are subtle

differences between the spectra, as highlighted in the insets, but these differences are hard to distinguish from noise. We observe no consistent trend with composition and no distinct features indicative of Mn^{3+}. Instead, each the spectral profile is consistent with Mn^{2+} spectra seen in literature.[186,187]

A.4 Optoelectronic measurements

In addition to the ellipsometry measurements and modeling reported in the main text (Figure 2.6C), we conducted transmission and reflection UV-vis measurements on select substrates deposited on EXG, a transparent substrate (Figure A.12). Transmission (T) and reflectance (R) spectra were collected in the UV-Vis-NIR spectral ranges (300–1100 nm) using a home-built thin film optical spectroscopy system equipped with deuterium and tungsten/halogen light sources and a Si detector array. The collected spectra were then used to calculate absorbance using the relation Absorbance, $A = \ln[T/(1-R)]$. Unfortunately, the UV-vis spectrometer did not reach a sufficiently low energy to observe the absorption onset (1 eV, 1200 nm). However, these data support a low energy absorption onset without the need for modeling of the spectra (as needed for ellipsometry).

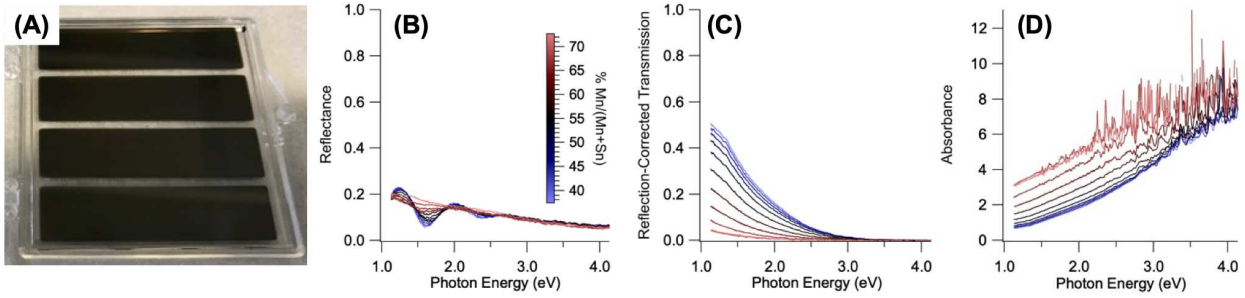

Figure A.12: A) Photo of a library deposited on a 2x2" Eagle XG glass substrate. The library was deposited at a set point of 250 °C, which corresponds to a substrate temperature of < 225 °C as evidenced by the lack of decomposition of the $MnSnN_2$ phase (confirmed by XRD). The film is dark brown in color. B) Reflectance *R* and C) Reflection-corrected transmittance *T* were used to calculate the absorbance via Absorbance $A = \ln \frac{T}{1-R}$, as implemented in Combigor.[65] D) The absorbance is high across measurable range. The colorbar shown in panel B is used for panels C and D as well.

In addition to measuring electrical conductivity of a film on EXG (Figure 2.6), we also conducted temperature dependent electrical measurements on select samples deposited on an insulating 100 nm of SiO_2 on Si (Figure A.13). These measurements were consistent with our observations for the sample on EXG (Figure 2.6B), showing increasing conductivity with increasing temperature. However, these blanket films on 100 nm of SiO_2 have

a tendency to short across such a narrow insulating layer if cleaved (as for these samples). To ensure we were exclusively measuring conductivity of the film, rather than the Si substrate, we repeated the measurement on EXG and report that in the main body of the text.

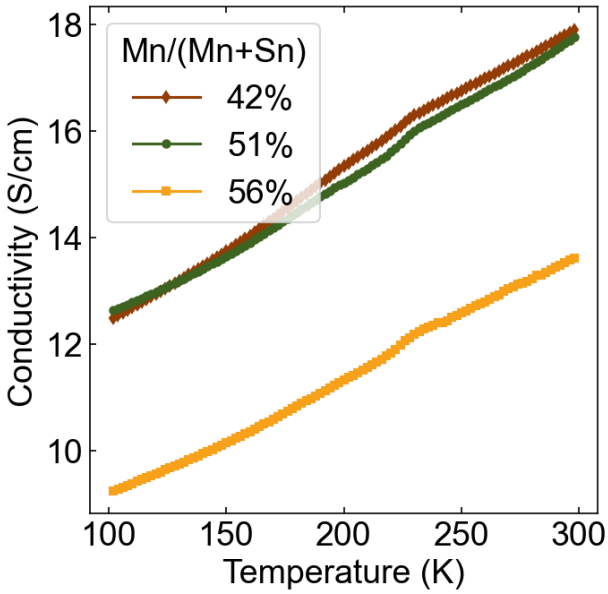

Figure A.13: Conductivity measurements on 5 mm $\times$ 5 mm squares scribed from a library deposited at $T_{\text{dep}} = 225$ °C on Si with 100 nm SiO_2.

A.5 Magnetic properties

A.5.1 Background subtraction and data analysis

As noted in the main text, for each magnetic measurement performed, an analogous blank substrate was measured with identical scan parameters, allowing for direct, point by point background subtraction. The blank was a 5 mm $\times$ 5 mm square of the substrate alone (100 nm SiO_2 on pSi), taken from the same wafer batch used for the deposition. Background subtraction was scaled by the relative mass of the blank (0.0328 g) and the samples (Table A.1). The differences in masses are likely due to differences in how the silicon substrate fractured, rather than in differing masses of the film deposited on the surface. Figure A.14 show examples of the background subtraction for temperature- and applied field-dependent measurements, respectively.

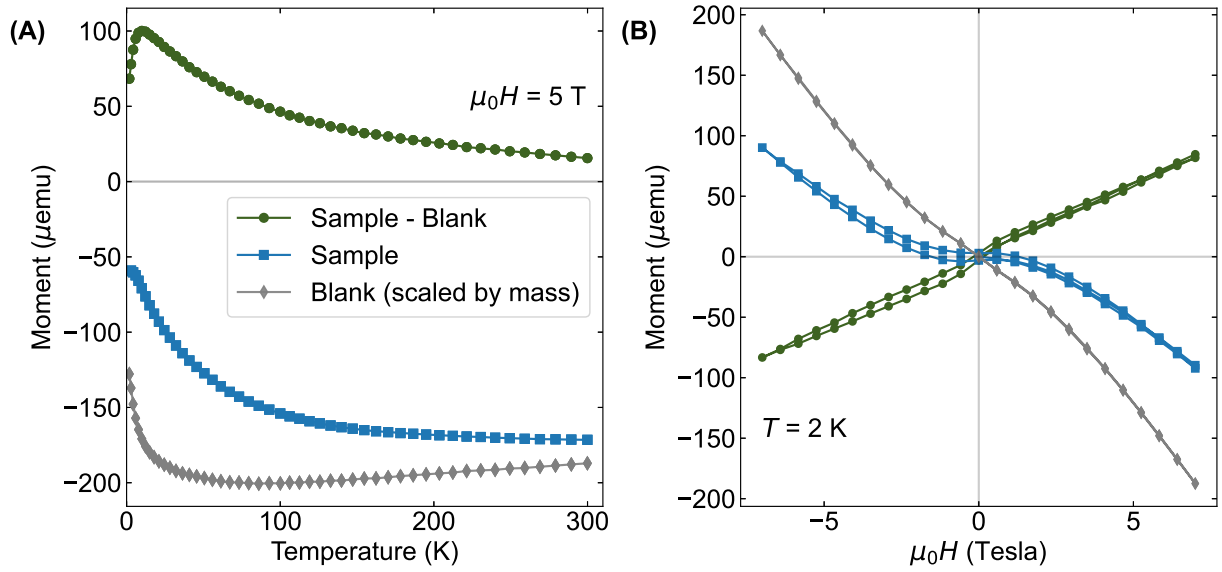

Figure A.14: (A) Background subtraction example for zero-field cooled temperature sweeps measured at $\mu_0 H = 5$ T. The raw moments of the sample (Mn/[Mn+Sn] = 51 %) and a blank substrate are shown, along with the background-subtracted data showing magnetism from the film alone (sample − blank). (B) Background subtraction example for applied field sweeps measured at $T = 2$ K is shown using the same legend.

Table A.1: Sample masses measured on a 4-decimal balance. For the purposes of background subtraction, we considered this mass to be the mass of the substrate, as the mass of the film is calculated to be less than the limit of resolution of the instrument (< 0.0001 g).

% Mn/(Mn+Sn)	Sample Mass (g)
42	0.0348
47	0.0346
51	0.0353
56	0.0354

Following background subtraction, the susceptibility (χ) was calculated using the background-subtracted raw moment value described above and the number of moles of $Mn_{2x}Sn_{2-2x}N_2$. Here, x is the Mn fraction of cation content (Mn/[Mn+Sn]). The % Mn/(Mn+Sn) values were determined by XRF on the individual squares. The number of moles of $Mn_{2x}Sn_{2-2x}N_2$ was calculated by dividing the film volume (Table A.2) by the unit cell volume and multiplying by Avogadro's number (Table A.3, assuming one $Mn_{2x}Sn_{2-2x}N_2$ unit per cell). The film volume (V_{film}) was calculated from the area (25 mm^2) and thickness of each film, which was interpolated from mapping profilometry measurements of the original sample library. The film mass is calculated from the number of moles and the molar mass. We note that the small mass of $Mn_{2x}Sn_{2-2x}N_2$ present during the measurements and the several possible sources of error in the film mass calculation and background subtraction make direct, quantitative comparisons of the magnitude of χ between samples difficult.

Table A.2: Molar mass for $Mn_{2x}Sn_{2-2x}N_2$ was calculated from XRF-measured composition. Film thickness was interpolated from profilometry measurements. Film volume was calculated from thickness and surface area (25 mm^2).

% Mn/(Mn+Sn)	Molar Mass (g/mol)	Thickness (μm)	Film Vol. (μm^3)
42	212	0.31	7.6E+06
47	206	0.30	7.6E+06
51	201	0.30	7.6E+06
56	194	0.30	7.6E+06

Table A.3: Lattice parameters for each film was refined from GIWAXS measurements, and the cell volume was calculated from the lattice parameters given the hexagonal spacegroup ($P63mc$). Film moles were calculated from the film volume and the unit cell. Film mass was calculated given the number of moles and molar mass.

% Mn/(Mn+Sn)	a(Å)	c (Å)	Cell Vol. (Å^3)	Film moles	Film mass (g)
42	3.444	5.626	57.81	2.2E-07	0.000047
47	3.441	5.562	57.03	2.2E-07	0.000046
51	3.438	5.536	56.67	2.2E-07	0.000045
56	3.436	5.512	56.37	2.2E-07	0.000043

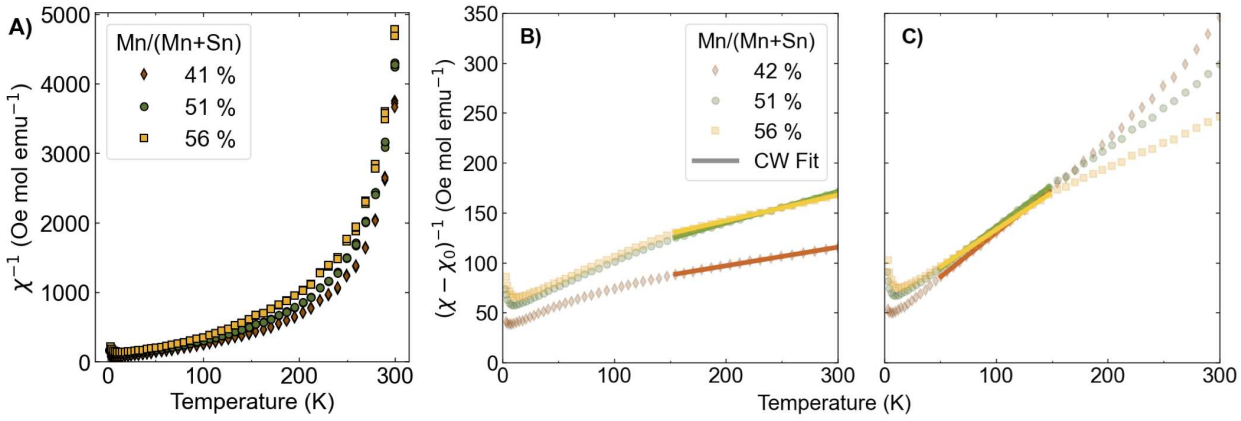

Figure A.15: A) Inverse susceptibility plotted without a diamagnetic correction factor shows significant non-linearity. Inverse susceptibility data and Curie-Weiss fits performed with a diamagnetic correction (χ_0) between B) 150–300 K C) 50–150K. The fits are shown as solid bars. Parameters Θ_{CW} and χ_0 are shown in Table A.4.

A.5.2 Additional data

Inverse susceptibility data as a function of temperature show an approximately linear region above the T^* ∼10 K transition temperatures for each composition, provided a diamagnetic correction (χ_0) is applied (Figure A.15). Inverse χ without a diamagnetic correction exhibits significant non-linearity (Figure A.15A). Therefore, Curie-Weiss fits were performed on $(\chi - \chi_0)^{-1}$ from 150–300 K, as shown in Figure A.15B. As the inverse χ plots exhibited a second linear region (50–150 K), we also applied Curie-Weiss analysis to this lower temperature region (Figure A.15C), which resulted in a smaller magnitude Θ_{CW} and a smaller magnitude χ_0 than the high temperature fits (Table A.4). Weiss temperatures from both fit ranges indicate antiferromagnetic (AFM) correlations. The change in slope may indicate a change in the energy scale of the dominant interactions in different temperature regions, or the emergence of competing interactions, although further investigation will be required to elucidate these subtle differences. We note that the uncertainty in background subtraction and film mass discussed above and in the main text inhibits quantitative extraction of Curie constants (C) or effective moments (μ_{eff}) from the Curie-Weiss fits.

Table A.4: Weiss temperatures (Θ_{CW}) extracted from Curie-Weiss fits performed from 50–150K and 150–300 K with the diamagnetic corrections (χ_0) listed.

% Mn/(Mn+Sn)	50–150 K		150–300 K	
	Θ_{CW} (K)	χ_0 (emu/Oe mol)	Θ_{CW} (K)	χ_0 (emu/Oe mol)
42	-47	-0.0025	-196	-0.0047
51	-63	-0.0030	-206	-0.0034
56	-79	-0.0038	-307	-0.0036

Figure A.16 shows the background-subtracted moment as a function of applied field measured at $T = 2$ K for all samples. This low-temperature behavior (below the transition temperature) is consistent with an AFM ground state across the composition series. The small hysteresis and net ferromagnetic moment noted in the Mn/(Mn+Sn) = 51% sample (Figure 2.8 in the main text) are also present across the measured composition range, supporting our assignment of this moment arising from canting or defects. The samples do not exhibit a plateau in moment, suggesting that the magnetism is not saturated at the limit of the instrument ($\mu_0 H = 7$ T). The moment at $\mu_0 H = 7$ T decreases with increasing Mn/(Mn+Sn) content, attributable to either the substitution of Mn^{3+} for Mn^{2+} or uncertainty in the mass used for normalization. Also, the low-field slope changes with increasing Mn/(Mn+Sn): at Mn/(Mn+Sn) = 56%, it appears to have two components, while at Mn/(Mn+Sn) = 42% there is only one component. This behavior may be related to uncompensated moments from Mn^{3+}.

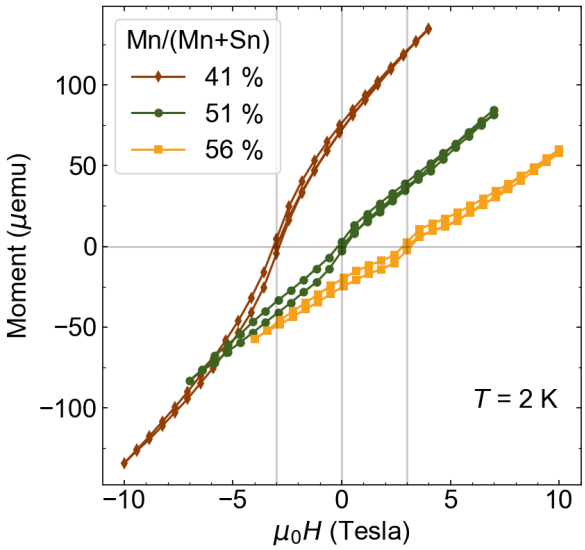

Figure A.16: Isothermal magnetic moment measurements at 2 K of $MnSnN_2$ samples show decreasing moment with increasing Mn content. Traces are offset horizontally by $\mu_0 H = 3$ T for clarity (grey lines guide the eye to each origin). The substrate contribution has been subtracted.

Appendix B

Supporting Information for Chapter 3: Bulk and film synthesis of three new ternary Mg-W-N materials

RTA experiments conducted on a sample of Mg_3WN_4 deposited in the h-BN structure reveal that heating this polymorph causes a conversion to the RS polymorph after annealing at 900 °C for 3 min (Figure B.1). These films were capped with approximately 20 nm of TiN to prevent Mg loss by volatization during annealing. This result suggests that h-BN structure of Mg_3WN_4 may be metastable with respect to the RS polymorph. In contrast, annealing the RS polymorph of Mg_3WN_4 does not drive any additional structural changes that are detectable by diffraction (Figure B.2).

VESTA simulations provide insight on the expected diffraction patterns for differing degrees of cation ordering.[69] The $P6_3/mmc$ structure of the RL $MgWN_2$ phase is primarily defined by two alternating layers of Mg octahedra and W trigonal prisms. However, those coordination environments could persist with varying degrees of cation disorder across those two metal sites. Figure B.3 shows how cation disorder decreases the intensity of the (002) reflection relative to other peaks.

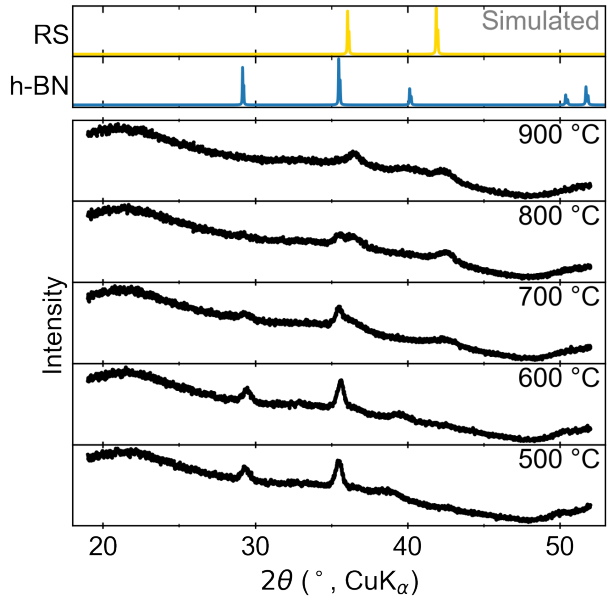

Figure B.1: Rapid thermal annealing experiments show that the h-BN structure converts to the RS structure as T_{anneal} increases, suggesting the h-BN structure is metastable relative to the RS structure. These films were capped with a 20 nm layer of TiN to minimize Mg loss by volatility.

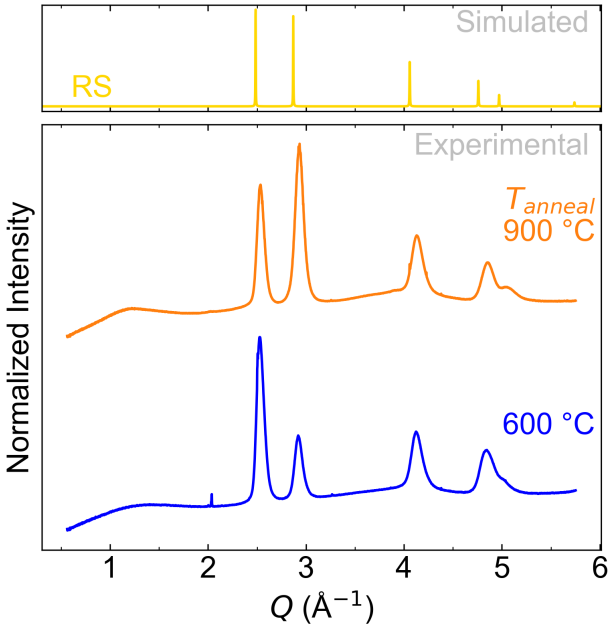

Figure B.2: GIWAXS patterns for a sample of Mg_3WN_4 annealed at 600 °C and 900 °C show that the initial RS structure persists through these anneals. Differences in peak intensity stem from initial texturing of the deposited film, rather than changes due to annealing.

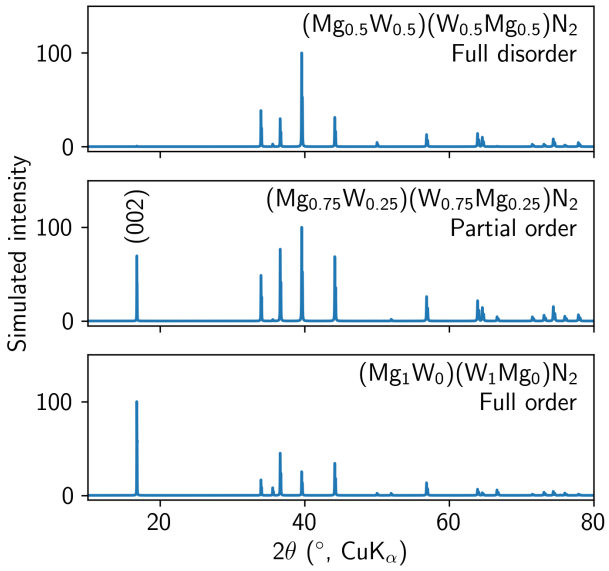

Figure B.3: Simulated diffraction patterns for the $MgWN_2$ phase in the RL polymorph ($P6_3/mmc$) with full cation disorder (top), partial cation disorder (middle), and full cation order (bottom). The relative intensity of the (002) supercell reflection increases with increasing ordering.

Appendix C

Supporting Information for Chapter 4: Bulk synthesis, structure, and electronic properties of magnesium zirconium nitride solid solutions

C.1 Precursor Characteristics

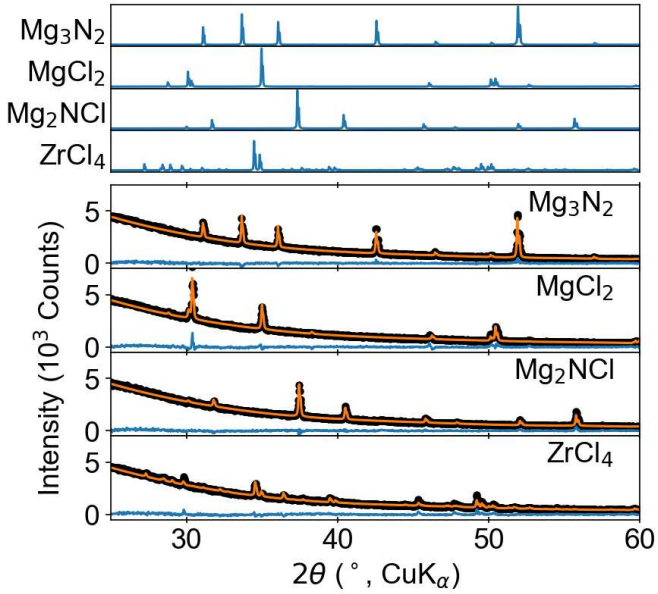

Figure C.1: PXRD patterns and Rietveld refinements show phase pure precursors. Peak intensity differences between the simulated traces (top) and the data (bottom) are due to preferred orientation of $MgCl_2$ along the (001) plane and $ZrCl_4$ along the (100) and (010) planes.

X-ray diffraction (XRD) data illustrate that the precursors used in this study appear phase pure (Figure C.1). However, XRD only detects crystalline components and cannot distinguish nitrogen vs oxygen occupancy. Therefore, the oxide impurities observed in the products may come from amorphous oxide-containing impurities in the reagents or from oxygen substitution on nitrogen sites in Mg_3N_2 or Mg_2NCl.

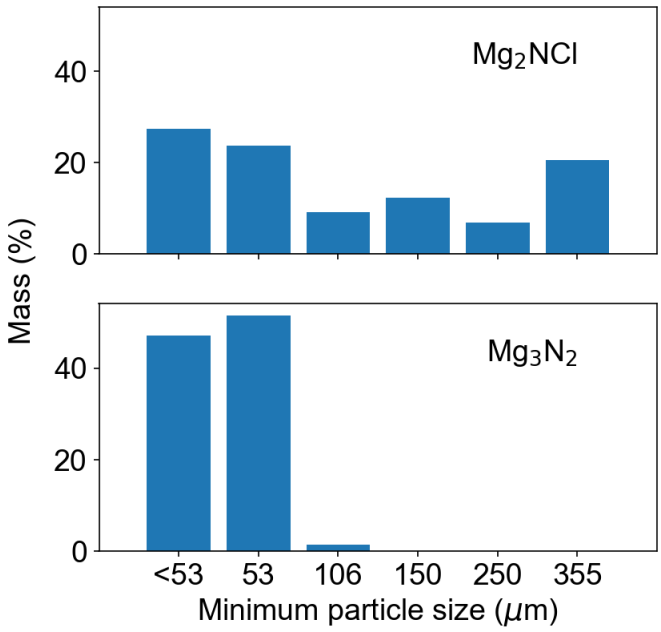

Figure C.2: Particle size distributions show that the Mg_3N_2 precursor is composed of smaller particles than the Mg_2NCl precursor. This distribution was measured by filtering each precursor through a series of sieves with increasingly fine mesh sizes and massing the material retained in each sieve.

Trends in particle size cannot explain the observed trends in reactivity. If reactivity were primarily governed by particle size, then one would expect Mg_3N_2 to react at lower temperatures than Mg_2NCl, because the Mg_3N_2 precursor is composed of smaller particles than the Mg_2NCl precursor (Figure C.2). However, quantitative phase analysis of *in situ* XRD data shows that the reverse is true, with Mg_2NCl reacting at lower temperatures (near 350 °C), while Mg_3N_2 does not react until $T_{rxn} = 420$ °C (Figures 4.3, C.8).

C.2 Analysis of X-ray diffraction

Initial attempts to wash away $MgCl_2$ using reagent grade ethanol on the benchtop (i.e. outside of the glovebox) resulted in degradation of the rock salt product and the appearance of oxide and oxynitride phases (Figure C.3). We suspect the ternary is therefore moisture sensitive. Therefore, all post-synthetic procedures were conducted in an inert environment glovebox unless otherwise noted.

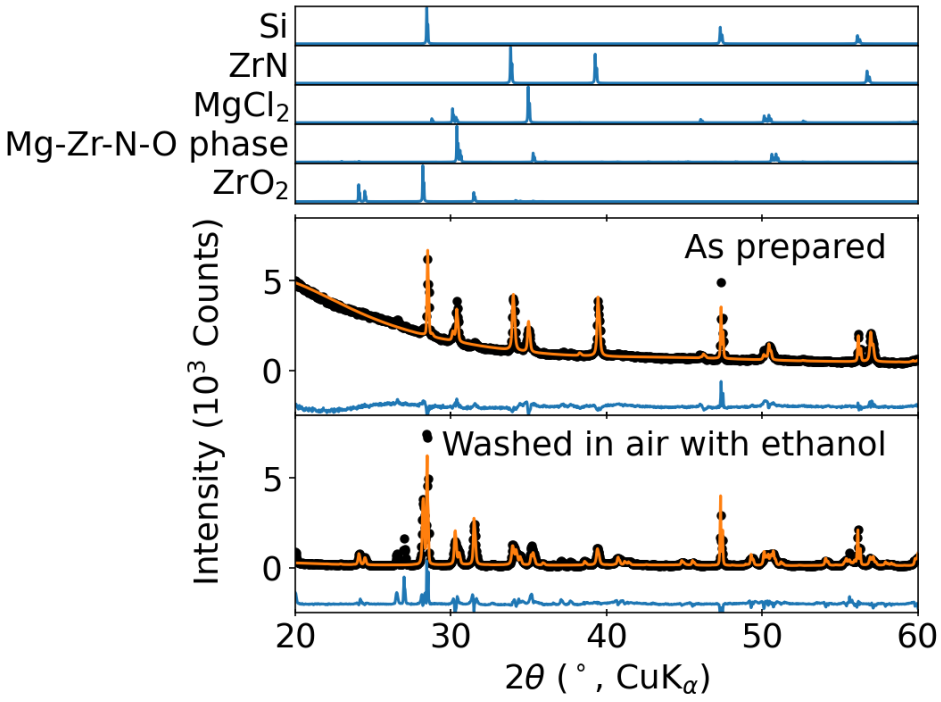

Figure C.3: PXRD of a product from the reaction between $2Mg_2NCl + ZrCl_4$ heated to 1100 °C for 18 h and then recovered into the glovebox (top). Washing the sample outside of the glovebox with reagent grade ethanol (bottom) leads to degradation of the $MgZrN_2$ phase and the formation of ZrO_2 and an orthorhombic Mg-Zr-N-O phase modeled as $Mg_{0.85}Zr_{6.15}N_{0.91}O_{11.8}$ (PDF Card 04-009-6080), along with other unindexed phases.

SPXRD patterns collected at 11-BM (Advanced Photon Source, Argonne National Lab) show no evidence of supercell ordering. Cation ordered $MgZrN_2$ ($I4_1/amd$) would be identified by a supercell reflection at approximately $Q = 1.8$ Å^{-1}, but no such peak is observed (Figure C.4). Instead, the cation disordered rock salt $MgZrN_2$ ($Fm\bar{3}m$) indexes the observed peaks, and a rock salt phase with variable cation occupancy ($Mg_xZr_{2-x}N_2$) is used in Rietveld analysis of the patterns.

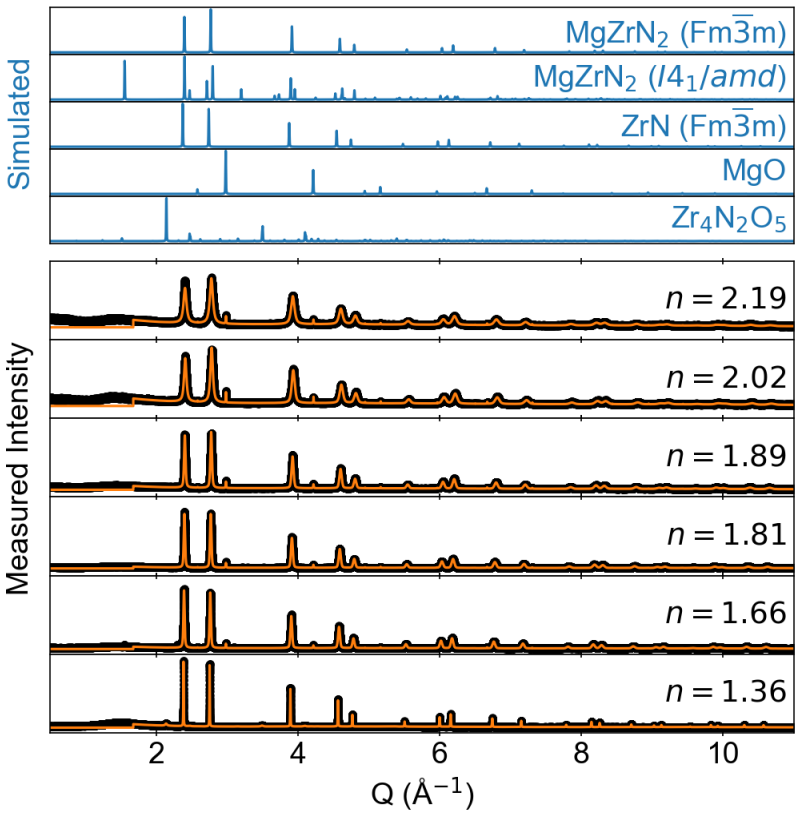

Figure C.4: SPXRD of samples heated to 500 °C set points for 12 h, then 800 °C set points for 12 h show that increasing Mg_2NCl relative to $ZrCl_4$ leads to a smaller unit cell for the rock salt structure. Data (black dots), Rietveld refinements (orange trace), and difference curves (blue trace) are shown. Focused 2θ range is shown in the main text, Figure 4.1. A trace impurity of MgO is present in some scans $n = 2.19$ to $n = 1.66$, and a trace impurity of $Zr_4N_2O_5$ is present in the $n = 1.36$ scan. Impurities constitute < 5 wt% of the product. $\lambda = 0.457879$ Åor 0.457900 Å.

A reaction of $1.16Mg_2NCl + ZrCl_4$ yielded a mix of ZrN, $MgCl_2$, and ZrNCl, as predicted by the thermodynamic calculations shown in Figure C.17b. The stoichiometric reactions are:

$$Mg_2NCl + ZrCl_4 \longrightarrow ZrNCl + 2\,MgCl_2 \tag{C.1}$$

and

$$\frac{4}{3}Mg_2NCl + ZrCl_4 \longrightarrow ZrN + \frac{1}{6}N_2 + \frac{8}{3}MgCl_2 \tag{C.2}$$

Intermediate precursor ratios ($1 < n < \frac{4}{3}$) yield a linear combination of Equations C.1 and C.2.

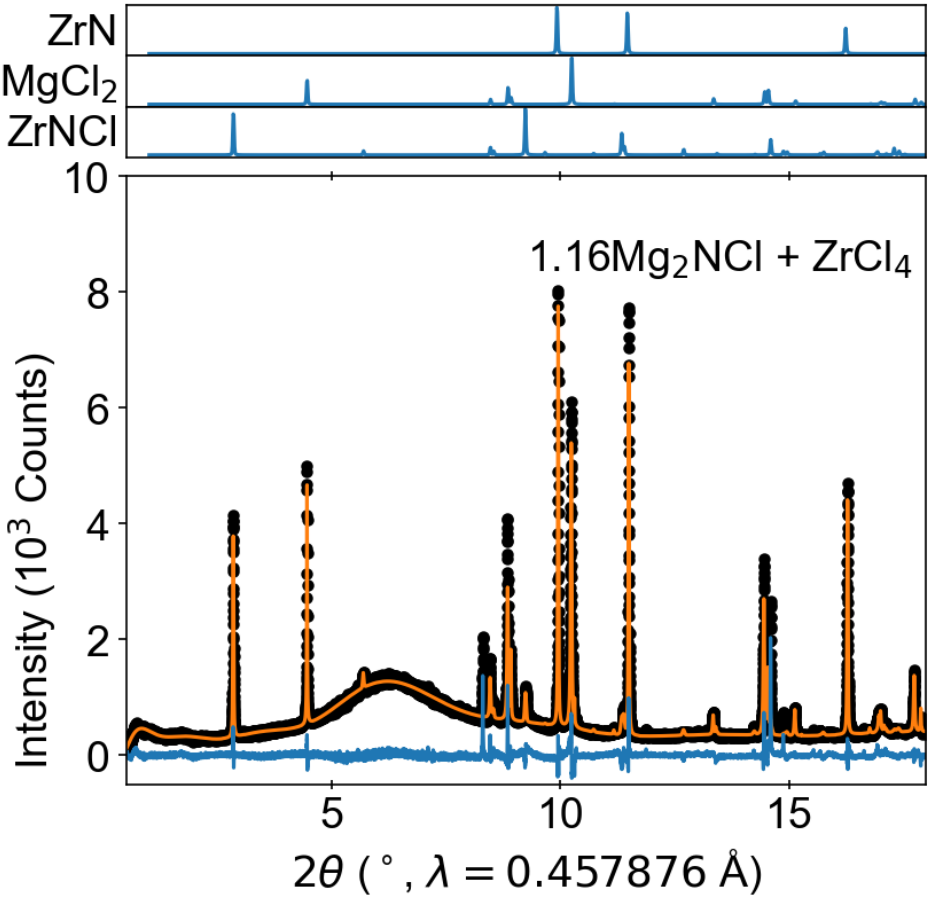

Figure C.5: SPXRD of a sample with $1.16Mg_2NCl + ZrCl_4$ that was reacted at a 950 °C set point for 12 h, showing the formation of $MgCl_2$, ZrN, and ZrNCl, as is expected from the thermodynamic equilibrium shown in Figure C.17.

The two-step heating profile was chosen to minimize the evolution of nitrogen gas and then induce crystallization of the ternary. Thermodynamic calculations described below led us to dwell for 12 h at 500 °C to minimize the loss of N_2 while ensuring reactivity. *Ex situ* PXRD shows that $2Mg_2NCl + ZrCl_4$ react completely during this step (Figure C.7), although $MgCl_2$ is the only crystalline product. Presumably, an amorphous mixture accounts for the remaining material. A second heating of 12 h at 800 °C was used to crystallize the ternary (Figure C.6).

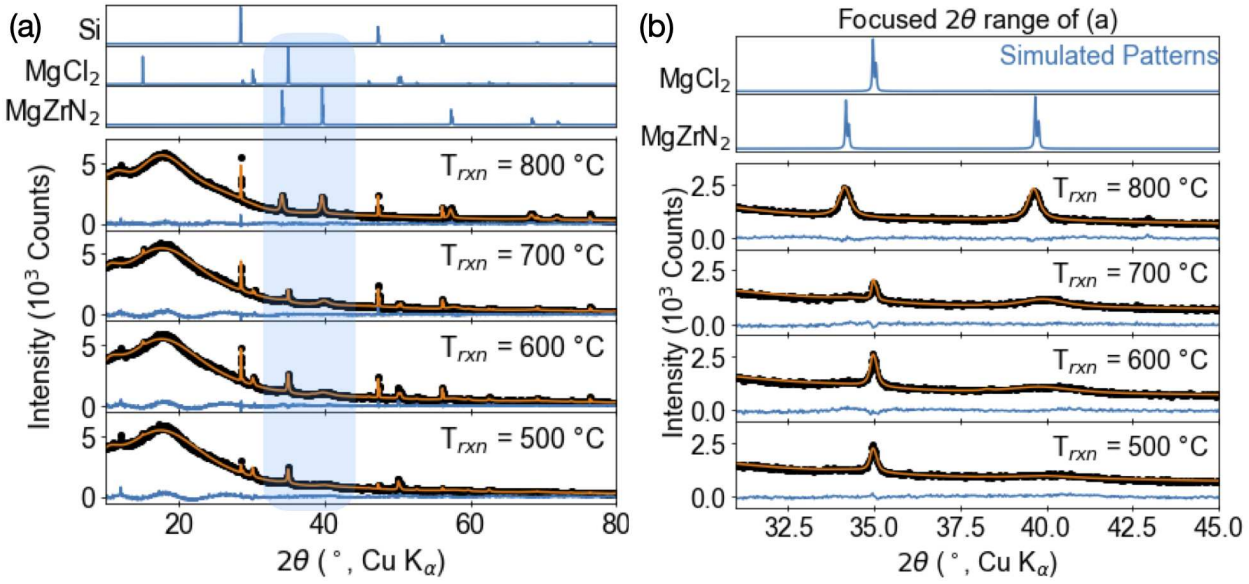

Figure C.6: XRD of samples of $2\,Mg_2NCl + ZrCl_4$ heated first to 500 °C set points for 12 h, then hotter for 24 h. (a) Full patterns are shown, with the highlighted area in blue shown in more detail in (b). At temperatures below 800 °C, the rock salt phase is nanocrystalline, but the phase anneals to a strained structure by 800 °C. In the 800 °C sample, $MgCl_2$ was removed by vapor transport to the far end the ampule, held at approximately 700 °C.

In situ XRD also supports this heating profile, with reactivity beginning at low temperatures and ternary crystallization occurring at higher temperatures (Figure C.8).

C.3 Sequential Rietveld Analysis

In Rietveld analysis, metal occupancy x in $Mg_xZr_{2-x}N_2$ is highly correlated with scale factor. To systematically determine the influence of x on refinement quality and to better

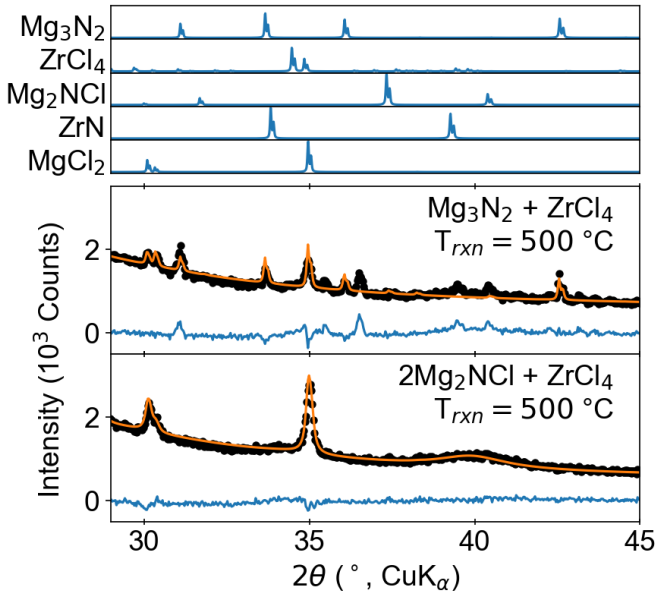

Figure C.7: *Ex situ* PXRD of reactions annealed at a 500 °C set point for 12 h show that the precursors for $2\,Mg_2NCl + ZrCl_4$ are fully consumed, producing $MgCl_2$ and an amorphous / nanocrystaline Mg-Zr-N product (bottom). In contrast, a mixture of $Mg_3N_2 + ZrCl_4$ heated under identical conditions does not react fully, as evidenced by residual Mg_3N_2 (top).

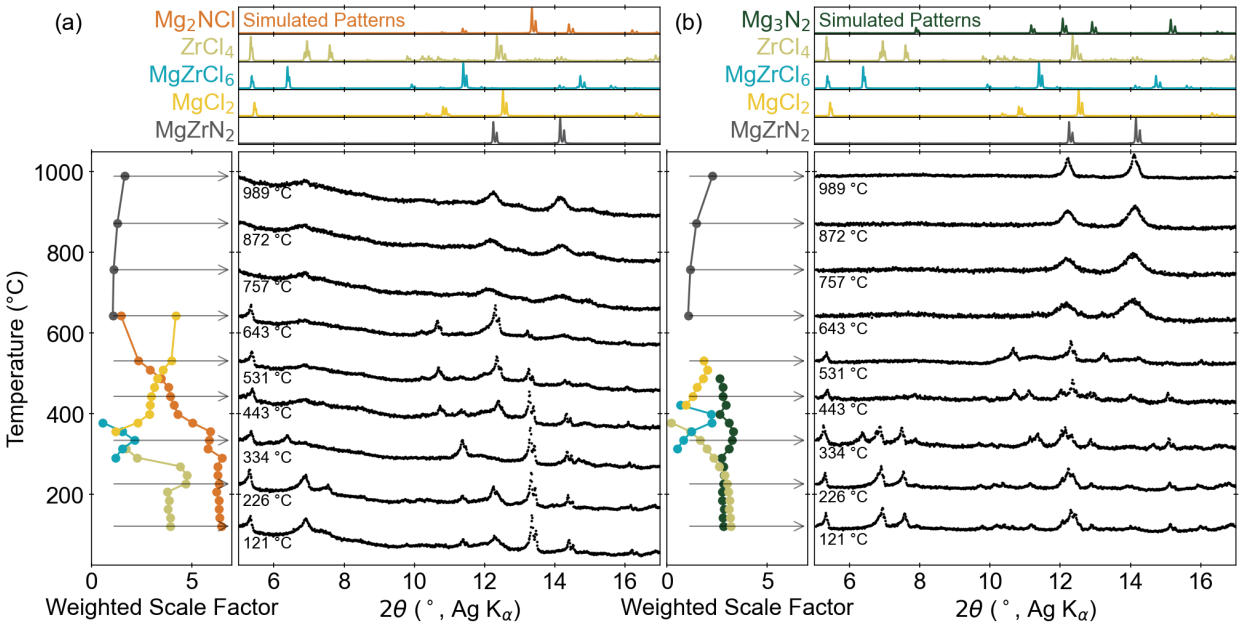

Figure C.8: Selected *in situ* PXRD patterns are shown with reference to simulated patterns for the reactions of (a) $2Mg_2NCl + ZrCl_4$ and (b) $Mg_3N_2 + ZrCl_4$. Weighted scale factors for each phase, as determined by Rietveld analysis, are shown to the left of each set of scans, as also shown in the body of the text (Figure 4.3). Arrows match the Rietveld analysis to the associated scan.

estimate the error in x refined by this method, we conducted sequential refinements as described in the Methods section (Figures C.9, C.10). In these sequential refinements, each PXRD or SPXRD pattern was refined with x fixed between $x = 0$ and $x = 2$ at intervals of 0.1, with all other parameters refining freely. The resulting goodness of fit (G.o.F.) values were fit to a 6th order polynomial, with the minimum of that polynomial taken as the best fit. An increase of 1% in the G.o.F. parameter relative to the best fit was arbitrarily selected as the cutoff for our error bars. Relative G.o.F. is used for easier comparison between samples.

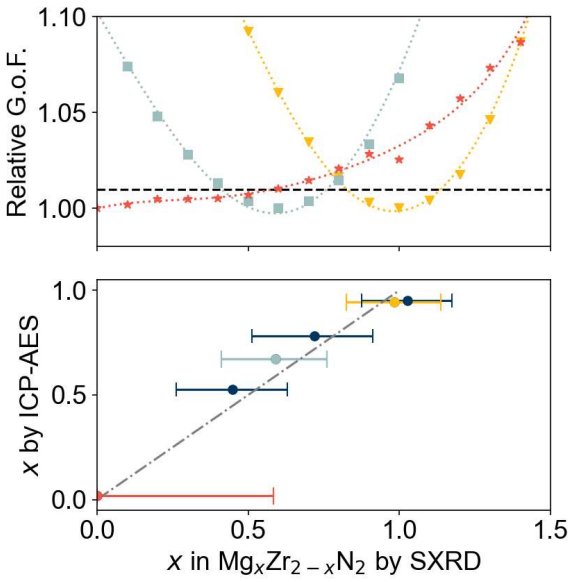

Figure C.9: Sequential Rietveld refinements were conducted by systematically varying Mg-occupancy (x) and refining all other parameters as described in the Methods. Selected sequential refinement results are shown (top). Solid points show the refinement goodness of fit (G.o.F.) relative to the best fit (minimized G.o.F.), and dotted traces show the 6th order polynomial fit to those points. The horizontal dashed line shows a 1% increase in G.o.F. The minimum of this polynomial fit was used to determine Mg-occupancy by SPXRD, and SPXRD error bars were calculated from a 1% increase in the relative G.o.F.(bottom). These error bars correspond to the grey area in Figure 4.7. Colors from the top subplot correspond to the selected samples from the bottom plot. The dot-dash trace in the bottom plot guides the eye along perfect agreement between the SPXRD and ICP-AES techniques.

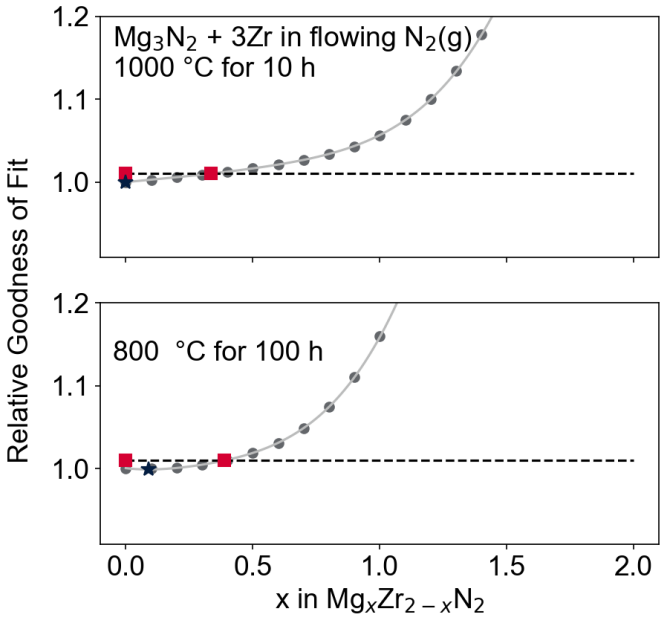

Figure C.10: Sequential refinements of the control reaction XRD data displayed in Figure 4.4 show that, when $Mg_3N_2 + 3\,Zr$ are heated under purified flowing nitrogen, ZrN forms with minimal Mg incorporation. Horizontal black dashed trace indicates a 1% increase in the goodness of fit parameter relative to the best fit. Dark grey circles indicate the sequential refinement values, the light grey trace indicates the sixth-term polynomial fit to those data, the navy star indicates the local minima of the fits, and the red squares indicate the error bars around the local minima where the Relative Goodness of Fit increases by 1% over the best fit.

C.4 Balanced Chemical Equations

The balanced reaction from the main text (Equation 4.7) is visualized in Figure C.11.

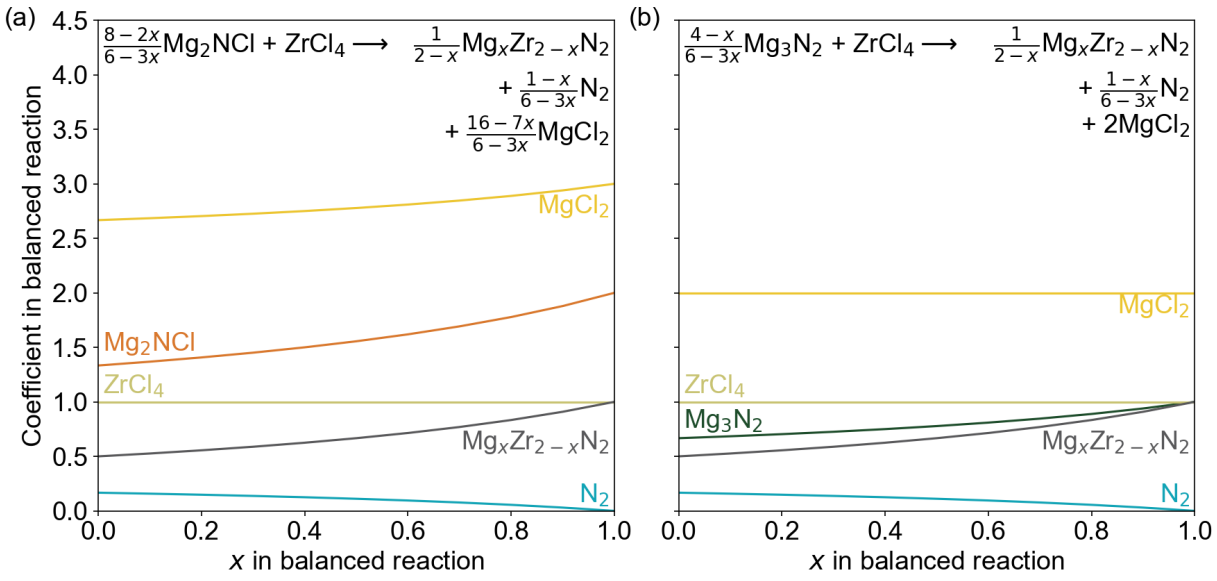

Figure C.11: (a) The coefficients for the balanced reaction for Equation 4.7 show that as x increases, the reaction requires a larger proportion of Mg_2NCl relative to $ZrCl_4$ and produces less N_2 as a byproduct. (b) A similar trend occurs when Mg_3N_2 is used as a reactant.

C.5 EDS Analysis

Energy Dispersive X-ray Spectroscopy (EDS) was used to semi-quantitatively measure the metal ratios in each sample. Mg/Zr quantity varied with precursor ratio, as shown in Figure C.12. However, anion content could not be reliably quantified (Figure C.13). The nitrogen signal greatly exceeds what would be expected given the metal ratios. Additionally, carbon and oxygen are detected in non-trivial quantities by EDS. These signals may come from the carbon tape used to adhere the sample to the stub, or from adventitious organic compounds in the instrument (e.g., vacuum grease).

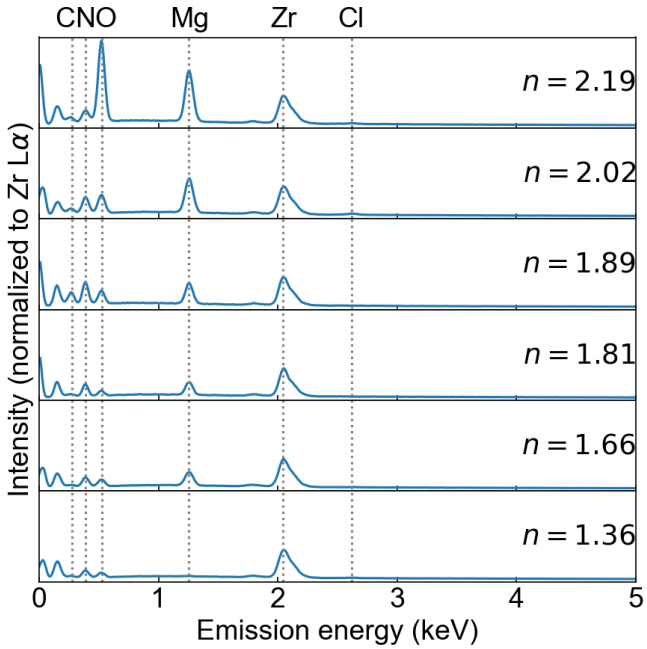

Figure C.12: Representative EDS spectra from six washed samples show that Mg and Zr ratios vary as a function of precursor ratio (n) in $n\mathrm{Mg_2NCl} + \mathrm{ZrCl_4}$. Main X-ray emission peaks are labeled with their respective elements and vertical dotted lines. Significant oxygen incorporation can be observed for the most Mg-rich sample ($n = 2.19$). Spectra intensities are normalized to the Zr Lα emission at 2.04 keV.

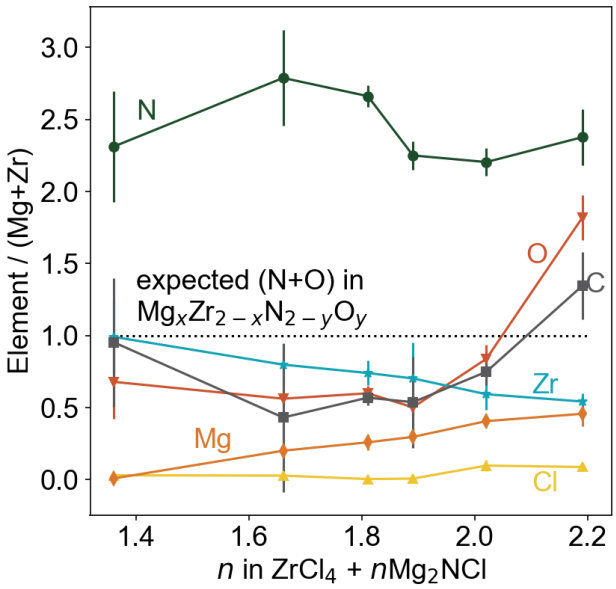

Figure C.13: Elemental quantification by SEM-derived EDS shows unexpected high nitrogen and oxygen content relative to metal content. The rock salt phase should have a cation:anion ratio of 1:1. The signals for N and O are likely a combination of the $Mg_xZr_{2-x}N_{2-y}O_y$ phase, carbon tape, and adventitious carbon, as indicated by the non-zero carbon signal. Vertical error bars show one standard deviation about the mean from the six measurements that were averaged for each sample.

C.6 Thermodynamic Calculations

Thermodynamic data from the Materials Project were used to calculate reaction energies shown in the text (Figure 4.6). The phases used are shown in the ternary isopleths of the quaternary Mg-Zr-N-Cl phase space (Figure C.14). Formation energies for relevant compounds are tabulated below (Table C.1). Reaction energies as a function of temperature for Equations 4.4, 4.5, or 4.6 are shown in Figure C.15.

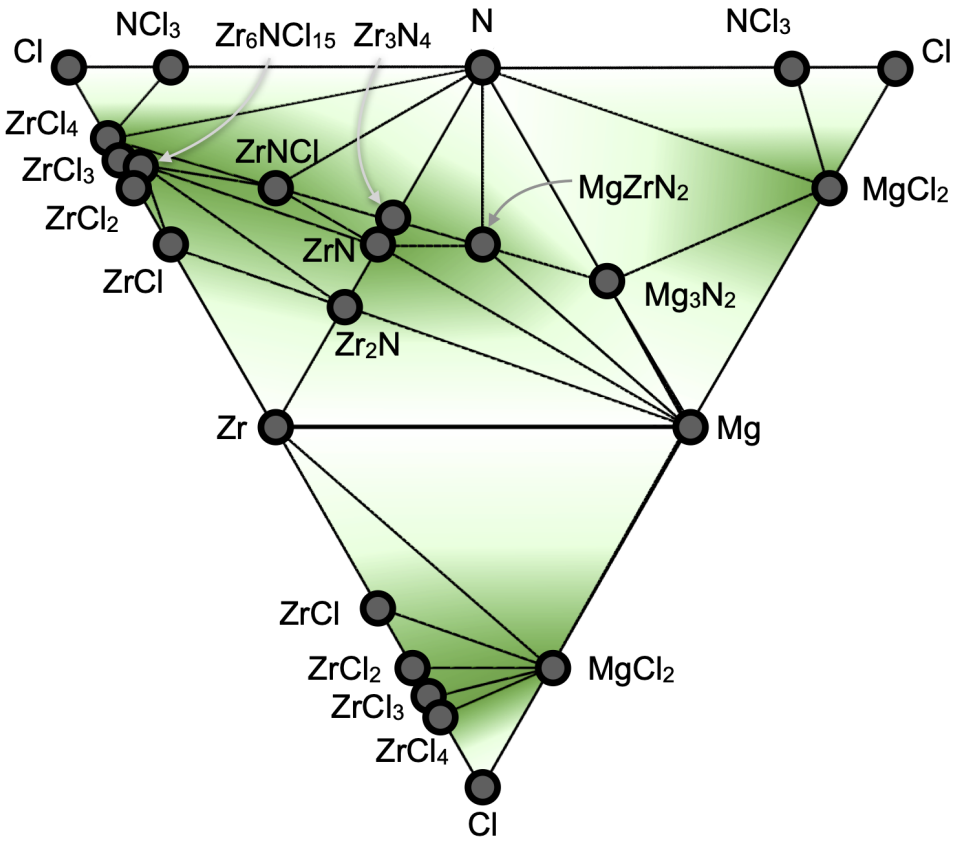

Figure C.14: Ternary isopleths of the quaternary phase space, projected into two dimensional ternary phase diagrams. Thermodynamically stable phases at ($T = 0$ K) listed in the Materials Project from the Mg-Zr-N-Cl system are shown. Darker green indicates a more negative ΔH_f. Mg_2NCl does not appear in this diagram because it is not listed in the Materials Project, and our DFT calculations for the phase suggest that Mg_2NCl is energetically within error of the binaries. The phases shown here were used to calculate the convex hull in Figure 4.6.

Table C.1: ΔG_f (eV/atom) values for relevant phases are tabulated as a function of temperature. These values were calculated using the method described by Bartel, et al.[119]

Phase	ΔG_f(300 K)	ΔG_f(600 K)	ΔG_f(900 K)	ΔG_f(1200 K)
Mg_2NCl	-1.24	-1.10	-0.97	-0.83
Mg_3N_2	-0.78	-0.66	-0.55	-0.42
$MgCl_2$	-2.09	-1.93	-1.79	-1.67
$MgZrN_2$	-1.38	-1.24	-1.11	-0.98
$ZrCl_4$	-2.08	-1.91	-1.75	-1.60
ZrN	-1.73	-1.58	-1.45	-1.32
N_2	0.00	0.00	0.00	0.00
ZrNCl	-1.93	-1.76	-1.62	-1.47

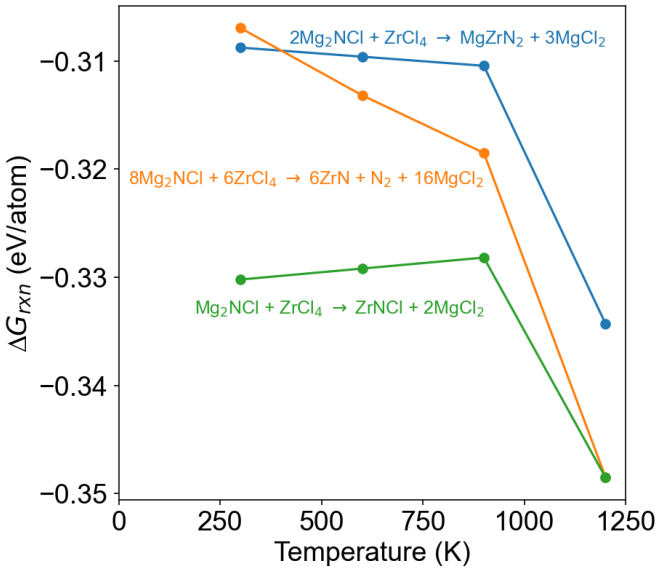

Figure C.15: Reaction energies for Equations 4.4, 4.5, or 4.6 are calculated as a function of temperature using values from Table C.1. For reference, $MgCl_2$ melts at 987 K. $ZrCl_4$ sublimes readily and exhibits a triple point at 710 K.

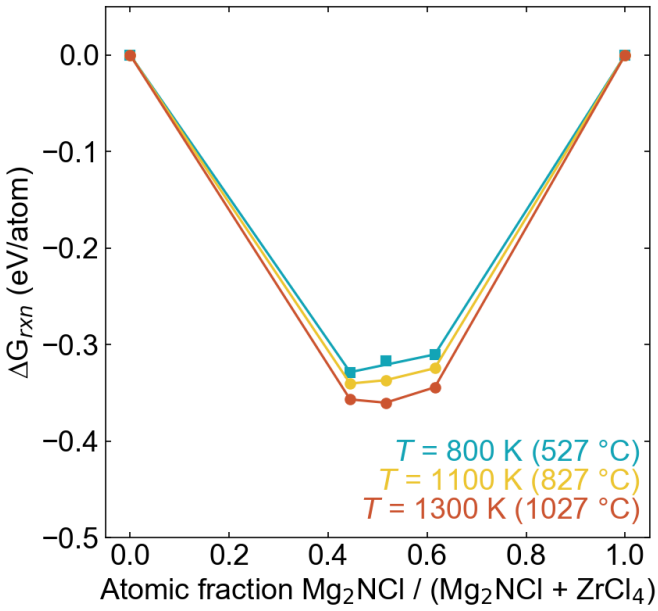

Figure C.16: Gibbs free energy calculations show that only three reactions are thermodynamically favorable across the range of Mg_2NCl and $ZrCl_4$ combinations. A more detailed plot is shown in Figure 4.6

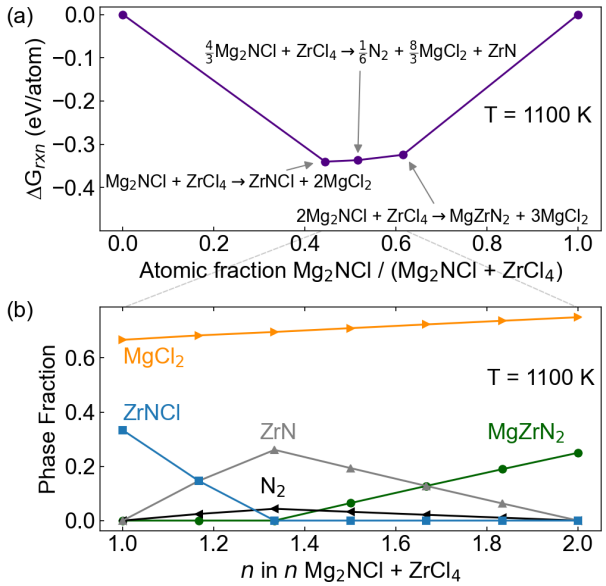

Figure C.17: (a) Gibbs free energy calculations show that $MgZrN_2$ is on the thermodynamic hull of the Mg_2NCl–$ZrCl_4$ phase space, along with ZrNCl and ZrN. ΔG_{rxn}(1100 K) calculations used ΔG_{f}(1100 K) values determined via the method described by Bartel, et al.[119] (b) Equilibrium phase fractions were calculated as described by Bartel, et al. and shown with respect to the molar precursor ratio (n) as used elsewhere in the text. Grey dashed lines between the subplots shows how relevant atomic fractions from (a) correspond to the horizontal axis of (b).

C.7 Optoelectronic Measurements

Optical measurements were conducted using an Ocean Optics Flame spectrometer with a Tungsten Halogen light source and integrating sphere. Samples were sealed in vials using electrical tape in an argon glovebox to maintain an inert atmosphere around the powders during UV-vis measurement outside the glovebox. Samples were placed on top of the integrating sphere such that light was directed upwards and reflected off the powder at the bottom of the vial, as pictured (Figure C.18). Measurements were averaged over 200

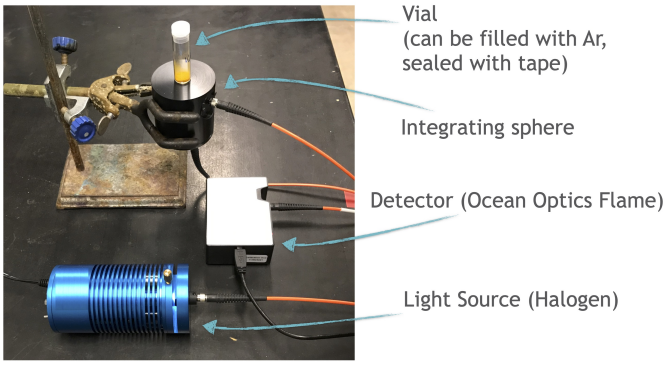

Figure C.18: Labeled photo of the optical measurement setup. In this photo, V_2O_5 (yellow) is shown in the vial as a control to test the system.

scans, with each scan taking approximately 300 ms. Raw reflectance data are shown in Figure C.19. These data were transformed into absorption spectra using the Kubelka-Munk method to generate Figure 4.11 shown in the main text.

Electrochemical Impedance Spectroscopy (EIS) was used to assess the electronic properties of the materials. Sample conductivity (σ) was calculated from the sample resistance (R_s), pellet thickness (t), and cross sectional area ($A = 0.317$ cm^2) using $\sigma = (t)/(R_s A)$. R_s was calculated by subtracting the cell resistance ($0.051\ \Omega$) from the raw resistance measured at 300 mHz.

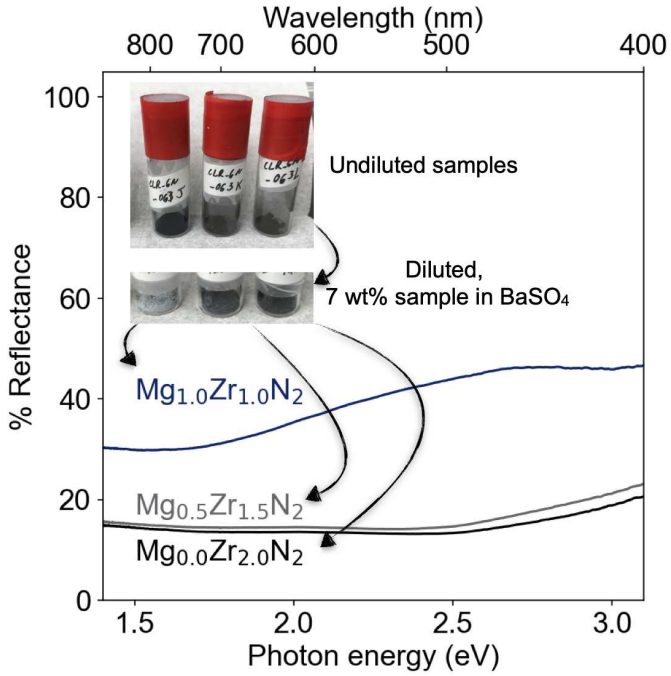

Figure C.19: Raw reflectance data used to calculate absorption in the main text Figure 4.11.

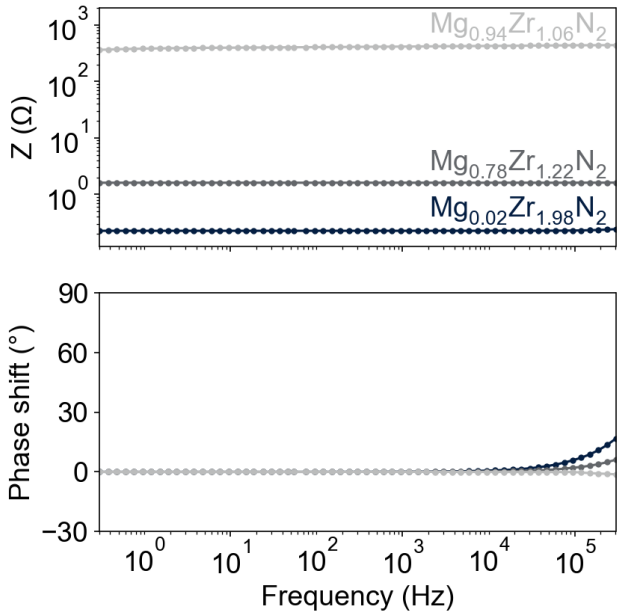

Figure C.20: Representative Bode plots from electrochemical impedance spectroscopy measurements show phase shifts near 0 ° across the frequency range, indicative of impedance due purely to an electronically conductive circuit element. The phase shift at high frequency is an artifact from the wiring of each sample. The conductivity values plotted in Figure 4.10 were calculated using the low frequency limit of the impedance (Z) at 300 mHz.

Table C.2: Measured values for raw resistance (R), sample resistance, thickness (t) and calculated sample conductivity (σ). The symbol n refers to the precursor ratio ($n\mathrm{Mg_2NCl} + \mathrm{ZrCl_4}$) and x refers to the magnesium content in $\mathrm{Mg}_x\mathrm{Zr}_{2-x}\mathrm{N}_2$ as determined by ICP-AES.

n	x	Raw R (Ω)	Sample R (Ω)	t(cm)	σ (S/cm)
2.19	0.951	1.4×10^4	1.4×10^4	0.157	3.3×10^{-5}
2.02	0.945	2.4×10^2	2.4×10^2	0.162	2.0×10^{-3}
1.89	0.781	1.6×10^0	1.5×10^0	0.136	2.7×10^{-1}
1.81	0.674	8.5×10^{-1}	8.0×10^{-1}	0.164	6.4×10^{-1}
1.66	0.525	2.2×10^{-1}	1.7×10^{-1}	0.090	1.6×10^0
1.36	0.017	1.3×10^{-1}	8.5×10^{-2}	0.104	3.8×10^0

Appendix D

Supporting Information for Chapter 5: Mechanistically-guided materials chemistry: synthesis of new ternary nitrides $CaZrN_2$ and $CaHfN_2$

D.1 Additional synthesis details for $CaZrN_2$ and $CaHfN_2$

To estimate the expected lattice parameter of $CaZrN_2$ in the rocksalt structure, we measured the Ca-N-Zr distance in the $R\bar{3}m$ structure, which is equivalent to the M-N-M distance defining the edge of the rocksalt unit cell (Figure D.1). This estimate was used for reference against our diffraction data (Figure 5.2). Full patterns from the samples highlighted in Figure 5.2 are shown in Figure D.2.

The lattice parameter and crystaline domain size of the rocksalt was influenced by the temperature, dwell time, and precursor ratios of the synthesis.

Figure D.3 shows that increasing the reaction temperature increases the peak sharpness of the $CaZrN_2$ rocksalt phase when reacting $1.2Ca_3N_2 + ZrCl_4$. This indicates the size growth of crystalline domains. Rietveld analysis confirms this increase in crystalline domain size. Ca-loss is suspected from the decrease in lattice parameter, although site occupancy could not be reliably refined from these patterns owing to overlaping peaks with the Ca_4Cl_6O phase, the few number of peaks in the rocksalt pattern, and the relative similarity of electron count for Ca and Zr.

For Ca-rich syntheses, increasing annealing time did not substantially change the lattice (Figure D.4). However, Ca-poor syntheses exhibited Ca-loss with increasing dwell time (Figure D.5). As dwell time increases for a reaction of $1.0Ca_3N_2 + ZrCl_4$ or $2.0Ca_2NCl +$

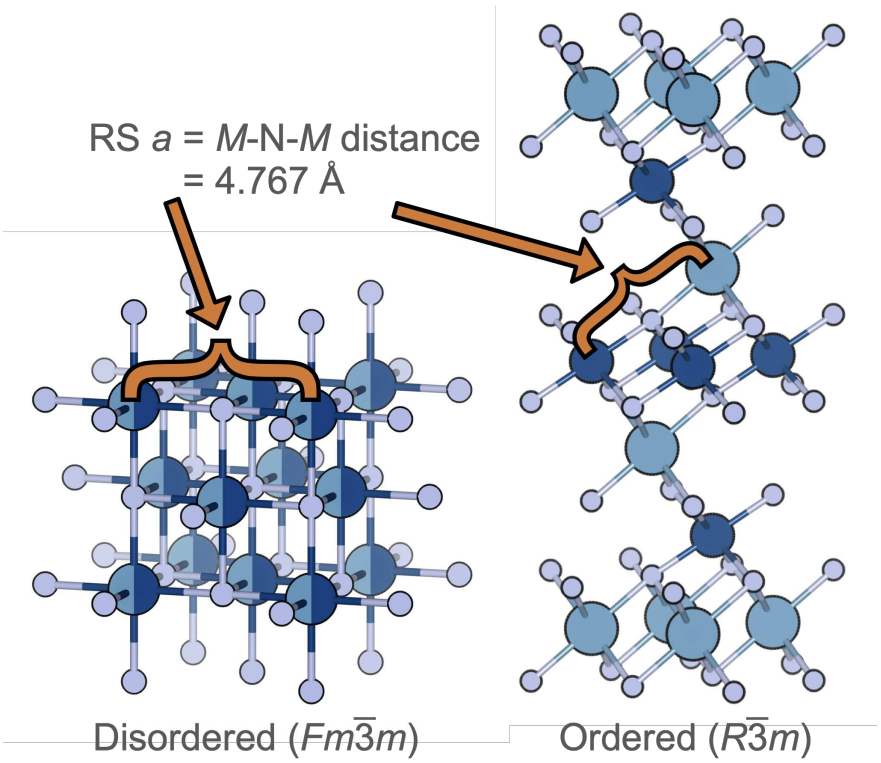

Figure D.1: We estimate the theoretical size of the rocksalt lattice parameter using the Ca-N-Zr distance from the computationally predicted ordered structure.

$ZrCl_4$, the rock salt lattice parameter decreases, suggesting a loss of Ca from the structure. One step reactions heating to 900 °C for 1 h yield disordered rock salts with unit cell dimensions of $a \sim 4.65$, above the range expected for ZrN (grey region) but below the range expected for $CaZrN_2$ (blue region). Longer reaction times yield rock salt products within the lattice parameter range of ZrN ($a \sim 4.58$Å).[130] This decrease in lattice parameter indicates that Ca is being lost from the structure, likely to react with chloride ions or the quartz tube.

A reaction between $1.21Ca_3N_2 + HfCl_4$ produced a $CaZrN_2$, as confirmed by PXRD and EDS (Figure D.6). PXRD shows a cation disordered rocksalt phase ($Fm\bar{3}m$) with a unit cell edge length of $a = 4.725$ Å, larger than ZrN ($a = 4.58$ Å), but smaller than $CaZrN_2$ ($a = 4.75$ Å). EDS measurements show a Ca (51.6 relative atomic %), Hf (41.2 relative atomic %), and Cl (7.2 relative atomic %). Assuming the Cl is bound to $CaCl_2$ leaves 48.0 at% Ca attributable to $CaHfN_2$, whereas assuming Ca is bound to Ca_2NCl leaves 37.2 at%

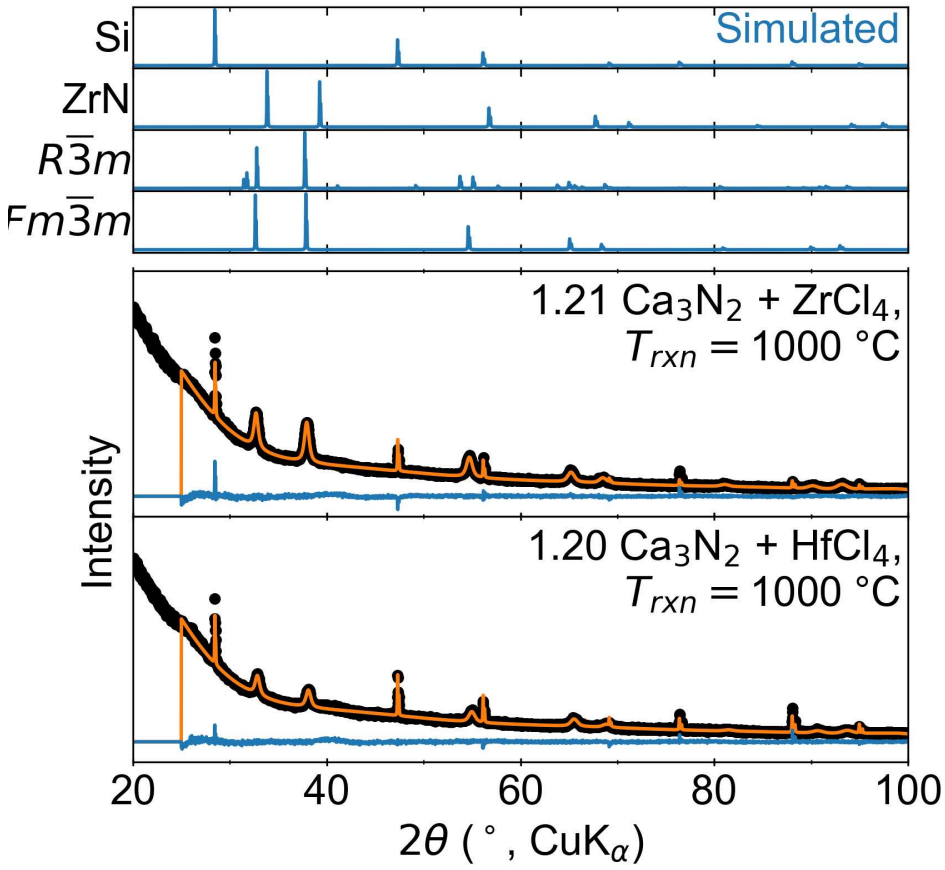

Figure D.2: Full diffraction patterns for the samples shown in Figure 5.2. The pattern fits start at 25 °.

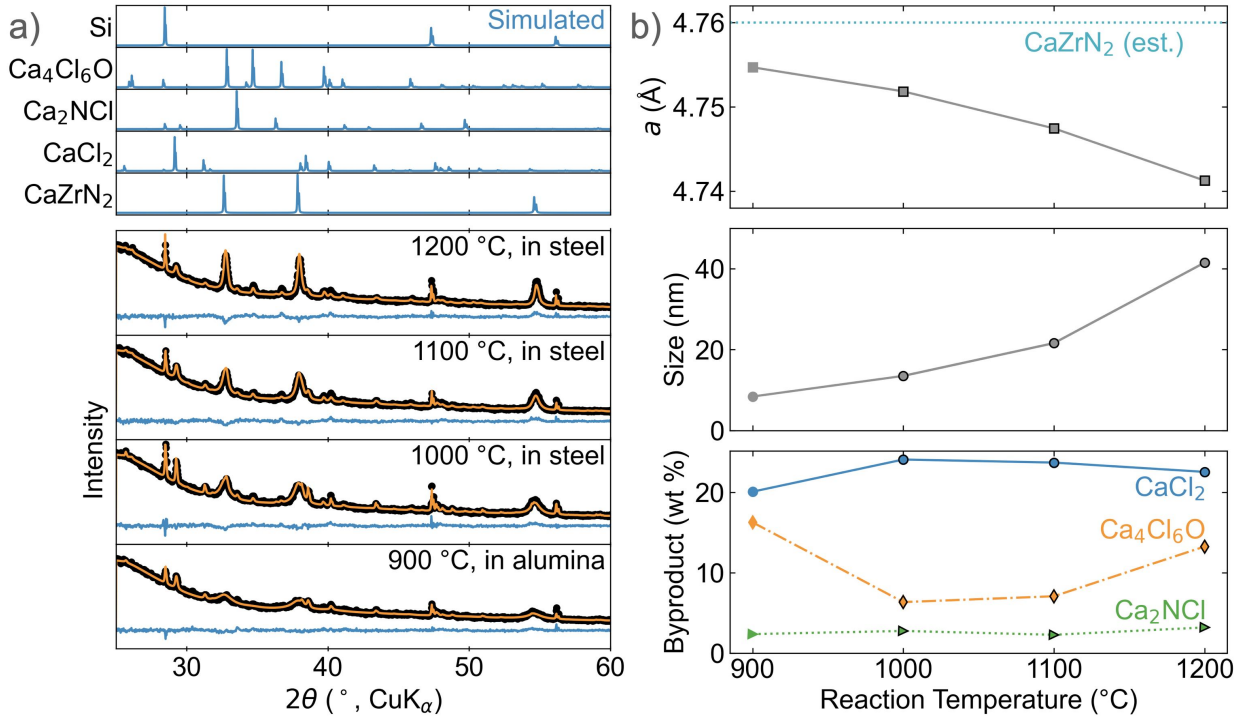

Figure D.3: a) PXRD of reactions between 1.2 $Ca_3N_2 + ZrCl_4$ heated at +5 °C/min to various dwell temperatures (10 min dwell, air quenched). The rocksalt $CaZrN_2$ peaks noticeably sharpen with increasing temperature, but cation ordering of the $R\bar{3}m$ was not detected. b) Rietveld analysis shows that the lattice parameter decreases slightly with increasing temperature (top), consistent with evaporative loss of Ca from the $Ca_xZr_{2-x}N_2$ structure. Crystalline domain size (middle) increases with temperature. Aside from the reaction in the alumina crucible at 900 °C, oxide impurity content in the form of Ca_4Cl_6O also increases slightly at higher temperatures (bottom), suggesting that the sample scavenges oxygen released by the tube. The outlined shapes emphasize reactions conducted in steel crucibles with a graphite getter.

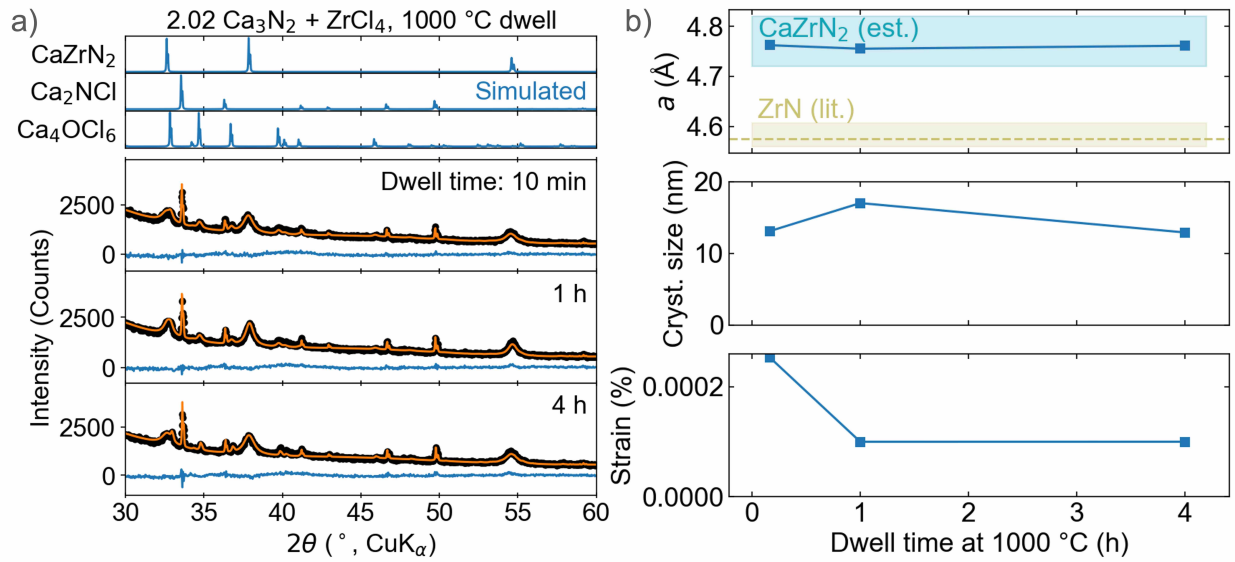

Figure D.4: a) XRD patterns of $CaZrN_2$, produced by a reaction between $2.02Ca_3N_2 + ZrCl_4$ change little as a function of increasing dwell time (dwell temperature = 1000 °C. b) Rietveld analysis shows that the lattice parameters for each $CaZrN_2$ phase are similar as a function of dwell time, and crystallite size and strain also change very little.

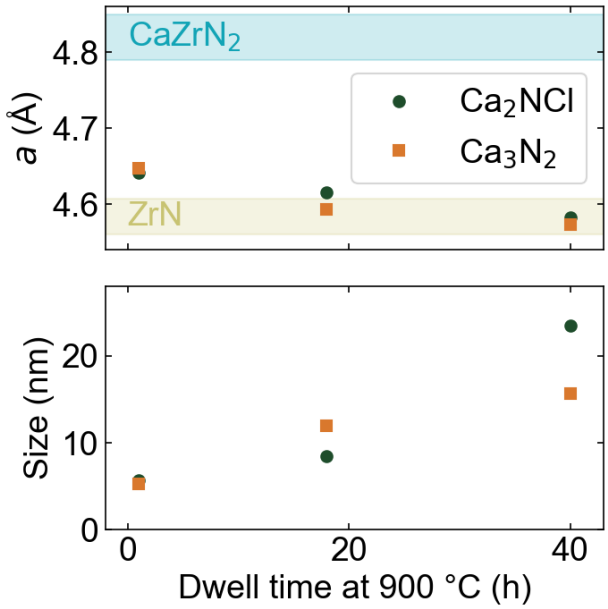

Figure D.5: A time series for reactions conducted targetting the stoichiometric synthesis route to $CaZrN_2$ produced increasingly Ca-poor phases with longer dwell times ($T = 900$ °C).

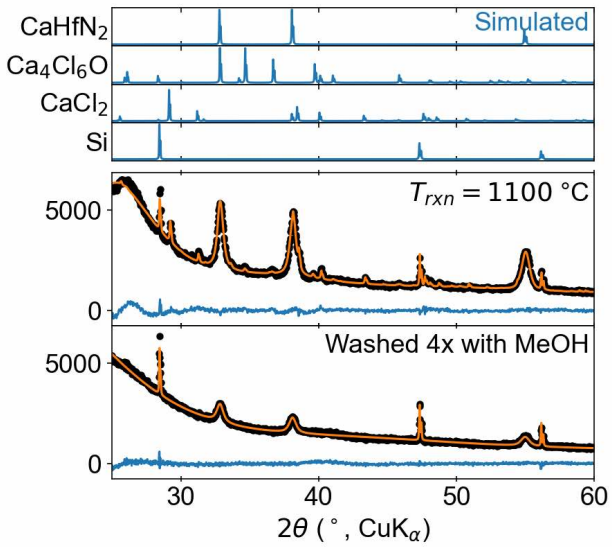

Figure D.6: PXRD patterns of a reaction between $1.21Ca_3N_2 + HfCl_4$ at 1100 °C for 10 min show a product distribution of $CaHfN_2$, $CaCl_2$, and Ca_4Cl_6O. Washing the sample removes the chlorides, leaving behind the $CaHfN_2$. Silicon was added for PXRD as an internal standard.

Ca attributable to $CaHfN_2$. Setting these values as upper and lower bounds for Ca content in $Ca_xZr_{2-x}N_2$ leads to $x = 1.14 \pm 6.6$, near the expected value of 1 for stoichiometric $CaHfN_2$. These findings indicate that $CaHfN_2$ can be synthesized by the same technique that yields $CaZrN_2$.

A ceramic synthesis approach targeting $CaZrN_2$ failed to yield the ternary phase. The reaction should nominally proceed through the stoichiometry of $Ca_3N_2 + 3\,Zr + 2\,N_2 \longrightarrow 3CaZrN_2$, but 40 mol% excess Ca_3N_2 was used to account for any Ca volatility. The reaction yielded only ZrN and substantial amounts of residual Ca_3N_2 indicating that the reaction ceased after the formation of the binary. We observed similar results in the Mg-Zr-N system. ZrN is used as a diffusion barrier in micro-electronics, and so the ceramic route is likely to be kinetically slow.

Figure D.9 shows that PXRD should be able to distinguish $CaZrN_2$ from CaZrNO rocksalt phases based on the lattice parameter. The lattice parameter of the rocksalt nitride $CaZrN_2$ ($a = 4.76$ Å) is larger than the lattice parameter of the hypothetical oxynitride CaZrNO ($a = 4.70$ Å), as estimated by Vegard's law between the rocksalt ZrN ($a = 4.58$ Å) and the

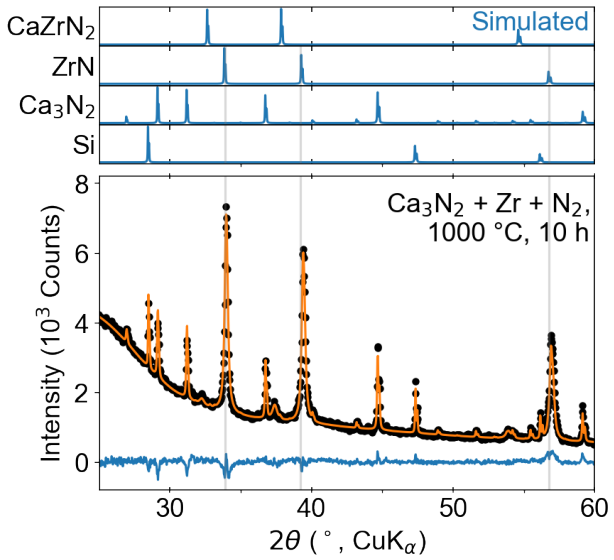

Figure D.7: A control reaction using a traditional ceramic approach of Ca_3N_2 + Zr under flowing N_2 at 1000 °C yielded only ZrN by PXRD, along with unreacted Ca_3N_2. Silicon was added as an internal standard, and the ZrN rocksalt lattice parameter refined to $a = 4.575$ Å. This value is slightly smaller than the reference ZrN, indicated by the grey vertical lines ($a = 4.585$ Å).[152] However, the rocksalt produced here is consistent with N-poor rocksalt phases made by heating Zr powder under flowing N_2 ($ZrN_{0.9}$, $a = 4.577$ Å).[188]

rocksalt CaO ($a = 4.80$ Å). However, the difference in unit cell size between $CaZrN_2$ and CaZrNO is less than the difference in size between $MgZrN_2$ ($a = 4.54$ Å, as we previously reported)[55]) and the hypothetical oxynitride MgZrNO. MgZrNO and CaZrNO have not been reported in literature, although oxynitrides in these phase spaces have been explored near the ZrO2 composition.[189,190] The differences in lattice parameter of these high symmetric cubic phases can be subtle and convoluted, and so additional elemental analysis is needed to verify composition.

Backfilling sealed ampules with a partial pressure of N_2 increased the rocksalt lattice parameter (suggesting greater Ca incorporation) but also introduced oyxgen contamination. Two reactions were conducted with a partial backfill of N_2 in the sealed ampules, starting with reagent mixtures of $1.02Ca_3N_2 + ZrCl_4$ held in alumina crucibles (Figure D.8). These reactions were heated to 1100 °C at a rate of $+5$ °C/min and air-quenched after a 1 min dwell. We hypothesized that increasing $P(N_2)$ would increase the rocksalt lattice

parameter by allowing more Ca to incorporate into the rocksalt, but counter-intuitively, the lower-pressure sample yielded a higher lattice parameter. We attribute this discrepancy to oxygen contamination from the backfill. Notably, only an oxychloride byproduct appears (Ca_4Cl_6O), with no evidence of $CaCl_2$. As CaO is also a rocksalt structure, we can use Vegard's law to show that CaO-$CaZrN_2$ solid solutions would yield a smaller lattice than $CaZrN_2$ alone (Figure D.9).

The synthesis of $CaHfN_2$ can be conducted analogously to the synthesis of $CaZrN_2$. Again, all manipulations were conducted in an Ar glovebox owing to the air and moisture sensitivity of the materials. $HfCl_4$ (Alfa Aesar, 98 % purity metals basis, except for < 2.7 % Zr) was purified once by vapor transport between a 400 °C zone and a 300 °C zone in sealed quartz ampule in a three-zone furnace. The purified halide was ground together with Ca_3N_2 (Alfa Aesar, 98 % purity, used as recieved), pelletized under ca. 300 MPa of pressure (1/4 inch diameter die), loaded into a steel crucible. The steel crucible was loaded into a quartz tube (along with a graphite rod to getter oxygen), transferred from the glovebox to a vacuum manifold using a custom vacuum attachment to prevent air exposure, and sealed under vacuum (< 30 mTorr) with a methane-oxygen torch. Sealed tubes were then heated at +5 °C/min to the specified reaction temperature (T_{rxn}), dwelled for 10 min, and quenched by placing the tube in firebrick on the benchtop. Samples were then recovered in the glovebox and washed four times with 5 mL aliquots of methanol (dried over 4 Å molecular sieves[117]).

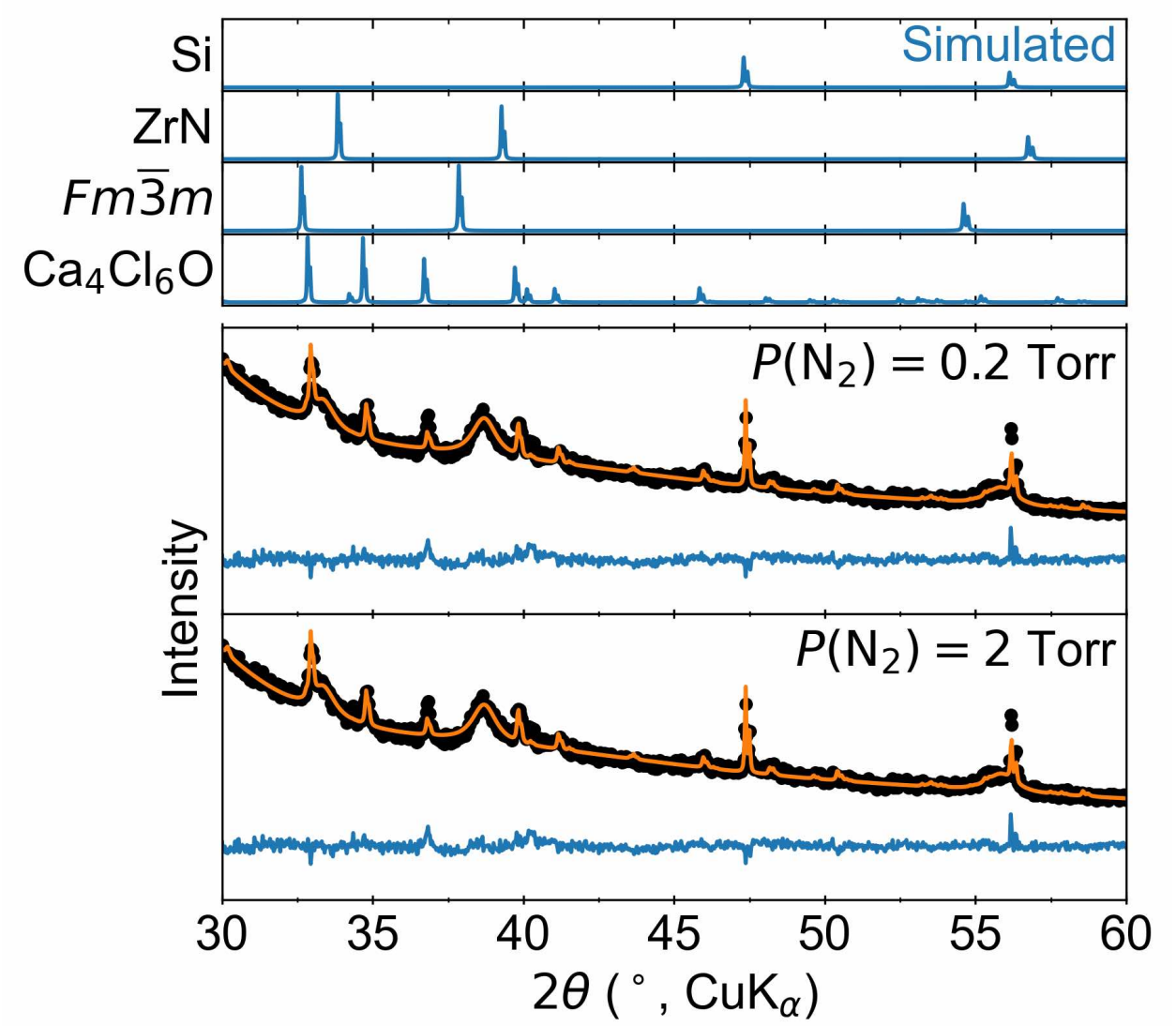

Figure D.8: PXRD of reaction products from two ampules containing precursor mixtures of $1.02Ca_3N_2 + ZrCl_4$ were backfilled with nitrogen to $P(N_2) = 0.2$ Torr (top) and $P(N_2) = 2$ Torr (bottom) at room temperature, then flame sealed. These pressures are approximately 1x and 10x the pressure expected from the decomposition of Ca_3N_2 during these reactions. Rocksalt lattice parameters refined to $a = 4.661$ Å and 4.617 Å, respectively.

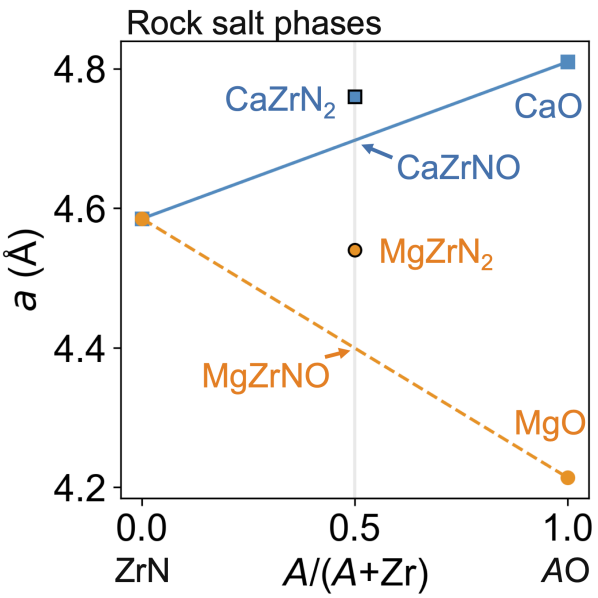

Figure D.9: Comparison of the lattice parameters of nitride, oxynitride, and oxide phases with rocksalt crystal structures in the Ca-Zr-N-O and Mg-Zr-N-O systems. CaZrNO and MgZrNO are hypothetical rocksalt phases extrapolated from a linear combination of ZrN and *A*O.

D.2 EDS analysis

Figure 5.3 includes a representative EDS spectrum for $CaZrN_2$, indicating the clear presence of Ca, Zr, and Cl peaks. The chloride persists despite multiple washes with dry methanol, in which $CaCl_2$ is soluble. As PXRD of washed samples indicate that $CaZrN_2$ is the only crystalline phase (Figure 5.2), we suspect that the Cl comes from small inclusions of $CaCl_2$ and/or Ca_2NCl between the crystalline domains of $CaZrN_2$. Despite thorough grinding of the powders prior to washing, such inclusions would not be accessible to the methanol and therefore could not be removed by this purification technique.

We attempted to account for this impurity when calculating the Ca/(Ca+M) ratios, and thus x in $Ca_xM_{2-x}N_2$ ($x = 2 \times$ Ca/(Ca+M)), by subtracting out Ca attributable to chloride impurities from the raw Ca content (Figure D.10). This subtraction creates a lower bound for Ca in the rocksalt (-Ca_2NCl, dark green trace), as well as an upper bound (-$CaCl_2$, light blue trace). The true Ca content of the $Ca_xM_{2-x}N_2$ lies between these two values. As this range is larger than the error bars from the standard deviations, we omit the error bars from the main plot and show the range as the highlighted region around the middle of this range (Figure 5.3).

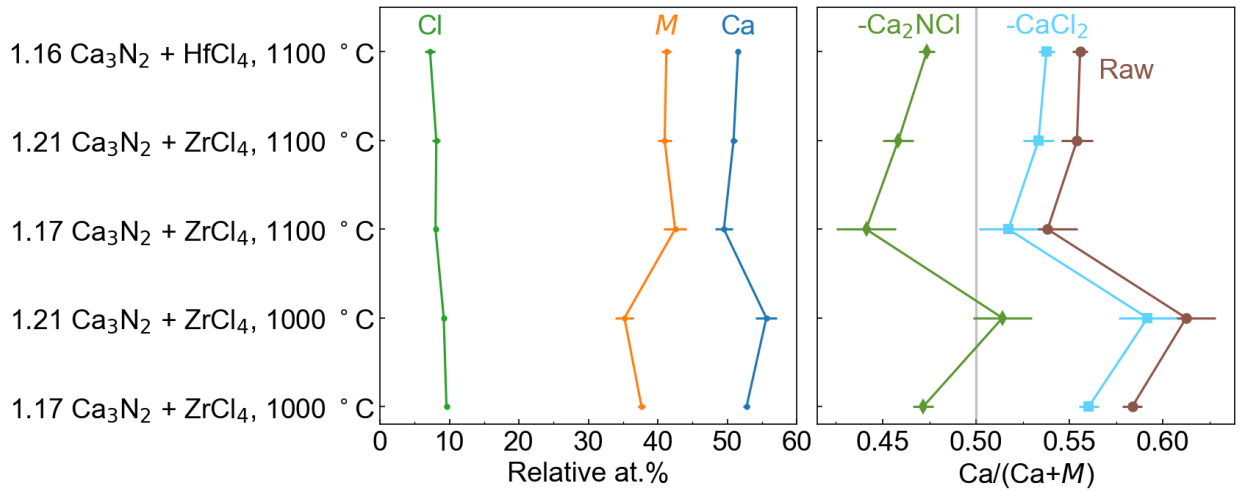

Figure D.10: EDS measurements of washed samples quantifying only Ca, M = (Zr or Hf), and Cl shows that Ca is more abundant than M, and that Cl makes up between 5 and 10 atomic % (left). Owing to this chloride impurity, quantifying the metal ratio using the raw value for Ca/(Ca+M) overestimates the amount of Ca in the $Ca_xM_{2-x}N_2$ structure (brown trace, right). Assuming this chloride is bound to either $CaCl_2$ or Ca_2NCl, we can subtract that amount of Ca in these impurities from the total, and calculate the Ca/(Ca+M) attributable to the rock salt (light blue and dark green traces, respectively). Produces a range of values approximately around the Ca/(Ca+M) = 0.5 expected for $CaMN_2$, indicated by the vertical grey line. Error bars show the standard deviations from the three mapping measurements used to calculate each average.

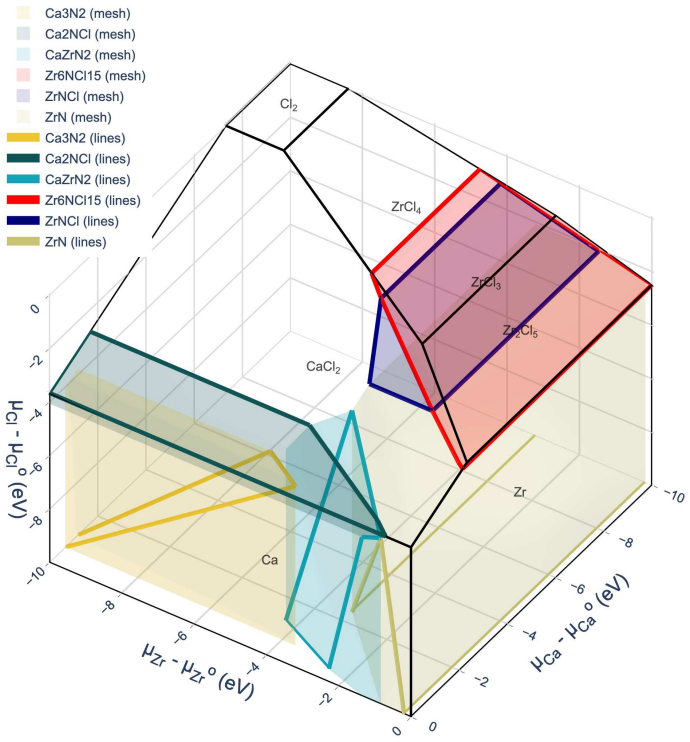

Figure D.11: Un-processed image of Ca-Zr-N-Cl predominance diagram generated by the code showing in Section D.3

D.3 Thermodynamic calculations

Predominance diagrams were generated using the pymatgen package.[101] The following codeblock was used to generate the Ca-Zr-N-Cl diagram shown in Figure D.11.

```
from pymatgen.core.structure import Structure
from pymatgen.entries.compatibility import
    MaterialsProject2020Compatibility
from pymatgen.entries.computed_entries import
    ComputedStructureEntry
from pymatgen.analysis.phase_diagram import PhaseDiagram,
    PDPlotter
```

```
from pymatgen.ext.matproj import MPRester
from rxn_network.thermo.chempot_diagram import ChempotDiagram
from rxn_network.entries.entry_set import GibbsEntrySet

import plotly.express as px

from pymatgen.core.composition import Element
with MPRester() as mpr:
    entries_Ca = mpr.get_entries_in_chemsys(["Ca","Zr","N","Cl"],
        inc_structure="final")
temp = 300+273 #Kelvin
gibbs_entries_CaZr = GibbsEntrySet.from_entries(entries_Ca, temp)
ZrCl3 = gibbs_entries_CaZr.get_min_entry_by_formula("ZrCl3")
gibbs_entries_CaZr.add(gibbs_entries_CaZr.stabilize_entry(ZrCl3))

limits={Element("Ca"): (-10, 0),
        Element("Zr"): (-10, 0),
        Element("Cl"): (-10, 0)}
cd = ChempotDiagram(gibbs_entries_CaZr, limits=limits)

fig = cd.get_plot(elements=["Ca","Zr","Cl"],
    formulas_to_draw=["CaZrN2", 'ZrNCl', 'ZrN', 'Ca2NCl', 'Ca3N2'
       , 'Zr6NCl15',],
    formula_colors = ['#C8C372', #CSU gold, ZrN
          'navy', # navy ZrNCl
          'red', #because Zr6NCl15 is red
          '#12A4B6', #reservoir for CaZrN2
```

```
            '#105456', #dark slate Ca2NCl
            '#ECC530', #sunshine Mg3N2
           ])

aspect_ratio = {"x": 1,"y": 1,"z": .8}

fig.update_scenes({"camera": dict(eye=dict(x=1.2, y=0.8, z=1.2),
    projection=dict(type="orthographic"))});

fig.update_layout(scene = dict(xaxis = dict(nticks=10, range
   =[-10, .05],),
    yaxis = dict(nticks=10, range=[-10.0, 0.05],),
    zaxis = dict(nticks=10, range=[-10.0, 0.05])))
fig.update_layout({"scene_aspectratio": aspect_ratio},
     font_family="Arial")

fig.write_image('CaZrCl_map_labeled.svg')
fig.write_image('CaZrCl_map_labeled.png', scale = 3)
```

Post-processing of the diagram was done in Keynote software to create Figure 5.6A. Analogous code was used to generate the Mg-Zr-N-Cl diagram, simply replacing 'Mg' for 'Ca'.

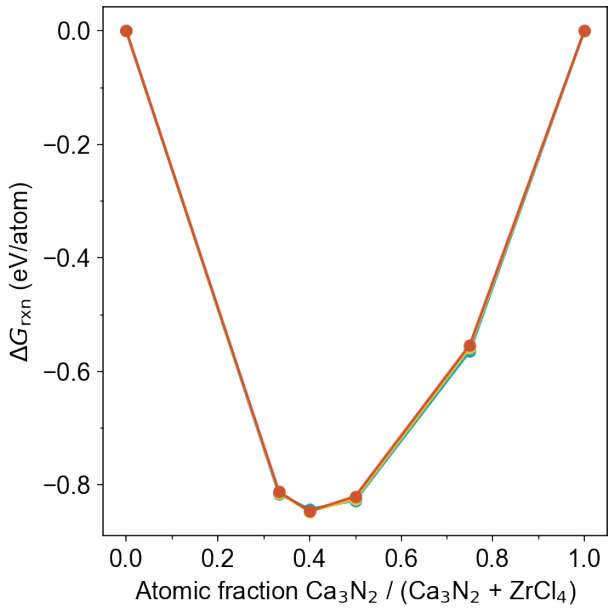

Figure D.12: The full convex hull for the subsection shown in Figure 5.5

Convex hull diagrams (Figure 5.5 and Figure D.12) were calculated as a function of temperature for the $Ca_3N_2 + ZrCl_4$ system using the method described by Bartel et al.[119] and as implemented in pymatgen.[101]

D.4 *In situ* synchrotron PXRD

Stacked diffraction patterns (every 7th scan plotted) for the reactions of $Ca_3N_2 + ZrCl_4$ and $2\,Ca_2NCl + ZrCl_4$ (Figure D.13) as well as $Mg_3N_2 + ZrCl_4$ and $2\,Mg_2NCl + ZrCl_4$ (Figure D.14). These data were fit using sequential Rietveld refinements to produce Figure 5.7. For reference, simulated patterns of the reactants are shown at the bottom of each plot, with simulated patterns of intermediates and product patterns shown in the top box. These structures are also visualized in Figures D.15.

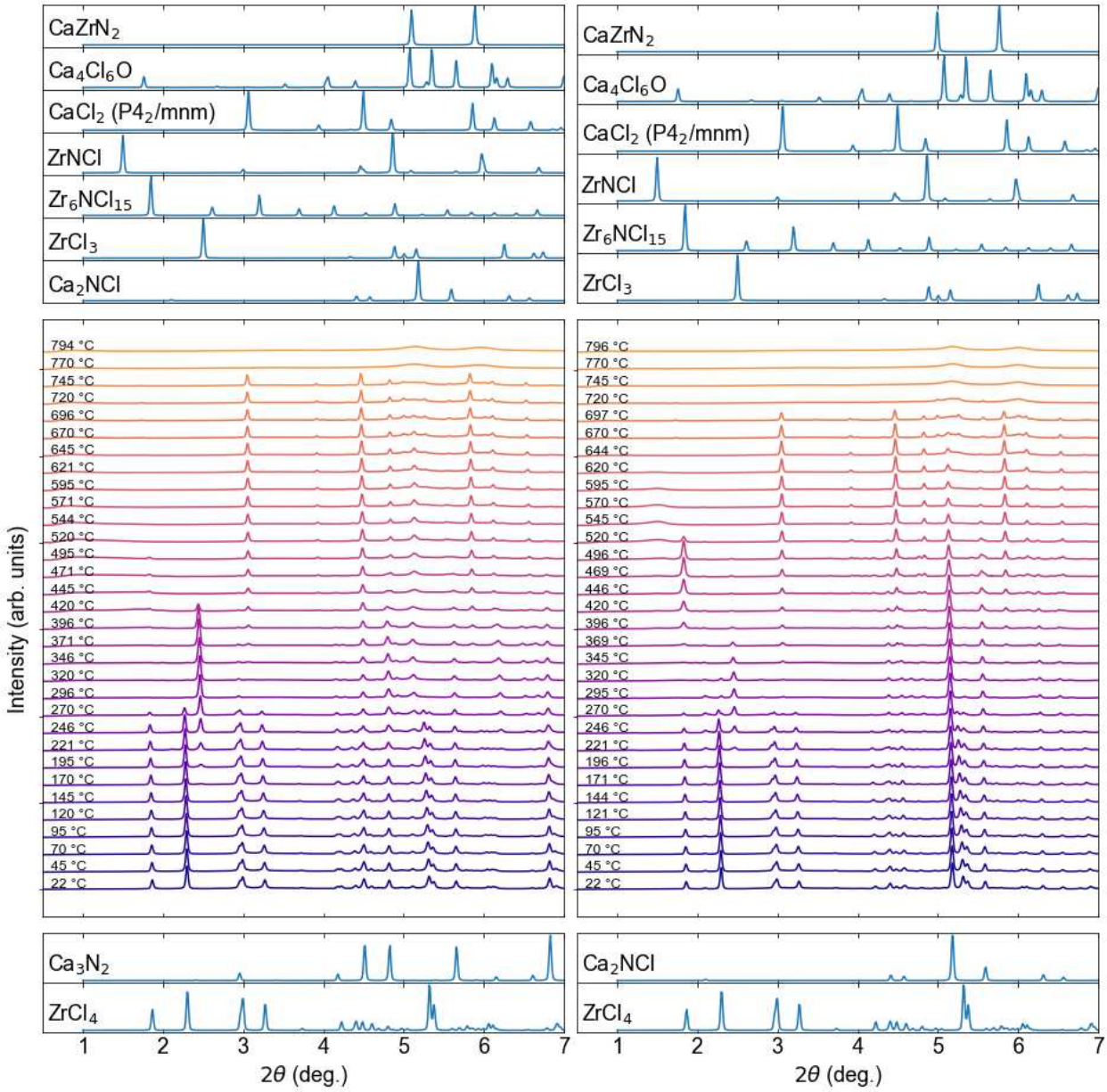

Figure D.13: *In situ* diffraction patterns for the reactions $Ca_3N_2 + ZrCl_4$ (left) compared with $2Ca_2NCl + ZrCl_4$ (right). Simulated patterns for precursors are shown in the bottom boxes, and simulated patterns for the intermediates and products are in the top boxes. Every 10th pattern is plotted from each experiment. Each sample was heated from room temperature to 800 °C at a rate of +5 °C/min. The simulated $CaZrN_2$ pattern assumes a $Fm\bar{3}m$ solid solution rock salt with $a = 4.8$ Å.

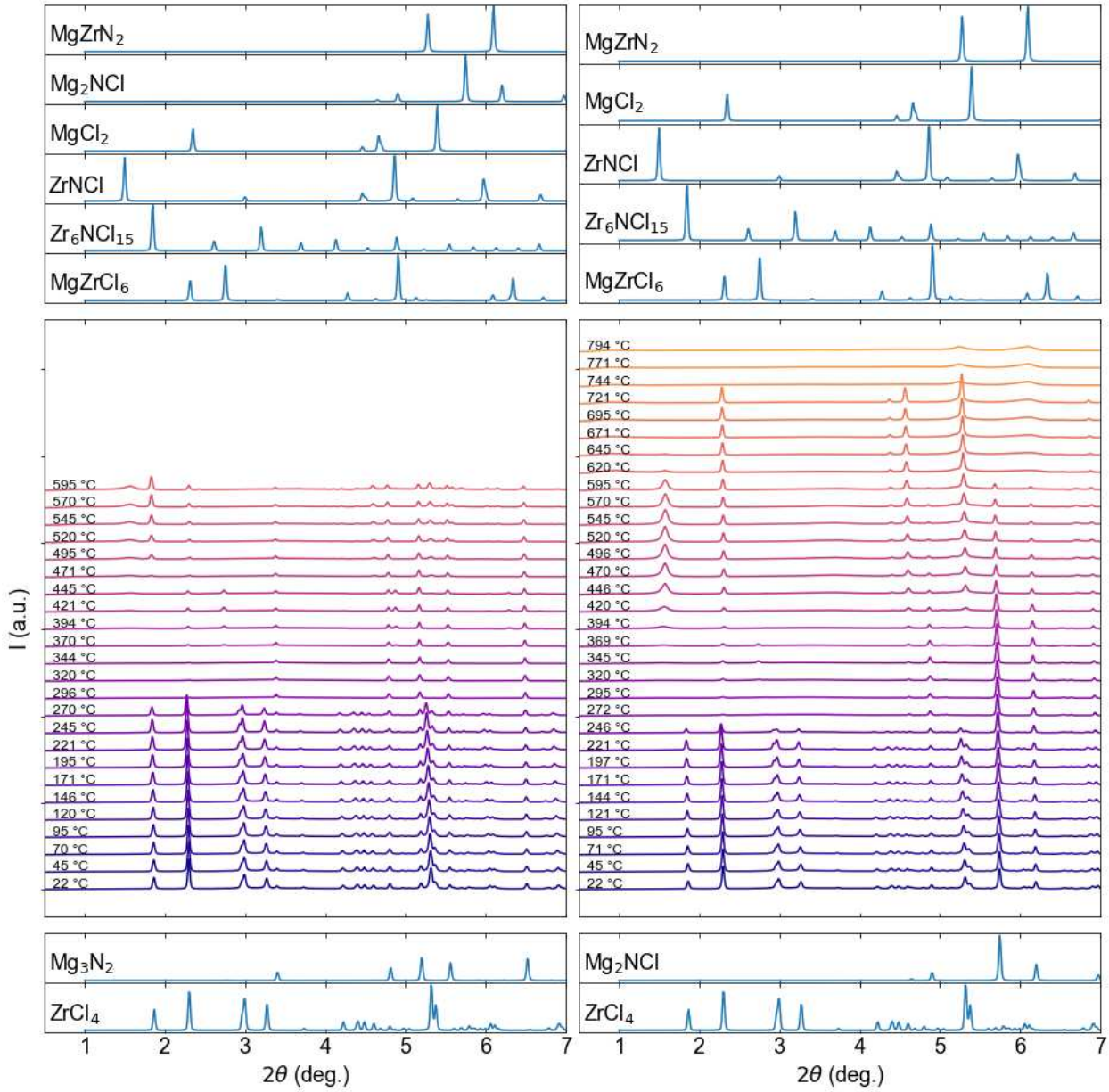

Figure D.14: *In situ* diffraction patterns for the reactions $Mg_3N_2 + ZrCl_4$ (left) compared with $2Mg_2NCl + ZrCl_4$ (right). Simulated patterns for precursors are shown in the bottom boxes, and simulated patterns for the intermediates and products are in the top boxes. Every 10th pattern is plotted from each experiment. Each sample was heated at a rate of $+5$ °C/min from room temperature to 600 °C (for the Mg_3N_2 reaction) and to 800 °C (for the Mg_2NCl reaction).

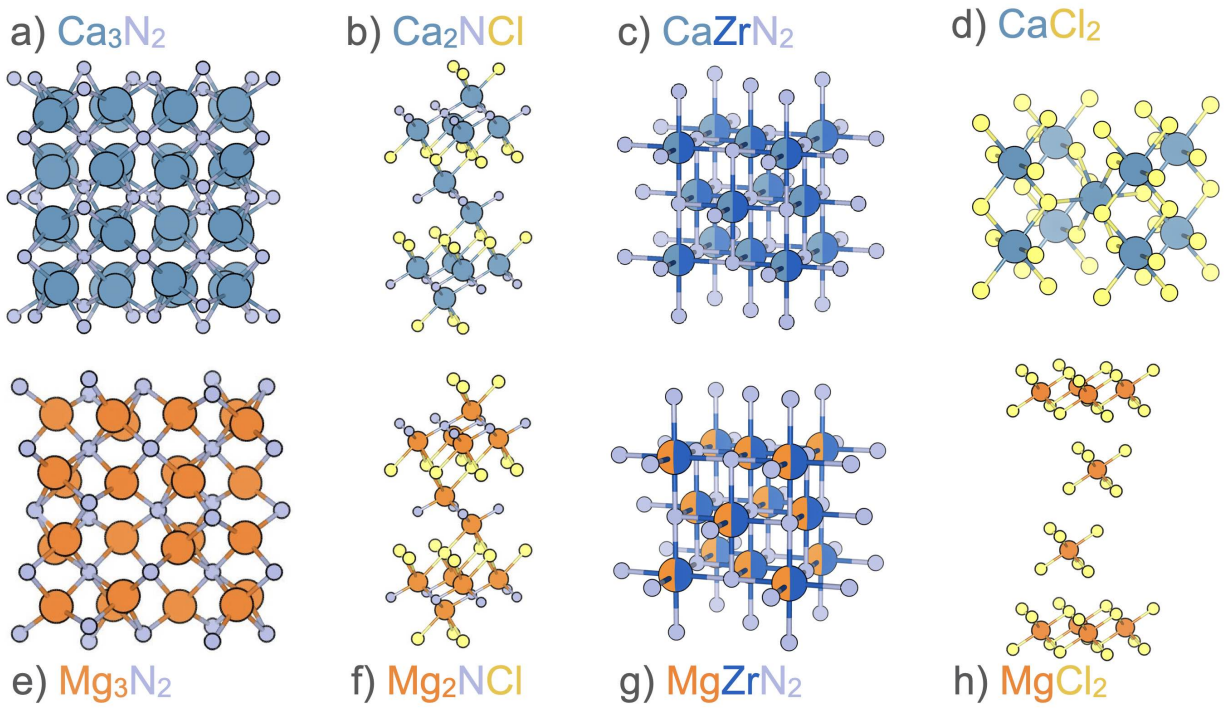

Figure D.15: Unit cells of the reactants and intended products of this study. a) antibixbyite Ca_3N_2 b) Ca_2NCl c) rock salt $CaZrN_2$ d) $CaCl_2$ and magnesium analogues e) Mg_3N_2 f) Mg_2NCl g) rock salt $MgZrN_2$ h) $MgCl_2$.